THÈSE

En vue de l'obtention du

DOCTORAT DE L'UNIVERSITÉ DE TOULOUSE

Délivré par :

Institut National Polytechnique de Toulouse (INP Toulouse)

Discipline ou spécialité :

Hydrologie, Hydrochimie, Sols, Environnement

Présentée et soutenue par :

Mme JIANWEI GUO

le mardi 22 septembre 2015

Titre :

MODELISATION NUMERIQUE DE LA DISSOLUTION DES CAVITES KARSTIQUES

Ecole doctorale :

Sciences de l'Univers de l'Environnement et de l'Espace (SDUEE)

Unité de recherche :

Institut de Mécanique des Fluides de Toulouse (I.M.F.T.)

Directeur(s) de Thèse :

M. MICHEL QUINTARD

Rapporteurs :

M. FABRICE GOLFIER, ECOLE NATIONALE SUPERIEURE DE GEOLOGIE

M. PHILIPPE ACKERER, UNIVERSITE STRASBOURG 1

Membre(s) du jury :

M. DAVID LABAT, UNIVERSITE TOULOUSE 3, Président

M. JEAN-PAUL SERIN, UNIVERSITE DE PAU ET DES PAYS DE L ADOUR, Membre

M. JOEL BILLIOTTE, MINESPARISTECH, Membre

M. MICHEL QUINTARD, INP TOULOUSE, Membre

Modélisation numérique de la dissolution des cavités karstiques

Résumé

La dissolution de cavités karstiques appelle à une description multi-échelle. A partir d'une discussion des hypothèses les plus fréquemment utilisées, un modèle à l'échelle du pore (ou micro-échelle) est développé pour des schémas réactifs géochimiques simples. L'impact du choix de conditions aux limites réactives ou équilibre thermodynamique est discuté. Ce modèle à l'échelle du pore est ensuite utilisé pour le développement de modèles aux échelles supérieures.

Le premier problème traité considère le transport sur une surface chimiquement hétérogène et rugueuse, caractérisée par une condition mixte pour le transfert de masse. Le modèle résultant est un modèle de *surface effective* (ESCM). Dans ce modèle, la surface initiale est remplacée par une surface localement lisse et homogène sur laquelle des conditions aux imites effectives sont imposées. Un exemple typique correspond à un écoulement laminaire sur une surface soluble contenant des particules de matière insoluble. Le concept de surface effective est développé à l'aide d'une méthode de décomposition de domaine. Dans ce contexte, vitesse, pression et concentration à la petite échelle près de la surface sont estimées par une méthode de développement asymptotique par rapport aux champs loin de la surface. Des problèmes de fermeture sont alors obtenus qui sont utilisés pour définir la position de la surface effective et les conditions aux limites effectives associées. L'effet sur les propriétés effectives de la position de la surface, des nombres de Reynolds, Schmidt et Damköhler est étudié. Une comparaison entre des résultats numériques à petite échelle avec ceux obtenus par le modèle effectif montre un bon accord.

Dans le cas du transport dans un milieu poreux, le deuxième problème de changement d'échelle étudié, une méthode de changement d'échelle basée sur la prise de moyenne spatiale est proposée (PMM) à partir du problème à l'échelle du pore avec des conditions aux limites d'équilibre thermodynamique ou réactives non-linéaires. Une expression générale du modèle macroscopique est obtenue impliquant plusieurs propriétés effectives qui sont données par la résolution de problèmes de fermeture à l'échelle du pore. Pour une cellule unitaire représentative stratifiée, les paramètres effectifs sont obtenus analytiquement ou numériquement, alors que les propriétés pour des cellules plus complexes 2D/3D sont obtenus numériquement. L'impact sur les paramètres effectifs des propriétés physiques à l'échelle du pore (en terme de nombre de Péclet, Damköhler et ordre de la réaction) est étudié pour des cellules unitaires

1D, 2D ou 3D. On montre que la tortuosité joue un rôle important dans les cas 2D et 3D, tandis qu'elle n'intervient pas classiquement pour le cas de cellules stratifiées. Quand le nombre de Damköhler est très petit, le coefficient de réaction effectif est identique à celui à l'échelle du pore, puis le modèle tend vers une situation équivalente à la condition d'équilibre thermodynamique lorsque le nombre de Damköhler devient très grand. En conséquence, le terme d'échange dans le bilan de masse macroscopique prend des formes mathématiques différentes. Un exemple d'application du modèle macroscopique est présentée en mettant l'accent sur l'apport potentiel des termes additionnels non-classiques sur la précision des prédictions.

Le modèle macroscopique de dissolution de milieu poreux est aussi utilisé comme un modèle à interface diffuse (DIM) pour décrire la dissolution d'une cavité à grande échelle, une cavité de gypse dans l'illustration traitée dans la thèse. Le modèle est basé sur l'approximation de pseudo-constituant, avec une condition d'équilibre à l'échelle du pore sur l'interface fluide-solide. Une méthodologie numérique est proposée pour choisir correctement les paramètres effectifs du DIM de façon à reproduire avec suffisamment de précision les flux et la vitesse de récession de l'interface. Une étude spécifique est effectuée sur l'impact du choix du modèle de bilan de quantité de mouvement macroscopique. De manière intéressante, les résultats numériques ne suggèrent pas un impact très important de ce choix dans le cas des problèmes aux limites traités. Des calculs ont aussi été effectués, dans le cadre d'une approximation de Boussinesq, pour évaluer l'impact éventuel de mouvements de convection naturelle. Les résultats indiquent un impact faible dans le cas de dissolution de cavités de gypse. Le potentiel de la méthode est illustré dans deux cas: un correspondant à une lentille de gypse dans un aquifère, l'autre au cas d'un pilier isolé dans une carrière souterraine. Les conséquences de la dissolution sur la stabilité mécanique sont étudiées à l'aide d'un modèle géomécanique simplifié. Enfin, un cas test est étudié montrant la possibilité d'utiliser le modèle dans le cas de dissolution d'une cavité saline, matériau plus soluble que le gypse.

Numerical modeling of the dissolution of karstic cavities

Abstract

The karstic cavity dissolution problems encountered worldwide are often studied from a hierarchical point of view. Based on a discussion of the frequently adopted assumptions, a pore-scale (or micro-scale) model is first developed for a simple geochemistry scheme. The impact of implementing reactive or thermodynamic equilibrium boundary condition at the dissolving surface is discussed. Such a pore-scale model is subsequently used as a basis for developing models at higher scale levels.

The first problem deals with transport from a heterogeneous and rough surface characterized by a mixed boundary condition. The resulting macro-scale model takes the form of an effective surface theory. In the homogenized model developed with the effective surface concept (denote ESCM), the original rough surface is replaced locally by a homogeneous and smooth surface, where effective boundary conditions are prescribed. A typical example corresponds to a laminar flow over a soluble salt medium which contains insoluble material. To develop the concept of effective surface, a multi-domain decomposition approach is applied. In this framework the velocity, pressure and concentration are estimated at the micro-scale with an asymptotic expansion of deviation terms with respect to macro-scale velocity and concentration fields. Closure problems for the deviations are obtained and used to define the effective surface position and the corresponding boundary conditions. The evolution of some effective properties and the impact of surface geometry, Reynolds (Re), Schmidt (Sc) and mean Damköhler ($\widehat{\mathrm{Da}}$) numbers are investigated. A comparison between the numerical results obtained with this effective model and those from direct numerical simulations with the original rough surface shows good agreements.

In the case corresponding to mass transport in porous media, upscaling is carried out with the method of volume averaging to develop a macro-scale porous medium model (denote PMM), starting from a pore-scale transport problem involving thermodynamic equilibrium or nonlinear reactive boundary conditions. A general expression to describe the macro-scale mass transport is obtained involving several effective parameters which are given by specific closure problems. For a representative unit cell with a simple stratified geometry, the effective parameters are obtained analytically and numerically, while for those with complicated geometries, the effective parameters are only obtained numerically by solving the corresponding closure problems. The im-

pact on the effective parameters of the fluid properties, in terms of pore-scale Péclet number (Pe), and the process chemical properties, in terms of pore-scale Damköhler number (Da) and reaction order (n), is studied for periodic stratified, 2D and 3D unit cells. It is found that the tortuosity effects play an important role on the longitudinal dispersion coefficient in the 2D and 3D cases, while it is negligible for the stratified geometry. When Da is very small, the effective reaction rate coefficient is nearly identical to the pore-scale one, while when Da is very large, the reactive condition turns out to be equivalent to pore-scale thermodynamic equilibrium, and the macro-scale mass exchange term is consequently given in a different form from the reactive case. An example of the application of the macro-scale model is presented with the emphasis on the potential impact of additional, non-traditional effective parameters appearing in the theoretical development on the improvement of the accuracy of the macro-scale model.

The above developed macro-scale porous medium model is also used as a Diffuse Interface Model (DIM) to describe the evolution of a gypsum cavity formation induced by dissolution. The method is based upon the assumption of a pseudo-component dissolving with a thermodynamic equilibrium boundary condition. A methodology is proposed based on numerical computations with fixed boundaries in *order to choose suitable parameters* for the DIM model and hence predict the correct dissolution fluxes and surface recession velocity. Additional simulations are performed to check which type of momentum balance equation should be used. The numerical results did not show a strong impact of this choice for the typical initial boundary value problems under consideration. Calculations with a variable density and Boussinesq approximation were also performed to evaluate the potential for natural convection. The results showed that the impact of density driven flows were negligible in the cases under investigation. The potential of the methodology is illustrated on two large-scale configurations: one corresponding to a gypsum lens contained within a porous rock layer and the other to an isolated pillar in a flooded gypsum quarry. Geomechanical consequences of the dissolution in terms of mechanical stability is evaluated with the help of a simplified geomechanical model. A final case is also studied in which gypsum is replaced by salt to show the applicability of the proposed methodology to a rapidly dissolving material.

Acknowledgement

I would like first to express my infinite gratitude to my supervisor, Michel Quintard, who made every effort in the past four years to help me complete the PhD study, introducing the fundamental principles of transport phenomena to me, teaching me the way of doing research, encouraging and guiding me to go further to investigate the unknowns, etc. It is a great honor to have had this opportunity to work with Michel and I am also grateful for his patience, without which I would not have had the courage and confidence to finish the PhD works.

I want to express my thanks to some important coworkers, Farid Laouafa, Stéphanie Veran-Tissoires and Haishan Luo, who are easy-going and offered me a lot of useful discussions and strong support during the collaboration.

A special friend, who accompanied me the longest time during the PhD study is the software COMSOL Multiphysics. Even though sometimes I really hate it when it did not work well, I should be grateful for the results it gave me for all the numerical simulations.

The financial support of China Scholarship Council is greatly appreciated. I am also grateful to Wei Huang and Bo Wang in Changjiang River Scientific Research Institute for their assistance in applying this scholarship.

The staff in the administrative and information technique department of IMFT, Celine Perles, Yannick Exposito and Pierre Fauret are appreciated for their kind assistance when I needed help. The secretary of SDU2E, Marie-Claude Cathala is appreciated for her patient response to all my questions.

Appreciations are also expressed to the group members of GEMP for their assistance in my daily life, for the happy time during the coffee break and for their teaching of "Tarot" :-) Sylvie Lorthois, Suzy Bernard, Rachid Ababou, Ruddy Soeparno, Cyprien Soulaine, Sophie Roman, Philippe Lefort, Yohan Davit, Hossein Davarzani, Laetitia Mottet, Benjamin Straubhaar, Mauricio Duenas Velasco, Sylvain Pasquier, Nahla Mansouri, Myriam Peyrounette, Fréderic Pierre, Jacques Franc and Ange Gourbil, thank you all!

I want to thank Sithan and Sovan Lek for their kind help to facilitate my life in Toulouse and many invitations of dinner at their home. My thanks are also expressed to the Chinese friends here, Haishan Luo, Yiming Gu, Qinglian Li, Jingmei Yao, Le Han, Lu Li, Chen Yang, Chen Chen, Qing Lv, Lina Zhang and Lingguo Du. It was good memory to celebrate the Chinese festivals together and sometimes to travel with you.

At last, I want to express my sincere thanks to my parents and my sisters for their deep love, their endless encouragement and their forever support. Special thanks are expressed to my husband, who is always standing by me to share his happiness with me, to encourage and help me overcome the hard times, to organize very well of our life and to give me a great happiness of being loved.

Contents

List of Figures

List of Tables

Nomenclature

Roman symbols

$\mathbf{A}$	closure variable for the velocity, dimensionless
a	closure variable for the concentration, dimensionless
a_{vl}	specific area, m^{-1}
A_0	fictitious surface separating Ω_0 and Ω_i
$A_{0,i}$	restriction of A_0 in Ω_i
A_e	upper surface of Ω
A_{eff}^c	effective surface under thermodynamic equilibrium
A_{eff}^v	effective surface with no-slip boundary condition
A_l	lateral surface of Ω
A_{li}	interfacial area between the liquid phase and the insoluble material, m^2
$A_{l,i}$	periodic lateral surface of Ω_i
A_{ls}	interfacial area between the liquid phase and the soluble material, m^2
A_r	rough solid-liquid interface
$\mathbf{B}$	closure variable for the velocity, m
b	closure variable for the concentration, m
$\mathbf{b}_l$	closure variable for the mass fraction, m
b_r	roughness width, m
c	$= \rho_l \omega_l$, mass concentration of the dissolved species defined in Ω, kg m^{-3}
c_{eq}	thermodynamic equilibrium concentration of the dissolved species, kg m^{-3}
c_s	mass concentration of the dissolved species defined at A_{ls}, kg m^{-3}
c_i	concentration of the dissolved species defined in Ω_i, kg m^{-3}

$\tilde{c_i}$	concentration deviation of the dissolved species in Ω_i, kg m^{-3}
c_0	concentration of the dissolved species defined in Ω_0, kg m^{-3}
d_0	diameter of the spheres in the 2D and 3D unit cells, m
D_0, D_l	diffusion coefficient, m^2 s^{-1}
$\mathbf{D}_l$, $\mathbf{D}_l^*$	dispersion tensor, m^2 s^{-1}
Da	Damköhler number, dimensionless
Da*	macro-scale Damköhler number, dimensionless
Da_{eff}^v	effective Damköhler number at A_{eff}^v, dimensionless
$\widehat{\mathrm{Da}}$	mean Damköhler number over surface A_r, dimensionless
$\mathbf{e}_1$	unit normal vector linked to x, dimensionless
$\mathbf{e}_2$	unit normal vector linked to y, dimensionless
$\mathbf{g}$	gravity, m s^{-2}
h_r	roughness height, m
$\mathbf{h}_l$, $\mathbf{h}_l^*$	additional gradient term coefficient, mol m^{-1} s^{-1}
k	reaction rate coefficient at A_r, m s^{-1}
K_g, K_{Ca}	mass exchange of the dissolving solid (gypsum) and Ca respectively, kg m^{-3} s^{-1}
K_0, K_f, K_l	permeability, m^2
$\mathbf{K}_l$	permeability tensor, m^2
k_{ls}	reaction rate coefficient at A_{ls}, m s^{-1}
k_{li}	reaction rate coefficient at A_{li}, m s^{-1}
k_{eff}^0	effective reaction rate coefficient at $y = 0$, m s^{-1}
k_{eff}^c	effective reaction rate coefficient at A_{eff}^c, m s^{-1}
k_{eff}^v	effective reaction rate coefficient at A_{eff}^v, m s^{-1}
k_{eff}^w	effective reaction rate coefficient at $y = w$, m s^{-1}
$\hat{k}^v$	surface average reaction rate coefficient at A_{eff}^v, m s^{-1}
k_s	surface reaction rate constant, mol m^{-2} s^{-1}
$k_{s,eff}$	effective reaction rate coefficient, mol m^{-2} s^{-1}
$l_\star$	micro-scale characteristic length, m
w_{cell}	width of Ω_i, m
L, L_r	macro-scale characteristic length, m
m	closure variable for the pressure, Pa s m^{-1}
M_g, M_{Ca}	molar weight of the dissolving solid (gypsum) and Ca respectively, g mol^{-1}

n	chemical reaction order, dimensionless
$\mathbf{n}_{li}$	normal vector pointing from the liquid towards the insoluble medium, dimensionless
$\mathbf{n}_{ls}$	normal vector pointing from the liquid towards the soluble solid, dimensionless
$\mathbf{n}_{0,i}$	unit normal vector on $A_{0,i}$ pointing towards the wall, dimensionless
p	global pressure, Pa
P	Darcy-scale pressure, Pa
p_0	pressure defined in Ω_0, Pa
p_i	pressure defined in Ω_i, Pa
Pe	micro-scale Péclet number, dimensionless
Pe^*	macro-scale Péclet number, dimensionless
$\tilde{p}_i$	pressure deviation defined in Ω_i, Pa
R_{diss}	surface reaction rate, mol $\mathrm{m}^{-2}\,\mathrm{s}^{-1}$
Re	micro-scale Reynolds number, dimensionless
Re_L	macro-scale Reynolds number, dimensionless
s	closure variable for the pressure, Pa s
s_l	closure variable for mass fraction of Ca, dimensionless
S_l	$= \varepsilon_l/\varepsilon$, fluid saturation
S_s	$= \varepsilon_s/\varepsilon$, solid gypsum saturation
Sc	micro-scale Schmidt number, dimensionless
Sh	Sherwood number, dimensionless
T	temperature, °C
u_l	x-component of the pore-scale velocity, $\mathrm{m\,s}^{-1}$
$\mathbf{u}$	fluid velocity defined in Ω, m s^{-1}
$\mathbf{u}_i$	fluid velocity defined in Ω_i, m s^{-1}
$\tilde{\mathbf{u}}_i$	fluid velocity deviation in Ω_i, m s^{-1}
$\mathbf{u}_0$	fluid velocity defined in Ω_0, m s^{-1}
U	magnitude of macro-scale velocity, m s^{-1}
$\mathbf{U}_l^*$	effective liquid velocity, $\mathrm{m\,s}^{-1}$
$\mathbf{v}_l$	pore-scale liquid velocity, $\mathrm{m\,s}^{-1}$
$\langle \mathbf{v}_l \rangle$	superficial average of the pore-scale liquid velocity, $\mathrm{m\,s}^{-1}$
$\langle \mathbf{v}_l \rangle^l$	intrinsic average of the pore-scale liquid velocity, $\mathrm{m\,s}^{-1}$
$\tilde{\mathbf{v}}_l$	deviation of pore-scale liquid velocity, $\mathrm{m\,s}^{-1}$
V	total volume of a representative unit cell, m^3

V_l	volume of the liquid phase within a representative unit cell, m^3
$\mathbf{V}_l$	Darcy-scale filtration velocity, $m\,s^{-1}$
V_s	volume of the soluble medium within a representative unit cell, m^3
w_x^c	distance between A_0 and A_{eff}^c, m
w_x^v	distance between A_0 and A_{eff}^v, m
$\mathbf{w}_{sl}$	interface velocity between the soluble solid and the liquid phase, $m\,s^{-1}$
x	abscissa, m
y	ordinate, m
Greek symbols	
α_0, α	mass exchange coefficient, s^{-1}
α_{DNS}, α_L	apparent reactive coefficient, s^{-1}
δ	effective surface position, m
δ_c, δ_v	position of effective surface under thermodynamic equilibrium and no-slip condition, respectively, dimensionless
δ_D, δ_{lc}, δ_{lv}	thickness of the diffusive interface, the mass boundary layer and the velocity boundary layer, respectively
ε	total volume fraction of the liquid phase and the soluble solid phase
ε_l, ε_s	volume fraction of the liquid phase and the soluble solid respectively, dimensionless
μ_l	fluid dynamic viscosity, Pa s
μ_l^*	effective fluid dynamic viscosity, Pa s
ρ_l	fluid density, kg m^{-3}
ρ_s	density of soluble medium, kg m^{-3}
ρ_i	density of insoluble material, kg m^{-3}
ω_{eq}	equilibrium mass fraction of Ca, dimensionless
ω_l, ω_s	mass fraction of Ca in the liquid and the soluble solid phase respectively, dimensionless
ω_b	bulk mass fraction, dimensionless
$\langle\omega_l\rangle^l$	intrinsic average of the mass fraction of Ca in the liquid phase, dimensionless
$\tilde{\omega}_l$	deviation of mass fraction of Ca in the liquid phase, dimensionless

Ω	global domain
Ω_0	subdomain associated with length scale L
Ω_i	pseudo-periodic unit cell
Ω_l	Darcy-scale mass fraction of the dissolved species

Introduction en français

La dissolution de cavités, et plus généralement de milieux poreux, est une problématique qui se retrouve dans de nombreux domaines [10–13]. Dans cette thèse, on s'intéresse plus précisément à la dissolution de milieux naturels, soit causée par une action volontaire, comme dans le "solution mining", soit comme conséquence des écoulements souterrains (sur lesquels une action anthropique n'est d'ailleurs pas à exclure). Sur ce dernier aspect on considérera principalement la genèse et l'évolution des karsts. La dissolution des karsts peut conduire à des sites touristiques remarquables (comme par exemple Tsingy de Bemaraha Strict Nature Reserve, à Madagascar, Fig. 1.1[1]). Les karsts interviennent aussi de manière très importante dans la gestion des ressources en eau. Enfin, la dissolution de cavités souterraines est aussi un danger potentiel pouvant conduire à l'effondrement de structures de tailles très importantes ("sinkhole" dans le texte en anglais) [14–16] (Figs. 1.3 et 1.4). Les structures qui motivent ce travail sont marquées par l'existence de plusieurs échelles caractéristiques, comme cela est illustré par exemple sur la Fig. 1.1. Cette thèse s'intéresse au développement de méthodes permettant de prendre en compte cet aspect multi-échelle au cours de diverses étapes de modélisation. C'est donc sur le transport dans un système multi-échelle complexe que l'accent est mis, au détriment de la complexité géochimique, qui sera traitée de manière beaucoup plus schématique dans ce manuscrit. Ces questions préalables sont traitées dans le chapitre 2.

Les diverses situations multi-échelles envisagées sont schématisées Fig. 1.7. La dissolution peut avoir lieu à la surface d'une roche soluble, qui peut être imperméable. Elle peut avoir lieu à l'intérieur du domaine rocheux si celui-ci est perméable (milieu poreux). On peut identifier les situations suivantes:

1. la dissolution d'une paroi imperméable pose souvent un problème de changement d'échelle. Les parois naturelles sont en effet souvent affectées par des rugosités et des hétérogénéités, à une échelle bien inférieure

[1] http://extra-velganza.blogspot.fr/2012/03/tsingy-de-bemaraha-strict-nature.html

le plus souvent à celle de la cavité que l'on souhaite modéliser. Il est donc intéressant de voir si on peut remplacer cette surface affectée de variations à petite échelle par une surface localement lisse et homogène, affectée de conditions aux limites effectives. Une telle problématique est celle de la mise en place d'une surface effective, problème qui sera traité au chapitre 3. La méthodologie utilisée pour atteindre ce but est celle d'une méthode de décomposition de domaine, avec un raccordement entre les équations de bilan dans le grand volume de la cavité et celles dans un volume élémentaire contenant un motif de la surface rugueuse et hétérogène. Deux points cruciaux sont en particulier examinés: (i) la position de la surface effective, (ii) les valeurs de conditions aux limites effectives à utiliser pour reproduire au mieux les champs à grande échelle.

2. la description macroscopique de la dissolution d'un milieu poreux. Il s'agit d'un problème de dispersion active, c'est à dire en présence d'une réaction chimique sur l'interface liquide/milieu soluble. Plusieurs cas ont été déjà traités dans la littérature. La thèse (chapitre 4) propose une extension de ces cas dans les directions suivantes: (i) la condition à l'interface liquide/soluble est du type réactive non-linéaire, avec un terme de réaction chimique, utilisé par exemple pour décrire la dissolution de gypse ou carbonate, (ii) sur le plan de la technique mathématique de changement d'échelle, qui est une théorie de prise de moyenne des équations microscopiques, la prise en compte des termes vitesse de l'interface de manière complète apporte des éclairages plus rigoureux sur l'apparition de certains termes dans les équations macroscopiques, (iii) la théorie produisant des termes complémentaires par rapport aux termes "classiques" de dispersion et de réactivité effective, l'impact de ceux-ci est étudié sur un cas macroscopiquement mono-dimensionnel et validé par simulation numérique directe.

Dans un dernier chapitre, un "workflow" est proposé pour aborder sur un cas de cavité réelle la mise en oeuvre de modèles de dissolution à interface diffuse (c'est à dire ne réclamant pas un suivi explicite de l'interface de dissolution). Plusieurs difficultés sont en effet rencontrées: (i) l'interface diffuse a une épaisseur qui peut venir interférer avec les couches limites massiques et visqueuses, (ii) les temps de dissolution peuvent être très longs, la forme des cavités très affectés par l'hydrodynamique, rendant une convergence aux paramètres numériques dans les cas 3D réels difficile à maîtriser. Ces divers aspects sont abordés à partir de plusieurs exemples:

1. un cas 2D d'une structure aquifère avec une lentille de gypse pouvant conduire à une situation de "sinkhole",
2. le cas de la dissolution d'un pilier de gypse dans une carrière souterraine,
3. la dissolution par "solution mining" d'une cavité de sel à partir d'un puits double.

Une première tentative, très simplifiée, est également proposée, en couplant le modèle de dissolution à un modèle géomécanique, pour estimer de manière plus quantitative le couplage entre la dissolution et les risques d'endommagement mécanique.

Chapter 1

Introduction

Dissolution of underground cavities and porous media can be found in many fields, such as solution salt mining, the formation of karstic structures, acid injection in petroleum engineering, CO_2 storage, etc, [10–13]. Among these different mentioned fields, karst, which results from the dissolution of soluble rocks, is particularly important because it characterizes almost one fifth of the continents and are particularly vulnerable to environmental problems such as pollution. The dissolution of karst bedrocks may lead to various structures and some become tourist attractions because of the fantastic views, for instance in Tsingy de Bemaraha Strict Nature Reserve, Madagascar, as presented in Fig. 1.1[1]. This is also a good example to illustrate the spatial heterogeneity and the multi-scale features of karst. In this figure, one may observe the narrow wavelength of the vertical patterns, as well as the horizontal distribution of the conical depressions on top of the rocks. Both shapes seem periodic but with different characteristic lengths. Despite of the pleasant features, the development of karst may induce various problems, such as high mineralization of groundwater, subsidence and collapse of land surface [1, 17], etc. Therefore, scientific management of karst is required and a good understanding of the dissolution mechanisms is of great significance to provide support for safety strategy making, engineering sites selections and so on, which is the motivation of this study.

The investigation of karstic formations can start from the study of cavities, the evolution of which is related to the development of nearly all the important karstic features [18]. Among various karstic structures related to caves as represented in Fig. 1.2 [2], we are particularly interested in the context

[1] http://extra-velganza.blogspot.fr/2012/03/tsingy-de-bemaraha-strict-nature.html
[2] geologuesprospecteurs. fr

Figure 1.1: Karst in Tsingy de Bemaraha Strict Nature Reserve, Madagascar.

of sinkhole development. Sinkhole hazards have drawn great attention from the public, the researchers and the engineers because of their worldwide extent of occurrence [13, 19–31] and their great impact on society. The depths and diameters of sinkholes may vary from a couple of meters up to several hundred meters [2, 12, 14, 15, 28, 32], which may threaten the safety of human beings, affect the stability of infrastructures and destroy farmland, etc. To illustrate the sinkhole disasters, an example of collapse sinkhole is provided in Fig. 1.3[3], which took place in northern Guatemala City in May 2010, leading to a three-story building falling in. Another example is that the occurrence of catastrophic subsidence induced a total damage worthy £1,000,000 in the urban area of Ripon, North Yorkshire, England [29], within only ten years in the late 20th century.

To better understand the sinkhole genesis, sinkhole classification was conducted in some recent studies [14–16], according to the generation process. The first group represents the solution sinkholes induced by the gradual solutional lowering of the ground, which seldom leads to hazard due to the *slow* process. The second group of sinkholes differ in that they are created by internal erosion and deformational processes of subsurface karstification. This second group of sinkholes can be further separated into different types, depending on the material and mechanism involved. A schematic description of different patterns

[3]http://geogiams4.wikispaces.com/images

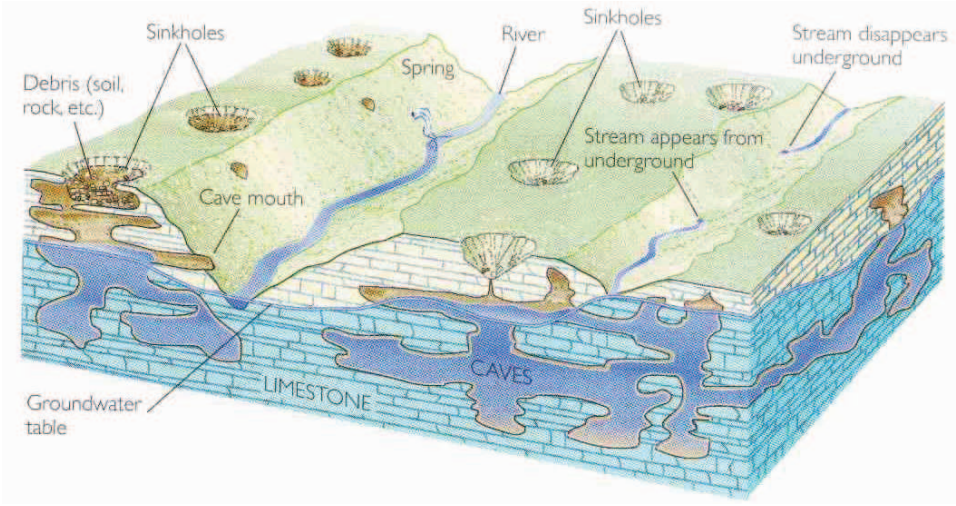

Figure 1.2: Karst landscapes.

Figure 1.3: A sinkhole example.

of sinkholes is provided in Fig. 1.4.

The upward propagation of the underground cavities leads to the breakdown of the overlying formations, which can be bedrock (soluble), caprock (insoluble) or unconsolidated cover, and creates collapse sinkholes. In terms of bedrocks, karst structures develop the most widely in carbonate environment such as limestone, marble and dolomite, etc [33,34], while salt (NaCl) and gypsum ($CaSO_4 \cdot 2H_2O$) are also important bedrocks with high solubilities, about 7500 and 150 times more soluble than limestone ($CaCO_3$), respectively [25]. As an illustration, the longest gypsum cave in the world, Optymistychna (Ukraine) had a record of 230 km passageways in 2006: the longest cave (limestone caves included) in Eurasia.

Collapse sinkholes are the most hazardous type and have received much

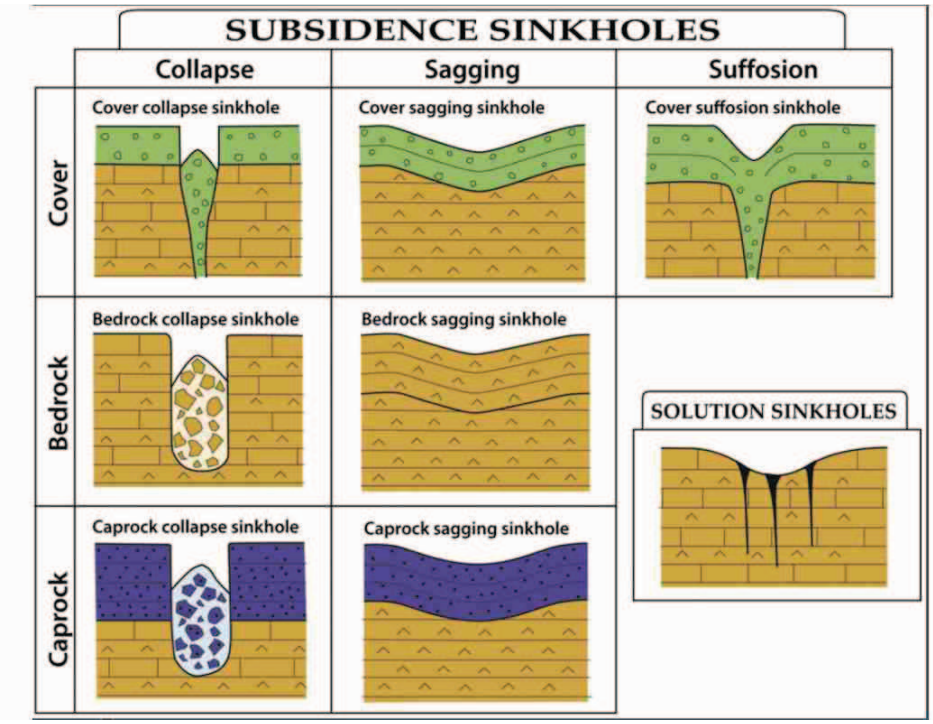

Figure 1.4: Sinkhole patterns [1].

attention because they may form within a relatively short time, only days, weeks or years before catastrophic collapse happens, especially in evaporite deposits (e.g. salt and gypsum) [25, 32]. In addition to the shallow subsurface environment, the lower mechanical strength and the greater heterogeneity of gypsum caves make it easier to lead to sinkholes than the carbonate ones [1, 15, 19, 25]. The evolution of the collapse sinkholes can be schematically illustrated by Fig. 1.5 and can be summarized by several stages. First, the preexisting fractures in rocks are enlarged by dissolution and gradually form an underground cavity. When the cavity reaches a certain size, the bedrock becomes overburdened and mechanical effects start to play a more important role than earlier, resulting in small detachments of rock slabs from the walls and ceilings of the cavity, especially around the faults. With the breakdown area approaching to the land surface, the system becomes unstable and collapse finally happens in a short time [2, 22].

In addition to natural processes, human activities such as mining and underground quarries accentuate karst development to lead to subsidence and collapse [13, 22, 23, 30, 35–37]. An example of the solution salt mining cavities is illustrated in Fig. 1.6. As shown in Fig. 1.6a, a concentric leaching well is drilled to the final depth of the salt layer, located at about 280 meters beneath the ground. The tubing is constituted by concentric tubes. Then fresh water

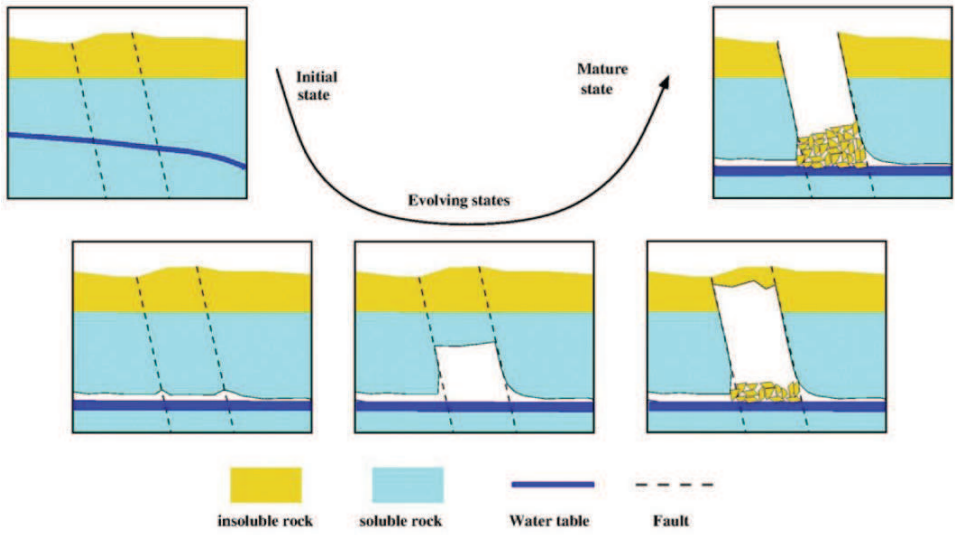

Figure 1.5: An example schematically illustrating the temporal evolution of a collapse sinkhole [2].

is injected through the central annulus with an inlet flow of 3 $m^3 h^{-1}$ during 4 days followed by 1.5 $m^3 h^{-1}$ during 8 days [3]. The cavity created is illustrated in Fig. 1.6b, with a radius about 1.4m after 12 days, showing a fast dissolution rate.

Examples regarding studies of different types of sinkholes are available in the literature, for instance, Salvati and Sasowsky [38] and Heidari et al. [24] investigated the development of cover collapse sinkholes in groundwater discharge areas. Gechter et al. [17] conducted an experiment and developed a conceptual model to study the upward enlargement of a rock salt cavity. Hiller et al. [39] carried out 3D modeling regarding the evolution of collapse sinkholes. Kaufmann [2] performed simulations to both solution and collapse sinkholes, involving different rock types.

A series of attempts, for instance field survey, laboratory experiments and numerical modelings to mention a few, have been done to investigate the karst morphologies and the geneses of underground cavities and sinkholes. However, the main interest of this study is the numerical aspect, i.e., models used to simulate the karst dissolution or similar reactive transport problems. In the following, a literature review concerning the numerical models at different scale levels is presented.

The research objectives for this thesis will be focused, on one hand, on the interaction of dissolution and fluid and solid mechanics, with the emphasis on modeling issues, and, on the other hand, on relatively rapidly dissolving materials. Therefore, the geochemistry taken into account in the models will

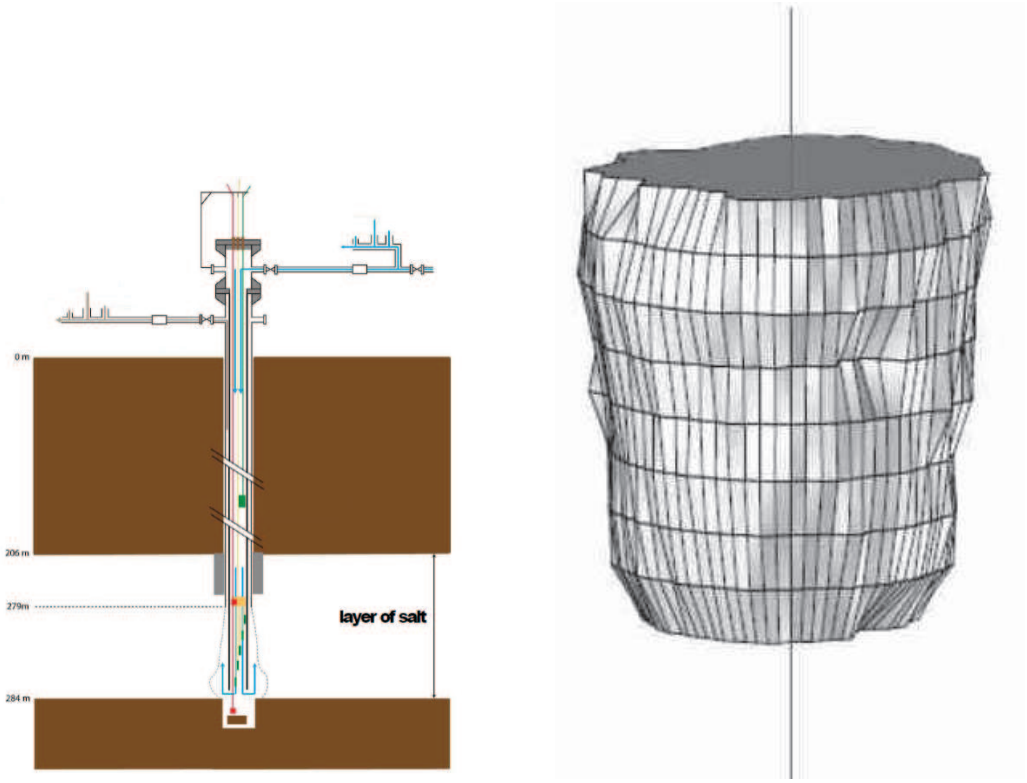

(a) (b)

Figure 1.6: (a) Schematic illustration of solution mining process; and (b) the shape of the cavity after 12 days, with a radius about 1.4m [3].

be relatively simple and more adapted to salt and gypsum dissolution. Many aspects of the findings, however, can be used to develop similar models for more complex geochemistry, like, for instance, the case of carbonate rocks dissolution.

1.1 Literature review on multi-scale models

Natural geological systems, such as underground cavities, must be generally considered as heterogeneous and multiple-scale systems. This is illustrated in Fig. 1.7, in which l is used to denote the liquid phase and s the solid phase, with the subscripts 1 and 2 representing different types of solid materials. One may consider, depending on the computational resources available, that metric to decimetric rock heterogeneities may be discriminated by the cavity-scale discretization. However, in most applications it is necessary to incorporate smaller heterogeneities into the mathematical description of the problem itself, i.e., the partial differential equations (PDEs) representative of the physics

involved. This is the case for the dissolving surface, which may be affected by heterogeneities, roughnesses created either by the dissolving heterogeneities or by a coupling between hydrodynamic instability in the vicinity of the dissolving surface and dissolution. The interface recession cannot be followed in the cavity-scale simulation at the correct small-scale, and this problem can be overcome by using hybrid models [40, 41] or the concept of effective surface [42, 43]. This is also the case if the solid formation is a porous medium or a small scale fractured system, which calls for the use of a porous medium macro-scale theory. Therefore, the various numerical models can be classified into different categories according to the scales involved.

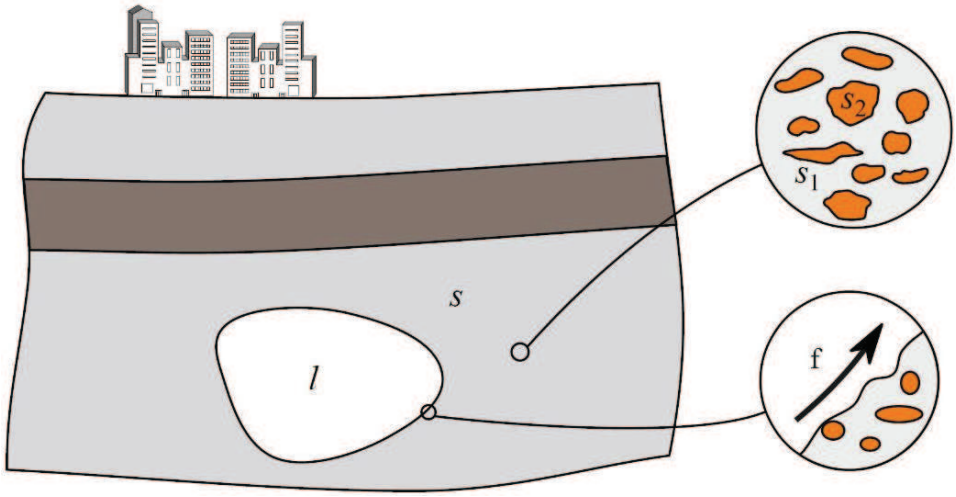

Figure 1.7: Multi-scale features of a sinkhole formation problem.

1.1.1 Pore-scale models

Either the effective surface model or the porous medium model is developed from a pore-scale (micro-scale) description of the dissolution problem. In the pore-scale study, three mechanisms are important as illustrated in Fig. 1.8, i.e., reactants transport by diffusion and advection to the dissolving surface, ions unbound from the solid and ions migrating through the diffusional boundary layer to the bulk flow by diffusion and advection [10, 44, 45].

The whole dissolution process is limited by the slowest mechanism, for instance if the mass transport to and away from the dissolving surface is slower than the dissolution rate, the process is mass transport-limited, while when the reaction kinetics is too slow to consume the reactants immediately after they get in contact, the process is reaction-limited. The dissolution of rock salt is the former case due to the fast chemical reaction kinetics, while the

dissolution of carbonate and sulfate minerals are controlled with comparable impact of chemical reaction and mass transport [10, 45].

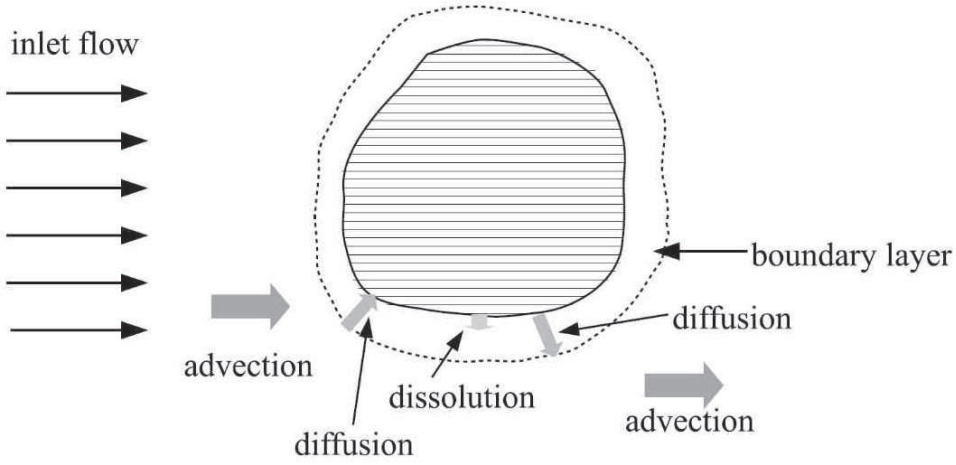

Figure 1.8: Schematic illustration of the dissolution of a crystal grain in a bulk solution.

The dissociation of salt, gypsum and limestone, which are important karst bedrocks, follow the reactions

$$\mathrm{NaCl} \rightleftharpoons \mathrm{Na^+ + Cl^-}, \tag{1.1}$$

$$\mathrm{CaSO_4 \cdot 2H_2O} \rightleftharpoons \mathrm{Ca^{2+} + SO_4^{2-} + 2H_2O}, \tag{1.2}$$

and

$$\mathrm{CaCO_3 + CO_2 + H_2O} \rightleftharpoons \mathrm{Ca^{2+} + 2HCO_3^-} \tag{1.3}$$

respectively.

Although there are different expressions of the surface reaction rates, the following equation

$$R_{diss} = k_s \left(1 - \frac{c_s}{c_{eq}}\right)^n, \tag{1.4}$$

or its equivalent form was used in some studies for limestone, calcite, gypsum or salt [39, 45–56], where k_s is the reaction rate coefficient, c_s the total concentration of the dissolved species at the surface, c_{eq} the corresponding thermodynamic equilibrium concentration and n the nonlinear reaction order. When surface reaction is fast, thermodynamic equilibrium at the dissolving surface is easily reached and the boundary condition becomes

$$c_s = c_{eq}, \tag{1.5}$$

which is the case of salt dissolution in water for instance [17].

When dealing with dissolution problems with a reactive boundary condition like Eq. 1.4, the assumption of a linear reaction, $n = 1$, was often adopted in the previous studies for the sake of simplicity [57,58]. However, it was claimed about two decades ago in [53] that with linear surface reaction, karst channels cannot form within geological realistic times, even if under the most favorable conditions. Experimental studies of the karst genesis obtained valuable results corresponding to the dissolution kinetics of various rock types and demonstrated the nonlinear property of the dissolution rates [39,47–49,51,53,55,59].

Carbonate rocks

In addition to the mixed kinetics of surface reaction and mass transport, the dissolution of $CaCO_3$ in the H_2O-CO_2-$CaCO_3$ system is also controlled by the slow kinetics of the reaction $CO_2 + H_2O = H^+ + HCO_3^-$ [44]. The conversion of CO_2 into H^+ and HCO_3^- is limited by two parallel processes

$$CO_2 + H_2O \rightleftharpoons H_2CO_3 \rightleftharpoons H^+ + HCO_3^-, \tag{1.6}$$

and

$$CO_2 + H_2O \rightleftharpoons CO_2 + H^+ + OH^- \rightleftharpoons H^+ + HCO_3^-. \tag{1.7}$$

In the first investigation of the reaction nonlinearity carried out by Plummer and Wigley for the Iceland spar (main component $CaCO_3$) dissolution in CO_2-saturated solutions [54], it was found that under 25°C and 1 atm total pressure the reaction orders follow

$$n \approx 2 \text{ when } c_s \leq 0.98 c_{eq} \text{ and pH} \leq 5.9, \tag{1.8}$$

and

$$n \approx 4 \text{ when } c_s > 0.98 c_{eq} \text{ and pH} > 5.9. \tag{1.9}$$

Similar results for Iceland spar dissolution were obtained by Palmer [18] by analyzing the data in [60], while different values were observed for natural limestone and marble dissolution rates by Svensson and Dreybrodt [48], whose measurements showed that n approached to between 3 and 4 when $c_s > 0.8 c_{eq}$.

Generally, the dissolution rate is dependent on various parameters, for in-

stance the solute saturation state, flow rate, temperature, solvent salinity, dissolving surface area and solute impurities, etc [2, 12, 32, 44, 47, 50, 61–63]. Therefore, the reaction order and reaction rate coefficient are also different corresponding to the lithology, the flow type and the environment involved. For example, in the case of a *laminar* flow of calcite aggressive water flowing through a narrow fracture of limestone with an initial aperture between 0.005 and 0.1 cm, the chemical reaction follows a linear rate law when the process is limited by the reaction illustrated in Eq. 1.6 and diffusional mass transport. While for the dissolution kinetics of natural limestone under *turbulent* flow conditions, in system open to CO_2, the empirical higher-order rate laws gave

$$R_{diss} = k_{n_1} (1 - c_s/c_{eq})^{n_1} \text{ for } c_s < \hat{c}_s, \tag{1.10}$$

$$R_{diss} = k_{n_2} (1 - c_s/c_{eq})^{n_2} \text{ for } c_s \geq \hat{c}_s, \tag{1.11}$$

according to [48, 53]. The obtained values are: n_1 between 1.6 and 2.1, n_2 between 2.8 and 4.1, $\hat{c}_s$ between $0.65c_{eq}$ and $0.8c_{eq}$, k_{n_1} about 1.8×10^{-10} mol cm $^{-2}$ s^{-1} and $k_{n_2} = kn_1 (1 - c_s/c_{eq})^{n_1 - n_2}$. The rate laws expressed in Eqs. 1.10 and 1.11 are also valid in system closed to CO_2, but with different reaction orders and reaction rate coefficients [53].

Gypsum

Parameters of Eq. 1.4 obtained by Jeschke et al. [49] for gypsum (through the interpretation of batch or disk experiments with the help of a transport model[4]) are:

$$n = 1.2 \pm 0.2 \text{ and } k_s = 1.3 \times 10^{-4} \,\text{mmol}\,\text{cm}^{-2}\text{s}^{-1} \pm 15\%, \tag{1.12}$$

for conditions far enough from equilibrium ($\frac{c_s}{c_{eq}} \leq 0.94$) and

$$n \approx 5 \text{ and } k_s = 20 \,\text{mmol}\,\text{cm}^{-2}\text{s}^{-1}, \tag{1.13}$$

for conditions close to equilibrium[5]. These values are consistent with values found in the literature, provided the part played by transport is accurately

[4] This is a difficult problem to separate surface kinetics from the global kinetics involving also the transport through the boundary layer and we shall not comment on the accuracy of such determination in the case when transport limitation is not negligible.

[5] These data are taken from Fig. 6 in [49].

determined [45, 64]. At this point of the literature review, we see that determining a local, in the sense of a Gibbs description of the interface, boundary condition for the dissolution reaction rate which is independent of the flow conditions in the neighborhood of the surface is very difficult. Going from the observed macro-scale kinetics to this point-wise boundary conditions, requires a very fine CFD (Computer Fluid Dynamics) modeling of the experimental setup, which is not always carried out to a great accuracy. This point has to be kept in mind when writing the pore-scale dissolution boundary-value problem.

In addition to the above experimental study of the dissolution kinetics, numerical modelings are also implemented with different methods at pore-scale in order to understand the physics of dissolution. For simulating the cavity evolution problem, as well as similar reactive transport problems with evolving solid structures, direct numerical simulation of the pore-scale problem is the most secure way because it makes a minimum of approximations, with the advantage of considering the porous structures.

The early work of Schechter and Gidley [65] investigated the effects of surface reaction on pore size evolution in porous medium and concluded that it is the large pores that determine the response of the system to acid. In [66], two numerical methods, random walks and finite difference, were used to investigate different configurations of porous media, with different regimes of the dissolution process distinguished, i.e., uniform dissolution over the solid phase under reaction-limited case and unstable dissolution under transport-limited case. Moreover, in the latter case, when diffusion is predominant, dissolution favors the wider parts of the pore space or larger pores, while when convection is predominant, dissolution localizes along the flow path. Similar results were obtained in [6] with pore network models. In [67], the authors investigated the evolution of fractures by dissolution and by the cycles of dissolution and deposition, and revealed the great impact of flow property on the geometry evolution of the fracture. In [56], the time evolution of fracture aperture over the length of the fractures was investigated using a finite difference method based numerical model, affected by the initial fracture geometry and the solute saturation content of the inflowing flow. Dimensionless numbers were also used as in [66, 67] to indicate the flow and reactive features, which have great impact on the the fracture geometry and solute transport.

Recently, the lattice Boltzmann method (LBM) [68, 69] and the smoothed particle hydrodynamics (SPH) approach [70–72] were widely used. LBM is

a grid-based method which is able to handle complex flows, not solving the Navier-Stokes or the Diffusion-Convection equations directly. Pan et al. [73] used Shan-Chen lattice Boltzmann approach for modeling immiscible two-fluid-phase flow in porous medium systems. Szymczak and Ladd [74, 75] studied the unstable nature of the dissolution front by simulating the dissolution of fracture, with an implicit LBM for the calculation of velocity field and a random walk method for the species transport. A resistor network model was constructed in [75] for the interaction between flow channels with the results comparable with the pore-scale ones, i.e., longer channels growing fast and shorter channels disappearing. SPH is a mesh-free Lagrangian particle method which has the advantage of not tracking the phase interfaces explicitly in the case involving moving interfaces [76]. A comprehensive theory regarding the SPH approach is available in [70]. The SPH method was used in [71] to study the impact of Damköhler number, Péclet number and pore-scale heterogeneity on the reactive transport in porous media and in [72] to simulate the diffusion and advection of species in macro-pores. Holmes et al. [76] extended the method to three dimensional for modeling porous flow, and indicated that the accuracy of SPH for flow with low Reynolds numbers is dependent on the implementation of no-slip boundary conditions.

While valuable information is obtained from these pore-scale simulations, the computational cost when dealing with large-scale problems, such as cavity evolution, is too expensive. Moreover, the explicit tracking of the moving interfaces in some circumstances induces numerical difficulties due to the large deformation of the configuration. In the engineering practice, one would be more interested in a macro-scale description of the dissolution problem which would filter the pore-scale details. Therefore, some sort of macro-scale modeling is necessary. In the case involving the dissolution of a solid formation with heterogeneous, rough surface, the macro-scale model often makes use of the effective surface theory, which is discussed in the next subsection.

1.1.2 Effective surface theory

For mass, heat and momentum transport phenomena taking place over heterogeneous and rough surfaces in the dissolution process, the surface characteristic length-scale (linked to the heterogeneities) is generally much smaller than the scale of the global mechanism, for instance in the cavity with stratified rough surface presented in Fig. 1.9. In such circumstances, direct numerical simulations (DNSs) become difficult to achieve in practical applications. To

overcome this difficulty, a traditional way of solving such problems is to incorporate the micro-scale behaviors into a boundary condition over a smooth, "homogenized" or effective surface.

Figure 1.9: An example of the karst underground cavity with stratified rough surface, taken from ladepeche.fr.

The concept of homogenization was first proposed in [77] for the application of multiscale asymptotic developments in periodic domains in nuclear reactors [78]. Since then, homogenization technique via asymptotic analysis has been applied in various fields. Recent studies include, for instance in [79], the authors studied the influence of the heterogeneities located at a surface in a three-dimensional elastic medium by using a homogenized interface model, which describes the heterogeneous zone as an interface with ad hoc transmission conditions. Explicit homogenized equations were derived in [80, 81] for the linear theory of electricity with very rough surfaces which oscillate between two parallel lines, separating two solids. In [82], homogenization was conducted in a nonlinear reaction-diffusion problem, considering both Dirichlet and Neumann boundary conditions, and was applied in extended predator-prey ecological models. Haouala and Doghri [83] proposed a two-scale time homogenization formulation for coupled viscoelastic-viscoplastic materials subject to large numbers of cycles, which is able to predict long time response. Zhao [84] studied the convergence rates for the homogenization of rapidly oscillating

Neumann boundary.

In a few studies, geometry changes were taken into consideration. For example, the interface recession of a heterogeneous surface due to ablation was taken into account through direct simulations in [85]. A recent study by Kumar et al. [86] also considered geometry changes explicitly when upscaling the reactive flow in a domain with oscillating boundaries, using matched asymptotic expansions.

Regarding a fluid flowing over a rough solid surface, domain decomposition and multi-scale asymptotic analysis were first introduced in the pioneer works of [87, 88] to develop an effective surface and the associated boundary conditions for laminar flow over rough surfaces. Later on, the effective surface concept was used to describe ablation processes in the aerospace or nuclear safety context (e.g. in [43] on mass and momentum transfer problem and in [42] on heat transfer problem). In the work of [89], an asymptotic approximate solution was constructed in the horizontal periodic domains bounded by a smooth wall on the bottom and a very rough wall on the top, filled by a viscous incompressible flow. Asymptotic approximations were constructed for the velocity and pressure in the H^1-norm and L^2-norm respectively, and a Navier type effective boundary condition was derived.

While there are some similarities (the very idea of an effective surface), one should not mix the solid-liquid problem with the problem of fluid flowing over a porous medium domain. For this latter case, one seeks to link a macro-scale description of the flow in the porous medium (e.g. Darcy's law) to a free fluid flow description in the channel (e.g., Navier-Stokes or Stokes equations, depending on the importance of inertia effects). Different, more or less heuristic, effective boundary conditions have been proposed [90–92] for the momentum balance equations. Formal developments using homogenization techniques can be found in [91–95] or using variants of averaging techniques and matching techniques in [87, 96–102]. Different upscaling methods such as volume averaging approach and asymptotic expansions have been implemented in order to obtain effective boundary conditions for various other transport problems [87, 96–100, 102].

In this work, the domain-decomposition technique developed in [42, 43] will be applied to a problem of a rough heterogeneous reactive surface typical of a medium with an insoluble material.

1.1.3 Porous medium macro-scale models

The second multi-scale problem of interest is the development of macro-scale models for flow in porous media by applying some sort of upscaling method to the pore-scale models. As a result, several effective parameters are introduced in the macro-scale models to relate the average behavior to the pore-scale features. Such attempts to develop macro-scale dissolution models can be found in the literature. Macro-scale models were developed for passive dispersion, i.e., with no exchange at the liquid-solid interface, starting with the well-known work of Taylor [103, 104] and Aris [105] for dispersion in tubes. In the general case, the macro-scale theory is proposed following various upscaling techniques: Brenner [106] using a method of moment, Eidsath et al. [107] using the method of volume averaging and Mauri [108] using the method of homogenization. All methods bring some theoretical support for the classical dispersion equation and also provide closure problems which can be used to directly calculate the dispersion tensor components for various representative unit cells. These theoretical methods have been used also to investigate the case of active dispersion, i.e., with thermodynamic equilibrium or reactive conditions at the fluid-solid interface.

The motivation of [109] is the determination of the effective properties in the macro-scale equations describing the dissolution of NAPL (non-aqueous-phase liquid) contaminants in porous media. In addition to the traditional effective parameters, for instance the dispersion tensor[6] and the effective mass transfer coefficient, some non-classical parameters were introduced and their importance were demonstrated in this work. Later, the active dispersion case was studied in [110] with the closure problems solved with finite volume methods in the first case and with network modeling in the second case. The influence of the NAPL volume fraction and the orientation of the average velocity field were also studied. Golfier et al. [10] developed a Darcy-scale local non-equilibrium model using the method of volume averaging [102], which allowed to capture all the observed features in terms of dissolution regimes and the optimum acid injection rate in the application of enhanced oil recovery. However, the Darcy-scale model could not be used directly in a large-scale reservoir description due to the requirement of a very fine grid imposed by the small-scale dissolution instabilities [111]. Consequently, it was further upscaled, leading to two different sets of models at core-scale, with one being the one-medium

[6] The theory provides an "active" dispersion tensor in this case, different from the classical passive dispersion case due to a different boundary condition at the liquid-solid interface.

(or one-equation) model and another being the two-medium (or two-equation) model [112]. Interestingly, the one-equation core-scale equations follow a form similar to those previously developed at Darcy-scale. Simulations show that the effective parameters are dependent on the dissolution process in a historical manner, at both Darcy and core-scale. In the first case, the assumption of a direct relationship between the different macroscopic properties and porosity was adopted, as classically made in geochemistry. Yet the case is more complicated at the core-scale, as studied in detail in [113]. The study of Golfier et al. [114] revealed that the mass transfer coefficient can be represented in terms of the eigenvalue expansion of a Green's function rather than a constant. The influence of steady state closure problems on the effective mass transfer coefficient was also investigated in this work and it was claimed that the results can be improved by taking into account the transient closures, at the expense of computational complexity. In [115], the author investigated the macro-scale coefficients that characterize the propagation and interaction of CO_2 molecules with the porous medium, using the macrotransport theory developed in [116]. A 3D porous medium model was built in [117] which consists of thousands of spherical particles and was divided into cells using Voronoi diagrams. The longitudinal and the transversal dispersion components were obtained by fitting with the effluent curves and the tortuosity effect was discussed.

Porous media macro-scale models can be used of course to solve for porous formation dissolution problems [118]. However, it has been recognized that non-equilibrium porous media models can approach results with sharp dissolution interfaces, see for instance [10], and this can be used to replace the original dissolution problem for solid-liquid systems by a diffuse interface model (DIM) [119, 120]. Properties of the DIM model used in this perspective were analyzed by Luo et al. [120], taking into account density variation effects. Such a DIM approach was also implemented for a three-phase (i.e., solid-liquid-gas) system, in the circumstances of cavity evolution [121]. These studies illustrate the possibility of using DIM methods to solve dissolution problems without an explicit treatment of the dissolving interface, allowing for the handling of highly complex dissolution behaviors with multi-moving interfaces. However, their implementation for solving very large cavity dissolution problems leads to a series of difficulties which will be examined in this study.

In addition to the investigations on the development of macro-scale models and the discussions on the generated effective parameters, another interesting topic which has drawn great attention from the researchers is the instability

problem. Two types of instabilities can be distinguished, with one being dissolution instabilities due to unstable dissolution process, i.e., dissolution front in large pores propagating faster than in the small ones [65, 66]. The work of Golfier et al. [10] mentioned above demonstrated the very important role in the stability diagram of local equilibrium and local non-equilibrium features. This allowed to predict wormhole propagation induced by dissolution instabilities quantitatively and to characterize the impact of flow properties. Later, [111] extended this analysis to domain of large extension. Two different regimes, namely "inlet" instability (instability in the dissolution of an entirely homogeneous porous matrix) and "front" instability (instability in a steadily propagating reaction front), were studied in [122]. The former approaches the maximum growth rate at a specific wavelength of perturbations depending on the flow conditions, while the latter keeps growing within a large range of wavelengths and is largely affected by diffusion. It was also revealed in [59] that the dissolution of a fracture is inherently two dimensional and the wavelengths are also dependent on reaction kinetics and flow rate but insensitive to the initial roughness of the fracture. In various studies of Zhao and coauthors [119, 123, 124], the impact of various factors on the morphology and propagating speed of the unstable front between a fluid and a porous medium was investigated, such as the domain shapes, Zhao number (representation of advection, diffusion/dispersion and chemical dissolution mechanism), the permeability ratio between the artificial permeability in the fluid domain and the real permeability in the porous medium domain, etc.

The second type of instability involves the coupling with hydrodynamic instabilities, which remains to be an open complex problem, with an important point being natural convection induced by density variation in dissolution processes. Many attempts have been made to gain better understandings of buoyancy-driven flow, for instance in [125–128]. The studies of [120, 121] are examples related to the use of macro-scale transport models in such a problem, showing the presence of convective plumes and impact of buoyancy effects on the evolution of dissolving surfaces, which developed under large Rayleigh numbers and may be enhanced in the condition with large Péclet numbers.

1.1.4 Other models

In addition to the pore-scale and macro-scale models introduced above, there are some models coupling descriptions at different scales, for instance, the pore network model and the hybrid model. Moreover, different from the

transport models, there are enormous studies investigating the karst genesis, especially in the context of conduit development, by analyzing the related hydraulic parameters. Although such methods are not used in this study, they provide valuable knowledge of the cavity dissolution problems and brief introductions are also given below.

Pore network models

Pore network models (PNM) are meso-scale representation of the porous medium. The pore-scale geometry is transformed in a network of pore bodies connected by pore throats. Flow dynamics in the system is resolved by using approximations such as Poiseuille flows for the momentum balance. Such a conceptual representation of the porous medium considers the topological effects, such as the connectivity, the aspect ratio and tortuosity, etc [129]. In some studies, for instance [130] and [68], PNM was classified as a pore-scale model, somehow improperly since the problem solved is not exactly the original pore-scale problem. However, it is able to approximately reproduce the pore-scale dissolution process to a certain accuracy and thus solve for much larger volumes, i.e., including a larger number of pores, than pore-scale models [41].

As illustrated in Fig. 1.10a, the simple network uses idealized pore geometry and topology. While the geometry illustrated in Fig. 1.10b can better represent the real pore medium structures since it is extracted from real porous materials. It is indicated in [130] that the accuracy of PNM relies on the accurate characterization of the 3D pore structure, pore-throat geometry and accurate modeling of flow behavior in the medium. Therefore, using physically representative networks will improve the ability of PNM as a quantitative, predictive model.

PNM has been used in many works to study dissolution problems. Algive et al. [131], Varloteaux et al. [132] and Nogues et al. [133] used PNM to study the impact of dissolution on permeability and porosity modification in the context of diagenetic cycle or geological carbon sequestration. It was revealed that a nearer-to-equilibrium solution and convective flow may lead to larger permeability change than their counterparts, i.e., a far-from-equilibrium solution and diffusive flow. PNM was used in [41] to study various reaction regimes and the effect of concentration distribution on the macroscopic properties. The authors indicated the requirements of special treatment when using PNM at high Péclet numbers due to the large discrepancy observed when compared to the pore-scale model results in such circumstances. Békri et al. [6] conducted a study with PNM on mass transfer with mineral reaction in a single phase

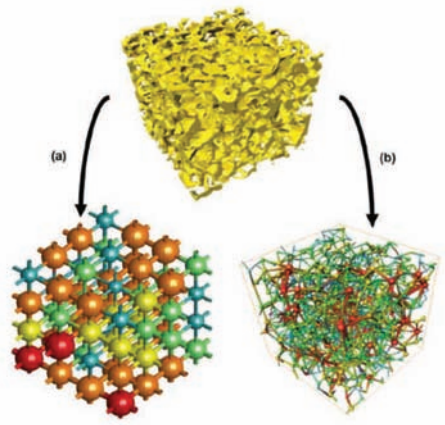

Figure 1.10: Pore network models: (a) model reconstructed with a regular lattice in order to reproduce petrophysical properties of a real porous media ([4]); (b) model extracted from the micro tomography images in order to get the same structure as the real rock sample ([5]). Taken from [6].

porous media as well as the impact of some dimensionless numbers. Core-scale parameters were calculated with geometry evolutions due to mineral reaction taken into account.

Hybrid models

In hybrid models, a small-scale model with high resolutions is used in part of the overall domain and is linked to a large-scale model with coarser resolutions used in the rest of the domain [134]. Hybrid models are imperative in the conditions that pore-scale modeling is too expensive while macro-scale modeling fails to describe the phenomena in a small portion of the studied domain [40]. In [135], the authors illustrated a macro-scale model breakdown example in the case of mixing-induced precipitation on (and/or dissolution of) a porous matrix. Hybrid models have been studied by many authors in the past few years, however the applications of hybrid models to subsurface water flow and reactive transport remain limited [134]. In [136], the coupling of a network model describing the pore-scale water flow and a continuum-scale model describing the flow in a porous medium was used to obtain boundary conditions for the network model that are representative of the larger-scale flow patterns. Such a coupling reflects both the heterogeneity in the pore-scale region and the resistance in the continuum region as the flow responds to the adjacent heterogeneity. The hybrid models that link the pore- and Darcy-scale descriptions are also able to handle the highly localized heterogeneities [137]. In [40, 72, 134, 137], the applicability of the hybrid models was tested by com-

paring the results of pore-scale simulations, obtained with the finite-volume method or the SPH method, and (or) the analytical solutions, and they showed good accuracy in the condition that the solute transport by advection is negligible. In the study of Tomin and Lunati [138], the authors proposed a general framework for a pore- and Darcy-scale hybrid algorithm extended from the multi-scale finite volume method, and applied it to a two-phase flow problem. The results demonstrated the ability of such hybrid methods to model the transition from stable to unstable flow regimes. A particular feature obtained in [139] is that the parameters in PNM may be dependent on the macro-scale properties that take place at a larger characteristic length, which enables to incorporate a dynamic fracture model in the proposed hybrid models.

Conduit evolution models

Among various studies concerning the genesis of karst cavities, a large proportion of them involve the investigation of the early stage of karst aquifer development. Originally, underground cavities intend to develop along preexisting fractures, with about 60% of the cave conduits following bedding planes and the rest following joints [18, 140]. The density, penetrability and linkage of fractures and bedding planes, as well as the hydraulic parameters involved have strong impact on the cave morphology [12]. Numerically speaking, some models have been developed to simulate the early stage of conduit evolution, i.e., the dissolution enlargement of the preexisting fractures in rock matrix, especially from a hydraulic perspective. Such studies usually focused on predicting the so-called "breakthrough time", which terminates the early stage of the evolution of karst aquifer, defined as the time to reach dramatic enlargement of conduit and turbulent flow [53, 57, 140]. Early studies about the karstification process used 1D pipe models to analyze the single conduit development in limestone, [18, 52, 53, 141]. A main conclusion of these studies was that the positive feedback of mutual enhancement of conduit enlargement and flow rate governed the early stage of karst genesis. An approximation of the breakthrough time was obtained in [53] , with

$$T = const(l_f/i_h)^{4/3} a_0^{-3} k_{n2}^{1/3} c_{eq}^{-4/3} \text{ years} \tag{1.14}$$

in which l_f is the length of flow path; i_h is the hydraulic gradient; a_0 is the initial fracture width.

Since 1D models were not able to capture the geometric features of the conduit development, 2D pipe network models representing interconnected conduits were developed in [142–144] for more complex limestone structures, and

flow types were extended from laminar to turbulent. It was reported in these works that both flow patterns and hydraulic boundary conditions have significant impact on cave patterns, with laminar flow and fixed hydraulic recharge boundary conditions favoring the development of single passages while turbulent flow and fixed hydraulic head boundary conditions intending to develop maze caves. However, such models still did not take into account the important impact of the fissure systems, which was improved by later models, considering the dual nature of karst formation and distinguishing correspondingly the two flow types, i.e., flow in the fissure systems and flow in the conduits. The coupling of the two different types of structures and flows was realized by the so-called continuum-pipe flow models, which considered the fissure system as a continuum and regarded the fractures as pipes as before [140, 145–147]. Due to the long residual time of water in the fissure systems, it was assumed that the flowing water in the continuum is nearly saturated with respect to the studied dissolving species. Such continuum-pipe models were employed in the mentioned works to investigate the impacting factors of conduit development in limestone or calcite. The assumptions of fixed hydraulic heads or the combined fixed hydraulic heads/fixed discharge boundary conditions were also often adopted in the continuum-pipe models and it was revealed in these papers that the initial diameter of the conduit, the initial hydraulic gradient and the flow exchange between the prominent fracture and surrounding fissures are the most important factors that affect the conduit enlargement and conduit patterns. Birk and Rehrl, et al. [55,57,148] improved the continuum-pipe models by using time-variant hydraulic boundary conditions, and investigated the gypsum caves other than the frequently studied carbonate formations. Gypsum dissolution process was assumed to be limited by the diffusion of calcium and sulfate from the dissolving surface to the bulk flow, due to the high solubility of gypsum. The simulation results demonstrated that the development of maze caves in the artesian areas is subject to the presence of the structural preference, or else vertical shafts develop without structural preference. One improvement of [149] is the consideration of the dissolution nonlinearity, when modeling the cave evolution in a limestone aquifer. More recently, Schwarz and Enzmann [150] conducted sensitive analysis of the geometrical properties of the fractures on the fluid flow properties in reactive transport problems, and it was reported that the average fracture permeability is most sensitive to the average aperture and fracture roughness. While many interesting qualitative or semi-quantitative results have been obtained for more or less schematic mod-

els, the question of the accuracy of the simulations has not been thoroughly analyzed, and this was one objective of the thesis work.

1.2 Motivation and objectives of this thesis

The motivation of this thesis is to better understand the dissolution mechanism of (karstic) cavities from multi-scale perspectives, especially in the context of sinkhole formations. The objective of this present work are indicated as follows:

1. a comprehensive discussion of the dissolution problem at the pore-scale from a transport perspective, with gypsum dissolution as an example;

2. the development of a macro-scale effective surface model, in which a homogeneous, smooth surface is used to replace the original heterogeneous, rough surface, where the mass transport takes place;

3. the development of a macro-scale porous medium model with the method of volume averaging, which also behaves as a diffuse interface model to describe the dissolution of a solid formation;

4. application of the proposed macro-scale models.

1.3 Outline of this thesis

This thesis consists of six chapters. In Chap. 1, a general introduction is given, including a literature review about the multi-scale numerical models of the dissolution problem, as well as the objectives of this thesis.

In Chap. 2, the general assumptions in modeling the dissolution problems are presented, followed by the mathematical pore-scale dissolution model and a comparison of using different boundary conditions at the dissolving surface.

In Chap. 3, the effective surface theory is implemented to a problem involving mass transport over a heterogeneous, rough surface within the boundary layer of a laminar flow. An effective homogeneous, smooth surface is sought to replace the original surface with the corresponding effective boundary conditions. The impact of the roughness geometry and the flow and chemical properties on the effective surface position and the effective behaviors of the flow is investigated.

In Chap. 4, a macro-scale model is developed with the method of volume averaging, starting from the pore-scale model developed in Chap. 2. The effective parameters in the macro-scale model are obtained by the resolution of the closure problems, which represent the averaged behaviors of the pore-scale features. The impact of the flow and chemical features on the effective parameters, as well as the influence of some non-classical effective parameters on the accuracy of the macro-scale model are discussed.

In Chap. 5, the above developed macro-scale model is applied in the modeling of a large-scale cavity evolution problem. The macro-scale model is used either in a porous medium dissolution problem, or as a diffuse interface model (DIM) in the solid formation dissolution problem. A workflow is proposed to choose the Darcy-scale momentum equations and the proper mass exchange coefficient, in order to reproduce an accurate dissolving interface recession rate with the DIM. In addition, the potential of the approach is shown on the 3D modeling of gypsum lenses and pillars in a gypsum quarry which may lead to the formation collapse.

In Chap. 6, the conclusions of this present study and the perspectives of future works are presented.

Chapter 2

Pore-scale dissolution mechanism

In this chapter, the pore-scale model is developed, taking the gypsum dissolution as an example. Several objectives are considered, including: (i) the clarification of the assumptions adopted in the modeling; (ii) the general mathematical formulation for the mass fraction field, fluid-solid interface movement, etc.; and (iii) the impact of the different forms of boundary conditions for describing the mass transport at the interface, i.e., kinetic boundary condition versus thermodynamic equilibrium condition. In so doing, a general multicomponent formulation is discussed to assess the accuracy of a gypsum pseudo-component formulation, which is often used for mechanistic modeling[1], followed by the mathematical description of the dissolution physics and the comparison of results obtained with different boundary conditions at the dissolving surface.

2.1 Modeling assumptions

In this section, the focus is on the mass transport problem, leaving aside the momentum and energy equations. While most models [57, 148] assume that the solid dissolution is controlled by transport, the assumption is not made at this point. As a matter of fact, this question cannot be resolved without an explicit description of the problem under consideration since the contribution of transport will depend strongly on the initial boundary value

[1] A complex geochemical model may lead to very cumbersome computations at the expense of an accurate description of the flow dynamics. Since the objective of the thesis is a thorough investigation of this latter point, especially for very large cavities, subsequent chapters make use of the simplified geochemistry models discussed in this chapter.

problem (IBVP) to be solved, in particular the geometry and flow parameters which will determine the possible development of a boundary layer of thickness sufficient to make surface reaction negligible.

A hierarchical, multi-scale system is considered as schematically depicted in Fig. 2.1. The porous medium under consideration consists of three phases at the pore-scale: two solid phases, one being soluble, denoted s, the other insoluble, denoted i, and a liquid phase (in general water + dissolved species), denoted l. The pore-scale characteristic length are corresponding to l_i, l_s and l_l and the cavity scale is related to L.

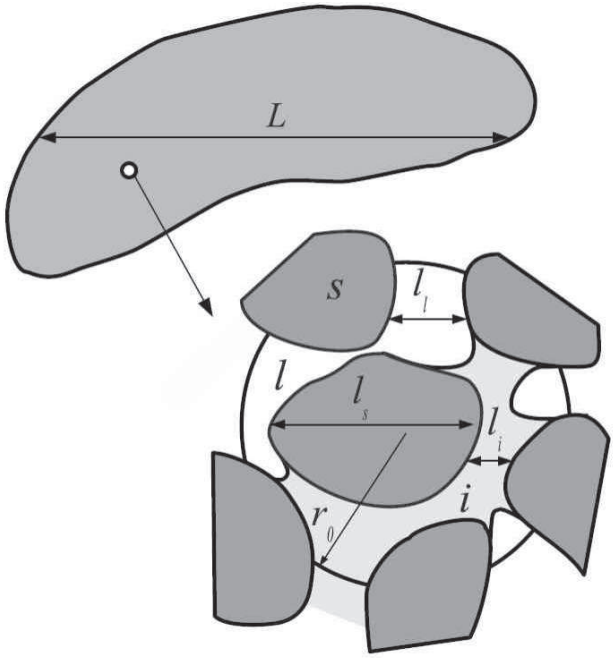

Figure 2.1: An example of the multiple scales associated with dissolution in a porous medium.

In the case of s-phase being gypsum, several assumptions have been adopted. First, it is assumed that the activity of the solute in the liquid phase is not modified near the solid surface of the insoluble material, so no solute deposition occurs since the bulk concentration is below the equilibrium concentration. There are many experiments with various salts and passive solid surfaces, for instance, that are compatible with this assumption (a common situation indeed in laboratory experiments aimed at measuring dissolution rates). Even if initially a layer of salt covers the insoluble material, a case which is covered by the model, the thin layer is likely to dissolve more rapidly than the salt grains and leads to a situation in which both soluble and insoluble surfaces are present. Second, solid dissolution can be described by the dissolution of

a single pseudo component. In practice, most soluble materials have a complex chemistry, which implies that dissolution brings several chemical species in the liquid. The water composition will be affected by geochemistry and by segregation due to different transport properties. For instance, gypsum ($CaSO_4 \cdot 2H_2O$) dissolution will produce several water components, which will require in principle to follow at least [151]: H^+, OH^-, SO_4^{2-}, HSO_4^-, HSO_4^-, H_2SO_4, Ca^{2+}, $CaSO_4$ and finally H_2O! An example of water composition at thermodynamic equilibrium computed from PHREEQC [152] is given in Table 2.1, under T=12°C and pH = 7.061. This example shows that gypsum primary cation and anion, i.e., Ca^{2+} and SO_4^{2-}, have a concentration significantly larger than the other compounds. The composition of the water may not all the time reflect the one associated with the gypsum-water thermodynamic equilibrium. The presence of other dissolving species, calcium carbonates for instance, may affect the water composition. Indeed, calcite dissolution, for instance, has been observed to hinder gypsum dissolution under some circumstances [61], the reverse being true, i.e., modification of calcite dissolution through gypsum precipitation [153]. A notation is adopted below which corresponds to a mass balance equation for one ion, let us say Ca^{2+} in our gypsum illustration, which is denoted Ca. Third, the fluid density ρ_l and viscosity μ_l are assumed constant. Similarly, the diffusion coefficient is supposed constant. One may consult [154] for an example of introduction of nonlinear diffusion coefficients within the averaging scheme.

Table 2.1: An example of water composition after gypsum dissolution.

Species	Molality	Species	Molality
H^+	1.044e-07	O_2	0.000e+00
OH^-	4.847e-08	$S(^{2-})$	3.097e-20
H_2O	5.551e+01	HS^-	1.574e-20
Ca	1.464e-02	H_2S	1.523e-20
Ca^{2+}	1.014e-02	S^{2-}	1.435e-26
$CaSO_4$	4.497e-03	S(6)	1.464e-02
$CaOH^+$	1.172e-08	$SO_4{}^{2-}$	1.014e-02
$CaHSO_4{}^+$	2.398e-09	$CaSO_4$	4.497e-03
H(0)	4.117e-15	HSO_4^-	3.887e-08
H_2	2.059e-15	$CaHSO_4{}^+$	2.398e-09
O(0)	0.000e+00		

The question of the spatial differentiation of the various component concentrations due to different diffusion coefficients is more complicated. Indeed, the diffusion coefficients of some of the components obtained after gypsum

dissolution are slightly different, as shown in Table 2.2 [155]. If one look at the major ions (see above discussions and Table 2.1), i.e., Ca^{2+} and SO_4^{2-}, there is a small difference between the two diffusion coefficients. An important question is how much this difference has to be taken into account in modeling underground water flow? This can be evaluated by considering the following 1D transport problem: a 1D flow over an infinite domain, at a constant velocity u, with initial condition

$$c_{Ca^{2+}} = 1 \; ; \; c_{SO_4^{2-}} = 1 \quad \text{for } x < 0, \tag{2.1}$$

$$c_{Ca^{2+}} = 0 \; ; \; c_{SO_4^{2-}} = 0 \quad \text{for } x > 0, \tag{2.2}$$

where $c_{Ca^{2+}}$ and $c_{SO_4^{2-}}$ represent respectively the concentration of Ca^{2+} and SO_4^{2-}, and the value 1 refers to the thermodynamic equilibrium concentration. The concentration field at any time is given by

$$c_i = \frac{1}{2}\left(1 - erf\left(\frac{x - ut}{2\sqrt{D_i t}}\right)\right), \quad i = Ca^{2+},\ SO_4^{2-}, \tag{2.3}$$

where D_i denotes the diffusion coefficient of species i, i.e., Ca^{2+} or SO_4^{2-}. The location of the maximum difference between the two concentrations can be calculated as

$$x_{max} = ut + \sqrt{2}\sqrt{\frac{t\, D_{SO_4^{2-}}\, D_{Ca^{2+}} \log\left(\frac{D_{Ca^{2+}}}{D_{SO_4^{2-}}}\right)}{D_{Ca^{2+}} - D_{SO_4^{2-}}}}, \tag{2.4}$$

and the resulting maximum concentration difference is a constant equal to

$$\max(c_{SO_4^{2-}} - c_{Ca^{2+}}) = \frac{\operatorname{erfc}\left(\frac{y}{\sqrt{2}\sqrt{D_{SO_4^{2-}}}}\right)}{2} - \frac{\operatorname{erfc}\left(\frac{y}{\sqrt{2}\sqrt{D_{Ca^{2+}}}}\right)}{2}, \tag{2.5}$$

with

$$y = \sqrt{\frac{D_{SO_4^{2-}}\, D_{Ca^{2+}} \log\left(\frac{D_{Ca^{2+}}}{D_{SO_4^{2-}}}\right)}{D_{Ca^{2+}} - D_{SO_4^{2-}}}}. \tag{2.6}$$

Given the diffusion coefficients presented in Table 2.2, it was obtained that $\max(c_{SO_4^{2-}} - c_{Ca^{2+}})$ equal to 0.0331, 0.0335 and 0.0364 at 0°C, 18°C and 25°C

respectively with $u = 10^{-6}\,\mathrm{m\,s^{-1}}$. The maximum values obtained under various temperatures are relatively small and suggest that the spatial differentiation of the two concentrations can be neglected. Of course, other IBVPs may lead to slightly different estimates, but the trend should not be much different. In addition, this estimate is based on a pure fluid transport, in the absence of geochemistry. In the case of a porous medium, $D_{\mathrm{Ca}^{2+}}$ and $D_{\mathrm{SO}_4^{2-}}$ must be replaced by the effective diffusion/dispersion coefficients. If the pore-scale Péclet number is sufficiently large, which is often the case in classical groundwater flow problems, then the dispersion part overcomes the diffusive part and the resulting effective diffusion coefficients are *equal* and the difference becomes nil in that case.

Table 2.2: Diffusion coefficients in water at infinite dilution for some ions ($10^{-9}\,\mathrm{m^2\,s^{-1}}$).

Compound	0°C	18°C	25°C
H^+	5.61	8.17	9.31
OH^-	2.56	4.49	5.27
HSO_4^-	-	-	1.33
Ca^{2+}	0.373	0.673	0.793
SO_4^{2-}	0.5	0.89	1.07

As a conclusion, with all the above assumptions, while more complex geochemistry should not be discarded in cases where the water and solid involve several other components than those of gypsum dissolution, the assumption that gypsum dissolution can be described by the dissolution of a pseudo-gypsum water component is adopted in this study. For convenience, and for the purpose of future introduction in more complex geochemistry models, the ion Ca^{2+} is followed. Based on this assumption, pore-scale numerical simulations are presented below to evaluate the impact of the dissolving surface boundary condition.

2.2 Mathematical model

The momentum balance equations in the fluid phase are written as

$$\frac{\partial \rho_l \mathbf{v}_l}{\partial t} + \rho_l \mathbf{v}_l \cdot \nabla \mathbf{v}_l = -\nabla p_l + \rho_l \mathbf{g} + \mu_l \nabla^2 \mathbf{v}_l \quad \text{in the } l\text{-phase}, \tag{2.7}$$

$$\text{B.C. I} \quad \mathbf{v}_l - \mathbf{n}_{ls}\mathbf{n}_{ls} \cdot \mathbf{v}_l = 0 \quad \text{at } A_{ls}, \tag{2.8}$$

where ρ_l is the liquid density, $\mathbf{v}_l$ the pore-scale liquid velocity, $\mathbf{g}$ the gravity, μ_l the dynamic viscosity and A_{ls} the interfacial area between the solid and the liquid phase. According to [45], the gypsum solubility in water is about 2.63 kg m^{-3}. Assuming gypsum is the pseudo component in water as discussed above, the water density variation is less than 0.3%, which is negligible. Therefore, with the assumption of constant liquid density, mass balance equations for the liquid phase and the dissolved species can be written as follows

$$\nabla \cdot \mathbf{v}_l = 0 \quad \text{in the } l\text{-phase}, \tag{2.9}$$

$$\frac{\partial \omega_l}{\partial t} + \mathbf{v}_l \cdot \nabla \omega_l = \nabla \cdot (D_l \nabla \omega_l) \quad \text{in the } l\text{-phase}, \tag{2.10}$$

with ω_l the mass fraction of Ca in the liquid phase and D_l the molecular diffusion coefficient.

The boundary conditions for Ca^{2+} mass balance at the solid-liquid interface may be written as a kinetic condition as follows

$$\begin{aligned} \mathbf{n}_{ls} \cdot (\rho_l \omega_l (\mathbf{v}_l - \mathbf{w}_{sl}) - \rho_l D_l \nabla \omega_l) &= -M_{Ca} k_s \left(1 - \frac{\omega_l}{\omega_{eq}}\right)^n \\ &= \mathbf{n}_{ls} \cdot (\rho_s \omega_s (\mathbf{v}_s - \mathbf{w}_{sl})) \quad \text{at } A_{ls}, \end{aligned} \tag{2.11}$$

In this equation, ρ_s is the solid (gypsum) density, ω_s is the mass fraction of Ca in the solid phase, $\mathbf{v}_s$ is the solid velocity, $\mathbf{w}_{sl}$ is the interface velocity, M_{Ca} is the molar weight of Ca, k_s is the reaction rate coefficient and n is the nonlinear reaction order. The thermodynamic equilibrium mass fraction ω_{eq} is estimated as

$$\omega_{eq} = M_{Ca} \left(1.32 \times 10^{-2} + 1.31 \times 10^{-4} T - 1.47 \times 10^{-6} T^2\right), \tag{2.12}$$

with T denoting temperature with the unit of °C. Mass balance for the solid phase gives the following boundary condition

$$\begin{aligned} \mathbf{n}_{ls} \cdot (\rho_s (\mathbf{v}_s - \mathbf{w}_{sl})) &= \nu_s \mathbf{n}_{ls} \cdot (\rho_l \omega_l (\mathbf{v}_l - \mathbf{w}_{sl}) - \rho_l D_l \nabla \omega_l) \\ &= -\nu_s M_{Ca} k_s \left(1 - \frac{\omega_l}{\omega_{eq}}\right)^n \qquad \text{at } A_{ls}, \end{aligned} \tag{2.13}$$

where $\nu_s = M_g/M_{Ca}$ and M_g is the molar weight of gypsum. The total mass balance boundary condition may be written formally as

$$\mathbf{n}_{ls} \cdot (\rho_l (\mathbf{v}_l - \mathbf{w}_{sl})) = \mathbf{n}_{ls} \cdot (\rho_s (\mathbf{v}_s - \mathbf{w}_{sl})) \qquad \text{at } A_{ls}, \tag{2.14}$$

In this thesis, it is assumed that the solid phase is immobile, i.e., $\mathbf{v}_s = 0$, therefore $\mathbf{v}_s$ will not appear anymore in the expressions for the boundary conditions. With this assumption, Eqs. 2.13 and 2.14 can be rewritten as the following two equations

$$\mathbf{n}_{ls} \cdot \mathbf{w}_{sl} = \rho_s^{-1} M_g k_s \left(1 - \frac{\omega_l}{\omega_{eq}}\right)^n \qquad \text{at } A_{ls}, \tag{2.15}$$

$$\mathbf{n}_{ls} \cdot \rho_l \mathbf{v}_l = \mathbf{n}_{ls} \cdot (\rho_l - \rho_s) \mathbf{w}_{sl} = -\left(1 - \frac{\rho_l}{\rho_s}\right) M_g k_s \left(1 - \frac{\omega_l}{\omega_{eq}}\right)^n \quad \text{at } A_{ls}, \tag{2.16}$$

which can be used to calculate the *interface velocity* and *liquid velocity* respectively. Eqs. 2.13 and 2.14 can be combined to provide a different expression for the calculation of the interface velocity, which is more convenient in the case of an equilibrium condition. This leads to

$$\mathbf{n}_{ls} \cdot \mathbf{w}_{sl} = \frac{\nu_s}{\rho_s (1 - \nu_s \omega_l)} \mathbf{n}_{ls} \cdot (\rho_l D_l \nabla \omega_l) \qquad \text{at } A_{ls}. \tag{2.17}$$

When assuming a negligible mass fraction of the dissolved species, the interface velocity can be approximated as $|\mathbf{n}_{ls} \cdot \mathbf{w}_{sl}| \approx 9.69 \times 10^{-8}\,\mathrm{m\,s^{-1}}$, which is negligible compared to the liquid velocity used in the following. Consider also Eq. 2.8, Eq. 2.11 can be simplified into

$$\text{B.C. III} \quad \mathbf{n}_{ls} \cdot (-\rho_l D_l \nabla \omega_l) \approx -M_{Ca} k_s \left(1 - \frac{\omega_l}{\omega_{eq}}\right)^n \quad \text{at } A_{ls}. \tag{2.18}$$

Together with the mass balance of the solid phase in V_s, and boundary conditions at the interface between the liquid phase and the insoluble material, A_{li}, the pore-scale problem can be finally written as

$$\frac{\partial \rho_l}{\partial t} + \nabla \cdot (\rho_l \mathbf{v}_l) = 0 \qquad \text{in } V_l, \tag{2.19}$$

$$\frac{\partial \rho_l \omega_l}{\partial t} + \nabla \cdot (\rho_l \omega_l \mathbf{v}_l) = \nabla \cdot (\rho_l D_l \nabla \omega_l) \qquad \text{in } V_l, \tag{2.20}$$

$$\text{B.C. I}\quad \mathbf{n}_{ls}\cdot\left(\rho_l\omega_l\left(\mathbf{v}_l-\mathbf{w}_{sl}\right)-\rho_l D_l\nabla\omega_l\right)=-M_{Ca}k_s\left(1-\frac{\omega_l}{\omega_{eq}}\right)^n \quad \text{at } A_{ls}, \tag{2.21}$$

$$\begin{aligned}\text{B.C. II}\qquad \mathbf{n}_{ls}\cdot\left(-\rho_s\mathbf{w}_{sl}\right) &= \mathbf{n}_{ls}\cdot\left(\rho_l\left(\mathbf{v}_l-\mathbf{w}_{sl}\right)\right)\\ &= \nu_s\mathbf{n}_{ls}\cdot\left(\rho_l\omega_l\left(\mathbf{v}_l-\mathbf{w}_{sl}\right)-\rho_l D_l\nabla\omega_l\right)\\ &= -\ M_g k_s\left(1-\frac{\omega_l}{\omega_{eq}}\right)^n \qquad \text{at } A_{ls},\end{aligned} \tag{2.22}$$

$$\frac{\partial\rho_s}{\partial t}=0 \quad \text{in } V_s, \tag{2.23}$$

$$\text{B.C. III}\qquad \mathbf{n}_{li}\cdot\left(\rho_l\omega_l\mathbf{v}_l-\rho_l D_l\nabla\omega_l\right)=0 \qquad \text{at } A_{li}, \tag{2.24}$$

$$\text{B.C. IV}\qquad \mathbf{n}_{li}\cdot\mathbf{v}_l=0 \qquad \text{at } A_{li}. \tag{2.25}$$

The problem has to be completed with momentum balance equations, for instance, Eqs. 2.7 and 2.8. When the velocity of dissolution is small compared to the relaxation time of the viscous flow[2], and considering constant ρ_l and μ_l, the problem for the momentum balance equations is independent of the concentration field and therefore can be treated independently. Consequently, the focus below is on the transport problem assuming that $\mathbf{v}_l$ and its average value are known fields.

Finally, the dissolution problem with a thermodynamic equilibrium description is simply the above problem in which the boundary condition at the dissolving interface, Eq. 2.21, is simply replaced by

$$\text{B.C. I}\qquad \omega_l=\omega_{eq} \qquad \text{at } A_{ls}, \tag{2.26}$$

2.3 Numerical modeling

The work presented in this thesis involves a lot of numerical computations: the pore-scale problem described above, resolution of closure problems and macro-scale equations as will be described later. All Partial Derivative Equa-

[2] About $\rho_l l_l^2/\mu_l$, which is on the order of 1 s for water and a pore-scale of 1 mm, indeed rather small compared to dissolution characteristic times.

tions (PDE) have been solved in this work with the help of the Finite Element software COMSOL®. This code offers various possibilities in terms of:

- meshing routines,
- finite element discretization,
- linear and non-linear solvers,
- time integration,
- direct solution of moving boundary problems through ALE (Arbitrary Lagrangian-Eulerian Method).

The implementation work consisted mainly in (i) introducing the proper physical properties, source terms, etc., in the software PDE templates for various types of equations, (ii) numerical tests in order to choose numerical parameters leading to an acceptable convergence. All numerical choices corresponded to well-known solutions for the classical PDEs to be solved: Navier-Stokes equations, advection-diffusion equations, etc.... Therefore, the details will not be given in this manuscript, unless some specific problems were encountered and required special attention.

2.4 Surface reaction versus transport limitation

In this section, the impact of a reactive boundary condition versus thermodynamic equilibrium is evaluated by solving the pore-scale problem for a typical small-scale situation, in order to assess the possible introduction of a further simplification of the model, i.e., the use of a thermodynamic equilibrium interfacial boundary condition. A half of the 2 D axisymmetric geometry under consideration is represented in Fig. 2.2. The interface evolution was calculated using the ALE method. Several simulations were performed with the data given in Table 2.3 (other parameters were given by the above proposed correlations). The boundary conditions were: uniform velocity U_0 and $\omega_l = 0$ at the entrance, convective flux conditions at the exit boundary, symmetry conditions over the axis and wall conditions elsewhere.

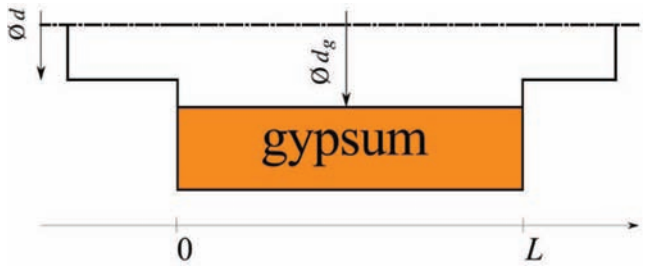

Figure 2.2: 2D Geometry of the solid (gypsum)-liquid (water) system at pore-scale.

Table 2.3: Parameters used in the simulations.

parameter	value
ρ_l	$1000\ \mathrm{kg\,m^{-3}}$
ρ_s	$2310\ \mathrm{kg\,m^{-3}}$
T	12°C
D_l	$10^{-9}\,\mathrm{m^2\,s^{-1}}$
d	$2\times10^{-3}\,\mathrm{m}$
d_g	$3\times10^{-3}\,\mathrm{m}$
L	$6\times10^{-3}\,\mathrm{m}$

2.4.1 Impact of reaction rate correlation

In this subsection, the impact of the choice of parameters in the surface kinetic reaction rate is tested. A first set of computations were made with the parameters in the reaction rate Eq. 1.4 given by $k_s = 1.3\times10^{-4}\ \mathrm{mmol\,cm^{-2}\,s^{-1}}$ and $n = 1.2$, i.e., a one-rate reactive boundary condition. Results for the normalized mass fraction ω_l/ω_{eq} are given in Fig. 2.3 for a velocity $U_0 = 10^{-4}\,\mathrm{m\,s^{-1}}$, i.e., a large Péclet number ($\mathrm{Pe} = \frac{U_0 d}{D_l} = 200$). Fig. 2.3a is obtained after a short transient regime corresponding to the establishment of a quasi-steady mass fraction fields, only slightly perturbed by the slow dissolution of the interface and Fig. 2.3b is obtained after a significant dissolution. The reactive condition at the dissolving surface does not impose that the mass fraction is equal to ω_{eq}, i.e., thermodynamic equilibrium. The maximum value of the ratio ω_l/ω_{eq} is given in the figure legends. The following comments can be drawn from these results: (i) there is a relatively thin boundary layer near the dissolving interface, due to a relatively large Péclet number, and (ii) the ratio ω_l/ω_{eq} is not equal to 1, but very close.

The second set of computations has the following boundary condition

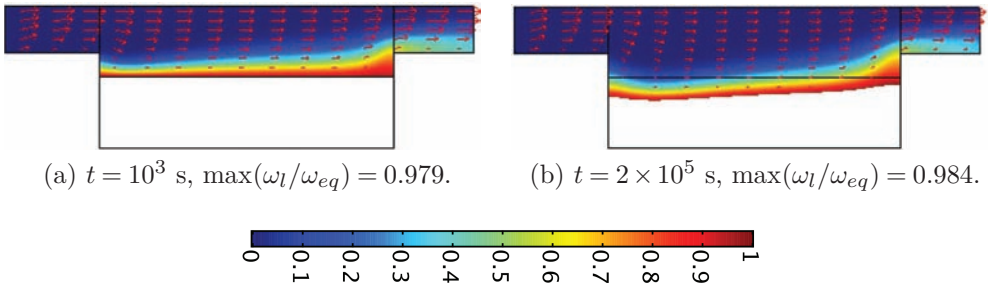

(a) $t = 10^3$ s, $\max(\omega_l/\omega_{eq}) = 0.979$. (b) $t = 2 \times 10^5$ s, $\max(\omega_l/\omega_{eq}) = 0.984$.

(c) legend

Figure 2.3: Field ω_l/ω_{eq} for $U_0 = 10^{-4}\,\mathrm{m\,s^{-1}}$, i.e., $\mathrm{Pe} = 200$ for the one-rate reactive case.

$$\begin{cases} n & = 5; \quad k_s = 20\,\mathrm{mmol\,cm^{-2}\,s^{-1}} \quad \text{if } \omega_l/\omega_{eq} \geq 0.95685, \\ n & = 1.2; \quad k_s = 1.3 \times 10^{-4}\,\mathrm{mmol\,cm^{-2}\,s^{-1}} \quad \text{else if,} \end{cases} \tag{2.27}$$

which is named a two-rate reactive case. Corresponding fields are plotted in Fig. 2.4. General comments on the field structure are the same as for Fig. 2.3. Looking at the $\max(\omega_l/\omega_{eq})$ values, one sees indeed an impact of the slowing down of the reaction rate. This impact seems to be relatively small, as emphasized by the results plotted in Fig. 2.5, which represent the outlet fluxes

$$\bar{m} = \int_d \mathbf{n}_{ls} \cdot (\rho_l \omega_l \mathbf{v}_l - \rho_l D_l \nabla \omega_l)\, dA, \tag{2.28}$$

for both boundary conditions versus time. While the relative difference is smaller than 1%, the boundary condition expressed by Eqs. 2.27 is kept in the following subsection.

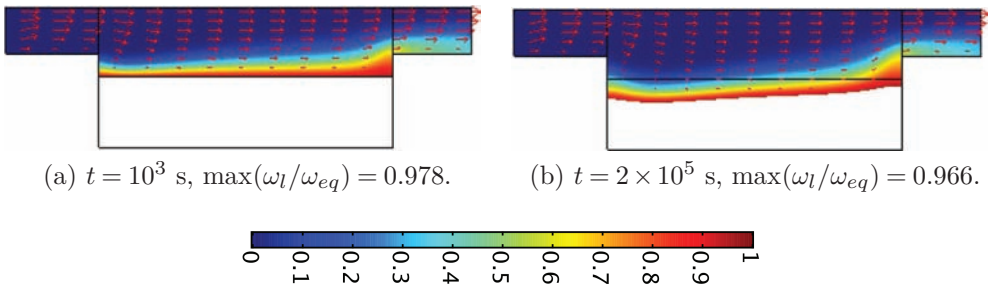

(a) $t = 10^3$ s, $\max(\omega_l/\omega_{eq}) = 0.978$. (b) $t = 2 \times 10^5$ s, $\max(\omega_l/\omega_{eq}) = 0.966$.

(c) legend

Figure 2.4: Field ω_l/ω_{eq} for $U_0 = 10^{-4}\,\mathrm{m\,s^{-1}}$, i.e., $\mathrm{Pe} = 200$ for the two-rate reactive case.

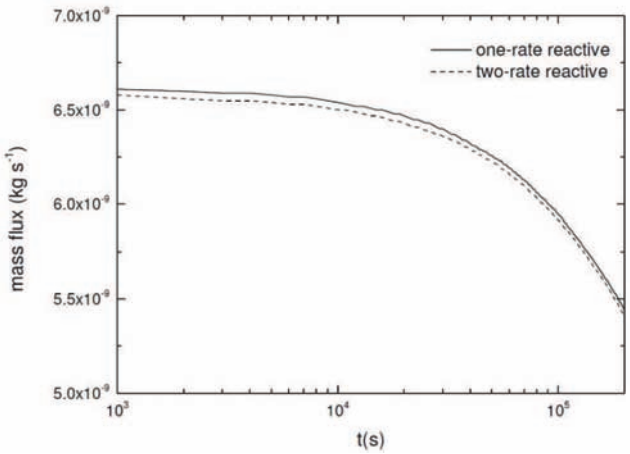

Figure 2.5: Mass flux over the outlet section versus time for the one-rate and two-rate reactive boundary condition cases.

2.4.2 Diffusive case

In this subsection, results are presented for a more diffusive case, with a Péclet number equal to 2, obtained by taking a velocity $U_0 = 10^{-6}\,\mathrm{m\,s^{-1}}$. Results are plotted in Fig. 2.6 for the normalized mass fraction field versus time. In this case the boundary layer becomes thicker and the surface maximum mass fraction becomes closer to the thermodynamic equilibrium value but still short of it. It should be noted that the field at $t = 1000$ s is not completely relaxed to the "quasi-steady" solution as can be seen from the outflow mass fraction value which is not close to the thermodynamic equilibrium value, while this is the case at $t = 2 \times 10^5$ s. This is coherent with the characteristic time based on the diffusion over the cross section which may be estimated as $d_g^2/4D_l \approx 2250\,\mathrm{s}$. Once again, the maximum value of ω_l/ω_{eq} observed over the interface is not equal to 1 but relatively close. The possibility of approximating the boundary condition by the thermodynamic equilibrium value is further investigated in the next subsection.

2.4.3 Reaction kinetics versus thermodynamic equilibrium boundary conditions

Results obtained with the full reaction rate boundary conditions are compared with results obtained from the thermodynamic equilibrium condition, i.e.,

$$\text{B.C. I } \omega_l = \omega_{eq} \quad \text{at } A_{ls}, \tag{2.29}$$

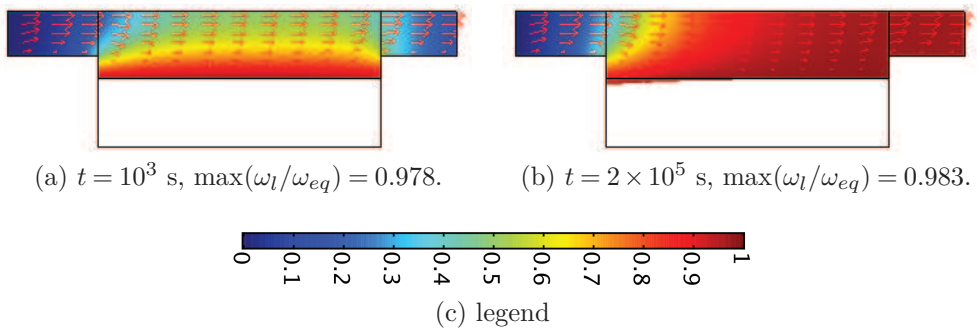

(a) $t = 10^3$ s, $\max(\omega_l/\omega_{eq}) = 0.978$. (b) $t = 2 \times 10^5$ s, $\max(\omega_l/\omega_{eq}) = 0.983$.

(c) legend

Figure 2.6: Field ω_l/ω_{eq} for $U_0 = 10^{-6}\,\mathrm{m\,s^{-1}}$, i.e., $\mathrm{Pe} = 2$ for the diffusive case.

which is the limit of the reactive condition for large Damköhler numbers. In that case, the interface velocity is calculated using

$$\mathbf{n}_{ls} \cdot \mathbf{w}_{sl} = \frac{\nu_s}{\rho_s \left(1 - \nu_s \omega_l\right)} \mathbf{n}_{ls} \cdot \left(\rho_l D_l \nabla \omega_l\right). \tag{2.30}$$

There are small differences between the mass fraction fields obtained with two-rate reactive or thermodynamic equilibrium boundary conditions. In order to analyze quantitatively the impact, the time evolutions of the total mass flux, $\bar{m}$, passing through a cross section, is presented in Fig. 2.7. The comparisons are performed in the cases of $\mathrm{Pe} = 2$ and $\mathrm{Pe} = 200$ respectively. The differences are about 2% in the diffusive case, i.e., $\mathrm{Pe} = 2$, and about 3% in the convective case, i.e., $\mathrm{Pe} = 200$, in favor of thermodynamic equilibrium dissolution as expected. Such differences can probably be neglected for most practical dissolution estimates, given the other uncertainties in characterizing a real natural system, but may be necessary for more accurate analyses.

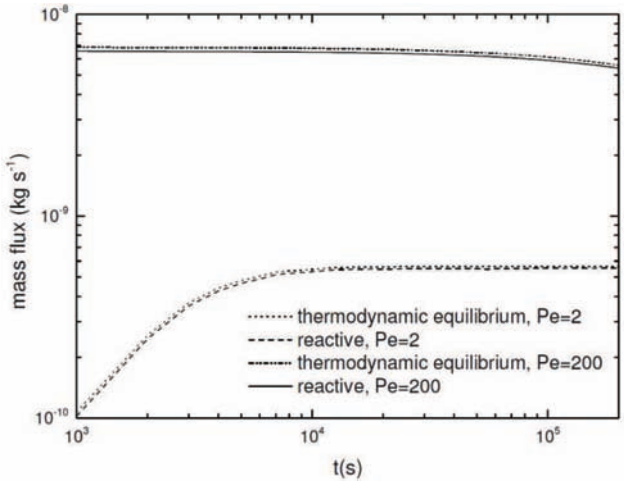

Figure 2.7: Mass flux over the outlet section versus time for two-rate reactive and thermodynamic equilibrium boundary conditions.

2.5 Conclusion

In this chapter, the pore-scale dissolution models and the corresponding constraints were studied. Based on available data in the literature and the numerical computations performed with the model, it was shown that dissolved gypsum may be treated as a pseudo-component, provided a few percent incertitude is acceptable for the mass fraction field calculation. The impact of the use of different boundary conditions was also analyzed: the use of a two-rate reactive boundary condition compared to the one-reaction rate, as well as to a thermodynamic equilibrium condition, only produces a very small difference less than 4%. While it is not numerically difficult to keep a complex reactive boundary condition when solving directly the equations, for instance using ALE method, the choice of a thermodynamic equilibrium is more relevant with the later use of the diffuse interface model based on a thermodynamic equilibrium condition at the pore-scale interface (or any model using such a boundary condition). This screening study shows that such an approach would give acceptable results with an error up to a few percent.

Chapter 3

Effective surface and boundary conditions for heterogeneous surfaces with mixed boundary conditions

3.1 Introduction

In this chapter, the case of a rough heterogeneous surface with mixed boundary conditions is studied, i.e., part of the surface is subject to a Dirichlet condition while the rest is subject to a no-flux Neumann condition. Such problems may arise when dealing with dissolution problems, especially when working on large-scale cavity formation in geological structures (solution mining, karst formations, etc.). A similar mathematical problem arises when one considers the drying rate of a surface with wet and dry patches such as a porous surface [156] or for atmosphere-scale problems [157]. Taking the development of karstic cavity for example, it often involves multi-scale problems as schematized in Fig.3.1, and it is generally difficult to take into consideration the small-scale heterogeneities or roughnesses over the interface while working at the cavity scale. Therefore, the implemented models of such dissolution problems take in practice the form of an effective surface modeling, with a heuristic boundary condition. In general one uses the Dirichlet condition as the macro-scale boundary condition, even if heterogeneities (e.g., insoluble material) and roughnesses are present. The position of the effective surface itself is guided by meshing consideration without an explicit link to the physics of the problem. These questions are addressed in this chapter and a methodol-

ogy is proposed to build and position the effective surface with appropriate boundary conditions.

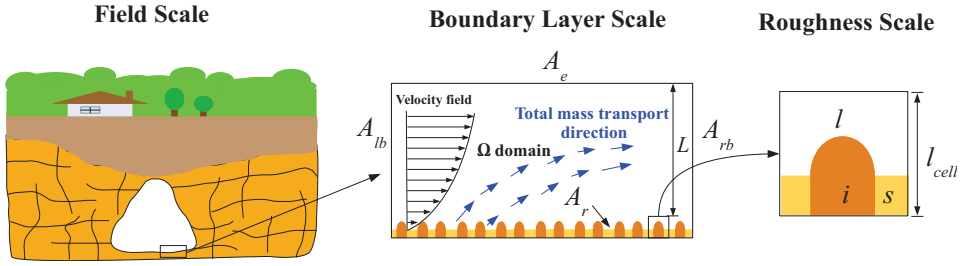

Figure 3.1: Multi-scale description of the system. The dissolving medium is denoted as the s-phase and the non-dissolving part as the i-phase.

In this study, it is focused as a guideline on mass and momentum transfer in the case of a laminar boundary layer over an heterogeneous surface composed of a dissolving medium and a non-dissolving one. Two length scales are important to describe the phenomena taking place at the surface: one is the characteristic length of the large-scale cavity, L, for instance the depth of the large-scale boundary layer developing over the rough surface, and the other one is the roughness length scale l_{cell}. As illustrated in Fig. 3.1, the consideration is the laminar steady-state flow in a domain Ω of a fluid l, over a rough, heterogeneous surface A_r, made of a salt medium, s, and an insoluble material, i. Mass transport over the rough surface in contact with the fluid, can be modeled by different boundary conditions. Two configurations are particularly interesting. In case I, it is assumed that the surface is composed by patches under thermodynamic equilibrium (A_{ls}), with surrounding areas with no flux (A_{li}). In case II, the boundary condition at A_{ls} is replaced by a reactive one such as Eq. 1.4.

The steady-state mass and momentum transfer problem can be described as follows:

Pb I in Ω

$$\rho_l\,(\mathbf{u}\cdot\nabla)\,\mathbf{u}-\mu_l\triangle\mathbf{u}+\nabla p=0 \quad \text{in } \Omega, \tag{3.1}$$

$$\nabla\cdot\mathbf{u}=0 \quad \text{in } \Omega, \tag{3.2}$$

$$\mathbf{u}\cdot\nabla c=\nabla\cdot(D_l\nabla c) \quad \text{in } \Omega, \tag{3.3}$$

$$\mathbf{u}=0 \quad \text{at } A_r, \tag{3.4}$$

$$-\mathbf{n}\cdot D_l\nabla c=0 \quad A_e,\ A_{li} \text{ and } A_{rb} \tag{3.5}$$

$$\text{(B.C. I)} \quad c=c_{eq} \quad \text{at } A_{ls}, \tag{3.6}$$

$$\text{or (B.C. II)} \quad -\mathbf{n}_{ls}\cdot D_l\nabla c=-k\,c_{eq}\left(1-\tfrac{c}{c_{eq}}\right) \quad \text{at } A_{ls}, \tag{3.7}$$

$$c=0 \quad \text{at } A_{lb} \tag{3.8}$$

$$\mathbf{n}\cdot(-p\mathbf{I}+\mu_l(\nabla\mathbf{u}+\nabla\mathbf{u}^T))=\mathbf{0} \quad \text{at } A_e \text{ and } A_{rb} \tag{3.9}$$

$$\mathbf{u}=U_0\mathbf{e}_1 \quad \text{at } A_{lb} \tag{3.10}$$

where c is the concentration of the dissolved species in $\mathrm{kg\,m^{-3}}$, k is the reaction rate coefficient in $\mathrm{m\ s^{-1}}$ which may depend on the position of the surface, $\mathbf{n}$ is the normal vector pointing outward from the studied domain at A_e, A_{lb}, A_{rb} and the later mentioned $A_{l,i}$, and U_0 denotes the magnitude of the inlet velocity. One has $\mathbf{n}$=$\mathbf{n}_{ls}$ at A_r, with $\mathbf{n}_{ls}$ the normal vector of A_r pointing towards the solid phase. B.C. I and B.C. II refer to case I and case II problems, respectively. It is worthy noticing that the no flux condition at A_e and the constant velocity condition at A_{lb} are not unique, which can be replaced, for instance, by zero concentration condition at A_e and constant pressure at A_{lb}, respectively.

Eq. 3.7 has a form similar to rate laws proposed in [47, 48, 140] for limestone and gypsum dissolution. Additional assumptions are used: the fluid is incompressible and its physical properties do not vary significantly with concentration, and hydrostatic pressure has been included in the field p. While we have in mind potential evolution of the surface A_r due to the dissolution process, it is assumed that the relaxation time for the transport problem is smaller at the roughness scale than the one of the dissolution process. Therefore, the transport problem is considered steady-state for a given geometry. The evolution of the geometry in the case of a dissolution process is not within the scope of this chapter. The reader my refer to [85] for a study of the impact of the actual dissolution process on the surface roughness and hence on the effective surface behavior.

A typical solution of this multi-scale problem would feature large-scale evo-

lution of the pressure, velocity and concentration far from the surface and deviations from this large-scale pattern in the neighborhood of the roughnesses. This situation is schematically represented in Fig. 3.2. It is distinguished in this figure a bulk domain, Ω_0, where the variables do not show fluctuations induced by the roughnesses at the l_{cell}-scale, and a series of elementary volumes, Ω_i, characteristic of the surface geometry. Assuming some kind of periodicity is typical of most situations and it is also adopted in this study. Clearly, this suggests that some kind of effective boundary condition may be imposed at the surface of A_0 in order to reproduce the same bulk fields. Under such circumstances, one technique to derive effective surface and effective boundary conditions is based on a multi-domain decomposition method, as illustrated by [42, 43, 87]. The idea is to solve the flow and mass transport problems in each Ω_i by introducing an asymptotic expansion of deviation terms based on the macro-scale bulk velocity and concentration fields. In general, closure problems may be found for variables mapping the deviations onto the bulk variables and their derivatives. This can be used to provide a set of effective boundary conditions that may be applied at the boundary A_0. It is often interesting in terms of efficiency to place the effective surface in a different location than A_0, which will be discussed in Sec. 3.3. Effective parameter calculations will be provided in Sec. 3.4 for some simple roughness geometries. Finally, a comparison of DNS results and effective surface results is proposed in Sec. 3.5 for a typical boundary layer problem in order to illustrate the application of the concept of effective surface. This allows to discuss the practical implementation of the effective surface model, and, in particular, the choice of the "optimal" position of the effective surface.

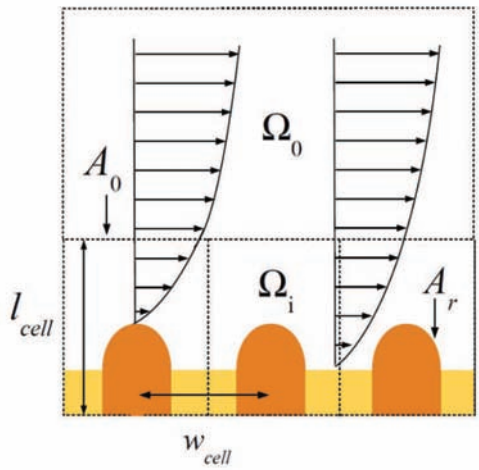

Figure 3.2: Close-up view of the velocity field near the rough surface.

3.2 Multi-domain decomposition

As discussed in the introduction chapter, the domain decomposition methodology has already been used to model diverse transport phenomena [42,43,87]. In this section, the domain decomposition is presented, which splits the problem over Ω into a problem over Ω_0 and Ω_i subdomains, and is applied to our specific transport problem.

As previously introduced, the characteristic length-scale of the rough heterogeneous surface, l_{cell}, is much smaller than the one of the global domain Ω, L, e.g., the depth of the large-scale boundary layer. Therefore, it is assumed that all fluctuations of velocity and concentration resulting from the wall non-uniformity vanish far from the wall. By introducing an arbitrary surface A_0, the Ω domain is decomposed into a global external subdomain, Ω_0 (with $\star_0$ quantities), and local subdomains, Ω_i (with $\star_i$ quantities), which contains the wall perturbations, roughness and heterogeneity. This decomposition is illustrated in Fig. 3.3.

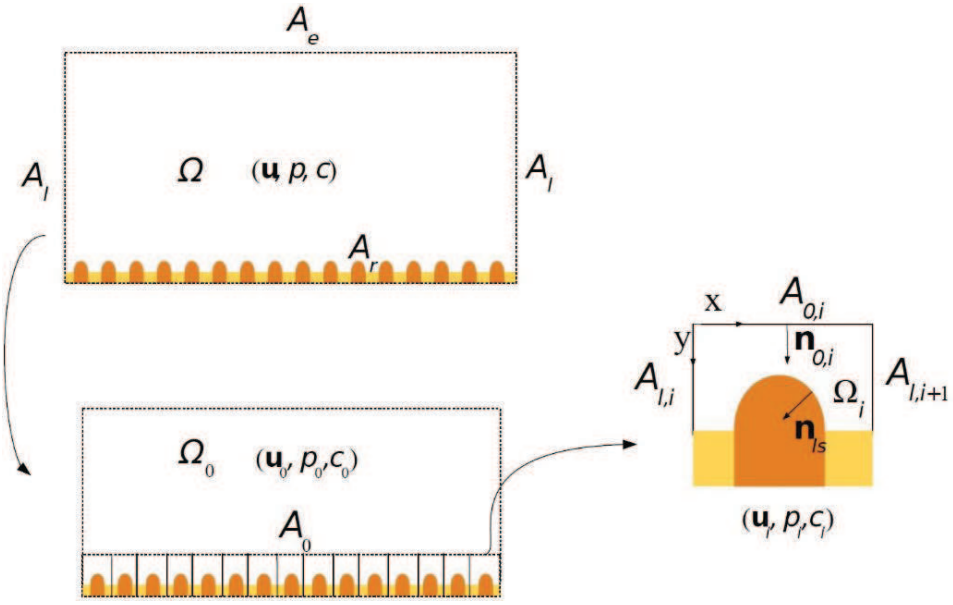

Figure 3.3: Multi-domain decomposition.

The wall surface, A_r, is assumed to have a periodic structure. As a result, the initial problem will be decomposed as a Ω_0 problem and a series of Ω_i problems. It is noteworthy that A_0 has no defined position. It should be located at an appropriate position to ensure that all fluctuations are contained in Ω_i subdomains and that the assumption $l_{cell} \ll L$ is valid. For sake of simplicity, the development is presented in 2D ($(\mathbf{e}_1, \mathbf{e}_2)$ plane), with $\mathbf{e}_1$ (x-coordinate) corresponding to the infinite flow direction and $\mathbf{e}_2$ (y-coordinate)

to the opposite direction of the macroscopic wall normal, as sketched in Fig. 3.3.

Velocity, pressure, concentration, mass flux and stress tensor are all continuous across A_0, which give

$$\mathbf{u}_0 = \mathbf{u}_i, \tag{3.11}$$

$$p_0 = p_i, \tag{3.12}$$

$$c_0 = c_i, \tag{3.13}$$

$$\mathbf{n}_{0,i} \cdot (-D_l \nabla c_0 + \mathbf{u}_0 c_0) = \mathbf{n}_{0,i} \cdot (-D_l \nabla c_i + \mathbf{u}_i c_i), \tag{3.14}$$

$$\mathbf{n}_{0,i} \cdot (-p_0 \mathbf{e}_2 + \mu_l (\nabla \mathbf{u}_0 + \nabla \mathbf{u}_0^T)) = \mathbf{n}_{0,i} \cdot (-p_i \mathbf{e}_2 + \mu_l (\nabla \mathbf{u}_i + \nabla \mathbf{u}_i^T)), \tag{3.15}$$

at $A_{0,i}$, with $A_{0,i}$ referring to the intersection between Ω_0 and Ω_i, and $\boldsymbol{n}_{0,i}$ referring to the normal vector to $A_{0,i}$ pointing from Ω_0 towards Ω_i.

As the initial global domain has been decomposed into subdomains at different scales, Ω_0 and Ω_i problems can be written separately while linked by the continuity conditions across A_0 presented above. In Ω_0, equations for the flow and the mass transport problems are similar to the ones in the initial domain, adding Eqs. 3.11 to 3.15 for continuity conditions:

Pb II (in Ω_0) (i.e., macro-scale problem)

$$\rho_l (\mathbf{u}_0 \cdot \nabla) \mathbf{u}_0 - \mu_l \triangle \mathbf{u}_0 + \nabla p_0 = 0 \quad \text{in } \Omega_0, \tag{3.16}$$

$$\nabla \cdot \mathbf{u}_0 = 0 \quad \text{in } \Omega_0, \tag{3.17}$$

$$\mathbf{u}_0 \cdot \nabla c_0 = \nabla \cdot (D_l \nabla c_0) \quad \text{in } \Omega_0, \tag{3.18}$$

$$c_0 = 0 \quad \text{at } A_{lb}/\Omega_0 \tag{3.19}$$

$$-\mathbf{n} \cdot D_l \nabla c_0 = 0 \quad \text{at } A_e \text{ and } A_{rb}/\Omega_0 \tag{3.20}$$

$$\mathbf{n} \cdot (-p_0 \mathbf{I} + \mu_l (\nabla \mathbf{u}_0 + \nabla \mathbf{u}_0^T)) = \mathbf{0} \quad \text{at } A_e \text{ and } A_{rb}/\Omega_0 \tag{3.21}$$

$$\mathbf{u}_0 = U_0 \mathbf{e}_1 \quad \text{at } A_{lb}/\Omega_0 \tag{3.22}$$

where A_{lb}/Ω_0 and A_{rb}/Ω_0 denote the parts of lateral boundaries contained in Ω_0.

As a result of the wall periodic motif and assuming that the transverse flux through $A_{l,i}$ (i.e., the interface of two unit cells) is negligible compared to the one in the vertical direction (across $A_{0,i}$), pseudo-periodic conditions are prescribed at the l_{cell}-scale. With the continuity conditions unchanged at $A_{0,i}$,

the following problem for Ω_i is obtained:

Pb III (in Ω_i) (i.e., micro-scale problem)

$$\rho_l\left(\mathbf{u}_i\cdot\nabla\right)\mathbf{u}_i-\mu_l\triangle\mathbf{u}_i+\nabla p_i=0 \quad \text{in } \Omega_i, \tag{3.23}$$

$$\nabla\cdot\mathbf{u}_i=0 \quad \text{in } \Omega_i, \tag{3.24}$$

$$\mathbf{u}_i\cdot\nabla c_i=\nabla\cdot\left(D_l\nabla c_i\right) \quad \text{in } \Omega_i, \tag{3.25}$$

$$\mathbf{u}_i\left(x+w_{cell}\right)=\mathbf{u}_i(x) \quad \text{at } A_{l,i}, \tag{3.26}$$

$$p_i\left(x+w_{cell}\right)=p_i(x) \quad \text{at } A_{l,i}, \tag{3.27}$$

$$\mathbf{n}\cdot\left(-p_i\mathbf{I}+\mu_l(\nabla\mathbf{u}_i+\nabla\mathbf{u}_i^T)\right)=\mathbf{0} \quad \text{at } A_{l,i} \text{ and } A_{0,i} \tag{3.28}$$

$$c_i\left(x+w_{cell}\right)=c_i(x) \quad \text{at } A_{l,i}, \tag{3.29}$$

$$\mathbf{u}_i=0 \quad \text{at } A_r, \tag{3.30}$$

$$-\mathbf{n}\cdot D_l\nabla c_i=0 \quad \text{at } A_{li} \text{ and } A_{l,i}, \tag{3.31}$$

$$\text{(B.C. I)} \quad c_i=c_{eq} \quad \text{at } A_{ls}, \tag{3.32}$$

$$\text{or (B.C. II)} \quad -\mathbf{n}_{ls}\cdot D_l\nabla c_i=-k\,c_{eq}\left(1-\tfrac{c_i}{c_{eq}}\right) \quad \text{at } A_{ls}. \tag{3.33}$$

with w_{cell} denoting the width of the unit cell Ω_i, as illustrated in Fig. 3.2.

Solving these problems in a direct manner will make little benefit compared to DNSs. To gain computational efficiency, one should look for generic expressions of variables in the Ω_i subdomains and describe the microscopic behaviors by some kind of averaging, instead of considering all the details induced by the surface non-uniformity. Asymptotic expansions are used in the next section to estimate $\mathbf{u}_i$ and c_i at first order. By means of closure problems, these estimates can be found, and effective boundary conditions can be built for effective surfaces defined at different positions.

3.3 Effective boundary conditions

Since first proposed by Carrau [158], effective boundary conditions, or wall laws, have been the research topic of many scholars. With a multi-domain decomposition technique and an asymptotic approach, Achdou et al. [87, 88, 159, 160] studied both mathematically and numerically the problem of laminar flows over periodic rough surfaces with no-slip condition. This problem was reviewed by Jäger and Mikelić, including the problem of the interface between a liquid domain and a porous domain [93, 95, 161]. Veran et al. [43] and Introïni et al. [42] developed the concept of effective surface for

momentum and mass (or heat) transfer on a rough surface, with a particular attention on the question of positioning the effective surface. This study makes use of similar ideas, incorporating not only the reactive case as in [43] (however with a different expression of the reaction rate in our study suitable for dissolution problems), but also the case of surface under thermodynamic equilibrium and taking into account parts of the surface corresponding to insoluble or non-reactive material.

In this section, the momentum and mass transfer problems are solved separately. Assuming that the flow properties are independent of c, the momentum problem can be decoupled from the mass transport one. The momentum transfer problem has already been worked out in the above cited literature. Therefore, the development is rapidly reviewed for reader's understanding, following similar notations and presentation proposed in [42, 43]. Estimates are first made for $\mathbf{u}_i$ and p_i by the sum of macroscopic terms and deviations. The macroscopic terms are then developed by Taylor expansion from A_0. The deviation terms are decomposed by means of closure mapping variables. Closure problems are then used to get first order estimates of the deviations, and this in turn can be utilized to determine the effective boundary conditions. The problem for mass transfer is solved in a similar manner.

3.3.1 Momentum effective boundary conditions

As detailed previously, the micro-scale variables are partitioned as shown below

$$\mathbf{u}_i = \mathbf{u} + \tilde{\mathbf{u}}_i, \qquad p_i = p + \tilde{p}_i, \tag{3.34}$$

where $\mathbf{u}_i$, $\tilde{p}_i$ and later mentioned $\tilde{c}_i$ are the deviations, which are defined as the difference between micro- and macro-scale variables. The global field $\mathbf{u}$ and p are equal to $\mathbf{u}_0$ and p_0 in Ω_0 and some smooth continuation of these fields in Ω_i. Approximating $\mathbf{u}$ and p in Ω_i with Taylor expansions in the normal direction to the fictitious surface A_0, the estimates of $\mathbf{u}_i$ and p_i can be written as

$$\mathbf{u}_i = \mathbf{u}_0|_{y=0} + \mathbf{y}\cdot\nabla\mathbf{u}_0|_{y=0} + \frac{1}{2}\mathbf{y}\mathbf{y}\cdot\nabla\nabla\mathbf{u}_0|_{y=0} + \cdots + \tilde{\mathbf{u}}_i, \tag{3.35}$$

$$p_i = p_0|_{y=0} + \mathbf{y}\cdot\nabla p_0|_{y=0} + \frac{1}{2}\mathbf{y}\mathbf{y}\cdot\nabla\nabla p_0|_{y=0} + \cdots + \tilde{p}_i. \tag{3.36}$$

Taking into consideration the no-slip boundary condition described by Eq. 3.30, the following relation is established between the different velocities in terms of order of magnitude

$$O\left(\tilde{\mathbf{u}}_i\right) = O\left(\mathbf{u}_0|_{y=0}\right) = O\left(\frac{l_{cell}}{L}U\right), \tag{3.37}$$

with U the magnitude of the global velocity $\mathbf{u}$ and L the depth of the bulk flow boundary layer.

In order to characterize the flow features at the different length-scales, the macro- and micro-scale Reynolds numbers are introduced respectively, following the discussion in [42], as

$$\mathrm{Re}_L = \frac{\rho_l U L}{\mu_l}, \tag{3.38}$$

and, since the roughnesses are well included in the boundary layer,

$$\mathrm{Re} = \frac{\rho_l \epsilon U l_{cell}}{\mu_l}, \tag{3.39}$$

where $\epsilon = \frac{l_{cell}}{L}$ and the reference velocity is estimated linearly in the roughness domain as compared to U.

From the above two equations, one can write immediately

$$\mathrm{Re} = \epsilon^2 \mathrm{Re}_L. \tag{3.40}$$

It has been assumed that the roughnesses are much smaller than the thickness of the boundary layer, which gives $\epsilon \ll 1$. Assuming a laminar flow implies that the boundary layer thickness scales as $\mathrm{Re}_L^{-1/2}$. With these two hypotheses one obtains $\mathrm{Re}_L \ll \epsilon^{-2}$. By substituting this relation into Eq. 3.40, it is obtained that $\mathrm{Re} \ll 1$.

Using the approximations of $\mathbf{u}_i$ and p_i defined by Eqs. 3.34, Eq. 3.23 can be rewritten as

$$\rho_l \left(\left(\mathbf{u} + \tilde{\mathbf{u}}_i\right) \cdot \nabla\right) \left(\mathbf{u} + \tilde{\mathbf{u}}_i\right) - \mu_l \triangle \left(\mathbf{u} + \tilde{\mathbf{u}}_i\right) + \nabla\left(p + \tilde{p}_i\right) = 0 \text{ in } \Omega_i. \tag{3.41}$$

Subtracting Eq. 3.1 from Eq. 3.41 results

$$\rho_l \left(\mathbf{u} \cdot \nabla\right) \tilde{\mathbf{u}}_i + \rho_l \left(\tilde{\mathbf{u}}_i \cdot \nabla\right) \mathbf{u} + \rho_l \left(\tilde{\mathbf{u}}_i \cdot \nabla\right) \tilde{\mathbf{u}}_i - \mu_l \triangle \tilde{\mathbf{u}}_i + \nabla \tilde{p}_i = 0 \text{ in } \Omega_i, \tag{3.42}$$

which can be expressed in a dimensionless form, as

$$\mathrm{Re}\left(\mathbf{u}'\cdot\nabla'\right)\tilde{\mathbf{u}}_i'+\mathrm{Re}\left(\tilde{\mathbf{u}}_i'\cdot\nabla'\right)\mathbf{u}'+\mathrm{Re}\left(\tilde{\mathbf{u}}_i'\cdot\nabla'\right)\tilde{\mathbf{u}}_i'-\triangle'\tilde{\mathbf{u}}_i'+\nabla'\tilde{p}_i'=0 \text{ in } \Omega_i, \tag{3.43}$$

where the dimensionless variables ($\star'$ quantities) are defined as follows

$$\mathbf{u}'=\frac{\mathbf{u}}{\epsilon U}\ ,\nabla'=\nabla l_{cell},\ \ \tilde{\mathbf{u}}_i'=\frac{\tilde{\mathbf{u}}_i}{\epsilon U}\ \text{ and }\ \tilde{p}_i'=\frac{\tilde{p}_i l_{cell}}{\mu_l \epsilon U}. \tag{3.44}$$

Given that $\mathrm{Re}\ll 1$, Eq. 3.43 can be simplified by omitting the first three terms. Going back to a dimensional form, it gives

$$-\mu_l\triangle\tilde{\mathbf{u}}_i+\nabla\tilde{p}_i=0. \tag{3.45}$$

Hereby the Navier-Stokes equations have been transformed into a Stokes problem in Ω_i, which is a simplification similar to that proposed in [42, 43, 93].

First order estimates of $\mathbf{u}_i$ and p_i are

$$\mathbf{u}_i=\mathbf{u}_0|_{y=0}+\mathbf{y}\cdot\nabla\mathbf{u}_0|_{y=0}+\tilde{\mathbf{u}}_i,\qquad p_i=p_0|_{y=0}+\mathbf{y}\cdot\nabla p_0|_{y=0}+\tilde{p}_i. \tag{3.46}$$

In a developed boundary layer, the velocity is mainly tangential and the gradients for both velocity and pressure are dominated by the components normal to the wall, i.e., $\frac{\partial}{\partial x}\ll\frac{\partial}{\partial y}$. The first order term of the above estimates can be rewritten as

$$\mathbf{y}\cdot\nabla\mathbf{u}_0|_{y=0}=y\frac{\partial u_0}{\partial y}\Big|_{y=0}\mathbf{e}_1,\qquad \mathbf{y}\cdot\nabla p_0|_{y=0}=y\frac{\partial p_0}{\partial y}\Big|_{y=0}. \tag{3.47}$$

The obtained equations for the deviations are summarized as the following boundary value problem

Pb III$_{\tilde{\mathbf{u}}_i}$(in Ω_i):

$$
\begin{aligned}
-\mu_l \triangle \tilde{\mathbf{u}}_i + \nabla \tilde{p}_i = 0 \qquad & \text{in } \Omega_i, && (3.48)\\
\nabla \cdot \tilde{\mathbf{u}}_i = 0 \qquad & \text{in } \Omega_i, && (3.49)\\
\mathbf{n} \cdot (-\tilde{p}_i \mathbf{I} + \mu_l (\nabla \tilde{\mathbf{u}}_i + \nabla \tilde{\mathbf{u}}_i^T)) = \mathbf{0} \qquad & \text{at } A_{0,i} \text{ and } A_{l,i} && (3.50)\\
\tilde{p}_i = 0 \qquad & \text{at } A_{0,i} && (3.51)\\
\tilde{\mathbf{u}}_i (x + w_{cell}) = \tilde{\mathbf{u}}_i (x) \qquad & \text{at } A_{l,i}, && (3.52)\\
\tilde{p}_i (x + w_{cell}) = \tilde{p}_i (x) \qquad & \text{at } A_{l,i}, && (3.53)\\
u_0|_{y=0} \mathbf{e}_1 + y \frac{\partial u_0}{\partial y}\Big|_{y=0} \mathbf{e}_1 + \tilde{\mathbf{u}}_i = 0 \qquad & \text{at } A_r. && (3.54)
\end{aligned}
$$

So far, the resolution of this set of equations still remains expensive, due to the coupling of micro- and macro-scale variables. As discussed in [42], and given the linear structure of the problem, the macroscopic terms can be considered to be generators of the deviations. From Eq. 3.54, it is obvious that if the terms with macroscopic variables are zero, the deviations of velocity and pressure will both go zero. Therefore, one can represent the deviation terms in the following form:

$$
(1)\ \tilde{\mathbf{u}}_i = \mathbf{A} u_0|_{y=0} + \mathbf{B} \frac{\partial u_0}{\partial y}\Big|_{y=0}, \qquad (2)\ \tilde{p}_i = m u_0|_{y=0} + s \frac{\partial u_0}{\partial y}\Big|_{y=0}. \tag{3.55}
$$

Closure problems for closure variables$(\mathbf{A}, m)$ and $(\mathbf{B}, s)$ are given by

Pb III$_{(\mathbf{A},m)}$(in Ω_i):

$$
\begin{aligned}
-\mu_l \triangle \mathbf{A} + \nabla m = 0 \qquad & \text{in } \Omega_i, && (3.56)\\
\nabla \cdot \mathbf{A} = 0 \qquad & \text{in } \Omega_i, && (3.57)\\
\mathbf{n} \cdot (-m\mathbf{I} + \mu_l (\nabla \mathbf{A} + \nabla \mathbf{A}^T)) = \mathbf{0} \qquad & \text{at } A_{0,i} \text{ and } A_{l,i} && (3.58)\\
\mathbf{A} (x + w_{cell}) = \mathbf{A}(x) \qquad & \text{at } A_{l,i}, && (3.59)\\
m (x + w_{cell}) = m(x) \qquad & \text{at } A_{l,i}, && (3.60)\\
\mathbf{A} + \mathbf{e}_1 = 0 \qquad & \text{at } A_r. && (3.61)
\end{aligned}
$$

Pb III$_{(\mathbf{B},s)}$(in Ω_i):

$$-\mu_l \triangle \mathbf{B} + \nabla s = 0 \qquad \text{in } \Omega_i, \tag{3.62}$$

$$\nabla \cdot \mathbf{B} = 0 \qquad \text{in } \Omega_i, \tag{3.63}$$

$$\mathbf{n} \cdot (-s\mathbf{I} + \mu_l(\nabla \mathbf{B} + \nabla \mathbf{B}^T)) = \mathbf{0} \qquad \text{at } A_{0,i} \text{ and } A_{l,i} \tag{3.64}$$

$$\mathbf{B}(x + w_{cell}) = \mathbf{B}(x) \qquad \text{at } A_{l,i}, \tag{3.65}$$

$$s(x + w_{cell}) = s(x) \qquad \text{at } A_{l,i}, \tag{3.66}$$

$$\mathbf{B} + y\mathbf{e}_1 = 0 \qquad \text{at } A_r. \tag{3.67}$$

At this point, one can see that $(\mathbf{A}, m)$=$(-\mathbf{e}_1, 0)$ is a solution for closure problem $\mathbf{Pb\ III}_{(\mathbf{A},m)}$. Inserting this solution into Eq. 3.55-1 gives

$$\tilde{\mathbf{u}}_i = -u_0|_{y=0}\mathbf{e}_1 + \mathbf{B}\frac{\partial u_0}{\partial y}\Big|_{y=0}. \tag{3.68}$$

According to velocity continuity at $A_{0,i}$, it gives $\tilde{\mathbf{u}}_i\,|_{y=0} = 0$. By introducing $-w_x^v = B\,|_{y=0}$, with B the x-component of $\mathbf{B}$, the velocity at $A_{0,i}$ can be written as

$$\mathbf{u}_0|_{y=0} = u_0|_{y=0}\mathbf{e}_1 = -w_x^v \frac{\partial u_0}{\partial y}\Big|_{y=0}\mathbf{e}_1 \quad \text{at } A_{0,i}, \tag{3.69}$$

which has the form of a Navier condition.

Following [42,43], it is interesting to look at the modification of this boundary condition for another position of the effective surface. For a given effective surface A_{eff}, defined by its position at $y = w$, a first order Taylor expansion allows us to write

$$\mathbf{u}_0|_{y=w} = \mathbf{u}_0|_{y=0} + w\frac{\partial u_0}{\partial y}\Big|_{y=0}\mathbf{e}_1, \tag{3.70}$$

and the new boundary condition can be obtained from Eq. 3.69 as

$$\mathbf{u}_0|_{y=w} = (w - w_x^v)\frac{\partial u_0}{\partial y}\Big|_{y=0}\mathbf{e}_1 \text{ at } A_{eff}. \tag{3.71}$$

It is shown that a position of A_{eff} exists where one can recover a no-slip boundary condition. This specific position is defined by $w = w_x^v$ (cf. Fig. 3.4) and it plays an important role in the macro-scale simulations.

Up to this point, the homogenization procedure has been finished to build the effective boundary condition at an effective surface for the momentum transfer problem. This effective boundary condition depends on the chosen position of the effective surface. In the next section, the same method is

applied to the mass transfer problem.

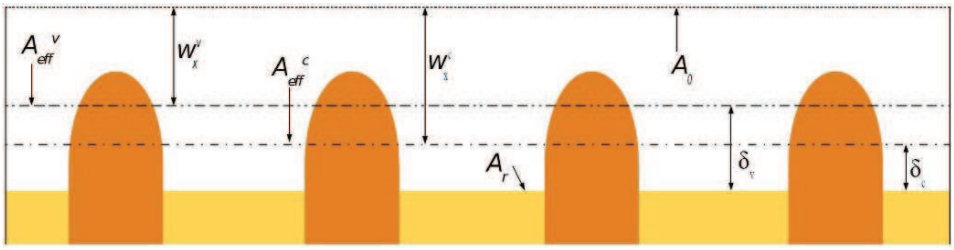

Figure 3.4: Definition of effective surfaces for velocity and concentration.

3.3.2 Mass effective boundary condition

First order estimate for c_i can be written as

$$c_i = c_0|_{y=0} + y\frac{\partial c_0}{\partial y}\Big|_{y=0} + \tilde{c}_i. \tag{3.72}$$

Consequently, Eq. 3.25 can be transformed into

$$v\frac{\partial c_0}{\partial y}\Big|_{y=0} + \mathbf{u}_i \cdot \nabla \tilde{c}_i = \nabla \cdot (D_l \nabla \tilde{c}_i), \tag{3.73}$$

with $v = \mathbf{u}_i \cdot \mathbf{e}_2$. The reader are reminded that $\mathbf{e}_2$ corresponds to the direction of the y-coordinate, normal to $A_{0,i}$ and pointing from Ω_0 towards Ω_i. The boundary conditions can be rewritten as

$$-\mathbf{n}_{ls} \cdot \left(D_l \frac{\partial c_0}{\partial y}\Big|_{y=0} \mathbf{e}_2 \right) - \mathbf{n}_{ls} \cdot D_l \nabla \tilde{c}_i = 0 \quad \text{at } A_{li}, \tag{3.74}$$

$$\text{(B.C. I)} \qquad c_0|_{y=0} + y\frac{\partial c_0}{\partial y}\Big|_{y=0} + \tilde{c}_i = c_{eq} \quad \text{at } A_{ls}, \tag{3.75}$$

$$\text{or (B.C. II)} \quad -\mathbf{n}_{ls} \cdot \left(D_l \frac{\partial c_0}{\partial y}\Big|_{y=0} \mathbf{e}_2 \right) - \mathbf{n}_{ls} \cdot D_l \nabla \tilde{c}_i$$
$$= -k\, c_{eq} \left(1 - \frac{c_0|_{y=0} + y\frac{\partial c_0}{\partial y}|_{y=0} + \tilde{c}_i}{c_{eq}} \right) \text{ at } A_{ls}. \tag{3.76}$$

Adding the continuity conditions across $A_{0,i}$ and the periodic constraints, the problem for $\tilde{c}_i$ can be written as

Pb III$_{\tilde{c}_i}$(in Ω_i):

$$v\frac{\partial c_0}{\partial y}\Big|_{y=0} + \mathbf{u}_i \cdot \nabla \tilde{c}_i = \nabla \cdot (D_l \nabla \tilde{c}_i) \qquad \text{in } \Omega_i, \tag{3.77}$$

$$\tilde{c}_i\,(x + w_{cell}) = \tilde{c}_i(x) \qquad \text{at } A_{l,i}, \tag{3.78}$$

$$\tilde{c}_i = 0 \qquad \text{at } A_{0,i}, \tag{3.79}$$

$$-\mathbf{n}_{ls} \cdot \left(D_l \frac{\partial c_0}{\partial y}\Big|_{y=0} \mathbf{e}_2 \right) - \mathbf{n}_{ls} \cdot D_l \nabla \tilde{c}_i = 0 \qquad \text{at } A_{li}, \tag{3.80}$$

$$\text{(B.C. I)} \qquad c_0|_{y=0} + y\frac{\partial c_0}{\partial y}\Big|_{y=0} + \tilde{c}_i = c_{eq} \qquad \text{at } A_{ls}, \tag{3.81}$$

$$\begin{aligned} \text{or (B.C. II)} \; & -\mathbf{n}_{ls} \cdot \left(D_l \frac{\partial c_0}{\partial y}\Big|_{y=0} \mathbf{e}_2 \right) - \mathbf{n}_{ls} \cdot D_l \nabla \tilde{c}_i \\ & = -k\, c_{eq} \left(1 - \frac{c_0|_{y=0} + y\frac{\partial c_0}{\partial y}|_{y=0} + \tilde{c}_i}{c_{eq}} \right) \text{ at } A_{ls}. \end{aligned} \tag{3.82}$$

To solve this problem, a solution is sought by linking the deviation to the macroscopic concentration, i.e., it writes

$$\tilde{c}_i = a(c_0|_{y=0} - c_{eq}) + b\frac{\partial c_0}{\partial y}\Big|_{y=0}, \tag{3.83}$$

where a and b are first-order mapping variables.

Substituting Eq. 3.83 into Eqs. 3.80 to 3.82 , one has at A_{li}

$$-\mathbf{n}_{ls} \cdot \left(D_l \frac{\partial c_0}{\partial y}\Big|_{y=0} (\mathbf{e}_2 + \nabla b) \right) - \mathbf{n}_{ls} \cdot D_l\,(c_0|_{y=0} - c_{eq})\,\nabla a = 0, \tag{3.84}$$

and at A_{ls}

$$\text{(B.C. I)} \; (1+a)(c_0|_{y=0} - c_{eq}) + (y+b)\frac{\partial c_0}{\partial y}\Big|_{y=0} = 0, \tag{3.85}$$

$$\begin{aligned} \text{or (B.C. II)} \quad & -\mathbf{n}_{ls} \cdot \left(D_l \frac{\partial c_0}{\partial y}\Big|_{y=0} (\mathbf{e}_2 + \nabla b) \right) - \mathbf{n}_{ls} \cdot D_l\,(c_0|_{y=0} - c_{eq})\,\nabla a \\ = \quad & k\, c_{eq} \left(\frac{(1+a)\left(c_0|_{y=0} - c_{eq}\right) + (b+y)\frac{\partial c_0}{\partial y}|_{y=0}}{c_{eq}} \right). \end{aligned} \tag{3.86}$$

Pb III$_{\tilde{c}_i}$ may be transformed into two independent problems for a and b as follows:

Pb III$_a$ (in Ω_i):

$$\mathbf{u}_i \cdot \nabla a = \nabla \cdot (D_l \nabla a) \quad \text{in } \Omega_i, \tag{3.87}$$

$$a(x + w_{cell}) = a(x) \quad \text{at } A_{l,i}, \tag{3.88}$$

$$a = 0 \quad \text{at } A_{0,i}, \tag{3.89}$$

$$-\mathbf{n} \cdot D_l \nabla a = 0 \quad \text{at } A_{li} \text{ and } A_{l,i} \tag{3.90}$$

$$\text{(B.C. I)} \quad 1 + a = 0 \quad \text{at } A_{ls}, \tag{3.91}$$

$$\text{or (B.C. II)} \quad -\mathbf{n}_{ls} \cdot D_l \nabla a = k(1 + a) \quad \text{at } A_{ls}. \tag{3.92}$$

Pb III$_b$ (in Ω_i):

$$v + \mathbf{u}_i \cdot \nabla b = \nabla \cdot (D_l \nabla b) \quad \text{in } \Omega_i, \tag{3.93}$$

$$b(x + w_{cell}) = b(x) \quad \text{at } A_{l,i}, \tag{3.94}$$

$$b = 0 \quad \text{at } A_{0,i}, \tag{3.95}$$

$$-\mathbf{n}_{ls} \cdot (\mathbf{e}_2 - \nabla b) = 0 \quad \text{at } A_{li}, \tag{3.96}$$

$$\text{(B.C. I)} \quad y + b = 0 \quad \text{at } A_{ls}, \tag{3.97}$$

$$\text{or (B.C. II)} \quad -\mathbf{n}_{ls} \cdot D_l (\mathbf{e}_2 + \nabla b) = k(b + y) \quad \text{at } A_{ls}. \tag{3.98}$$

It is noted that $b = -y$ is a solution of **Pb III**$_b$. Consequently, c_i can be simply expressed as

$$c_i = a(c_0|_{y=0} - c_{eq}) + c_0|_{y=0}. \tag{3.99}$$

With the continuity conditions $\mathbf{u}_0 = \mathbf{u}_i$ and $c_0 = c_i$ at $A_{0,i}$, the mass flux balance described by Eq. 3.14 can be rewritten as

$$\int_{A_{0,i}} \mathbf{n}_{0,i} \cdot D_l \nabla c_0 dA = \int_{A_{0,i}} \mathbf{n}_{0,i} \cdot D_l \nabla c_i dA \text{ at } A_{0,i}. \tag{3.100}$$

which can be transformed into

$$\mathbf{n}_{0,i} \cdot (-D_l \nabla c_0) = -\frac{c_0|_{y=0} - c_{eq}}{A_{0,i}} D_l \int_{A_{0,i}} \frac{\partial a}{\partial y} dA \text{ at } A_{0,i}. \tag{3.101}$$

For later use, an effective reaction rate coefficient k^0_{eff} is defined as

$$k^0_{eff} = -\frac{D_l \int_{A_{0,i}} \frac{\partial a}{\partial y} dA}{A_{0,i}}, \tag{3.102}$$

and the effective boundary condition at A_0 can be recast into

$$-\mathbf{n}_{0,i}\cdot D_l\nabla c_0|_{y=0} = -k^0_{eff}\,c_{eq}\left(1-\frac{c_0|_{y=0}}{c_{eq}}\right) \quad \text{at } A_0. \tag{3.103}$$

Remarkably, *the obtained effective boundary condition is, mathematically speaking, of a reactive type, even in the case with micro-scale thermodynamic equilibrium.* Of course, the effective boundary condition has the same form in case I and case II, but the values of k^0_{eff} are given by different closure problems.

For A_{eff} at an arbitrary position $y = w$, the first order estimate of the macro-scale concentration is developed as

$$c_0|_{y=w} = c_0|_{y=0} + w\left.\frac{\partial c_0}{\partial y}\right|_{y=0}. \tag{3.104}$$

Assuming at first order that $\frac{\partial c_0}{\partial y}|_{y=w} = \frac{\partial c_0}{\partial y}|_{y=0}$, Eq. 3.101 is rewritten as

$$D_l\left.\frac{\partial c_0}{\partial y}\right|_{y=w} = k^0_{eff}\,c_{eq}\left(1-\frac{c_0|_{y=w} - w\frac{\partial c_0}{\partial y}|_{y=w}}{c_{eq}}\right) \text{ at } y=w. \tag{3.105}$$

Therefore, the following reactive condition at an arbitrary effective surface is obtained for case I and case II

$$\mathbf{n}_{0,i}\cdot(-D_l\nabla c_0) = -k^w_{eff}\,c_{eq}\left(1-\frac{c_0|_{y=w}}{c_{eq}}\right) \quad \text{at } A_{eff} \tag{3.106}$$

with

$$k^w_{eff} = \frac{k^0_{eff}}{1-\frac{w}{D_l}k^0_{eff}}. \tag{3.107}$$

Again, the remarkable result is obtained that, whatever the boundary condition at A_{ls} (i.e., thermodynamic equilibrium or reactive), the effective boundary condition has the same reactive form.

However, it is possible to define an effective surface, A^c_{eff}, such that an equilibrium condition is recovered, i.e., $c_0 = c_{eq}$. From Eq. 3.105, the position of this surface is given by

$$w^c_x = \frac{D_l}{k^0_{eff}} = -\frac{A_{0,i}}{\int_{A_{0,i}}\frac{\partial a}{\partial y}dA}. \tag{3.108}$$

3.3.3 Effective surface and effective boundary conditions

After resolution of the closure problems, it has been shown that the boundary condition for the flow problem is of Navier type (results already known, briefly presented here for completeness) and of Robin type for the mass transfer problem (the original part of this study). It has also been indicated how to estimate the effective boundary condition for a different position of the effective surface. Nevertheless, the three surfaces defined previously (i.e., A_0, the boundary surface between Ω_0 and Ω_i, A^v_{eff}, the surface with the no-slip boundary and A^c_{eff}, the one under thermodynamic equilibrium) are those of main interest, as discussed in the next sections. Effective parameters will be calculated in Sec. 3.4, and the obtained effective boundary value problem will be tested in Sec. 3.5.

The obtained general form of the effective boundary value problem consists of Pb II and the boundary conditions at the effective surface, for instance, Eqs. 3.71 and 3.106 for an arbitrary surface position A_{eff} (at $y = w$), which become

$$\mathbf{u}_i = -w^v_x \frac{\partial u_0}{\partial y}\Big|_{y=0} \mathbf{e}_1 \tag{3.109}$$

$$-\mathbf{n}_{ls} \cdot D_l \nabla c_0 = -k^0_{eff}\, c_{eq} \left(1 - \frac{c_0}{c_{eq}}\right) \tag{3.110}$$

at the fictive surface A_0, or

$$\mathbf{u}_i = 0 \tag{3.111}$$

$$-\mathbf{n}_{ls} \cdot D_l \nabla c_0 = -k^v_{eff}\, c_{eq} \left(1 - \frac{c_0}{c_{eq}}\right) \tag{3.112}$$

for effective surface A^v_{eff} with the no-slip condition at $y = w^v_x$, or

$$\mathbf{u}_i = (w^c_x - w^v_x) \frac{\partial u_0}{\partial y}\Big|_{y=0} \mathbf{e}_1 \tag{3.113}$$

$$c_0 = c_{eq}. \tag{3.114}$$

for effective surface A^c_{eff} at $y = w^c_x$, where the thermodynamic equilibrium condition is recovered.

3.4 Effective parameters calculations

The aim of this section is to analyze the impact of some factors, for instance the roughness features, the Péclet, the Schmidt and the mean Damköhler numbers, on the effective parameters. The Péclet and the Schmidt numbers are defined as

$$\mathrm{Pe} = \frac{u_{ref} w_x^0}{D_l}, \ \mathrm{Sc} = \frac{\mu_l}{\rho_l D_l}, \tag{3.115}$$

where the cell height, w_x^0, is used as a characteristic length. The reference flow velocity u_{ref} is chosen as the x-component of the velocity at A_0. The mean Damköhler number will be defined later.

Dimensionless forms of closure problem Pb $\mathrm{III}_{(\mathbf{B},s)}$ and Pb III_a are solved to obtain the effective surface position and boundary conditions, with the unit cell presented in Fig. 3.5. Two shapes of roughness are used in the simulations, semi-ellipse or rounded square. The height of the roughness h_r and its width b_r are the two independent parameters. The height and width of the unit cell are denoted as w_x^0 (with $w_x^0 = 8h_r$) and w_{cell}, respectively. In the following simulations, w_x^0 and h_r have fixed values, while w_{cell} and b_r are varied in order to modify either the roughness geometry or the roughness density as shown in Fig. 3.5.

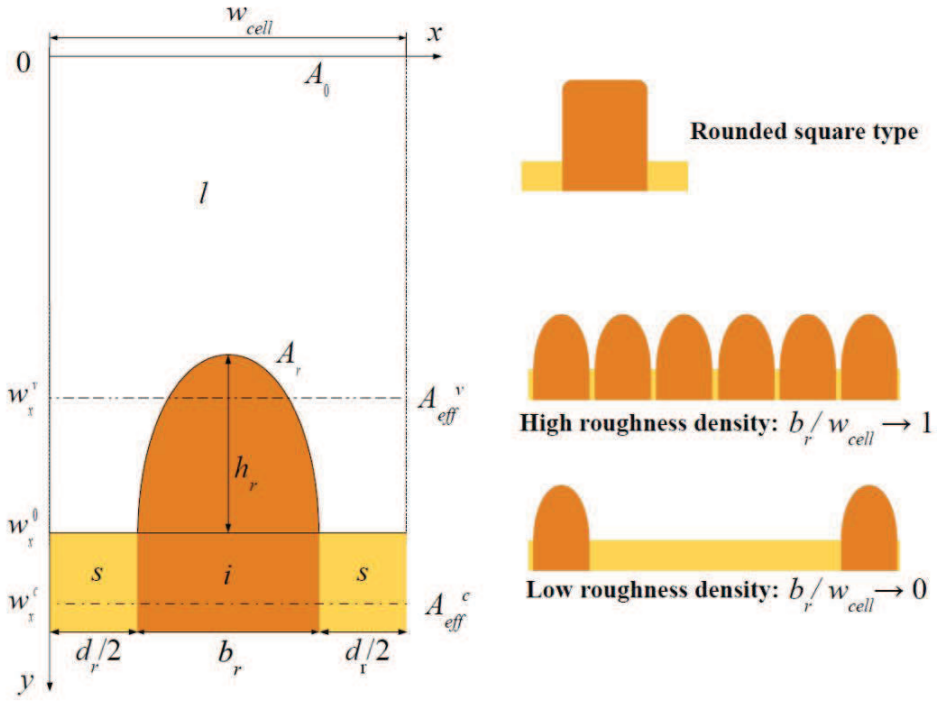

Figure 3.5: Unit cell geometry for the simulation (left) and illustration of roughness shape and roughness density (right).

All the following simulations are performed using COMSOL®. The linear systems are solved with the direct solver UMFPACK, which is based on the Unsymmetric MultiFrontal method. The velocity field in Pb III$_a$ is calculated by solving dimensionless steady-state Navier-Stokes equations. Quadratic Lagrange element formulation is used for the closure variables a, $\mathbf{B}$ and the velocity. Linear Lagrange element settings are used for pressure and its mapping variable s. Proper mesh qualities are obtained to ensure convergence. For example for the unit cell with $\frac{b_r}{w_{cell}} = 0.1$, $\mathrm{Pe} = 25$ and $\mathrm{Sc} = 1$, since further increase of the number of degrees of freedom larger than 10^4 leads to the variation of $\int_{A_{0,i}} \frac{\partial a}{\partial y} dA$ less than 1%, it is considered that the results are of appropriate quality in such circumstances. Given the fact that the unit cell geometry under study is quite simple, it is very easy to get converged results; therefore no more details of the procedure are provided here.

3.4.1 Effect of roughness features on effective surface positions

In this subsection the influences of the roughness geometry and density on the positions of A^v_{eff} and A^c_{eff} are investigated. Since w^v_x and w^c_x are values varying with the choice of A_0, it is more convenient to introduce the corresponding normalized values $\delta_v = \frac{w^0_x - w^v_x}{h_r}$ and $\delta_c = \frac{w^0_x - w^c_x}{h_r}$ to indicate the effective positions relative to the solid surface (see Fig. 3.4, where δ_v and δ_c are not normalized with respect to h_r). Results for four sets of simulations are presented in Fig. 3.6.

In Fig. 3.6a, it is observed that both the geometry and the roughness density have an impact on δ_v. One can observe that for higher roughness densities, i.e., $\frac{b_r}{w_{cell}} \to 1$, A^v_{eff} goes closer to the roughness height because the narrow gaps between asperities make it difficult for the fluid to flow through. The upper limit of δ_v is one and is nearly reached for the thin semi-ellipse and the rounded squares because their roughness shapes are steep. For roughnesses close enough to each other, the heterogeneous surface has a similar behavior in terms of momentum transport as a smooth surface located at the height of the roughnesses. For smoother roughnesses, the limit case where two roughnesses are adjacent gives a value of δ_v smaller than one as the fluid can still flow partially between the roughnesses. The three sets of simulations with semi-ellipse shape also show that thin roughnesses create more resistance to the flow than wider ones. The curves exhibit another limit when $\frac{b_r}{w_{cell}} \to 0$. Even if the two neighboring asperities are far enough from each other, e.g., $w_{cell} = 50 h_r$

in this case, the roughnesses still have some small impact on the flow and δ_v tends towards $0.1h_r$.

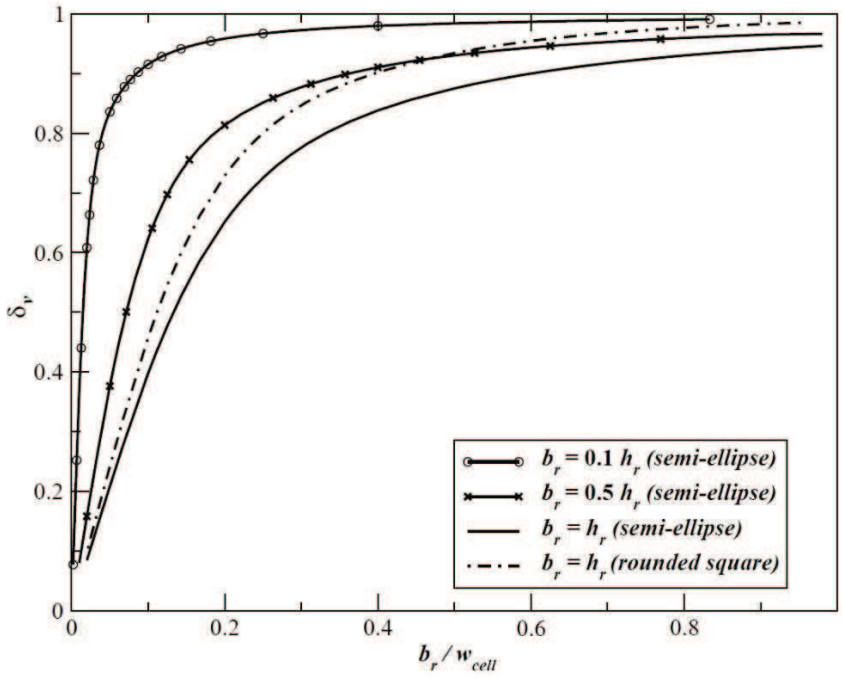

(a)

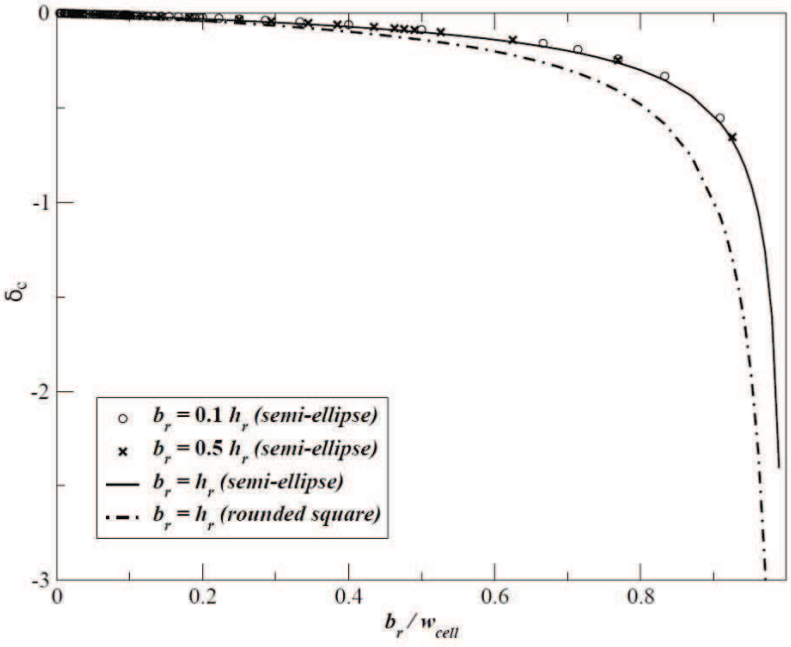

(b)

Figure 3.6: Effective surface position of A^v_{eff} (a) and A^c_{eff} (b) for different roughness geometries and densities.

In Fig. 3.6b, the negative values of δ_c mean that A^c_{eff} locates inside the

solid part. The presence of insoluble materials makes the averaged concentration on A_r smaller than the equilibrium concentration, therefore A^c_{eff} must be located beneath A_r to recover the thermodynamic equilibrium. Similar to the case with no-slip condition, both roughness shape and roughness density are playing a role on δ_c. However, one can observe that the three sets of simulations with semi-ellipse shapes are superposed, indicating that the width of the roughness has little impact on δ_c for a given ratio of $\frac{b_r}{w_{cell}}$. One sees from these results that δ_c tends towards $-\infty$ when the ratio $\frac{b_r}{w_{cell}}$ increases towards one, independently of the roughness geometry. For $\frac{b_r}{w_{cell}} \to 1$, the solid surface in contact with the fluid is mainly formed by the insoluble material and little mass transfer occurs between the solid and the fluid, which makes it difficult to recover thermodynamic equilibrium effective boundary condition. The upper limit of δ_c is equal to zero and is obtained for low roughness density ($\frac{b_r}{w_{cell}} \to 0$). In this case the solid-liquid interface behaves like a homogeneous soluble surface.

In Fig. 3.7, the low influence of the Péclet number and Schmidt number on δ_c is illustrated. In this set of simulations, the roughness shape is fixed to a rounded square roughness with $b_r = h_r$ and the roughness density is modified by varying the ratio $\frac{b_r}{w_{cell}}$. These results show that δ_c is mostly independent of the Péclet number and the Schmidt number as the four curves are superposed. As shown in the insert of Fig. 3.7, some small differences appear for low values of $\frac{b_r}{w_{cell}}$ and for the couple $\mathrm{Pe} = 1000$ and $\mathrm{Sc} = 1$.

3.4.2 Thermodynamic equilibrium case (B.C. I)

In this subsection, the dependence of k^v_{eff} on different factors is investigated first. Simulations are conducted for both advective-diffusive mass transport regime and purely diffusive regime. In the latter case, the effective reaction rate coefficient is denoted as $k^v_{eff_{diffu}}$. The flat part of the solid-liquid interface is under thermodynamic equilibrium. The roughness shape is semi-ellipse with a height of h_r. The other geometric parameters of the unit cell are $w^0_x = 8h_r$, $b_r = 0.5h_r$ and $w_{cell} = 5h_r$.

The ratio of $\frac{k^v_{eff}}{k^v_{eff_{diffu}}}$ as a function of Pe and Sc is plotted in Fig. 3.8.

One sees in the figure that $\frac{k^v_{eff}}{k^v_{eff_{diffu}}}$ increases globally with Pe and Sc, which means that the flow has a stronger impact on mass transport, as advection becomes more important when increasing (Pe, Sc). For all tested Sc, when $\mathrm{Pe} < 10$, the effective reaction rate coefficient with advection is nearly the

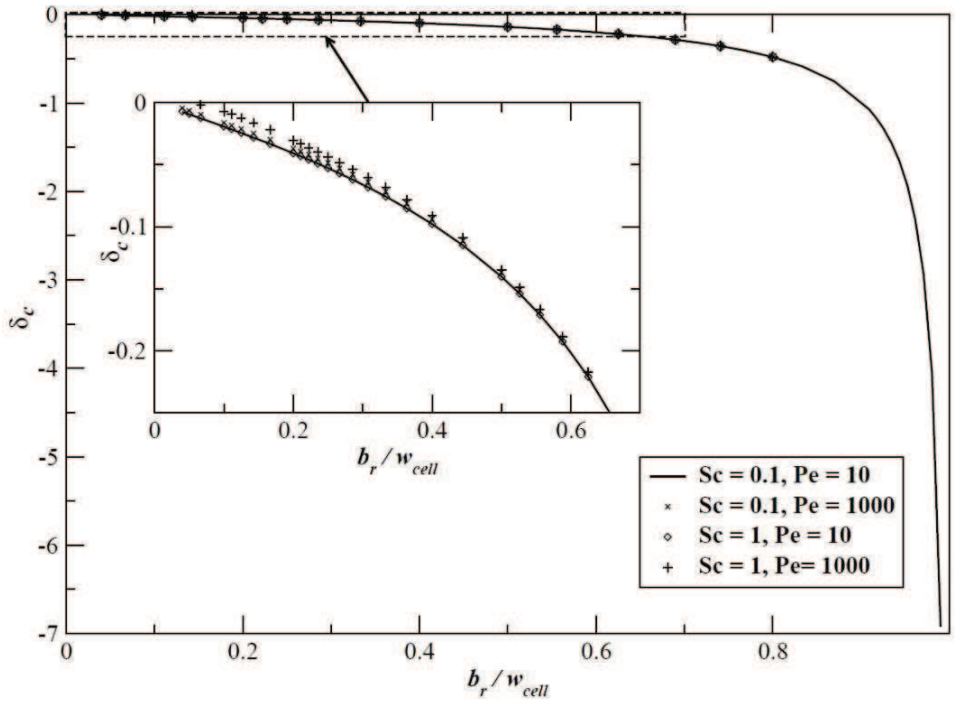

Figure 3.7: Effective surface position A^c_{eff} for a rounded square roughness for different densities, Pe and Sc values. Insert: zoom of the upper part of the initial graph.

same as the one under a purely diffusive regime. For $\mathrm{Sc} < 0.1$, the difference between k^v_{eff} and $k^v_{eff_{diffu}}$ is less than 1% for $\mathrm{Pe} < 1000$. Consequently, the mass transport problem can be simplified into a pure diffusion case in such circumstances, producing an error smaller than 1%. For the cases with Sc close to 1, $\frac{k^v_{eff}}{k^v_{eff_{diffu}}}$ reaches a maximum at high Pe values, then decreases and increases again. For higher Sc the ratio increases with Pe with different rate except for $\mathrm{Sc} = 100$ and $\mathrm{Sc} = 1000$ that are superposed on the studied range of Pe. One has to pay attention that the considered situation in this study is laminar flow within a boundary layer. Therefore for the cases with small Sc, the considered Pe should not be too large.

To illustrate the different regimes between mass transport governed by diffusion or by advection, the streamlines of the total flux of a versus Sc and Pe are plotted in Fig. 3.9. With small Pe (10 and 50), the variation of Sc only has some small impact on the streamlines, which illustrates the weak influence of the flow on the mass exchange at the reactive surface. The value of k^v_{eff} is therefore close to the value in the purely diffusive case (with a difference less than 1%) as illustrated in Fig. 3.8. With larger Pe values, increasing Sc (i.e., increasing the viscosity) delays the occurrence of recirculations close to

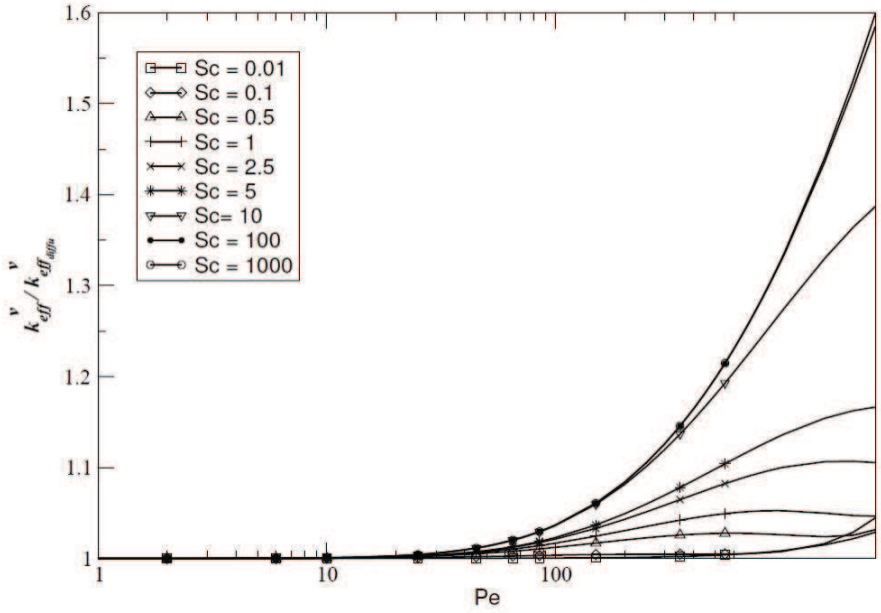

Figure 3.8: Ratio between k^v_{eff} with advection and its value in the purely diffusive case, as a function of Pe and Sc. Semi-ellipse roughness was used with $b_r = 0.5h_r$ and $\frac{b_r}{w_{cell}} = 0.1$.

the rough surface, which explains the maximum values observed in Fig. 3.8. The recirculations first limit mass transport towards the soluble material, and then enhance it for increasing Pe, corresponding to the decrease and increase of $\frac{k^v_{eff}}{k^v_{eff_{diffu}}}$ after the maximum values.

In a second set of simulations, the influence of the rough surface geometry on $\frac{k^v_{eff}}{k^v_{eff_{diffu}}}$ is investigated by changing the roughness density. From the results presented in Fig. 3.10, a high roughness density leads to a delay in the transition between the advective and diffusive regime. One can observe for example that for $\frac{b_r}{w_{cell}} = 0.4$ and $\frac{b_r}{w_{cell}} = 0.5$, the flow alone has a small impact on the effective reaction rate coefficient (less than 1%) even for high Pe values. In these configurations, $k^v_{eff_{diffu}}$ is a good estimate of k^v_{eff}. As the roughness density decreases, $\frac{k^v_{eff}}{k^v_{eff_{diffu}}}$ increases because the flow can pass through the roughness more easily, and therefore more solid surface under thermodynamic equilibrium is available for mass transfer.

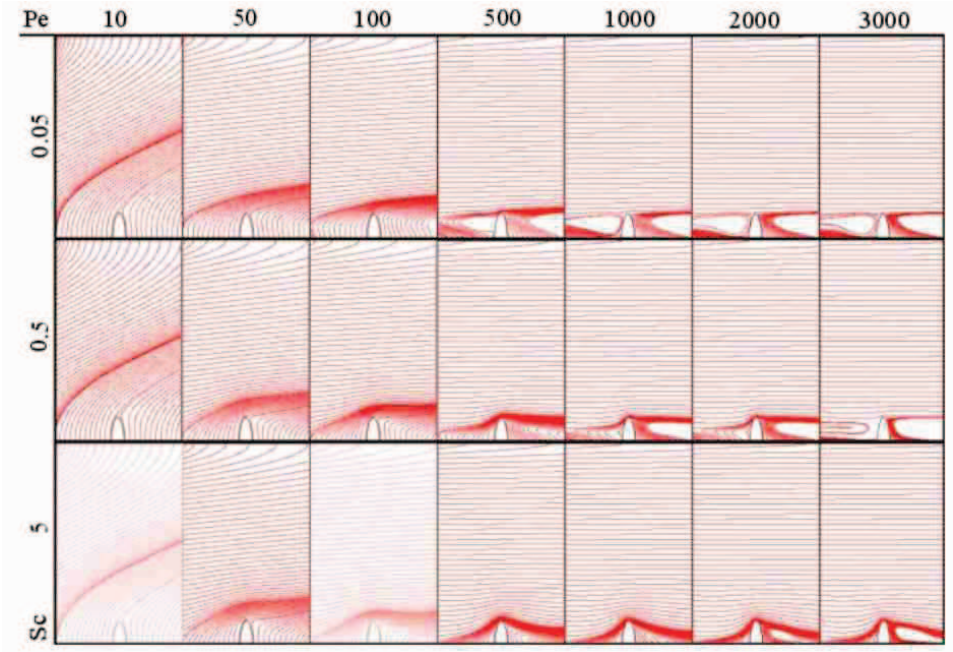

Figure 3.9: Total flux streamlines of closure variable a for different Sc and Pe. The roughness shape is a semi-ellipse with $b_r = 0.5h_r$ and $\frac{b_r}{w_{cell}} = 0.1$.

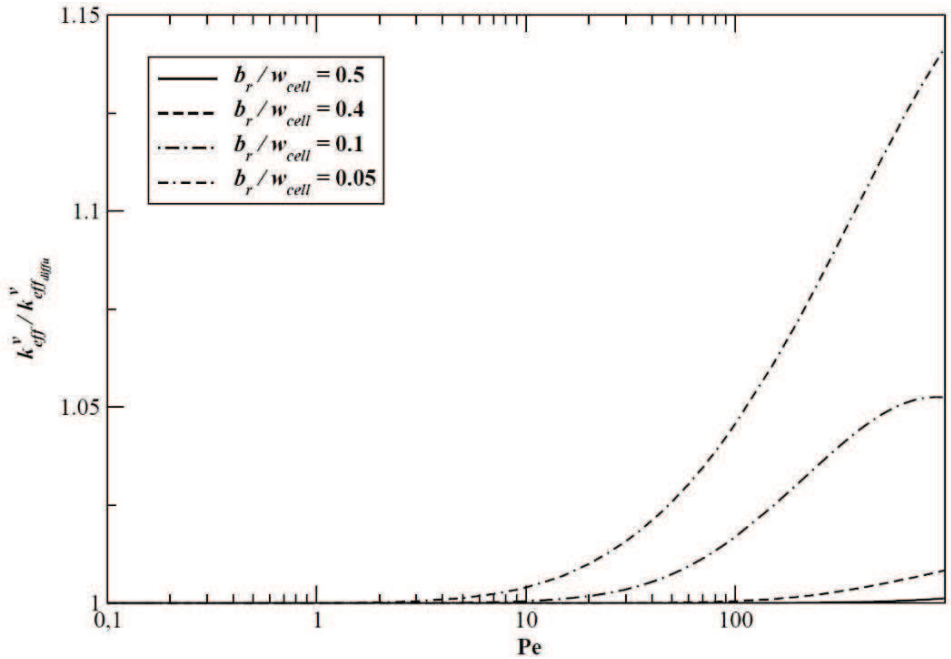

Figure 3.10: Ratio between k^v_{eff} with convection and its value in the purely diffusive case, as a function of the local Péclet number, for different roughness densities given by $\frac{b_r}{w_{cell}}$.

3.4.3 The case of a reactive surface (B.C. II)

In this subsection, the flat part of the solid-liquid interface is reactive. To study the impact of the chemical features on the effective reaction rate coefficient, some parameters are first introduced. Let k_{li} denote the reactivity at surface A_{li}. One should note that k_{li} is equal to zero in this study since the i-phase is non-reactive. The surface average reaction rate coefficient for a heterogeneous surface can be approximated as $\hat{k} = \frac{k_{ls}A_{ls}+k_{li}A_{li}}{A_{ls}+A_{li}}$, with A_{ls} and A_{li} representing the surface areas of A_{ls} and A_{li}, respectively. According to the mass conservation from A_r to A^v_{eff}, the surface average reaction rate coefficient at A^v_{eff} can be estimated as $\hat{k}^v = \frac{k_{ls}A_{ls}+k_{li}A_{li}}{A_v}$, with A_v denoting the surface area of A^v_{eff}. The structure of the concentration field inside the domain will depend on the ratio between reaction characteristic rates and diffusion, corresponding to a mean Damköhler number defined as $\widehat{\mathrm{Da}} = \frac{\hat{k}w^0_x}{D_l}$.

The roughness shape under consideration is semi-ellipse. The height and width of the roughness, as well as the height of the unit cell remain unchanged, with $b_r = 0.5h_r$ and $w^0_x = 8h_r$. Two roughness densities, $w_{cell} = 5h_r$ and $w_{cell} = 10h_r$, are considered.

The results of $\frac{k^v_{eff}}{\hat{k}^v}$ versus $\widehat{\mathrm{Da}}$ are presented in Fig. 3.11 for different Pe and Sc. For small $\widehat{\mathrm{Da}}$, $\frac{k^v_{eff}}{\hat{k}^v}$ tends towards one despite of the flow properties. In such circumstances, the characteristic time of reaction is long compared to the mass-transfer kinetics, and the process is consequently limited by reaction. With the increase of $\widehat{\mathrm{Da}}$, mass transfer becomes insufficient and the process is therefore limited by the mass transport. In other words, $\hat{k}^v$ tends to infinity while k^v_{eff} remains a constant, leading to $\frac{k^v_{eff}}{\hat{k}^v}$ tending towards zero.

For a fixed roughness density, $w_{cell} = 5h_r$ or $w_{cell} = 10h_r$, when $\mathrm{Pe} = 1$, an increase of Sc does not affect $\frac{k^v_{eff}}{\hat{k}^v}$ since the curves of $\mathrm{Sc} = 1$ and $\mathrm{Sc} = 1000$ are superposed, while when Sc remains unchanged, the increase of Pe delays the decrease of $\frac{k^v_{eff}}{\hat{k}^v}$. These results illustrate that only relatively large Pe have some impact on k^v_{eff}, consistent with the following discussion about Da^v_{eff} and with the results illustrated later by Fig. 3.13. For the geometry with $w_{cell} = 10h_r$, the decrease of $\frac{k^v_{eff}}{\hat{k}^v}$ is delayed since the fluid can flow through the roughness more easily thus enhance mass transfer. Therefore, it can be concluded that the roughness density, the flow properties in terms of Pe and the chemical features in terms of $\widehat{\mathrm{Da}}$ have an important influence on k^v_{eff}.

Since it is not convenient to use the ratio $\frac{k^v_{eff}}{\hat{k}^v}$ when $\widehat{\mathrm{Da}}$ is large because it tends to zero, an effective Damköhler number defined as $\mathrm{Da}^v_{eff} = \frac{k^v_{eff}w^0_x}{D_l}$ is

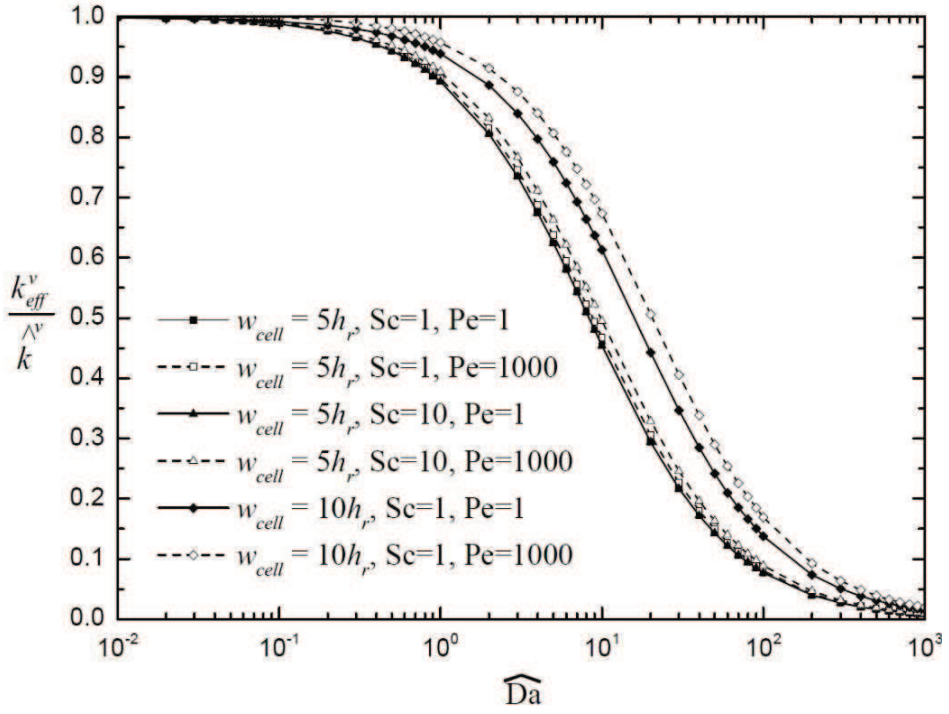

Figure 3.11: The ratio of effective reaction rate coefficient k^v_{eff} over the surface average reaction rate coefficient $\hat{k}^v$, as a function of the mean Damköhler number, with different surface geometries.

introduced to indicate the evolution of k^v_{eff} with $\widehat{\mathrm{Da}}$. Results are plotted in Fig. 3.12. Da^v_{eff} is proportional to $\widehat{\mathrm{Da}}$ before it reaches a plateau when mass transport becomes the limiting factor of the chemical process, consistent with the results of a similar analysis in [162]. Quantitatively, when Pe remains unchanged, Da^v_{eff} for $w_{cell} = 10h_r$ is twice as large as for $w_{cell} = 5h_r$ in the limit of large $\widehat{\mathrm{Da}}$. This is also explained by the fact that mass transport is limiting the process under large $\widehat{\mathrm{Da}}$ and increasing the proportion of the dissolving phase is equivalent to increasing mass transport. Moreover, flow and roughness density have only a small impact on Da^v_{eff} for small $\widehat{\mathrm{Da}}$ because in such circumstances it is the surface reaction rate coefficient but not mass transport that controls the process. Furthermore, Da^v_{eff} increases with roughness density under small $\widehat{\mathrm{Da}}$ and decreases with roughness density under large $\widehat{\mathrm{Da}}$, which is due to the transition of the limiting factor.

Finally, the importance of mass transport by advection is studied by plotting $\frac{k^v_{eff}}{k^v_{eff_{diffu}}}$ versus Pe for two $\widehat{\mathrm{Da}}$ values and for different Sc, as shown in Fig. 3.13. One sees from the figure that with the increase of Pe, the ratio $\frac{k^v_{eff}}{k^v_{eff_{diffu}}}$ tends to increase since the advection term becomes more important. The curves with the same Sc have similar trends but with different magni-

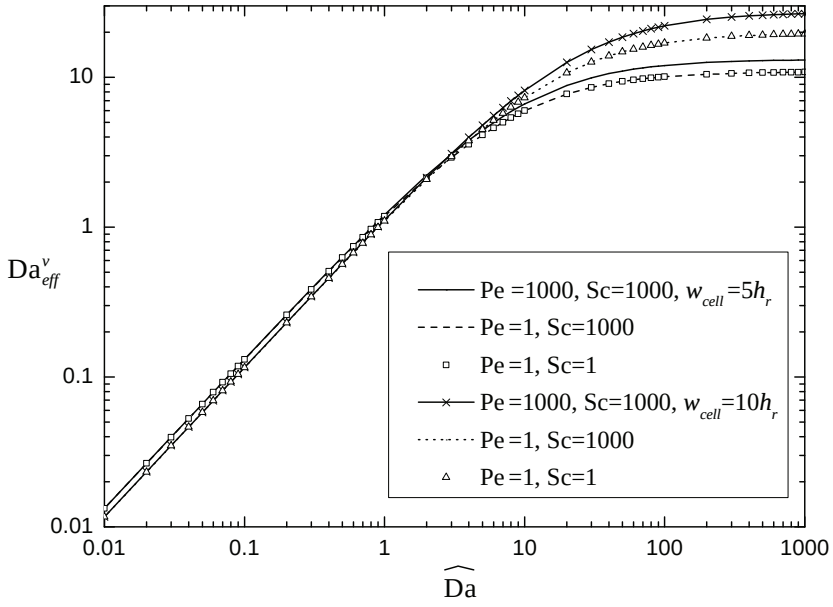

Figure 3.12: The functionality of the effective Damköhler number Da^v_{eff} with the mean Damköhler number $\widehat{Da}$.

tudes. In the case with higher $\widehat{Da}$, the role of advection is more important and the transitions from the diffusive regime to the advective regime take place at smaller Pe. For the curves with $Sc = 0.1$, the increases happen at relatively large Pe and can lead to larger $\frac{k^v_{eff}}{k^v_{eff_{diffu}}}$ than the curves with $Sc = 10$ in some circumstances, because the growth of $\frac{k^v_{eff}}{k^v_{eff_{diffu}}}$ with $Sc = 10$ slows down at about $3000 < Pe < 7000$. This trend is similar to the results obtained with the thermodynamic equilibrium boundary condition. Recirculations close to the rough surface have a similar impact, first limiting the mass transport towards the reactive surface and then enhancing it. To summarize, to estimate k^v_{eff} by $k^v_{eff_{diffu}}$ will produce an error less than 5% for the studied cases with $\widehat{Da} = 1$, because the reaction rate coefficient is the limiting factor of process and the flow properties have negligible impact. One has to be careful to represent k^v_{eff} by $k^v_{eff_{diffu}}$ at large $\widehat{Da}$ since the flow properties can have significant influence in such conditions.

3.5 Application of the effective surface model

As introduced in Sec. 3.3, there are different potential choices for the position of the effective surface, e.g., the fictive surface A_0, surface A^v_{eff} which recovers the no-slip boundary condition, surface A^c_{eff} which recovers the thermodynamic equilibrium condition, or any arbitrary location. In this section

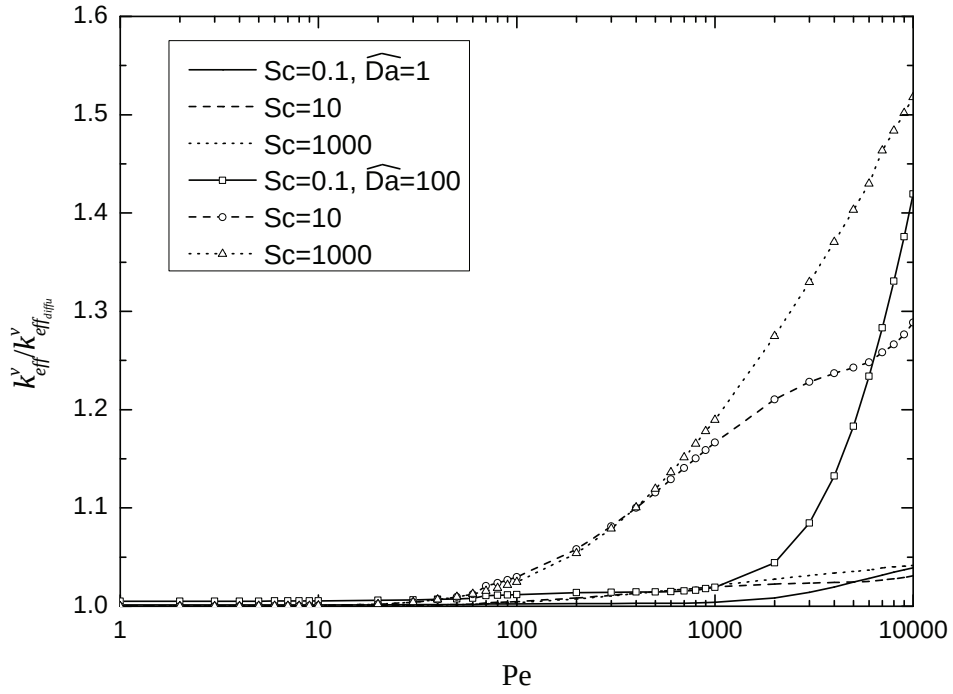

Figure 3.13: Ratio between k^v_{eff} with advection and its value in the purely diffusive case, as a function of the local Péclet number and for different Schmidt numbers. The roughness shape is a semi-ellipse with $b_r = 0.5h_r$ and $\frac{b_r}{w_{cell}} = 0.1$.

the objective is to identify the most appropriate effective surface by investigating the errors between direct numerical simulations (DNSs) over the original rough surface and simulations with the effective surface model. Two situations are considered, typical of the development of a mass boundary layer over a rough surface.

The first application corresponds to a boundary layer over a rough wall parallel to the flow. The original model for DNSs is illustrated by the upper drawing of Fig. 3.14a. The characteristic length of the system used to normalize the space variables is H_Ω, i.e., L, the height of the global domain. The system is $W = 3H_\Omega$ wide. A short flat zone is set with a length of $0.5H_\Omega$ before the rough surface in order to have an already developed boundary layer, which is closer to the periodic boundary condition hypothesis stated previously. In addition, the roughness height is chosen to be small enough to have $\epsilon = \frac{l_{cell}}{L} = 0.1$ and $l_{cell} = 8h_r$. The roughness has a shape of semi-ellipse with $b_r = 0.5h_r$. In terms of geometry for the effective models, the flat surface at the entrance remains unchanged and the original rough surface is replaced by a smooth effective one. The lower drawing in Fig. 3.14a gives an example of the effective model with no-slip condition at the effective surface. The original flat surface and the effective surface are connected by a small step. It is clear

that some assumptions of the homogenization are not valid in this particular area, which is a singularity (no-periodicity, etc...). Specific developments could be done to overcome this problem, but in the present work the general results are simply used to see if it is acceptable.

In the second application, the boundary layer develops on a rough cylinder perpendicular to the flow. As illustrated in Fig. 3.14b, the rough surface in the DNSs is replaced by the smooth circular surface in the effective model. Since the considered geometry is symmetric with respect to x-axis, only the transport in the upper half domain is simulated. The characteristic length of the system used to normalize the space variables is L, the cylinder diameter. The height of the half domain is $H_\Omega = 1.5L$ and the width is $W = 2.5L$.

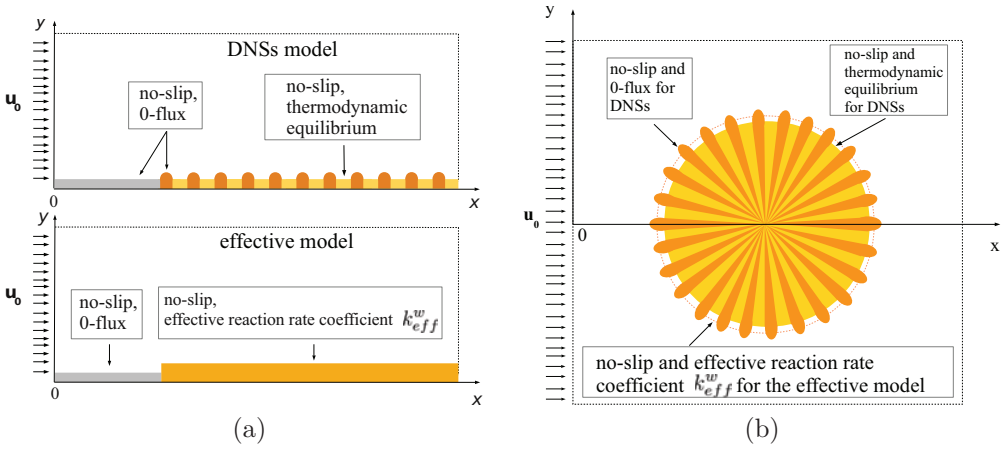

Figure 3.14: Schematic representation of the computational domain: DNSs over the heterogeneous surface and the first order effective models (application 1 in (a) and application 2 in (b)).

DNSs are performed using dimensionless forms of Pb I equations with B.C. I. For the effective model, the closure problems Pb III$_{(\mathbf{B},s)}$ and Pb III$_a$ i are solved first to obtain the effective surface position and the effective boundary conditions. Then the effective macro-scale problem Pb II is solved using these obtained effective boundary conditions. Similar numerical settings were used as in the last section.

The convergence behavior for the relative error (reference based on the calculation with the maximum number of DOF) of the normal total flux integrated over the reactive surface as a function of the number of degrees of freedom (DOF) is presented in Fig. 3.15, for both the rough surface and the effective surface with no-slip boundary condition in application 1. The mesh quality was considered good when a negligible increase of the flux was observed

with the increase of DOF. The DNS relative error is higher for an equal number of DOF. This also demonstrates the computational efficiency of the effective model. For a relative error of 1% there is a factor 2 between the number of DOF, as for lower relative error level the factor increases with the number of DOF. Similar analyses were done for application 2.

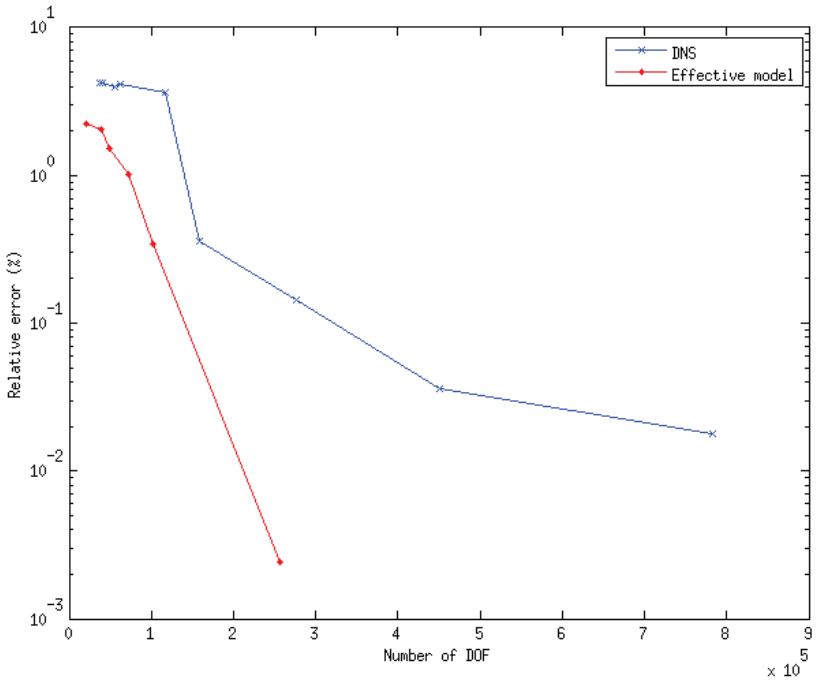

Figure 3.15: An example of convergence analysis for the effective model

3.5.1 Application 1: boundary layer over a rough wall parallel to the flow

The way to quantify the differences between the two simulations is to calculate the error on the integration of the total mass flux over the solid-liquid surface, called Q_{DNS} for the rough surface and Q_{eff} for the effective one. Simulations are done for flows with $\mathrm{Re}_L = 1$ and $\mathrm{Re}_L = 50$, with two roughness densities: $\frac{b_r}{w_{cell}} = 0.5$ and $\frac{b_r}{w_{cell}} = 0.1$. The relative errors on the total mass flux are plotted in Fig. 3.16 for different effective surface positions. For effective surface at a position lower than $2.5h_r$, the relative error committed by the model is smaller than 1%. At higher effective surface positions and for the different Reynolds numbers, the error increases when increasing the position of the effective surface. One can also observe that the roughness density has little impact on the error compared to the influence of Re_L. Increasing the dis-

tance between roughnesses by a factor of five only increases the error by less than 1%, while increasing Re_L from 1 to 50 nearly doubles the error. For the different flow conditions or geometry, a minimum value of the relative error is obtained around $y_{eff} = h_r$. It is closest to A^v_{eff} among the particular effective surface positions discussed before.

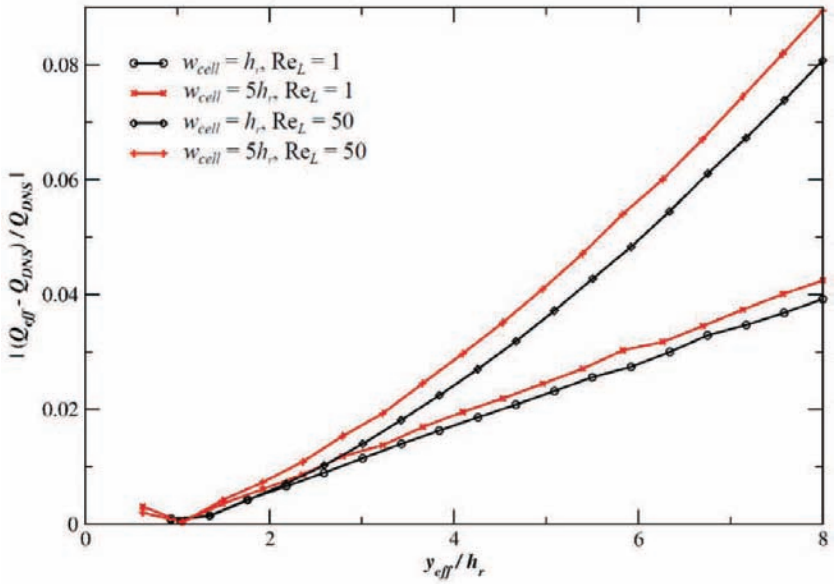

Figure 3.16: Relative error on Q_{eff} compared to Q_{DNS}, for different positions of the effective surface, with different surface geometries, $\mathrm{Sc} = 1$ and two values of Re_L.

To demonstrate the representativeness of the effective model with the effective surface located at A^v_{eff}, the results of DNSs and the first order effective model are compared in terms of velocity, concentration fields and the distribution of mass flux over the reactive surface as illustrated in Figs. 3.17 and 3.18, respectively. Results with the effective surface at A_0 are also shown in these figures to illustrate the discrepancies created by the large step between the flat zone and the effective surface.

In the upper graph of Fig. 3.17, one can observe that the velocity contours obtained by DNSs (solid line) and those obtained with the first order effective model with an effective surface at $\frac{w^v_x}{L}$, i.e., at A^v_{eff}, are overlapped, with negligible errors. This is consistent with previous findings in the literature for the momentum transport problem. Results with the effective surface at A_0 (dot line), give the good trend but are not precisely representing the DNSs velocity field. As for concentration contours, one sees in the lower graph of Fig. 3.17 that those obtained with the effective surface at $\frac{w^v_x}{L}$ are also well superposed

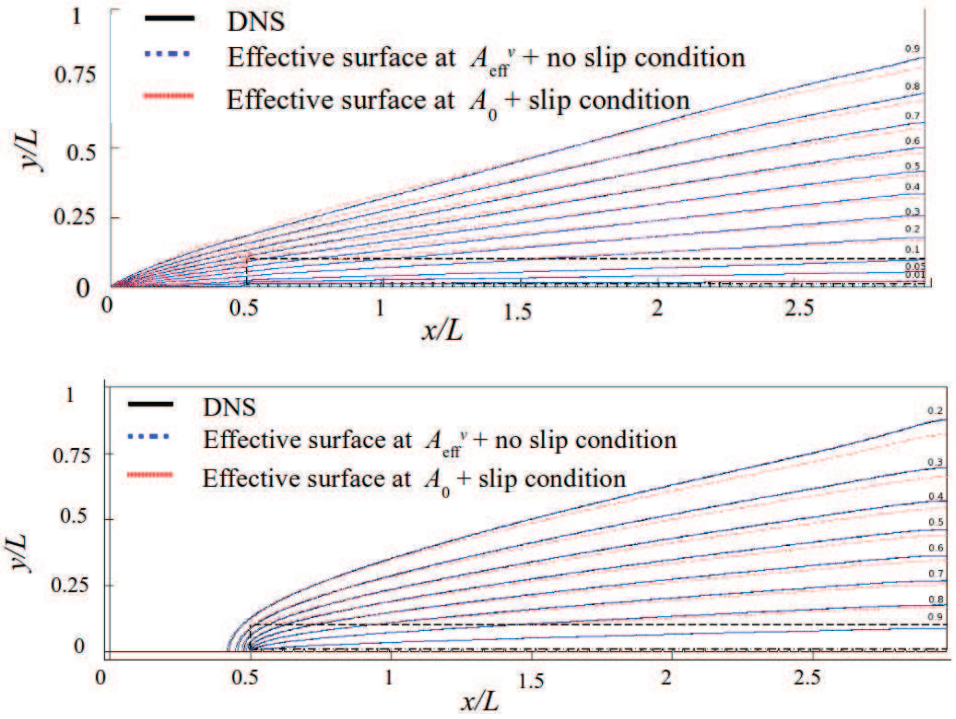

Figure 3.17: Dimensionless velocity field (upper graph) and concentration (lower graph) contours for the initial rough domain and two effective smooth domains, with an entrance dimensionless flow velocity of 1, $\mathrm{Re}_L = 25$ and $\mathrm{Sc} = 1$.

with the DNSs results, except inside the small entrance region where the conditions for upscaling break down as discussed previously. Quantitatively, this creates a small and rather acceptable discrepancy of 0.07% on the total mass flux. The iso-concentration contours obtained with the effective surface at A_0 show some discrepancies that increase with $\frac{x}{L}$, leading to a relative error on the total mass flux of around 6.2%.

In Fig. 3.18, the distribution of the normal mass flux, q, along the reactive surfaces in the effective model with A_{eff}^{v} and A_0 and that along the rough surface in the original model are compared. For the DNSs, values are discrete because q needs to be averaged for each w_{cell}. The results of the DNSs and the effective model with A_{eff}^{v} show a good agreement. For the model with the effective surface at A_0, q distribution differs from the DNSs in the entrance region after the step. This is mainly the consequence of the discrepancies observed in the velocity field.

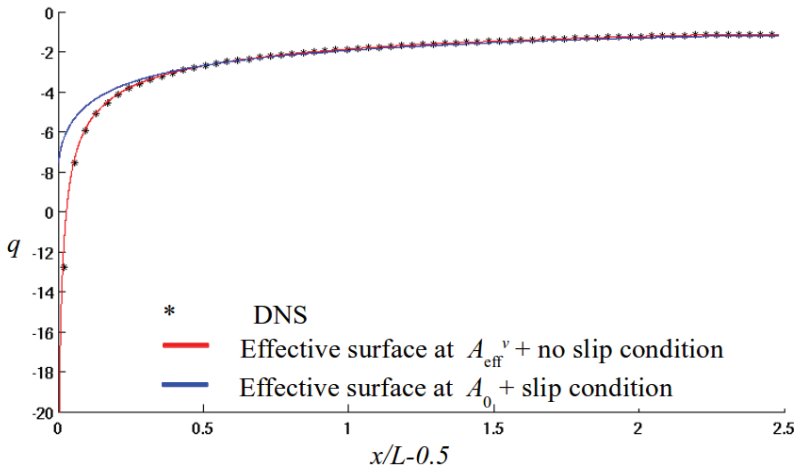

Figure 3.18: Normal flux along the reactive surfaces for the initial rough domain and two effective smooth domains, with an entrance dimensionless flow velocity of 1, $\mathrm{Re}_L = 25$ and $\mathrm{Sc} = 1$.

3.5.2 Application 2: rough cylinder in a laminar flow

This second case illustrates the accuracy of the effective model for a more complex configuration than the previous application. Simulations are done for a flow with $\mathrm{Re}_L = 0.1$ and $\mathrm{Sc} = 1000$, with 50 roughnesses distributed uniformly over the cylinder surface and $\epsilon = 0.1$. In the two graphs of Fig. 3.19, one can observe that both velocity contours (left) and concentration contours (right) obtained by DNSs (black solid line) and with an effective surface at A^v_{eff} (blue dashed line) are overlapped, with negligible errors. The error on Q is less than 0.1%, proving again the validity of the first order effective surface model. This error remains smaller than 0.1% even by increasing ϵ to 0.5 (the scale separation assumption is no more valid). However for $\mathrm{Re}_L = 1$, Sc= 1000 and $\epsilon = 0.5$, the model starts to show some limitations and gives results with an error around 3%.

3.5.3 Effective parameters estimates

In these last paragraphs, potential estimates of the effective properties are discussed in order to reduce computational costs, taking application 1 as an example. As mentioned previously in Sec. 3.4, for a high roughness density the effective surface position is close to the roughness height. One first possible approximation is to set the effective surface position at the roughness height, using a no-slip boundary condition and then use the effective reaction rate obtained for an effective surface at h_r, which will be called A^r_{eff}. Relative

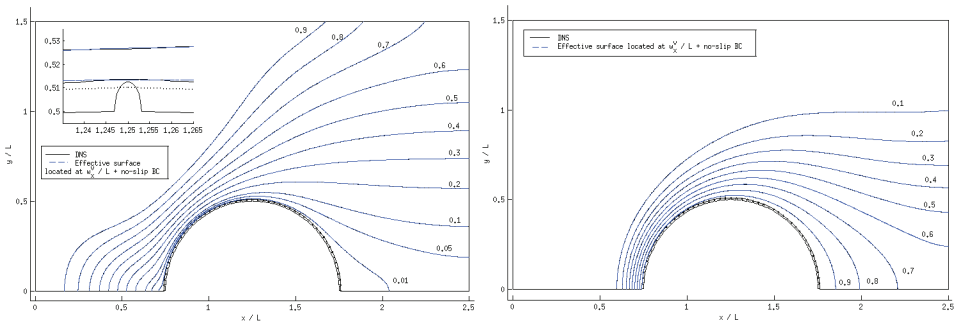

Figure 3.19: Dimensionless velocity field (left) and concentration (right) contours for the initial rough domain and the effective smooth domain, with an entrance dimensionless flow velocity of 1, $\mathrm{Re}_L = 0.1$ and $\mathrm{Sc} = 1000$.

errors committed on the total mass flux using this approximation are compared to the one with the correct effective model with A^v_{eff}. Results are assembled in Table 3.1 for $\mathrm{Re}_L = 25$ and $\mathrm{Sc} = 1$, and for rounded square roughnesses with $b_r = h_r$. The approximated model gives results with relative errors less than 1% even for roughness densities as low as 0.2, i.e., $\frac{b_r}{w_{cell}} = 0.2$ with $\delta_v = 0.73$. This first approximation gives good results for certain rough surface geometries and will save computational time as the closure problem for the flow does not need to be solved anymore.

$\frac{b_r}{w_{cell}}$	δ_v	A^v_{eff} (in %)	A^r_{eff} (in %)
0.8	0.977	0.262	0.179
0.67	0.964	0.234	0.117
0.2	0.729	0.372	0.674
0.1	0.458	0.581	1.63
0.067	0.318	0.675	2.03

Table 3.1: Relative errors committed on the total mass flux over the reactive surface between the effective model simulations and the DNSs, for different roughness densities with $b_r = h_r$ and rounded square roughnesses, an entrance dimensionless flow velocity of 1, $\mathrm{Re}_L = 25$ and $\mathrm{Sc} = 1$.

In addition to this first estimate, an approximation can be made on the effective reaction rate as well. In the range of Re_L used for the global simulations (1 to 1000), the corresponding micro-scale Péclet number will not exceed 100 for Schmidt numbers below 10. From the parametric study of Sec. 3.4, it has been observed that the effective reaction rate obtained for pure diffusion can be a good approximation of the effective reaction rate with flow. As a result, Pb III_a with B.C. I can be simplified into a purely diffusive one in these application ranges. For example, the largest difference between errors on Q,

committed with and without accounting for the flow in k^v_{eff} is 0.002 (obtained with $\frac{b_r}{w_{cell}} = 0.1$, $\mathrm{Re}_L = 500$ and $\mathrm{Sc} = 5$ which has a ratio $\frac{k^v_{eff}}{k^v_{eff_{diffu}}} \approx 1.02$).

To sum up, all these numerical results demonstrate the efficiency of using an effective surface model, characterized by a homogeneous and smooth surface, to reproduce the flow and reactive mass transport over a heterogeneous rough surfaces, with a good accuracy. The use of estimates without solving Pb $\mathrm{III}_{(\mathbf{B},s)}$ can help to gain computational time, but may need to be tested on larger domains.

3.6 Conclusion

The concept of effective surface has already proven its usefulness for several transport mechanisms. The main contribution of this study concerns mass (and momentum) transfer for a laminar flow over a heterogeneous rough surface characterized by *mixed* boundary conditions. A very important constraint necessary to develop the effective surface concept is the separation of scales between the global boundary layer thickness and the zone of influence of the surface heterogeneities within that boundary layer. Additional assumptions were made, like micro-scale pattern periodicity, which could probably be replaced by less restrictive constraints. Based on these assumptions, the methodology of multi-domain decomposition was used to decompose the domain under investigation into a macro-scale subdomain and a range of micro-scale unit cells.

To determine what boundary conditions should be prescribed and where the effective surface should be placed, first order estimates of the micro-scale variables were made by means of Taylor expansion, and the resolution was obtained by solving corresponding closure problems. After this homogenization procedure, alternative effective surface positions were found. General expressions for the effective boundary conditions were obtained, and, for some effective surfaces of interest, the related effective boundary conditions were derived from the generic form. Among the different choices, the effective surface with a no-slip boundary condition or any other position close to this surface have the advantage that it induces the smallest errors. For a rough surface with part under equilibrium and part with no flux, the effective boundary condition turns out to be of a *reactive type*, with an effective reaction rate coefficient depending on the geometry and flow properties. Interestingly, this establishes a fundamental relationship with the case of a reactive surface with non-uniform reaction rates ([43] and this study).

The influences of some parameters, including roughness geometry, flow properties and surface chemical characteristics, were studied. These analyses showed that the geometry of the asperities, in terms of density and shape, has a significant impact on the effective surface position. A higher roughness density leads to an effective surface farther from the lower part of the rough surface, and vice versa. Flow properties have a stronger impact for the case with smaller roughness density.

The study of the impact of flow properties showed that in some circumstances, the advective-diffusive flow regime can be simplified into a purely diffusive one. In addition, since the chemical characteristics are the limiting factors at small $\widehat{\mathrm{Da}}$, it is acceptable to approximate the effective reaction rate coefficient by the surface average. At large $\widehat{\mathrm{Da}}$, the chemical process is controlled by the mass transport, and the effective reaction rate coefficient should be calculated by the closure problems developed for the specific conditions. Due to the strong impact of flow properties at large $\widehat{\mathrm{Da}}$, the mass transport by advection should be taken into account.

At last, simulations were conducted for both the original model and the effective ones in application 1. The results comparison in terms of total flux showed that the one with the no-slip condition (A^v_{eff}) is more accurate than the fictive surface with slip condition (A_0). Contours of velocity and concentration, and total flux at a specific cross-section obtained by the original model and by the effective model with the effective surface at A^v_{eff} agreed very well. Velocity and concentration comparisons for a more complex geometry also showed good agreements. These two applications demonstrate the representativeness of the effective surface models to the original ones.

As indicated in the introduction, one of the motivation for this study was to model phenomena taking place at "dissolving" interfaces (drying, karstic and other underground cavities, etc.). Therefore, the surface geometry is not given a priori but is a result of the process. How the surface geometry changes with time under different conditions? What is the recession rate? And how these effects can be handled by a macro-scale theory (here the concept of effective surface) are open problems which are of major interest. Additional coupling may arise, in particular, hydrodynamic and dissolution instabilities may produce different surface patterns (as illustrated in [120]) and this also is an issue that needs to be considered in the future.

Chapter 4

Dispersion in porous media with heterogeneous nonlinear reactions

4.1 Introduction

In addition to the case which involves the treatment of rough solid-liquid dissolution surfaces, such as the problems studied in Chap. 3, another situation corresponds to the dissolution of a porous medium. To describe the dissolution of the soluble medium contained in a porous medium such as illustrated in Fig. 2.1, it is often not practical, even if this is the more secure way of handling the geometry evolution [66], to take into account all the pore-scale details by direct numerical modeling in a L-scale problem. Consequently, attempts have been made to filter the pore-scale information through the use of upscaling techniques.

The case of thermodynamic equilibrium at the interface leads, when local-equilibrium is considered, to a simple model stating that the macro-scale concentration is equal to the pore-scale surface equilibrium concentration. Non-equilibrium models have been obtained through the volume averaging method, neglecting contributions of the interface velocity in the closure problems and at several points in the averaging process, leading to the introduction of a linear exchange term in the macro-scale equation [10, 109, 110, 163]. These results have been extended to the case of mass exchange controlled by partitioning expressions (Raoult's law, Henry's law, etc.) in [164] and [165], with the additional terms associated to the interface recession velocity being taken into account in this latter paper. Non-traditional convective terms appear in the

macro-scale equations, which are often discarded in practical implementations of the macro-scale models. However, it was shown in [166] that they must be taken into account, at least for simple unit cells like tubes.

The case of heterogeneous reaction with a linear reaction has been investigated by a large amount of studies using the previously mentioned various upscaling techniques [41, 58, 108, 167–170]. The major feature of the resulting macro-scale models is the notion of effective reaction rate, which depends highly on the pore-scale Damköhler number, as well as the pore-scale medium geometry. In particular, the form and value of the reaction rate is in theory affected by the coupling between reaction and transport. In addition, contrary to most engineering practice, these upscaling studies show also that the resulting dispersion tensor is affected by the heterogeneous reaction, i.e., dispersion curves depend on the Damköhler number.

To our knowledge, few works have been published concerning macro-scale models developed from pore-scale problem with nonlinear reactions. Wood et al. [171] reported on the development of an effective macro-scale reaction rate using the method of volume averaging for a Michaelis–Menton reaction in the biotransformation problems and discussed the dependence of the effective macro-scale reaction rate on the closure variable, the Damköhler and the Péclet numbers respectively. Heße et al. [172] studied the upscaling of a Monod reaction at the interface of polluted water and biofilm through a *simple averaging scheme* based on DNS. Interestingly, the results show that the macro-scale reaction rate does not follow the Monod type in the transition zone between the reaction-limited regime and the diffusion-limited regime. This is also consistent with the findings of [173] about reactive transport in porous media with biofilms. This adds to the motivation of developing a more comprehensive averaging scheme. The nonlinear heterogeneous reactions at the dissolving interface are often expressed under the form of Eq. 1.4 and the dissolution kinetics were obtained by Jeschke et al. [49] for gypsum dissolution as mentioned in Chap. 1. Given this research survey, the objective of this study is to develop a general form of the macro-scale model, starting from pore-scale problems with thermodynamic equilibrium or *nonlinear* reactive boundary conditions, taking into account as much as possible the role of the interface velocity in the upscaling process.

This chapter is organized as follows. In Sec. 4.2 the method of volume averaging is used to develop a non-equilibrium macro-scale model, as well as the corresponding closure problems from which the effective parameters are

obtained, starting from the pore-scale model developed in Chap. 2. Some limiting cases in terms of Da are also discussed in order to connect our results to the literature. In Sec. 4.3 closure problems are resolved for the stratified and the 3D representative unit cells with nonlinear reaction rates, and the properties of the generated effective parameters are studied. In the last section an example of the use of this macro-scale model is presented in order to investigate the importance of the non-traditional effective parameters.

The main new features taken into account in this study are: (i) a more general form of the reaction rate, (ii) the introduction of the soluble material[1], (iii) a full coupling of the two closure variables in the closure problems, (iv) an investigation on the potential implications of non-traditional terms. The development are presented in a simplified manner with the emphasis on the original and specific points of our study. The reader are referred to the cited literature for more thorough developments on the classical aspects of the upscaling method.

4.2 Upscaling

As mentioned in the introduction, several upscaling methods can be adopted [174], for instance, volume averaging [102], ensemble averaging [175, 176], moments matching [106, 169] and multi-scale asymptotic [177]. In this present study, the developments of a macro-scale model are followed based on the method of volume averaging. The general framework has been developed over several decades and a comprehensive presentation can be found in [102]. Our present work extends the contribution of [58, 109, 165]. Therefore, the focus of this study is on the original contribution, while presenting the classical steps at a minimum necessary for reader's comprehension.

4.2.1 Averages and averaged equations

Averages are defined in the traditional[2] manner as

$$\langle \mathbf{v}_l \rangle = \frac{1}{V} \int_{V_l} \mathbf{v}_l dV = \varepsilon_l \langle \mathbf{v}_l \rangle^l , \tag{4.1}$$

[1] A non dissolving material was also introduced in [109, 164]

[2] For a more comprehensive use of spatial averaging, especially for simple periodic unit cells, see [178–182]

$$\varepsilon_l = \frac{1}{V}\int_{V_l} dV, \tag{4.2}$$

and

$$\langle \omega_l \rangle = \frac{1}{V_l}\int_{V_l} \omega_l dV, \tag{4.3}$$

where $\langle \mathbf{v}_l \rangle$ and $\langle \mathbf{v}_l \rangle^l$ denote the superficial and intrinsic average of the pore-scale liquid velocity, respectively, V denotes the volume of the representative unit cell, ε_l denotes the porosity and $\langle \omega_l \rangle^l$ denotes the intrinsic average of the mass fraction of Ca in the liquid phase. The following deviation fields are introduced

$$\omega_l = \langle \omega_l \rangle^l + \tilde{\omega}_l \tag{4.4}$$

$$\mathbf{v}_l = \langle \mathbf{v}_l \rangle^l + \tilde{\mathbf{v}}_l, \tag{4.5}$$

with $\tilde{\omega}_l$ and $\tilde{\mathbf{v}}_l$ denoting the deviation of mass fraction and liquid velocity, respectively.

The average of Eq. 2.19 gives simply

$$\frac{\partial \varepsilon_l \rho_l}{\partial t} + \nabla \cdot (\rho_l \langle \mathbf{v}_l \rangle) = -K_g, \tag{4.6}$$

with the mass exchange term corresponding to

$$K_g = \frac{1}{V}\int_{A_{ls}} \mathbf{n}_{ls} \cdot \rho_l (\mathbf{v}_l - \mathbf{w}_{sl})\, dA. \tag{4.7}$$

The average of the solid mass balance equation gives

$$\frac{\partial \varepsilon_s \rho_s}{\partial t} = K_g, \tag{4.8}$$

where Eq. 2.22 has been used to obtain

$$\begin{aligned} K_g &= \frac{1}{V}\int_{A_{ls}} \mathbf{n}_{ls} \cdot (-\rho_s \mathbf{w}_{sl})\, dA = \frac{1}{V}\int_{A_{ls}} \mathbf{n}_{ls} \cdot \rho_l (\mathbf{v}_l - \mathbf{w}_{sl})\, dA \\ &= -a_{vl} M_g k_s \left\langle \left(1 - \frac{\omega_l}{\omega_{eq}}\right)^n \right\rangle_{ls}, \end{aligned} \tag{4.9}$$

with the definition of the surface average and specific area as

$$\langle \star \rangle_{ls} = \frac{1}{A_{ls}} \int_{A_{ls}} \star dA, \tag{4.10}$$

and

$$a_{vl} = \frac{1}{V} \int_{A_{ls}} dA, \tag{4.11}$$

respectively.

Finally, the mass balance equation for the Ca component yields

$$\begin{aligned} &\frac{\partial \varepsilon_l \rho_l \langle \omega_l \rangle^l}{\partial t} + \nabla \cdot \left(\varepsilon_l \rho_l \langle \omega_l \rangle^l \langle \mathbf{v}_l \rangle^l \right) + \underbrace{\nabla \cdot \left(\rho_l \langle \tilde{\omega}_l \tilde{\mathbf{v}}_l \rangle \right)}_{\text{dispersion}} = \\ &\nabla \cdot \left(\varepsilon_l \rho_l D_l \nabla \langle \omega_l \rangle^l + \underbrace{\frac{1}{V} \int_{A_{ls}} \mathbf{n}_{ls} \rho_l D_l \tilde{\omega}_l dA + \frac{1}{V} \int_{A_{li}} \mathbf{n}_{li} \rho_l D_l \tilde{\omega}_l dA}_{\text{tortuosity}} \right) - K_{Ca}. \end{aligned} \tag{4.12}$$

The total mass exchange term is related to K_{Ca} by

$$K_{Ca} = \frac{M_{Ca}}{M_g} K_g = -a_{vl} M_{Ca} k_s \left\langle \left(1 - \frac{\omega_l}{\omega_{eq}} \right)^n \right\rangle_{ls}. \tag{4.13}$$

Using Eq. 4.6, Eq. 4.12 can be written as

$$\begin{aligned} &\varepsilon_l \rho_l \frac{\partial \langle \omega_l \rangle^l}{\partial t} + \varepsilon_l \rho_l \langle \mathbf{v}_l \rangle^l \cdot \nabla \langle \omega_l \rangle^l + \underbrace{\nabla \cdot \left(\rho_l \langle \tilde{\omega}_l \tilde{\mathbf{v}}_l \rangle \right)}_{\text{dispersion}} = \\ &\nabla \cdot \left(\varepsilon_l \rho_l D_l \nabla \langle \omega_l \rangle^l + \underbrace{\frac{1}{V} \int_{A_{ls}} \mathbf{n}_{ls} \rho_l D_l \tilde{\omega}_l dA + \frac{1}{V} \int_{A_{li}} \mathbf{n}_{li} \rho_l D_l \tilde{\omega}_l dA}_{\text{tortuosity}} \right) \\ &- K_{Ca} + K_g \langle \omega_l \rangle^l. \end{aligned} \tag{4.14}$$

4.2.2 Deviation equations and closure

At this point, an estimate for the concentration deviations has to be found. The governing equations are obtained by substituting Eq. 4.4 into the pore-scale mass balance equations, then subtracting the averaged equation (Eq. 4.14) divided by ε_l (neglecting spatial variations of the volume fraction and liquid density over the representative elementary volume). Using the following intermediate results, which make use of classical algebra and approximations about averages involving averages that are discussed at length in the averaging literature, in particular [178–182] and [102]

$$\nabla \cdot (\rho_l \omega_l \mathbf{v}_l) = \rho_l \omega_l \nabla \cdot \mathbf{v}_l + \rho_l \mathbf{v}_l \cdot \nabla \omega_l = \rho_l \mathbf{v}_l \cdot \nabla \langle \omega_l \rangle^l + \rho_l \mathbf{v}_l \cdot \nabla \tilde{\omega}_l, \tag{4.15}$$

$$\begin{aligned} -\varepsilon_l^{-1} \nabla \cdot \left(\varepsilon_l \rho_l D_l \nabla \langle \omega_l \rangle^l + \frac{1}{V} \int_{A_{ls}} \mathbf{n}_{ls} \rho_l D_l \tilde{\omega}_l dA + \frac{1}{V} \int_{A_{li}} \mathbf{n}_{li} \rho_l D_l \tilde{\omega}_l dA \right) \approx \\ -\nabla \cdot \left(\rho_l D_l \nabla \langle \omega_l \rangle^l + \frac{\varepsilon_l^{-1}}{V} \int_{A_{ls}} \mathbf{n}_{ls} \rho_l D_l \tilde{\omega}_l dA + \frac{\varepsilon_l^{-1}}{V} \int_{A_{li}} \mathbf{n}_{li} \rho_l D_l \tilde{\omega}_l dA \right), \end{aligned} \tag{4.16}$$

$$\begin{aligned} \varepsilon_l^{-1} K_{Ca} - \varepsilon_l^{-1} K_g \langle \omega_l \rangle^l = \varepsilon_l^{-1} \frac{1}{V} \int_{A_{ls}} \mathbf{n}_{ls} \cdot (\rho_l \omega_l (\mathbf{v}_l - \mathbf{w}_{sl}) - \rho_l D_l \nabla \omega_l) \, dA \\ -\varepsilon_l^{-1} \langle \omega_l \rangle^l \frac{1}{V} \int_{A_{ls}} \mathbf{n}_{ls} \cdot \rho_l (\mathbf{v}_l - \mathbf{w}_{sl}) \, dA = -\rho_l D_l \varepsilon_l^{-1} \frac{1}{V} \int_{A_{ls}} \mathbf{n}_{ls} dA \cdot \nabla \langle \omega_l \rangle^l \\ + \varepsilon_l^{-1} \frac{1}{V} \int_{A_{ls}} \mathbf{n}_{ls} \cdot (\rho_l \tilde{\omega}_l (\mathbf{v}_l - \mathbf{w}_{sl}) - \rho_l D_l \nabla \tilde{\omega}_l) \, dA \end{aligned} \tag{4.17}$$

$$\nabla \cdot \left(\frac{\varepsilon_l^{-1}}{V} \int_{A_{ls}} \mathbf{n}_{ls} \rho_l D_l \tilde{\omega}_l dA + \frac{\varepsilon_l^{-1}}{V} \int_{A_{li}} \mathbf{n}_{li} \rho_l D_l \tilde{\omega}_l dA \right) \ll \nabla \cdot (\rho_l D_l \nabla \tilde{\omega}_l), \tag{4.18}$$

one obtains

$$\rho_l \frac{\partial \tilde{\omega}_l}{\partial t} + \rho_l \mathbf{v}_l \cdot \nabla \tilde{\omega}_l + \rho_l \tilde{\mathbf{v}}_l \cdot \nabla \langle \omega_l \rangle^l - \varepsilon_l^{-1} \nabla \cdot (\rho_l \langle \tilde{\omega}_l \tilde{\mathbf{v}}_l \rangle) = \nabla \cdot (\rho_l D_l \nabla \tilde{\omega}_l)$$
$$+ \frac{\varepsilon_l^{-1}}{V} \int_{A_{ls}} \mathbf{n}_{ls} \cdot \rho_l \tilde{\omega}_l (\mathbf{v}_l - \mathbf{w}_{sl}) \, dA - \frac{\varepsilon_l^{-1}}{V} \int_{A_{ls}} \mathbf{n}_{ls} \cdot \rho_l D_l \nabla \tilde{\omega}_l dA$$
$$- \rho_l D_l \varepsilon_l^{-1} \frac{1}{V} \int_{A_{ls}} \mathbf{n}_{ls} dA \cdot \nabla \langle \omega_l \rangle^l . \qquad (4.19)$$

In addition, the assumption (see cited literature) that

$$\Omega_{ls} = \langle \omega_l \rangle_{ls} = \frac{1}{A_{ls}} \int_{A_{ls}} \omega_l dA \approx \langle \omega_l \rangle^l , \qquad (4.20)$$

is used, so any integral of the form $\frac{1}{V} \int_{A_{ls}} \omega_l dA$ will be approximated by

$$\frac{1}{V} \int_{A_{ls}} \omega_l dA \approx a_{vl} \langle \omega_l \rangle^l . \qquad (4.21)$$

Using Eq. 2.21, the boundary condition for the deviation may be written

$$\mathbf{n}_{ls} \cdot \left(\rho_l \langle \omega_l \rangle^l (\mathbf{v}_l - \mathbf{w}_{sl}) \right) + \mathbf{n}_{ls} \cdot (\rho_l \tilde{\omega}_l (\mathbf{v}_l - \mathbf{w}_{sl})) + \mathbf{n}_{ls} \cdot (-\rho_l D_l \nabla \tilde{\omega}_l)$$
$$+ \mathbf{n}_{ls} \cdot \left(-\rho_l D_l \nabla \langle \omega_l \rangle^l \right) = -M_{Ca} k_s \left(1 - \frac{\langle \omega_l \rangle^l + \tilde{\omega}_l}{\omega_{eq}} \right)^n \quad \text{at } A_{ls}. \qquad (4.22)$$

The crucial assumption now, which will be tested quantitatively against DNS in Sec. 4.4, is the approximation of the nonlinear reaction rate by a first-order Taylor expansion, i.e.,

$$\mathbf{n}_{ls} \cdot \left(\rho_l \langle \omega_l \rangle^l (\mathbf{v}_l - \mathbf{w}_{sl}) \right) + \mathbf{n}_{ls} \cdot (\rho_l \tilde{\omega}_l (\mathbf{v}_l - \mathbf{w}_{sl})) + \mathbf{n}_{ls} \cdot (-\rho_l D_l \nabla \tilde{\omega}_l)$$
$$+ \mathbf{n}_{ls} \cdot \left(-\rho_l D_l \nabla \langle \omega_l \rangle^l \right) = -M_{Ca} k_s \left(1 - \frac{\langle \omega_l \rangle^l}{\omega_{eq}} \right)^n + \frac{n M_{Ca} k_s}{\omega_{eq}} \left(1 - \frac{\langle \omega_l \rangle^l}{\omega_{eq}} \right)^{n-1} \tilde{\omega}_l$$
$$\text{at } A_{ls}, \qquad (4.23)$$

or

$$\mathbf{n}_{ls}\cdot\left(\rho_l\left\langle\omega_l\right\rangle^l\left(\mathbf{v}_l-\mathbf{w}_{sl}\right)\right)+\mathbf{n}_{ls}\cdot\left(\rho_l\tilde{\omega}_l\left(\mathbf{v}_l-\mathbf{w}_{sl}\right)\right)+\mathbf{n}_{ls}\cdot\left(-\rho_l D_l\nabla\tilde{\omega}_l\right)$$
$$+\mathbf{n}_{ls}\cdot\left(-\rho_l D_l\nabla\left\langle\omega_l\right\rangle^l\right)=-\frac{M_{Ca}k_s}{\omega_{eq}}\left(1-\frac{\left\langle\omega_l\right\rangle^l}{\omega_{eq}}\right)^{n-1}\left(\omega_{eq}-\left\langle\omega_l\right\rangle^l-n\tilde{\omega}_l\right)$$
$$\text{at } A_{ls}. \tag{4.24}$$

Similarly, Eq. 2.24 gives

$$\mathbf{n}_{li}\cdot\left(-\rho_l D_l\nabla\tilde{\omega}_l\right)+\mathbf{n}_{li}\cdot\left(-\rho_l D_l\nabla\left\langle\omega_l\right\rangle^l\right)=0\qquad\text{at } A_{li}. \tag{4.25}$$

Following the developments described in the literature [58,109,165], $\left(\left\langle\omega_l\right\rangle^l-\omega_{eq}\right)$ and $\nabla\left\langle\omega_l\right\rangle^l$ may be viewed as source terms in the above coupled macro-scale and micro-scale governing equations since they may act as generators of the deviation terms. Given the mathematical structure of these coupled equations, an approximate solution can be built based on an expansion involving the source terms and their higher derivatives under the following form

$$\tilde{\omega}_l=s_l\left(\left\langle\omega_l\right\rangle^l-\omega_{eq}\right)+\mathbf{b}_l\cdot\nabla\left\langle\omega_l\right\rangle^l+..., \tag{4.26}$$

which gives for the first-order derivatives

$$\nabla\tilde{\omega}_l=\nabla s_l\left(\left\langle\omega_l\right\rangle^l-\omega_{eq}\right)+\left(\nabla\mathbf{b}_l+s_l\mathbf{I}\right)\cdot\nabla\left\langle\omega_l\right\rangle^l+... \tag{4.27}$$

According to the length scale constraints $l_s,l_i,l_l\ll r_0\ll L$, terms involving higher order derivatives than $\nabla\left\langle\omega_l\right\rangle^l$ in Eq. 4.27 can be neglected. Substituting Eqs. 4.26 and 4.27 into Eq. 4.19, collecting terms for $\left(\left\langle\omega_l\right\rangle^l-\omega_{eq}\right)$ and $\nabla\left\langle\omega_l\right\rangle^l$ and then applying the fundamental lemma stated in [109], the following two "closure problems" were obtained, which depend on the macro-scale concentration $\left\langle\omega_l\right\rangle^l$ as a parameter. This latter result is entirely a consequence of the Taylor expansion approximation.

Problem I:

$$\rho_l\frac{\partial s_l}{\partial t}+\rho_l\mathbf{v}_l\cdot\nabla s_l=\nabla\cdot\left(\rho_l D_l\nabla s_l\right)+\varepsilon_l^{-1}\rho_l X_l\quad\text{in } V_l, \tag{4.28}$$

$$\text{B.C. I} \quad \mathbf{n}_{ls}\cdot\frac{\langle\omega_l\rangle^l}{\langle\omega_l\rangle^l-\omega_{eq}}\rho_l\left(\mathbf{v}_l-\mathbf{w}_{sl}\right)+\mathbf{n}_{ls}\cdot\left(\rho_l s_l\left(\mathbf{v}_l-\mathbf{w}_{sl}\right)-\rho_l D_l\nabla s_l\right)$$
$$=\frac{M_{Ca}k_s}{\omega_{eq}}\left(1-\frac{\langle\omega_l\rangle^l}{\omega_{eq}}\right)^{n-1}\left(1+n\,s_l\right)\qquad\text{at } A_{ls}(t), \tag{4.29}$$

$$\text{B.C. II} \quad \mathbf{n}_{li}\cdot\left(-\rho_l D_l\nabla s_l\right)=0\quad\text{at } A_{li}, \tag{4.30}$$

$$\langle s_l\rangle=0\quad\text{in } V_l, \tag{4.31}$$

$$s_l\left(\mathbf{x}+\mathbf{l}_i\right)=s_l\left(\mathbf{x}\right), \tag{4.32}$$

where the notation $A_{ls}(t)$ was used to remind the geometry evolution. In the above set of closure problem, the following notation has been used

$$\rho_l X_l = \frac{1}{V}\int_{A_{ls}}\mathbf{n}_{ls}\cdot\rho_l s_l\left(\mathbf{v}_l-\mathbf{w}_{sl}\right)dA-\frac{1}{V}\int_{A_{ls}}\mathbf{n}_{ls}\cdot\rho_l D_l\nabla s_l dA$$
$$-\frac{1}{V}\int_{A_{li}}\mathbf{n}_{li}\cdot\rho_l D_l\nabla s_l dA. \tag{4.33}$$

Taking the average of Eq. 4.28, and the fact that $\rho_l\left\langle\mathbf{v}_l\cdot\nabla s_l\right\rangle=\rho_l\nabla\cdot\left\langle\mathbf{v}_l s_l\right\rangle=0$ because of the periodicity conditions leads to the equation

$$\rho_l\frac{\partial\left\langle s_l\right\rangle}{\partial t}=-\frac{1}{V}\int_{A_{ls}}\mathbf{n}_{ls}\cdot\rho_l s_l\left(\mathbf{v}_l-\mathbf{w}_{sl}\right)dA+\frac{1}{V}\int_{A_{ls}}\mathbf{n}_{ls}\cdot\rho_l D_l\nabla s_l dA$$
$$+\frac{1}{V}\int_{A_{li}}\mathbf{n}_{li}\cdot\rho_l D_l\nabla s_l dA+\rho_l X_l\equiv 0, \tag{4.34}$$

which confirms the consistency of the proposed closure problem.

Problem II:

$$\rho_l\frac{\partial\mathbf{b}_l}{\partial t}+\rho_l\mathbf{v}_l\cdot\left(\nabla\mathbf{b}_l+s_l\mathbf{I}\right)+\rho_l\tilde{\mathbf{v}}_l-\varepsilon_l^{-1}\rho_l\left\langle\tilde{\mathbf{v}}_l s_l\right\rangle = \nabla\cdot\left(\rho_l D_l\left(\nabla\mathbf{b}_l+s_l\mathbf{I}\right)\right)$$
$$+\varepsilon_l^{-1}\rho_l\mathbf{u}_l\quad\text{in } V_l, \tag{4.35}$$

$$\text{B.C. I} \quad \mathbf{n}_{ls}\cdot\left(\rho_l\left(\mathbf{v}_l-\mathbf{w}_{sl}\right)\mathbf{b}_l-\rho_l D_l\left(\nabla\mathbf{b}_l+s_l\mathbf{I}\right)\right)-\rho_l D_l\mathbf{n}_{ls} = n\frac{M_{Ca}k_s}{\omega_{eq}}\left(1-\frac{\langle\omega_l\rangle^l}{\omega_{eq}}\right)^{n-1}\mathbf{b}_l \text{ at } A_{ls}(t), \tag{4.36}$$

$$\text{B.C. II} \quad \mathbf{n}_{li}\cdot\left(-\rho_l D_l\left(\nabla\mathbf{b}_l+s_l\mathbf{I}\right)\right)=\rho_l D_l\mathbf{n}_{li} \quad \text{at } A_{li}, \tag{4.37}$$

$$\langle\mathbf{b}_l\rangle=0 \quad \text{in } V_l, \tag{4.38}$$

$$\mathbf{b}_l\left(\mathbf{x}+\mathbf{l}_i\right)=\mathbf{b}_l\left(\mathbf{x}\right), \tag{4.39}$$

in which

$$\rho_l\mathbf{u}_l = \frac{1}{V}\int_{A_{ls}}\mathbf{n}_{ls}\cdot\rho_l\left(\mathbf{v}_l-\mathbf{w}_{sl}\right)\mathbf{b}_l dA-\frac{1}{V}\int_{A_{ls}}\mathbf{n}_{ls}\cdot\rho_l D_l\left(\nabla\mathbf{b}_l+s_l\mathbf{I}\right) -\frac{1}{V}\int_{A_{ls}}\mathbf{n}_{ls}\rho_l D_l dA. \tag{4.40}$$

Using the following relation[3]

$$-\nabla\varepsilon_l=\frac{1}{V}\int_{A_{ls}}\mathbf{n}_{ls}dA+\frac{1}{V}\int_{A_{li}}\mathbf{n}_{li}dA=0, \tag{4.41}$$

it may be written that

$$-\frac{1}{V}\int_{A_{ls}}\mathbf{n}_{ls}\rho_l D_l dA=\frac{1}{V}\int_{A_{li}}\mathbf{n}_{li}\rho_l D_l dA, \tag{4.42}$$

which becomes

$$-\frac{1}{V}\int_{A_{ls}}\mathbf{n}_{ls}\rho_l D_l dA=-\frac{1}{V}\int_{A_{li}}\mathbf{n}_{li}\cdot\left(\rho_l D_l\left(\nabla\mathbf{b}_l+s_l\mathbf{I}\right)\right)dA. \tag{4.43}$$

because of Eq. 4.37.

With that in hand, Eq. 4.40 may be recast into a more convenient form

[3]It must be reminded that neglecting spatial variations of the phase volume fractions is only made at the closure level, and is consistent with the use of periodicity conditions.

$$\rho_l \mathbf{u}_l = \frac{1}{V}\int_{A_{ls}} \mathbf{n}_{ls}\cdot\rho_l\left(\mathbf{v}_l-\mathbf{w}_{sl}\right)\mathbf{b}_l dA - \frac{1}{V}\int_{A_{ls}} \mathbf{n}_{ls}\cdot\rho_l D_l\left(\nabla\mathbf{b}_l + s_l\mathbf{I}\right)dA \\ -\frac{1}{V}\int_{A_{li}} \mathbf{n}_{li}\cdot\rho_l D_l\left(\nabla\mathbf{b}_l + s_l\mathbf{I}\right)dA, \tag{4.44}$$

which can be used to check the consistency relationship

$$\rho_l \frac{\partial\left\langle\mathbf{b}_l\right\rangle}{\partial t} \equiv 0. \tag{4.45}$$

In both closure problems, the zero average conditions on the mapping fields s_l and $\mathbf{b}_l$ ensure that the concentration deviation is zero. The initial conditions that must be added to the two sets of equations in order to get a complete problem remain unspecified. They depend on the specific problem to be solved in the transient case. Since only the steady-state behavior is considered in the next sections, this discussion is not pushed here.

Here one sees that a complete coupling between **Problem I** and **II** has been kept according to terms involving s_l in **Problem II**. As shown in [166], such a coupling may be necessary to get an accurate estimate of the exchanged flux. So far the interface velocity has not been discarded at any step, which provides a very consistent theory in the mass balance equations. In order to solve these problems, however, the interface position and velocity, as well as the macro-scale concentration must be known properties because of the reaction nonlinearity. The classical geochemistry problem faced here is that in principle, the coupled pore-scale (here the closure problems) and macro-scale equations must be solved at each time step in order to compute the interface evolution and $\left\langle\omega_l\right\rangle^l$. In geochemistry (or other problems involving changing geometries) it is often assumed a given interface evolution and the closure problems are solved for each realization, which in turn yields effective properties depending on, for instance, the medium porosity. In turn, these effective properties can be used in a macro-scale simulation without the need of a coupled micro-scale/macro-scale solution. Of course, it is well known that some history effects are lost in this process [66], but it has the advantage that this is far more practical than solving the coupled problem.

Assuming that mass fluxes near the interface are triggered by the diffusive flux, which is acceptable in most dissolution problems, approximate closure problems may be developed as indicated in Appendix A.

4.2.3 Macro-scale equation and effective properties

Introducing the deviation expression Eq. 4.26 in the averaged equation Eq. 4.12 leads to

$$\begin{aligned}
&\frac{\partial \varepsilon_l \rho_l \langle \omega_l \rangle^l}{\partial t} + \nabla \cdot \left(\varepsilon_l \rho_l \langle \omega_l \rangle^l \langle \mathbf{v}_l \rangle^l \right) + \nabla \cdot \left(\rho_l \langle \tilde{\mathbf{v}}_l s_l \rangle \left(\langle \omega_l \rangle^l - \omega_{eq} \right) + \rho_l \langle \tilde{\mathbf{v}}_l \mathbf{b}_l \rangle \cdot \nabla \langle \omega_l \rangle^l \right) \\
&= \nabla \cdot \left(\varepsilon_l \rho_l D_l \nabla \langle \omega_l \rangle^l \right) + \nabla \cdot \left(\frac{1}{V} \int_{A_{ls}} \mathbf{n}_{ls} \rho_l D_l \left(\mathbf{b}_l \cdot \nabla \langle \omega_l \rangle^l + s_l \left(\langle \omega_l \rangle^l - \omega_{eq} \right) \right) dA \right) \\
&\quad + \nabla \cdot \left(\frac{1}{V} \int_{A_{li}} \mathbf{n}_{li} \rho_l D_l \left(\mathbf{b}_l \cdot \nabla \langle \omega_l \rangle^l + s_l \left(\langle \omega_l \rangle^l - \omega_{eq} \right) \right) dA \right) - K_{Ca}, \quad (4.46)
\end{aligned}$$

with K_{Ca} defined by Eq. 4.13.

It is convenient to write Eq. 4.46 under the form of a generalized dispersion equation such as

$$\begin{aligned}
\frac{\partial \varepsilon_l \rho_l \langle \omega_l \rangle^l}{\partial t} + \nabla \cdot \left(\varepsilon_l \rho_l \langle \omega_l \rangle^l \langle \mathbf{v}_l \rangle^l + \varepsilon_l \rho_l \left(\langle \omega_l \rangle^l - \omega_{eq} \right) \mathbf{U}_l^* \right) &= \nabla \cdot \left(\varepsilon_l \rho_l \mathbf{D}_l^* \cdot \nabla \langle \omega_l \rangle^l \right) \\
&\quad - K_{Ca}, \quad (4.47)
\end{aligned}$$

with the dispersion tensor given by

$$\mathbf{D}_l^* = D_l \left(\mathbf{I} + \frac{1}{V_l} \int_{A_{ls}} \mathbf{n}_{ls} \mathbf{b}_l dA + \frac{1}{V_l} \int_{A_{li}} \mathbf{n}_{li} \mathbf{b}_l dA \right) - \langle \tilde{\mathbf{v}}_l \mathbf{b}_l \rangle^l, \quad (4.48)$$

and the non-traditional effective velocity given by

$$\mathbf{U}_l^* = \langle \tilde{\mathbf{v}}_l s_l \rangle^l - \frac{1}{V_l} \int_{A_{ls}} \mathbf{n}_{ls} D_l s_l dA - \frac{1}{V_l} \int_{A_{li}} \mathbf{n}_{li} D_l s_l dA. \quad (4.49)$$

The mass exchange term can be calculated as (neglecting higher order derivatives than $\nabla \langle \omega_l \rangle^l$)

$$\begin{aligned}
K_{Ca} = \frac{1}{V} \int_{A_{ls}} \mathbf{n}_{ls} \cdot \Big(&\rho_l \left(\mathbf{v}_l - \mathbf{w}_{sl} \right) \left(\langle \omega_l \rangle^l + \mathbf{b}_l \cdot \nabla \langle \omega_l \rangle^l + s_l \left(\langle \omega_l \rangle^l - \omega_{eq} \right) \right) \\
&- \rho_l D_l \left(\nabla \langle \omega_l \rangle^l + \left(\nabla \mathbf{b}_l + s_l \mathbf{I} \right) \cdot \nabla \langle \omega_l \rangle^l + \left(\langle \omega_l \rangle^l - \omega_{eq} \right) \nabla s_l \right) \Big) dA. \quad (4.50)
\end{aligned}$$

It can be recast into

$$K_{Ca} = \langle\omega_l\rangle_{ls} K_g + \frac{1}{V}\int_{A_{ls}} \mathbf{n}_{ls}\cdot\Big(\rho_l\left(\mathbf{v}_l-\mathbf{w}_{sl}\right)\left(\mathbf{b}_l\cdot\nabla\langle\omega_l\rangle^l + s_l\left(\langle\omega_l\rangle^l-\omega_{eq}\right)\right) - \rho_l D_l\left(\nabla\langle\omega_l\rangle^l + \left(\nabla\mathbf{b}_l + s_l\mathbf{I}\right)\cdot\nabla\langle\omega_l\rangle^l + \left(\langle\omega_l\rangle^l-\omega_{eq}\right)\nabla s_l\right)\Big) dA, \quad (4.51)$$

or

$$K_{Ca} = \langle\omega_l\rangle_{ls} K_g + \left(\langle\omega_l\rangle^l-\omega_{eq}\right)\frac{1}{V}\int_{A_{ls}} \mathbf{n}_{ls}\cdot\left(\rho_l s_l\left(\mathbf{v}_l-\mathbf{w}_{sl}\right)-\rho_l D_l\nabla s_l\right) dA + \left(\frac{1}{V}\int_{A_{ls}} \mathbf{n}_{ls}\cdot\left(\rho_l\left(\mathbf{v}_l-\mathbf{w}_{sl}\right)\mathbf{b}_l-\rho_l D_l\left(\nabla\mathbf{b}_l+s_l\mathbf{I}\right)\right) dA\right)\cdot\nabla\langle\omega_l\rangle^l - \rho_l D_l\left(\frac{1}{V}\int_{A_{ls}}\mathbf{n}_{ls}dA\right)\cdot\nabla\langle\omega_l\rangle^l. \quad (4.52)$$

This formula is useful in the sense that it emphasizes the structure of the mass exchange term regardless of the chosen expression used for the reaction rate (it could be also an equilibrium boundary condition). In particular it shows that the mass exchange term is not only depending on the averaged concentration but also on its gradient. Of course, it is also useful to relate this term to the reaction rate expression by a direct averaging of Eq. 4.13. The following expression may be written

$$K_{Ca} = -a_{vl} M_{Ca} k_s \left\langle\left(1-\frac{\langle\omega_l\rangle^l + s_l\left(\langle\omega_l\rangle^l-\omega_{eq}\right)+\mathbf{b}_l\cdot\nabla\langle\omega_l\rangle^l}{\omega_{eq}}\right)^n\right\rangle_{ls}. \quad (4.53)$$

The linearized version, as in Eq. 4.24, would lead to

$$K_{Ca} = -a_{vl}\frac{M_{Ca}k_s}{\omega_{eq}}\left(1-\frac{\langle\omega_l\rangle^l}{\omega_{eq}}\right)^{n-1}\left(\omega_{eq}-\langle\omega_l\rangle^l - n\langle\tilde{\omega}_l\rangle_{ls}\right), \quad (4.54)$$

or

$$K_{Ca} = -a_{vl}M_{Ca}\left(1-\frac{\langle\omega_l\rangle^l}{\omega_{eq}}\right)^n k_{s,eff} + a_{vl}M_{Ca}\left(1-\frac{\langle\omega_l\rangle^l}{\omega_{eq}}\right)^{n-1}\mathbf{h}_l^*\cdot\nabla\langle\omega_l\rangle^l. \quad (4.55)$$

where the *effective reaction rate* coefficient is given by

$$k_{s,eff} = k_s \left(1 + n \left\langle s_l \right\rangle_{ls}\right), \tag{4.56}$$

in a similar form as in [171] for the first-order reaction case. The additional gradient term coefficient is

$$\mathbf{h}_l^* = n \frac{k_s}{\omega_{eq}} \left\langle \mathbf{b}_l \right\rangle_{ls}. \tag{4.57}$$

One must remember that the macro-scale problem involves also the following averaged equations

$$\frac{\partial \varepsilon_l \rho_l}{\partial t} + \nabla \cdot \left(\rho_l \left\langle \mathbf{v}_l \right\rangle\right) = -K_g, \quad \frac{\partial \varepsilon_s \rho_s}{\partial t} = K_g. \tag{4.58}$$

The resulting macro-scale model is a generalization to nonlinear reaction rates of non-equilibrium models previously published. Such models are useful in many circumstances, for instance as diffuse interface models for modeling the dissolution of cavities [120, 121] or for studying instability of dissolution fronts [10].

4.2.4 Reactive limiting cases and thermodynamic equilibrium

It is useful to rewrite the above developed closure problems into a dimensionless form as presented in Appendix A, where two dimensionless numbers were generated therein with the following definitions

$$\mathrm{Pe} = \frac{U_r l_r}{D_l}, \quad \mathrm{Da} = \frac{M_{Ca}}{\rho_l \omega_{eq}} \frac{l_r k_s}{D_l} \left(1 - \frac{\left\langle \omega_l \right\rangle^l}{\omega_{eq}}\right)^{n-1}, \tag{4.59}$$

where Da is the second Damköhler number since the reaction takes place at the solid-liquid surface. The first limiting case of interest is obtained when Da is very small (cf. Appendix B) , which leads to

1. the mapping variable s_l is zero,

2. one recovers for $\mathbf{b}_l$ the closure problem for *passive dispersion.*

As a consequence, the mass exchange rate from Eq. 4.53 can be written as

$$K_{Ca} = -a_{vl} M_{Ca} k_s \left\langle \left(1 - \frac{\langle \omega_l \rangle^l + s_l \left(\langle \omega_l \rangle^l - \omega_{eq} \right) + \mathbf{b}_l \cdot \nabla \langle \omega_l \rangle^l}{\omega_{eq}} \right)^n \right\rangle_{ls}$$
$$= -a_{vl} M_{Ca} k_s \left\langle \left(1 - \frac{\langle \omega_l \rangle^l}{\omega_{eq}} \right)^n \right\rangle_{ls}, \tag{4.60}$$

where the estimate

$$\mathbf{b}_l \cdot \nabla \langle \omega_l \rangle^l \approx \mathcal{O}\left(\frac{l_l}{L} \langle \omega_l \rangle^l \right), \tag{4.61}$$

has been used to discard this term in front of $\langle \omega_l \rangle^l$.

The second limiting case of interest is obtained when Da is very large (cf. Appendix C), then Eq. 2.21 may be replaced by

$$\text{B.C. I} \qquad \omega_l = \omega_{eq} \qquad \text{at } A_{ls}, \tag{4.62}$$

and thermodynamic equilibrium at the dissolving interface is recovered at pore-scale. With the definition of Da by Eq. 4.59, this may be obtained under the following two conditions

1. the physical parameters must be such that $\frac{M_{Ca}}{\rho_l \omega_{eq}} \frac{l_r k_s}{D_l} \gg 1$,

2. $n = 1$ (since $\langle \omega_l \rangle^l$ has a tendency to grow up to ω_{eq}), which excludes nonlinear reaction rates!

As a consequence of Eq. 4.62, one recovers

$$s_l = -1 \quad \text{and} \quad \mathbf{b}_l = 0 \qquad \text{at } A_{ls}(t), \tag{4.63}$$

when $\text{Da} \gg 1$.

In the case of thermodynamic equilibrium at pore-scale, the macro-scale equations are the same as before obtained for the reactive case (Eqs. 4.46 to 4.49 and 4.58), but for a different expression of the mass exchange term which can be rewritten from Eq. 4.52 (one cannot use Eq. 4.55 because of the undetermined limit at large k_s), since $\langle \omega_l \rangle_{ls} = \omega_{eq}$, as

$$K_{Ca} = \langle \omega_l \rangle_{ls} K_g + \left(\langle \omega_l \rangle^l - \omega_{eq} \right) \frac{1}{V} \int_{A_{ls}} \mathbf{n}_{ls} \cdot \left(-\rho_l \left(\mathbf{v}_l - \mathbf{w}_{sl} \right) - \rho_l D_l \nabla s_l \right) dA + \left(\frac{1}{V} \int_{A_{ls}} \mathbf{n}_{ls} \cdot \left(\rho_l \left(\mathbf{v}_l - \mathbf{w}_{sl} \right) \mathbf{b}_l - \rho_l D_l \left(\nabla \mathbf{b}_l + s_l \mathbf{I} \right) \right) dA \right) \cdot \nabla \langle \omega_l \rangle^l - \rho_l D_l \left(\frac{1}{V} \int_{A_{ls}} \mathbf{n}_{ls} dA \right) \cdot \nabla \langle \omega_l \rangle^l, \quad (4.64)$$

or (since $\langle \omega_l \rangle_{ls} = \omega_{eq}$)

$$\begin{aligned} K_{Ca} &= \omega_{eq} K_g + \left(\langle \omega_l \rangle^l - \omega_{eq} \right) \frac{1}{V} \int_{A_{ls}} \mathbf{n}_{ls} \cdot \left(-\rho_l D_l \nabla s_l \right) dA \\ &\quad + \left(\frac{1}{V} \int_{A_{ls}} \mathbf{n}_{ls} \cdot \left(-\rho_l D_l \nabla \mathbf{b}_l \right) dA \right) \cdot \nabla \langle \omega_l \rangle^l, \end{aligned} \quad (4.65)$$

which can be formally written as

$$K_{Ca} = \omega_{eq} K_g + \rho_l \alpha_l \left(\langle \omega_l \rangle^l - \omega_{eq} \right) + \rho_l \mathbf{h}_l \cdot \nabla \langle \omega_l \rangle^l, \quad (4.66)$$

where the following notation for the mass exchange coefficient

$$\alpha_l = \frac{1}{V} \int_{A_{ls}} \mathbf{n}_{ls} \cdot \left(-D_l \nabla s_l \right) dA, \quad (4.67)$$

and the additional gradient term

$$\mathbf{h}_l = \left(\frac{1}{V} \int_{A_{ls}} \mathbf{n}_{ls} \cdot \left(-D_l \nabla \mathbf{b}_l \right) dA \right), \quad (4.68)$$

have been adopted. The case for a stratified unit cell is taken as an example in Appendix D.

One should note that the mass exchange term is often reduced in the literature to the single term $\rho_l \alpha_l \left(\langle \omega_l \rangle^l - \omega_{eq} \right)$.

When assuming that terms involving the interface velocity are small, the two closure problems are reminiscent of the closure problems encountered in NAPL dissolution and studied in [109]. One limiting case of this transport model is the local-equilibrium model, obtained when α_l is very large and that will impose

$$\langle \omega_l \rangle^l = \omega_{eq}, \quad (4.69)$$

as soon as the liquid is in contact with a zone containing the dissolving material. In that case, $\langle \omega_l \rangle^l = \omega_{eq}$ is put in Eq. 4.47 to calculate K_g in Eq. 4.58.

Of special interest is the case of a linear reaction rate, i.e., $n = 1$. The closure problems are presented in Appendix D and the mass exchange term can be written as

$$\frac{\omega_{eq}}{M_{Ca}} K_{Ca} = -a_{vl} k_{s,eff} \left(\omega_{eq} - \langle \omega_l \rangle^l \right) + a_{vl} k_s \langle \mathbf{b}_l \rangle_{ls} \cdot \nabla \langle \omega_l \rangle^l , \tag{4.70}$$

where an *effective reaction rate coefficient*, $k_{s,eff}$, has been introduced such as

$$\frac{k_{s,eff}}{k_s} \mid_{n=1} = (1 + \langle s_l \rangle_{ls}) . \tag{4.71}$$

The two limiting cases with respect to Da lead to

1. Da $\to 0$: $s_l = 0$ and hence $\frac{k_{s,eff}}{k_s} \mid_{n=1} = 1$;

2. Da $\to \infty$: the effective reaction rate becomes independent of Da and is only controlled by the transport problem.

Neglecting the additional coupling terms and the terms involving the interface velocity, the theoretical results presented in [58] are recovered.

4.3 Effective parameters for the nonlinear reactive case

In this section, the steady state form of the closure equations in Appendix A are solved for stratified (1D), 2D and 3D representative unit cells. All the unit cells in case I are composed of a solid (s), an insoluble (i) and a liquid (l) phase (cf. Figs. 4.1a, 4.1c and 4.1e). In case II all the solid phases are soluble (cf. Figs. 4.1b, 4.1d and 4.1f). The dependency of the macro-scale effective parameters on the flow properties and chemical features in terms of local Péclet (Pe) and Damköhler (Da) numbers defined by Eq. 4.59, as well as on the reaction nonlinearity, are investigated. In the dimensionless problems, the characteristic lengths for stratified geometry are $(l_i + l_l + l_s)$ and l_l in in case I and case II, respectively. The diameter of the circles and spheres, d_0 in the 2D and 3D geometries, are used as the characteristic length in both cases. The characteristic velocity U_r is defined as the x-component of the intrinsic

average velocity $\langle u_l \rangle^l$. For the stratified unit cell, the flow is of Poiseuille type given by the following expression

$$u_l = \frac{3}{2} \langle u_l \rangle^l \left(1 - \frac{(y - R_0)^2}{\left(\frac{l_l}{4}\right)^2} \right), \tag{4.72}$$

with $R_0 = \pm (l_i/2 + l_l/4)$ in case I and $R_0 = \pm (l_s + l_l)/4$ in case II, positive in the upper part and negative in the lower part of the domain. The velocity field is obtained numerically for the 2D and 3D flow problems, by solving dimensionless Navier-Stokes equations with $\mathrm{Re} = \frac{\rho U_r l_r}{\mu_l} = 10^{-6}$, i.e., negligible inertia effects.

4.3.1 Analytical solutions for the stratified unit cell

Three-phase case

Solving the dimensionless form of the simplified closure problems in Appendix A for the stratified unit cell presented in Fig. 4.1a, the analytical solutions for the effective parameters generated in Sec. 4.2 were obtained as

$$\frac{(\mathbf{D}_l^*)_{xx}}{D_l} = 1 + \frac{\mathrm{Pe}^2 \varepsilon_l^2 \left(11\mathrm{Da}^2 \varepsilon_l^2 n^2 - 3\mathrm{Da}^2 \varepsilon_l^2 n + 146\mathrm{Da}\varepsilon_l n + 16\mathrm{Da}\varepsilon_l + 480 \right)}{11200 \left(\mathrm{Da}\varepsilon_l n + 6 \right)^2}, \tag{4.73}$$

$$\frac{(\mathbf{D}_l^*)_{xy}}{D_l} = \frac{\mathrm{PeDa}\varepsilon_l^2 \left(4\mathrm{Da}\varepsilon_l n^2 + 3\mathrm{Da}\varepsilon_l n + 24n + 24 \right)}{320 \left(\mathrm{Da}\varepsilon_l n + 6 \right)^2}, \tag{4.74}$$

$$\frac{(\mathbf{D}_l^*)_{yx}}{D_l} = -\frac{\mathrm{PeDa}\varepsilon_l^2 \left(7\mathrm{Da}\varepsilon_l n^2 - 4\mathrm{Da}\varepsilon_l n + 42n - 126 \right)}{560 \left(\mathrm{Da}\varepsilon_l n + 6 \right)^2}, \tag{4.75}$$

$$\frac{(\mathbf{D}_l^*)_{yy}}{D_l} = \frac{3\mathrm{Da}\varepsilon_l n \left(4\mathrm{Da}\varepsilon_l n - \mathrm{Da}\varepsilon_l + 24 \right)}{16 \left(\mathrm{Da}\varepsilon_l n + 6 \right)^2}, \tag{4.76}$$

$$\frac{(\mathbf{U}_l^*)_x}{U_r} = \frac{\mathrm{Da}\varepsilon_l}{20 \left(\mathrm{Da}\varepsilon_l n + 6 \right)}, \tag{4.77}$$

$$\frac{(\mathbf{U}_l^*)_y}{U_r} = \frac{3\mathrm{Da}}{\left(\mathrm{Da}\varepsilon_l n + 6 \right) \mathrm{Pe}}, \tag{4.78}$$

$$\frac{k_{s,eff}}{k_s} = \frac{6}{\mathrm{Da}\varepsilon_l n + 6}, \tag{4.79}$$

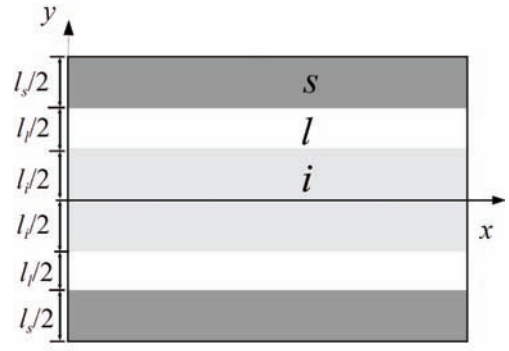

(a) Stratified unit cell with insoluble material.

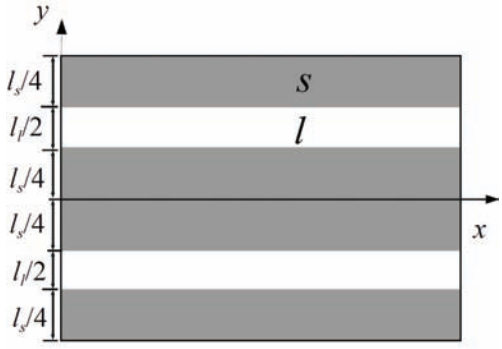

(b) Stratified unit cell without insoluble material.

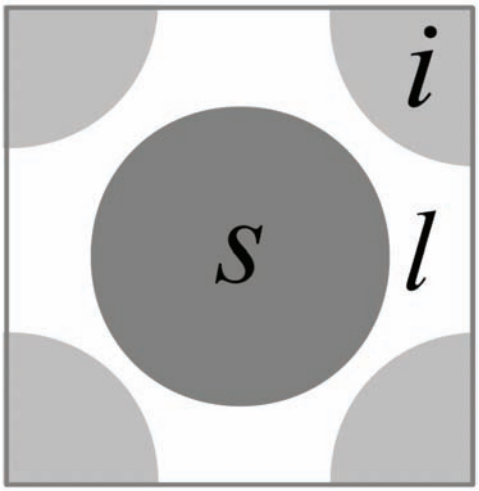

(c) 2D unit cell with insoluble material.

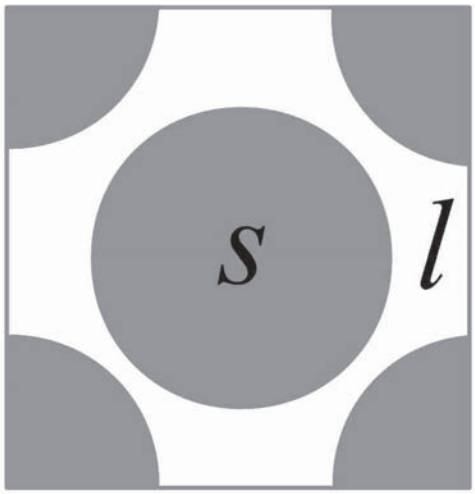

(d) 2D unit cell without insoluble material.

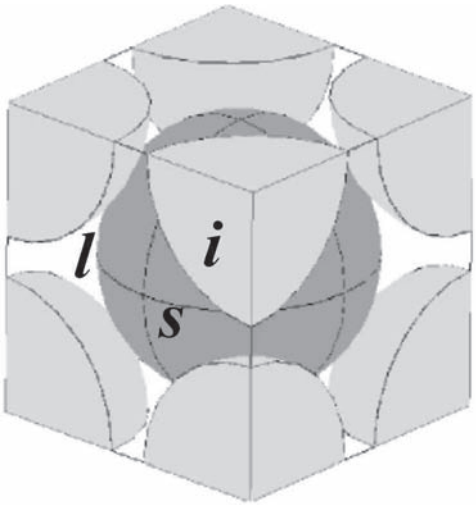

(e) 3D unit cell with insoluble material.

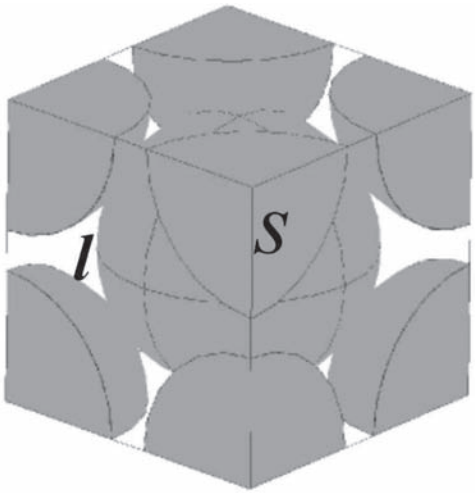

(f) 3D unit cell without insoluble material.

Figure 4.1: Unit Cells.

$$\frac{(\mathbf{h}_l^*)_x}{l_r} = \frac{n\,k_s \mathrm{Pe}\varepsilon_l^2\,(7\mathrm{Da}\varepsilon_l n + 17\mathrm{Da}\varepsilon_l + 42)}{280\omega_{eq}\,(\mathrm{Da}\varepsilon_l n + 6)^2}, \tag{4.80}$$

$$\frac{(\mathbf{h}_l^*)_y}{l_r} = -\frac{3n\,k_s\varepsilon_l\,(4\mathrm{Da}\varepsilon_l n - \mathrm{Da}\varepsilon_l + 24)}{8\omega_{eq}\,(\mathrm{Da}\varepsilon_l n + 6)^2}. \tag{4.81}$$

Values of the effective parameters in the transversal direction, i.e., the z-axis, perpendicular to the x-axis and the flow direction, can be estimated by taking the x-axis values with $\mathrm{Pe} = 0$. Regarding the impact of flow properties, the longitudinal dispersion coefficient $(\mathbf{D}_l^*)_{xx}/D_l$ has a classical square dependence on the local Péclet number (Pe) typical of Taylor dispersion. $(\mathbf{D}_l^*)_{xy}/D_l$, $(\mathbf{D}_l^*)_{yx}/D_l$ and $(\mathbf{h}_l^*)_x/l_r$ are linear functions of Pe. $(\mathbf{D}_l^*)_{yy}/D_l$, $(\mathbf{U}_l^*)_x/U_r$, $k_{s,eff}/k_s$ and $(\mathbf{h}_l^*)_y/l_r$ are independent of Pe, while $(\mathbf{U}_l^*)_y/U_r$ is inversely proportional to Pe. It must be understood that these results, because of the periodicity condition, correspond to a fully developed concentration field, i.e., at some distance of the entrance region (cf. [166]). If one wants to take into account precisely the entrance region effect (i.e., dissolution at the beginning of the front), one has to develop a non-local closure in which the distance from the front beginning will play a role.

When $\mathrm{Da} = 0$, the classical passive dispersion case is recovered, with the transport properties

$$\mathbf{U}_l^* = 0, \tag{4.82}$$

$$\frac{(\mathbf{D}_l^*)_{xx}}{D_l} = 1 + \frac{\mathrm{Pe}^2\varepsilon_l^2}{840}, \tag{4.83}$$

$$\frac{(\mathbf{D}_l^*)_{xy}}{D_l} = \frac{(\mathbf{D}_l^*)_{yx}}{D_l} = \frac{(\mathbf{D}_l^*)_{yy}}{D_l} = 0. \tag{4.84}$$

The effective reaction rate coefficient turns to be

$$\frac{k_{s,eff}}{k_s} = 1 \quad \text{in the limit } \mathrm{Da}\to 0 \quad \text{and} \quad \frac{k_{s,eff}}{k_s} = 0 \quad \text{in the limit } \mathrm{Da}\to\infty. \tag{4.85}$$

As stated previously, the condition of large Da can be obtained only in the linear reactive case with $n = 1$, with the analytical solution of the mass exchange coefficient at large Da calculated as

$$\frac{\alpha_l l_r^2}{D_l} = -\frac{1}{V'}\int_{A'_{ls}} \mathbf{n}_{ls}\cdot\nabla' s_l dA' = \frac{12}{\varepsilon_l}. \tag{4.86}$$

The impact of the heterogeneous reaction is clearly seen, for instance when comparing the passive and active dispersion coefficient. It is interesting to notice that the coefficient of nonlinearity, n, plays also an important role and this is discussed in the following subsection.

Two-phase case

For case II as illustrated in Fig. 4.1b, one obtains

$$\frac{(\mathbf{D}_l^*)_{xx}}{D_l} = 1 + \frac{\mathrm{Pe}^2\varepsilon_l^2\left(\mathrm{Da}^2\varepsilon_l^2 n^2 + \mathrm{Da}^2\varepsilon_l^2 n + 52\mathrm{Da}\varepsilon_l n + 32\mathrm{Da}\varepsilon_l + 480\right)}{2800\left(\mathrm{Da}\varepsilon_l n + 12\right)^2}, \tag{4.87}$$

$$\frac{(\mathbf{D}_l^*)_{xy}}{D_l} = \frac{(\mathbf{D}_l^*)_{yx}}{D_l} = 0, \tag{4.88}$$

$$\frac{(\mathbf{D}_l^*)_{yy}}{D_l} = \frac{n\,\mathrm{Da}\varepsilon_l}{n\,\mathrm{Da}\varepsilon_l + 4} \tag{4.89}$$

$$\frac{(\mathbf{U}_l^*)_x}{U_r} = \frac{\mathrm{Da}\varepsilon_l}{5\left(\mathrm{Da}\varepsilon_l n + 12\right)}, \tag{4.90}$$

$$\frac{(\mathbf{U}_l^*)_y}{U_r} = 0, \tag{4.91}$$

$$\frac{k_{s,eff}}{k_s} = \frac{12}{n\,\mathrm{Da}\varepsilon_l + 12} \tag{4.92}$$

$$\frac{(\mathbf{h}_l^*)_x}{l_r} = \frac{n\,k_s\mathrm{Pe}\varepsilon_l^2\left(7\mathrm{Da}\varepsilon_l n + 5\mathrm{Da}\varepsilon_l + 84\right)}{140\omega_{eq}\left(\mathrm{Da}\varepsilon_l n + 12\right)^2}, \tag{4.93}$$

$$\frac{(\mathbf{h}_l^*)_y}{l_r} = 0. \tag{4.94}$$

Comparing these results to the three-phase case, the impact of the insoluble materials is clearly seen. The problem is simpler with all the solid medium soluble, with $(\mathbf{D}_l^*)_{xy}/D_l$, $(\mathbf{D}_l^*)_{yx}/D_l$, $(\mathbf{U}_l^*)_y/U_r$ and $(\mathbf{h}_l^*)_x/l_r$ all being zero.

4.3.2 Numerical calculations

Special procedures have been devised to solve easily for the integro-differential equations involved in the closure problems for s_l and $\mathbf{b}_l^{'}$ which are presented in Appendix E. Following [109], the decompositions

$$s_l = -\frac{1}{n} + X_l^{'}\psi_s \quad \text{and} \quad \mathbf{b}_l^{'} = \mathbf{b}_0^{'} + \psi_b \mathbf{u}_l^{'}, \tag{4.95}$$

are introduced. The closure problems can be rewritten consequently for ψ_s, $\mathbf{b}_0^{'}$ and ψ_b, respectively without integro-differential terms. One may notice that the closure problems for ψ_s and ψ_b are identical, therefore the closure problems can be subsequently simplified by solving only one of them. The numerical simulations were performed with COMSOL® with proper choices of the mesh size and other numerical parameters to ensure convergence. For instance for the 3D geometry in case I, the mean element volume ratio, the element number and the number of degree of freedom (DOF) were equal to 5×10^{-4}, 7×10^4 and 176968 (plus 20634 internal DOFs), respectively. The porosity is taken at a value of 0.36 for all the unit cells, and the soluble and insoluble materials have the same volume fraction in case I. As introduced in [49] for gypsum dissolution, the reaction order may range from 1 to 4.5 at different stages, so in the following numerical simulations $n = 1, 3, 5$ are chosen as examples of the nonlinear reaction orders.

For the impact of parameter Da and n, it must be noticed that large values of n have practical applications only when the concentration is close to ω_{eq}. This situation is expected:

- when the time evolution of concentrations and compatible BCs make ω_l close to ω_{eq}.
- rapidly, whatever the initial and boundary conditions, when the Da number is large.

Therefore, we did not limit the range of value of Da when taking a large parameter n.

The effective parameters under investigation were the longitudinal dispersion coefficient $(\mathbf{D}_l^*)_{xx}/D_l$, the ratio of the effective and surface reaction rate coefficient $k_{s,eff}/k_s$, the x-component of the dimensionless effective velocity $(\mathbf{U}_l^*)_x/U_r$ and the x-component of additional gradient term coefficient in the form of $\left(\mathbf{h}_l^*\right)_x \omega_{eq}/(k_s l_r)$. For all these four parameters, the analytical solutions developed above for the stratified unit cell were verified by the numerical

results. As illustrated in Figs. 4.2, 4.8, 4.12 and 4.17, one observes that the analytical solutions agree very well with the corresponding numerical results for the studied effective parameters.

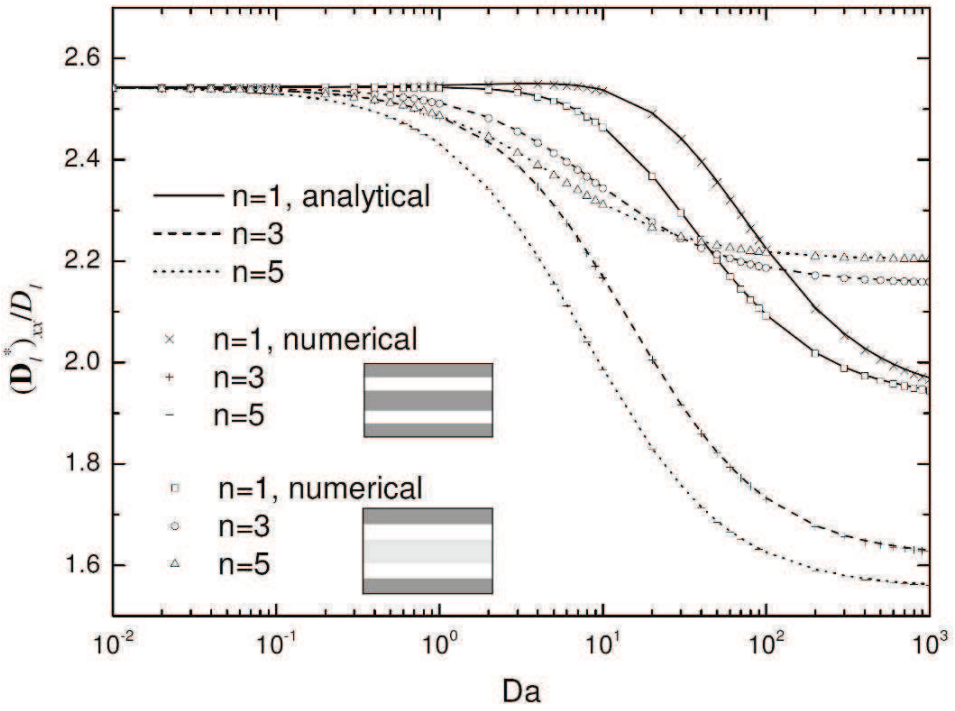

Figure 4.2: $(\mathbf{D}_l^*)_{xx}/D_l$ as a function of Da with Pe = 100 for the 1D geometries.

Dispersion

The results of $(\mathbf{D}_l^*)_{xx}/D_l$ as a function of Da with Pe = 100 (cf. Figs. 4.2 to 4.4) are discussed firstly, i.e., a case with important dispersion effects. One sees that when Da $\to 0$, i.e., in the passive case, dispersion reaches three different values for the 1D, 2D and 3D geometries, respectively, regardless of n, since a different value of n does not affect the limit of Da. In the limit for Da $\to \infty$, $(\mathbf{D}_l^*)_{xx}/D_l$ reaches constant values again which are dependent on the geometry, the proportion of the insoluble material and n. When Pe is large, the decrease of $(\mathbf{D}_l^*)_{xx}/D_l$ in the active case illustrated in Figs. 4.2 to 4.7 has been also observed previously [58, 109]. While the increase of $(\mathbf{D}_l^*)_{xx}/D_l$ with Da when Pe is small for the 2D and 3D geometries is attributed to the fact that a large Da makes the concentration field around the surface more uniform than the zero flux condition, which in turn produces less "tortuosity". The word tortuosity used in this study was not in the classical geometrical sense, i.e., path length, but rather as an indication of the decrease of the apparent diffusion coefficient in the macro-scale equation, which depends on the tortuous character of the geometry but also on transport properties, in

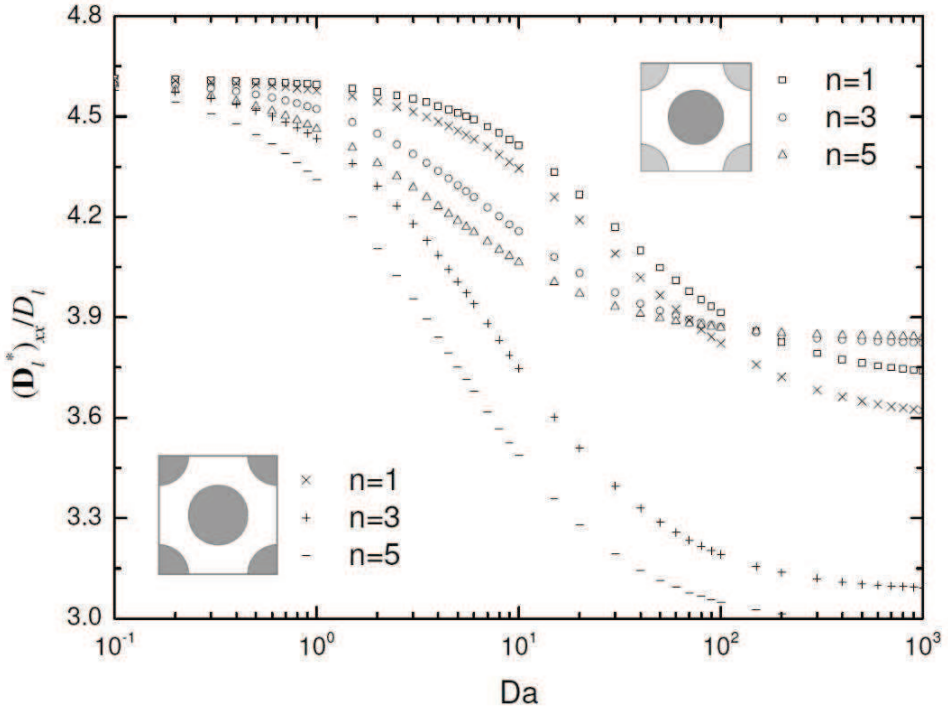

Figure 4.3: $(\mathbf{D}_l^*)_{xx}/D_l$ as a function of Da with Pe = 100 for the 2D geometries.

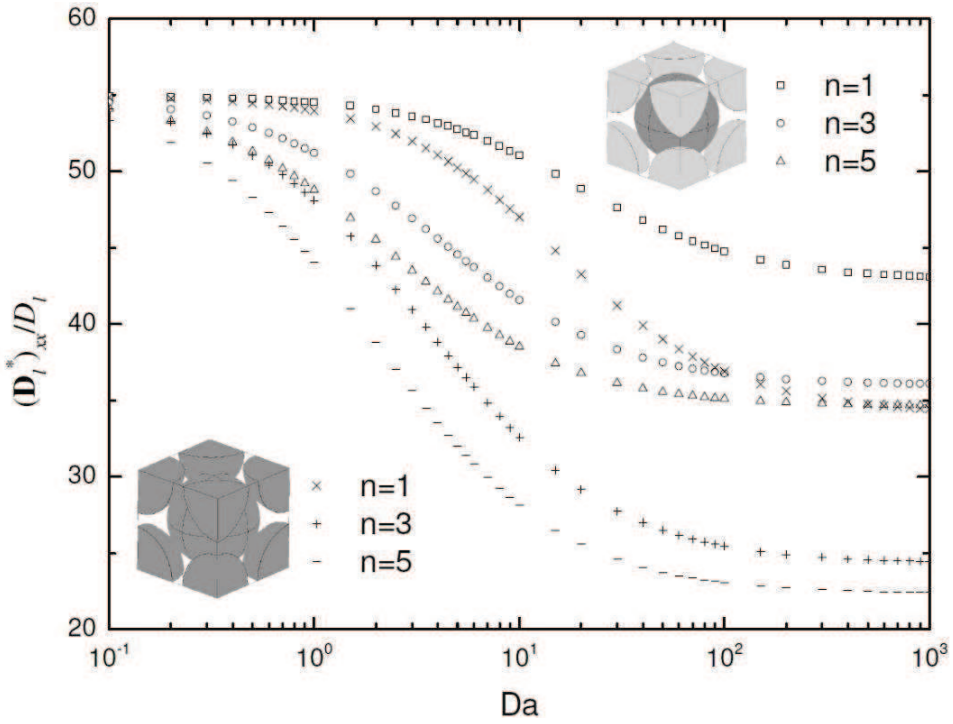

Figure 4.4: $(\mathbf{D}_l^*)_{xx}/D_l$ as a function of Da with Pe = 100 for the 3D geometries.

particular the boundary conditions at the liquid-solid interface as made clear by the closure problems. Results show that *nonlinearity has a significant impact*, dependent upon the topological properties of the unit cell: monotonous for the

3D unit cells and case II for the 1D and 2D geometries under consideration, with a transition at intermediate Da for case I of the 1D and 2D unit cells. It is interesting to note that the nonlinearity of the reaction rate, quantified through n, makes the effect of Da more dramatic for the 3D unit cell than for the stratified and the 2D unit cells. The influences of Da and n are, as one would expect, stronger for the case with only soluble solid than for the one with insoluble material.

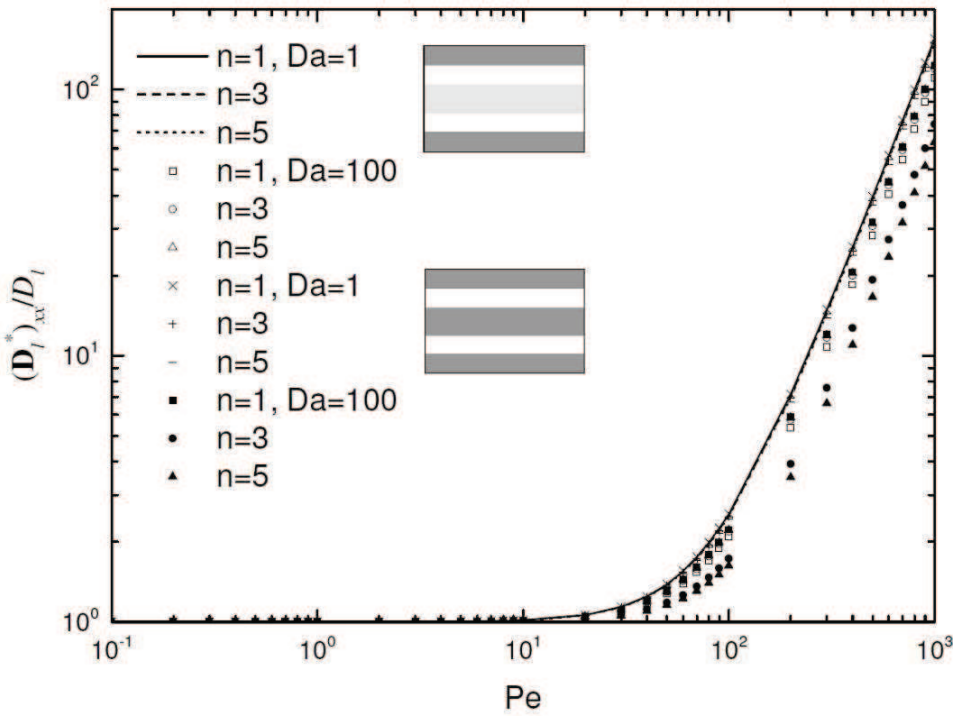

Figure 4.5: $(\mathbf{D}_l^*)_{xx}/D_l$ as a function of Pe for the 1D geometries .

Effective reaction rate

The second parameter under consideration is the effective reaction rate coefficient, in the form of $k_{s,eff}/k_s$. Regarding the impact of Pe on $k_{s,eff}/k_s$, one sees from Eqs. 4.79 and 4.92 that $k_{s,eff}/k_s$ is independent of Pe for the stratified unit cell, either with or without insoluble material, which must be attributed to the fact that periodicity conditions are corresponding to a fully developed regime. According to our numerical calculations, when increasing Pe from 0.1 to 1000, $k_{s,eff}/k_s$ increases 2.0%, 5.5% and 8.4% for $n = 1$, 3 and 5, respectively, for the 3D unit cell with insoluble material and $\mathrm{Da} = 1$. In summary, the Pe number is not important for the linear reactive case while it has larger impacts in the nonlinear reactive cases.

The results of $k_{s,eff}/k_s$ versus Da are presented in Figs. 4.8 to 4.10 for the three pairs of unit cells and for different values of n. One observes the classical

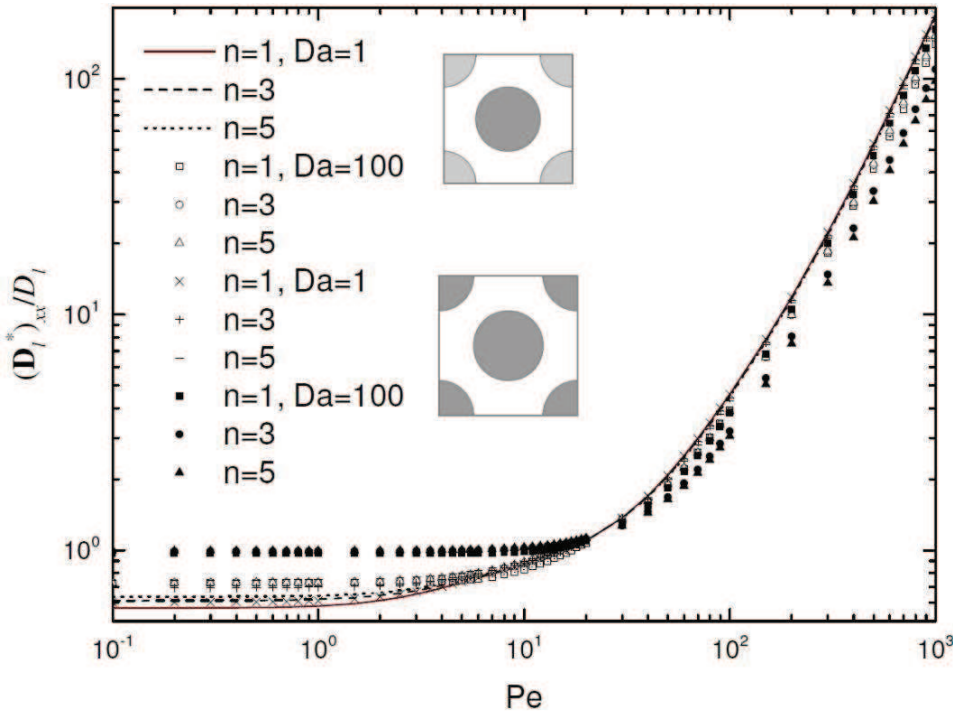

Figure 4.6: $(\mathbf{D}_l^*)_{xx}/D_l$ as a function of Pe for the 2D geometries .

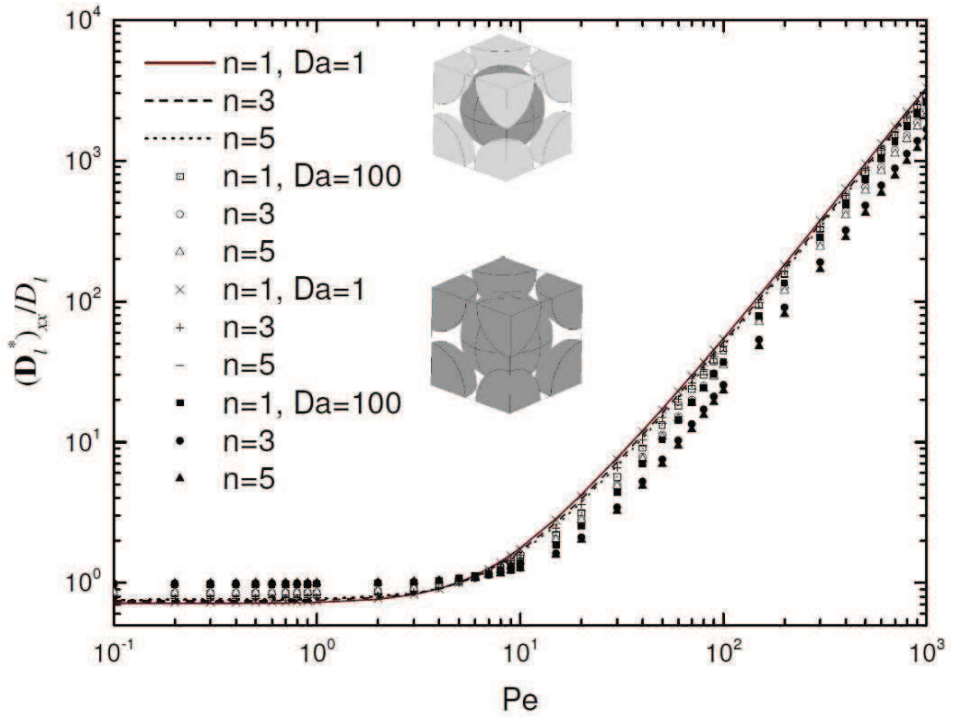

Figure 4.7: $(\mathbf{D}_l^*)_{xx}/D_l$ as a function of Pe for the 3D geometries.

behavior for the *ratio* $k_{s,eff}/k_s$, which is equal to one at small Da and tends to zero at large Da. Similar results were also reported in [58, 171] for different geometries with heterogeneous reactions. Nonlinearity in the reaction rate

and the presence of insoluble material tend to decrease $k_{s,eff}/k_s$, in a limited manner, for a given value of Da.

One should notice that, the increase of Da is also equivalent to an increase in k_s. Therefore, looking at the limit of $k_{s,eff}/k_s$ at large Da number is not informative. Instead, results for an effective Damköhler number, $\mathrm{Da}_{eff} = \frac{k_{s,eff}}{k_s}\mathrm{Da}$, are plotted in Fig. 4.11, taking some 1D and 3D unit cells as examples. One sees that $k_{s,eff}$ reaches a constant at large Da, i.e., in transport limited situations. The constant decreases with n and the proportion of insoluble material. One should also remember that in the case of large Da with $n = 1$, the boundary condition will become the one of thermodynamic equilibrium and the mass exchange coefficient should be predicted by Eq. 4.67 instead of Eq. 4.56, as already discussed.

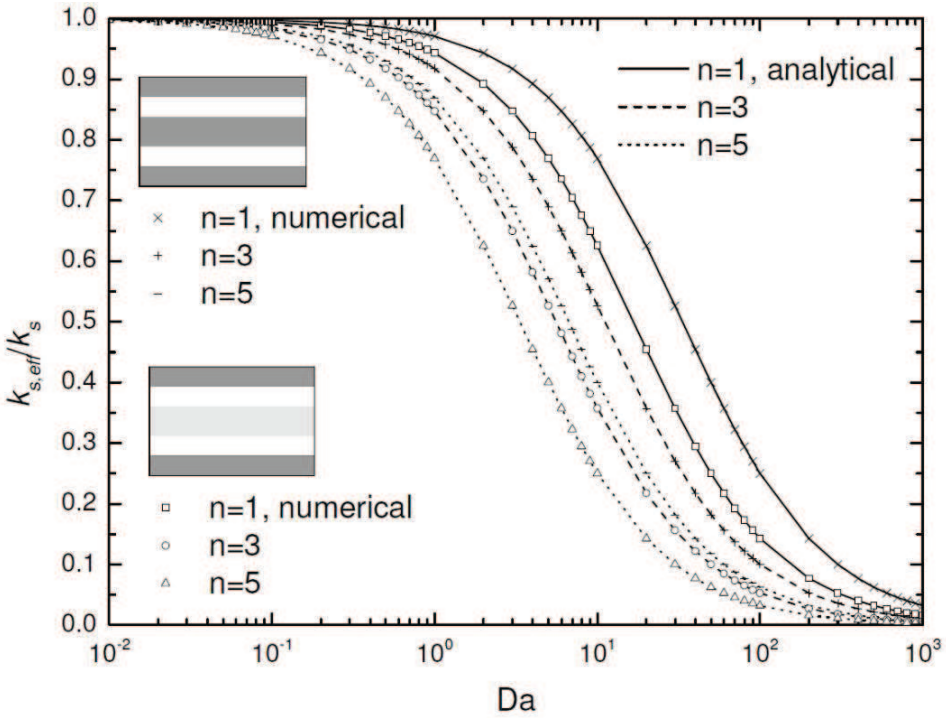

Figure 4.8: $k_{s,eff}/k_s$ as a function of Da for the 1D geometries.

Non-classical terms

The first non-classical term of interest is the x-component of the effective velocity, $(\mathbf{U}_l^*)_x$. The results of $(\mathbf{U}_l^*)_x/U_r$ versus Da for the 1D and 3D unit cells were plotted in Figs. 4.12 and 4.13. One sees that $(\mathbf{U}_l^*)_x/U_r$ can be estimated as a linear function of Da when $\mathrm{Da} < 1$, and in this range the reaction order does not play a role. With further increase of Da, the growth of $(\mathbf{U}_l^*)_x/U_r$ becomes slower and finally reaches an asymptote which decreases with increasing n. The asymptotic value decreases also when decreasing the amount of soluble

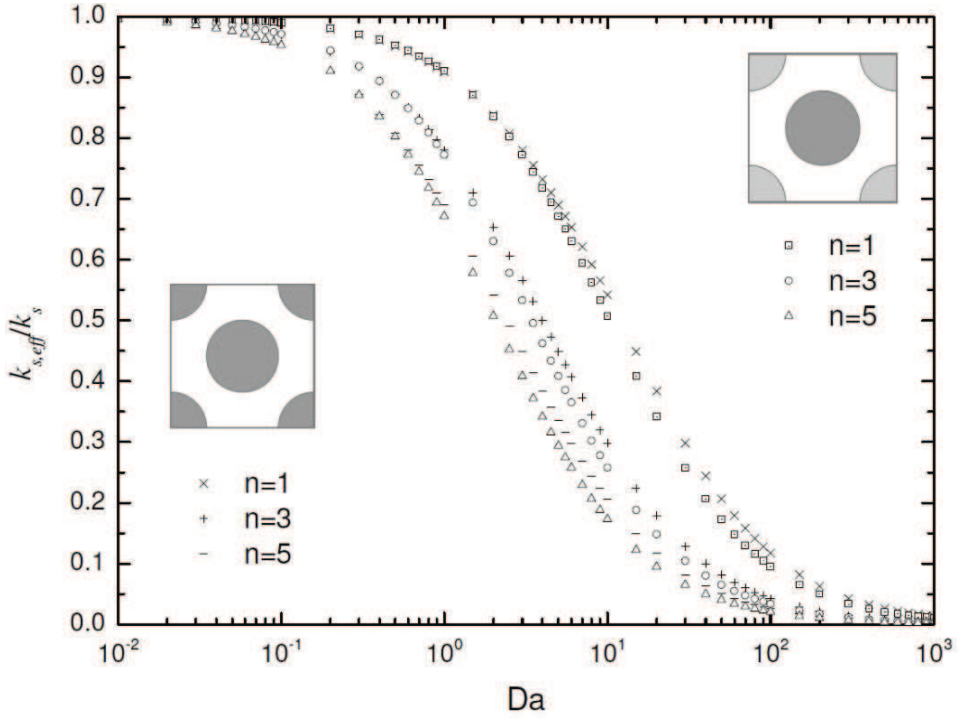

Figure 4.9: $k_{s,eff}/k_s$ as a function of Da with $\mathrm{Pe} = 1$ for the 2D geometries.

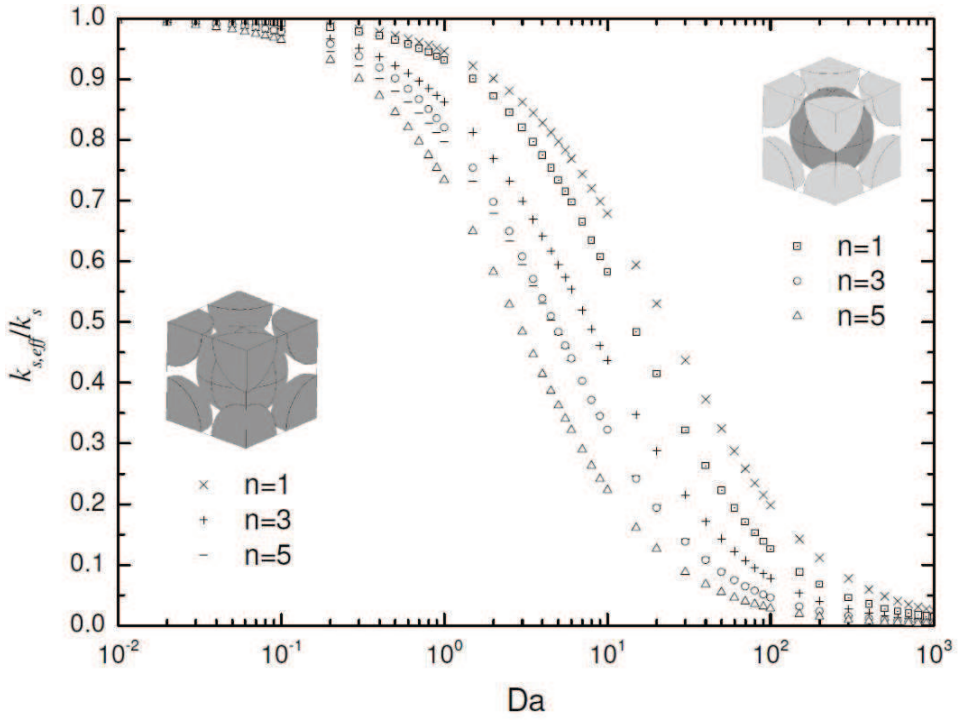

Figure 4.10: $k_{s,eff}/k_s$ as a function of Da with $\mathrm{Pe} = 1$ for the 3D geometries.

material in the unit cell. These results are a reminder of the discussion in [166] about the potential increase of the apparent advection velocity by the non-conventional terms. This effect may be up to 30% in the *linear* case for the

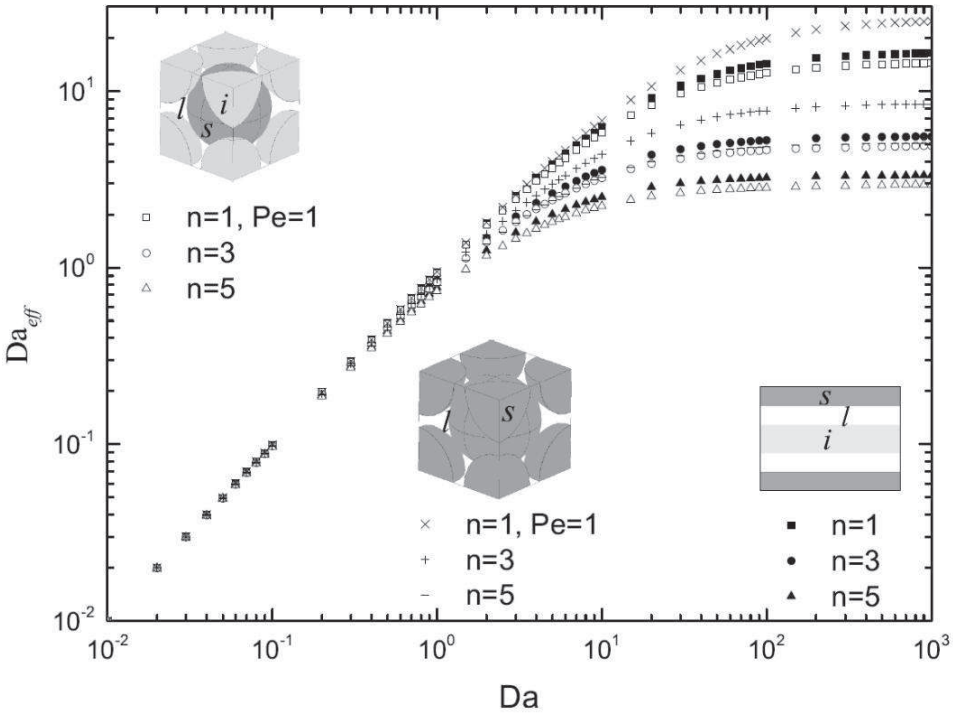

Figure 4.11: Da_{eff} as a function of Da with $\mathrm{Pe} = 1$.

3D geometry without insoluble material and for large Da.

For the 2D unit cell, the results of $(\mathbf{U}_l^*)_x/U_r$ as a function of Da are presented in Fig. 4.14. An overall comparison is that the curves show different shapes, and under some conditions the values of $(\mathbf{U}_l^*)_x/U_r$ are negative. Unlike the curves for the case with insoluble material, which show decreasing trends in the entire studied range of Da, those for the case without insoluble material undergo more complex variations, with a marked minimum. The reaction order n only plays a role when $\mathrm{Da} > 0.01$, and the largest effect is always observed with $n = 1$.

From Eqs. 4.77 and 4.90, one observes that the ratio $(\mathbf{U}_l^*)_x/U_r$ is independent of Pe for the stratified unit cell. The evolution of $(\mathbf{U}_l^*)_x/U_r$ as a function of Pe is illustrated in Figs. 4.15 and 4.16 for the 2D and 3D geometries, respectively. For the 2D unit cells, the curves show increasing trends, with negative values when Pe is small, which agrees with Fig. 4.14. The magnitude of $(\mathbf{U}_l^*)_x/U_r$ is larger for the case with insoluble material when Pe is small, and for the case without insoluble material when Pe is large. For the 3D unit cell with or without insoluble material, the common features of all the curves are two folds: the ratio $(\mathbf{U}_l^*)_x/U_r$ is constant for small and large Pe numbers. There is a transition regime at intermediate Pe numbers, with non-monotonous behavior when passive surfaces are present within the unit cell. The curves for

$\mathrm{Da} = 1$ show very small variations with Pe, and a negligible impact of n. The curves for $\mathrm{Da} = 100$ undergo complex and significant variations, with marked minimums at intermediate Pe for the case with insoluble materials. A higher reaction order decreases significantly $(\mathbf{U}_l^*)_x / U_r$.

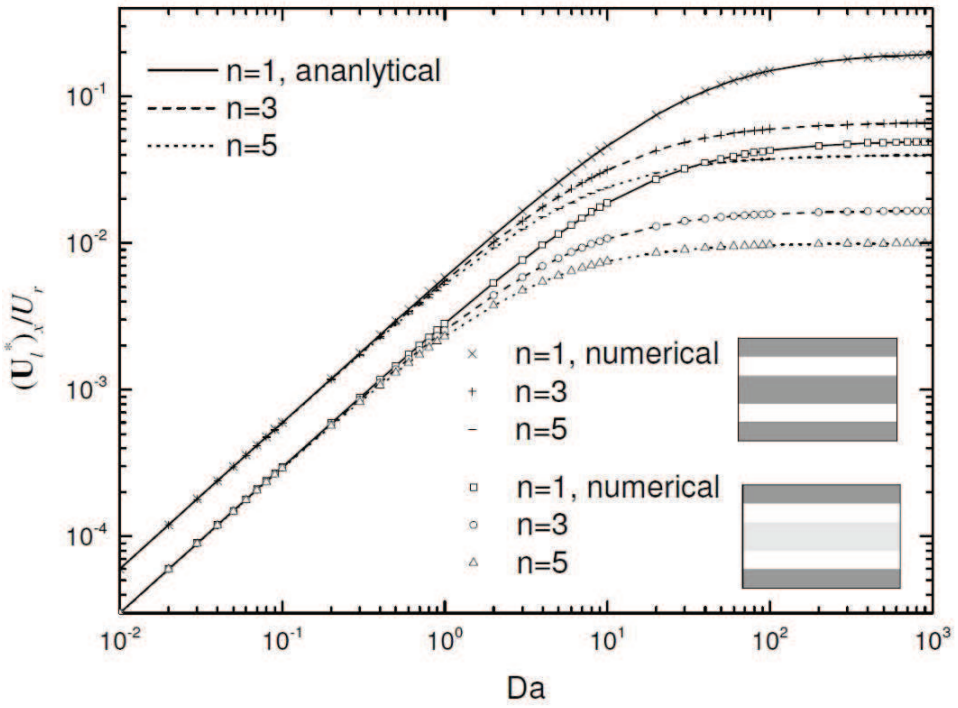

Figure 4.12: $(\mathbf{U}_l^*)_x / U_r$ as function of Da for the 1D geometries.

The second non-classical parameter to be studied is the x-component of the additional gradient term coefficient in the form of $\left(\mathbf{h}_l^*\right)_x \omega_{eq}/(k_s l_r)$, which contributes to the macro-scale mass exchange. According to analytical solution Eqs. 4.80 and 4.93 for the stratified unit cell and our numerical results for the 3D geometries, $\left(\mathbf{h}_l^*\right)_x \omega_{eq}/(k_s l_r)$ can be represented as a linear function of Pe. For the 2D geometry without insoluble material, there are some negative values for $\left(\mathbf{h}_l^*\right)_x \omega_{eq}/(k_s l_r)$ with intermediate Pe, while the positive $\left(\mathbf{h}_l^*\right)_x \omega_{eq}/(k_s l_r)$ is also proportional to Pe. The results of $\left(\mathbf{h}_l^*\right)_x \omega_{eq}/(k_s l_r)$ as a function of Da with $\mathrm{Pe} = 1$ are plotted in Figs. 4.17 and 4.18 for the 1D and 3D unit cells, respectively. It is shown that $\left(\mathbf{h}_l^*\right)_x \omega_{eq}/(k_s l_r)$ is almost a constant for small Da up to $\mathrm{Da} \approx 1$. The reaction order is important at this stage, and the linear reactive case leads to smaller magnitude of $\left(\mathbf{h}_l^*\right)_x \omega_{eq}/(k_s l_r)$ for all the geometries. After a transition zone, the values of $\left(\mathbf{h}_l^*\right)_x \omega_{eq}/(\mathrm{Pe} k_s l_r)$ become linear functions of Da. Moreover, the presence of insoluble medium has a tendency to increase $\left(\mathbf{h}_l^*\right)_x \omega_{eq}/(\mathrm{Pe} k_s l_r)$ for the 3D cases. The results of of $\left(\mathbf{h}_l^*\right)_x \omega_{eq}/(k_s l_r)$ as a function of Da with $\mathrm{Pe} = 1$ for the 2D unit cells are presented in Fig. 4.19.

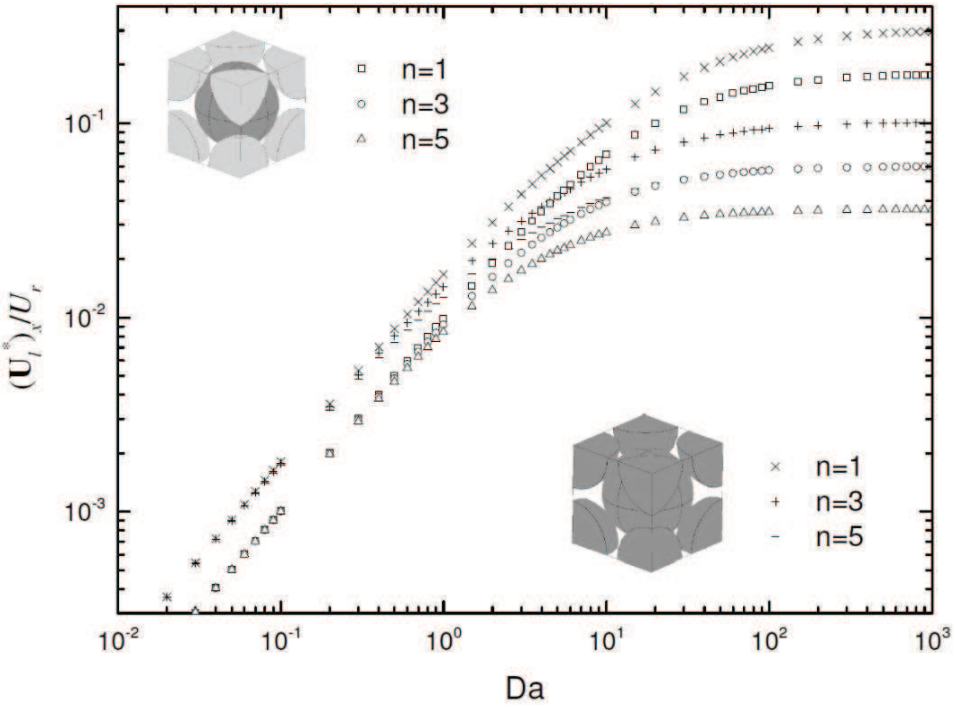

Figure 4.13: $(\mathbf{U}_l^*)_x/U_r$ as function of Da with $\mathrm{Pe}=1$ for the 3D geometries.

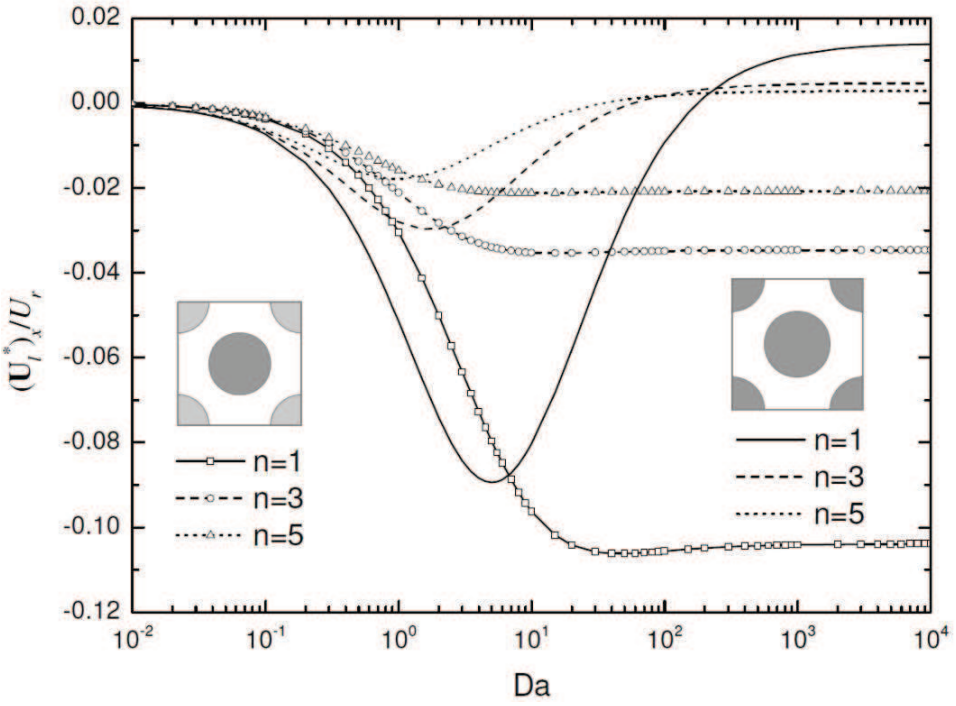

Figure 4.14: $(\mathbf{U}_l^*)_x/U_r$ as function of Da with $\mathrm{Pe}=1$ for the 2D geometries.

Once again, one sees negative values of $\left(\mathbf{h}_l^*\right)_x \omega_{eq}/(\mathrm{Pe}k_s l_r)$. Taking absolute values for the results, similar shapes of curves were obtained for the 2D geometry with three phases as the stratified and the 3D unit cells. While for the

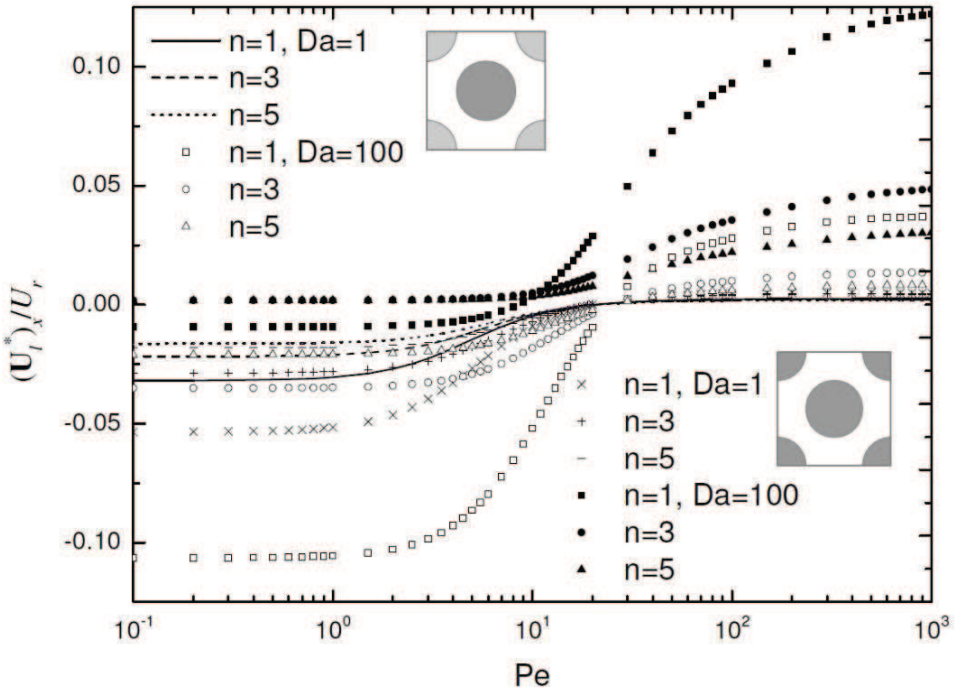

Figure 4.15: $(\mathbf{U}_l^*)_x/U_r$ as a function of Pe for the 2D unit cells.

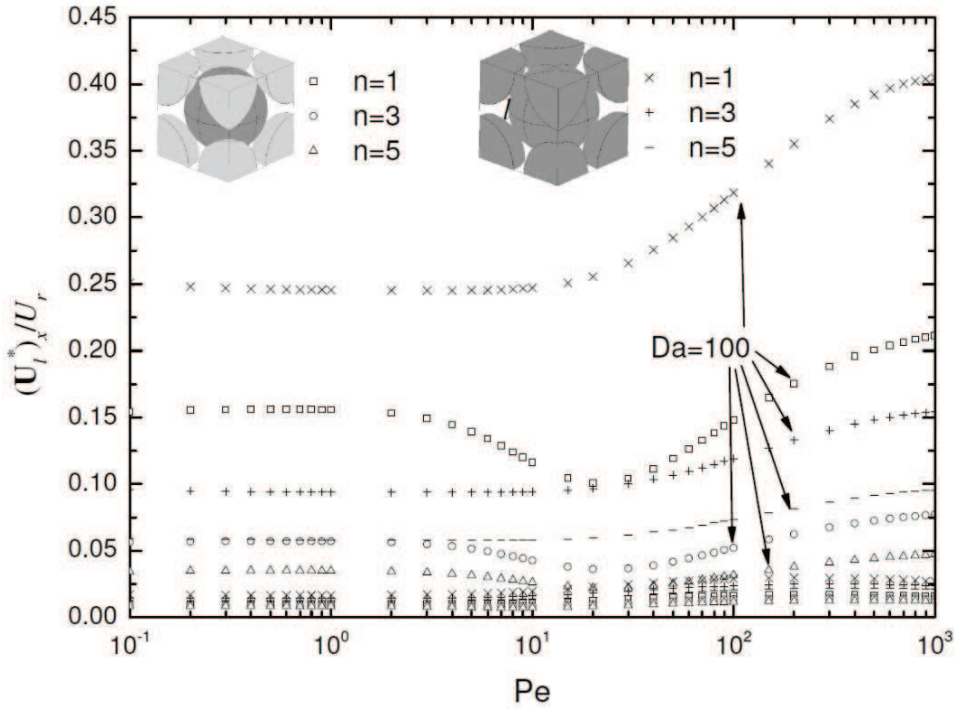

Figure 4.16: $(\mathbf{U}_l^*)_x/U_r$ as a function of Pe for the 3D unit cells, with $\mathrm{Da} = 100$ (curves indicated) and $\mathrm{Da} = 1$ (other curves).

case with only two phases, the curves are irregular with Da between 10 and 100.

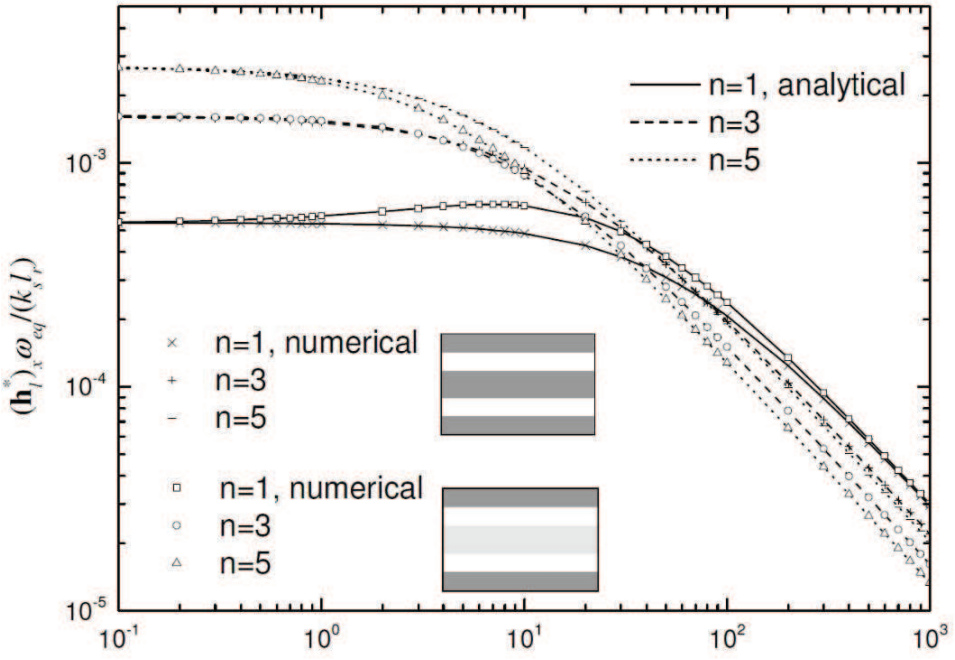

Figure 4.17: $\left(\mathbf{h}_l^*\right)_x \omega_{eq}/\left(\mathrm{Pe} k_s l_r\right)$ as a function of Da for the 1D geometries.

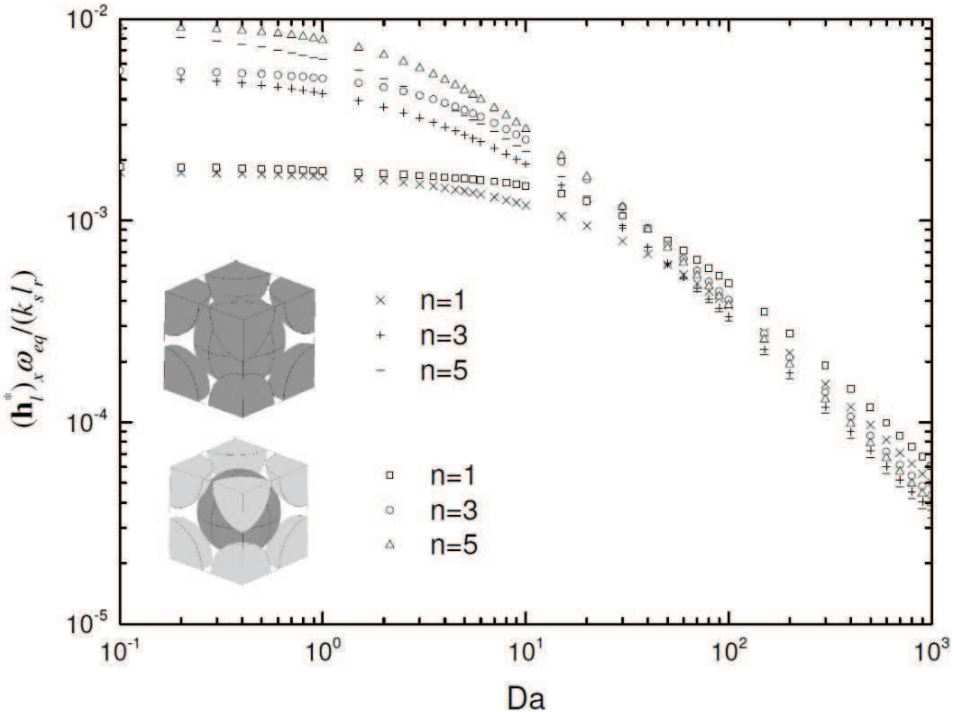

Figure 4.18: $\left(\mathbf{h}_l^*\right)_x \omega_{eq}/\left(\mathrm{Pe} k_s l_r\right)$ as a function of Da with $\mathrm{Pe} = 1$ for the 3D geometries.

So far the impact of the flow properties and chemical features on the four effective parameters has been presented. The results for $\left(\mathbf{D}_l^*\right)_{xx}/D_l$ and

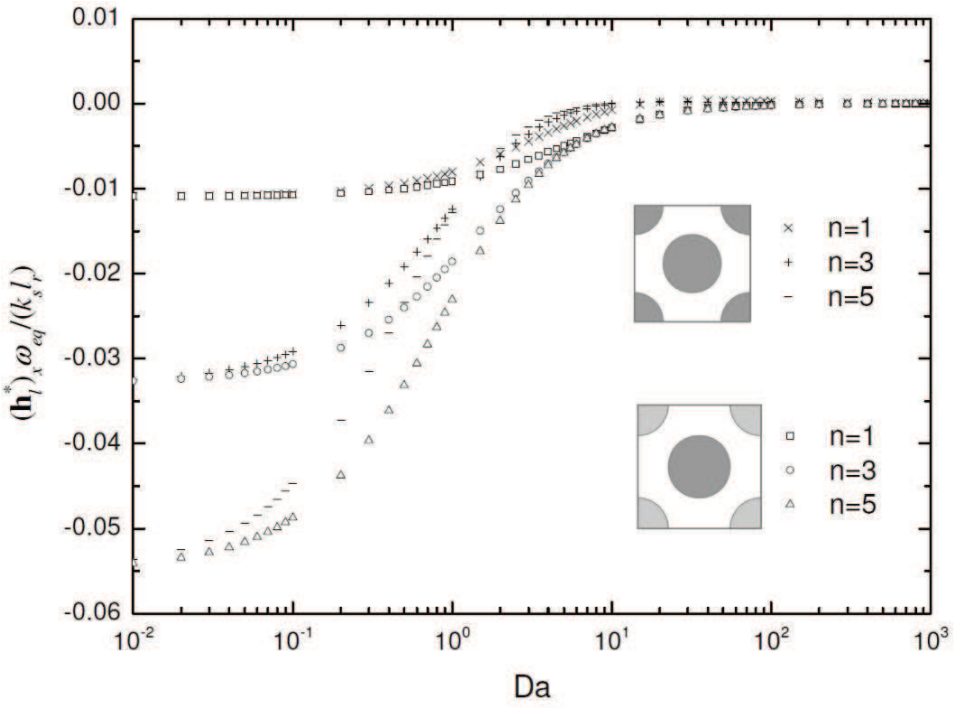

Figure 4.19: $\left(\mathbf{h}_l^*\right)_x \omega_{eq}/\left(\mathrm{Pe} k_s l_r\right)$ as a function of Da with $\mathrm{Pe}=1$ for the 2D geometries.

$k_{s,eff}/k_s$ agree well with the previous works which considered the first-order reactive case. Nonlinearity plays a significant role, similar to Da. Concerning the non-traditional items, $(\mathbf{U}_l^*)_x/U_r$ and $\left(\mathbf{h}_l^*\right)_x \omega_{eq}/(k_s l_r)$, it is clear that they are important with respect to the classical terms only under some conditions and neglecting their contributions may lead to errors when applying the macro-scale model. This point is further discussed in the next section where the macro-scale model against a reference obtained from DNS is tested.

4.4 Example of application to a macro-scale problem

In this section, the potential importance of the additional terms is further discussed based on a 1D macro-scale example. The corresponding macro-scale steady-state problem may be written in dimensionless form as

$$\begin{aligned}
&\mathrm{Pe}^*\varepsilon_l\left(U_l^{'}+U_l^{*'}\left(\left\langle\omega_l^{'}\right\rangle^l\right)\right)\frac{\partial\left\langle\omega_l^{'}\right\rangle^l}{\partial x^{'}}+\mathrm{Pe}^*\varepsilon_l\left(\left\langle\omega_l^{'}\right\rangle^l-\omega_{eq}^{'}\right)\frac{\partial U_l^{*'}\left(\left\langle\omega_l^{'}\right\rangle^l\right)}{\partial x^{'}}\\
&=-\left(-\frac{k_{s,eff}\left(\left\langle\omega_l^{'}\right\rangle^l\right)}{k_s}\left(1-\frac{\left\langle\omega_l^{'}\right\rangle^l}{\omega_{eq}^{'}}\right)+h_l^{*'}\left(\left\langle\omega_l^{'}\right\rangle^l\right)\frac{\partial\left\langle\omega_l^{'}\right\rangle^l}{\partial x^{'}}\right)\mathrm{Da}^*\left(\left\langle\omega_l^{'}\right\rangle^l\right)\\
&\qquad+\varepsilon_l\frac{\partial}{\partial x^{'}}\left(\frac{D_l^*\left(\left\langle\omega_l^{'}\right\rangle^l\right)}{D_r}\frac{\partial\left\langle\omega_l^{'}\right\rangle^l}{\partial x^{'}}\right) \qquad (4.96)
\end{aligned}$$

with the dimensionless numbers defined as

$$\begin{aligned}
\mathrm{Pe}^*=\tfrac{U_rL_r}{D_r}\ ,\ U_l^{'}=\tfrac{U_l}{U_r}\ ,\ U_l^{*'}\left(\left\langle\omega_l^{'}\right\rangle^l\right)=\tfrac{U_l^*}{U_r}\ ,\\
\left\langle\omega_l^{'}\right\rangle^l=\tfrac{\langle\omega_l\rangle^l}{\omega_{eq}},\ x'=\tfrac{x}{L_r}\ ,\ \omega_{eq}^{'}=\tfrac{\omega_{eq}}{\omega_{eq}}=1,\\
h_l^{*'}\left(\left\langle\omega_l^{'}\right\rangle^l\right)=\tfrac{h_l^*\omega_{eq}}{L_rk_s},\ \mathrm{Da}^*\left(\left\langle\omega_l^{'}\right\rangle^l\right)=\tfrac{a_{vl}^{'}M_{Ca}}{\rho_l\omega_{eq}}\tfrac{L_rk_s}{D_r}\left(1-\frac{\left\langle\omega_l^{'}\right\rangle^l}{\omega_{eq}^{'}}\right)^{n-1}\ , \qquad (4.97)
\end{aligned}$$

where L_r is the macro-scale characteristic length and D_r can be the molecular diffusion coefficient or alternatively the maximum dispersion coefficient, depending on the problem of interest. It must be emphasized that $\mathrm{Da}^*\left(\left\langle\omega_l^{'}\right\rangle^l\right)$ is not a constant in the nonlinear reactive cases and is dependent on the mass fraction distribution. Since closure problems depend on parameter Da, the effective parameters $D_l^*\left(\left\langle\omega_l^{'}\right\rangle^l\right)$, $U_l^{*'}\left(\left\langle\omega_l^{'}\right\rangle^l\right)$, $k_{s,eff}\left(\left\langle\omega_l^{'}\right\rangle^l\right)$ and $h_l^{*'}\left(\left\langle\omega_l^{'}\right\rangle^l\right)$ are also dependent on the distribution of mass fraction accordingly in the nonlinear reactive cases.

When taking $D_r=max\left(D_l^*\left(\left\langle\omega_l^{'}\right\rangle^l\right)\right)$ and $U_r=\langle u_l\rangle^l$, the mass transport by dispersion is small compared to that by convection in the case of large Pe*. Therefore, Eq. 4.96 can be simplified into

$$\mathrm{Pe}^*\varepsilon_l \frac{\partial \left\langle \omega_l' \right\rangle^l}{\partial x'} \approx \underbrace{\frac{\frac{k_{s,eff}\left(\left\langle \omega_l' \right\rangle^l\right)}{k_s}\mathrm{Da}^*\left(\left\langle \omega_l' \right\rangle^l\right)}{\left(1+U_l^{*'}\left(\left\langle \omega_l' \right\rangle^l\right)+\frac{h_l^{*'}\left(\left\langle \omega_l' \right\rangle^l\right)\mathrm{Da}^*\left(\left\langle \omega_l' \right\rangle^l\right)}{\mathrm{Pe}^*\varepsilon_l}\right)}}_{\text{apparent reactive term}} \left(1-\frac{\left\langle \omega_l' \right\rangle^l}{\omega_{eq}'}\right). \tag{4.98}$$

Even though the full Eq. 4.96 was employed in the actual computations, this simplified form is interesting since it shows that additional terms may be incorporated in an apparent reactive term, as suggested in [166]. Let us introduce $H\left(\left\langle \omega_l' \right\rangle^l\right) = h_l^{*'}\left(\left\langle \omega_l' \right\rangle^l\right)\mathrm{Da}^*\left(\left\langle \omega_l' \right\rangle^l\right)/\left(\mathrm{Pe}^*\varepsilon_l\right)$. To investigate the contributions of the non traditional terms $U_l^{*'}\left(\left\langle \omega_l' \right\rangle^l\right)$ and $H\left(\left\langle \omega_l' \right\rangle^l\right)$ to the apparent reactive term, the closure problems were solved for a 2D representative unit cell which contains only the l and s phases (cf. Fig. 4.20a), as well as for the 3D representative unit cell containing the three phases as illustrated in Fig. 4.1e. The location in the (Pe, Da) plane of points having the property $U_l^{*'}\left(\left\langle \omega_l' \right\rangle^l\right) = 0.05$ and $H\left(\left\langle \omega_l' \right\rangle^l\right) = 0.05$ are plotted in Figs. 4.21a and 4.21b for the 2D and 3D geometries, respectively, and for different reaction orders. In the regions above the curves, here at large Pe and Da, the magnitudes of $U_l^{*'}\left(\left\langle \omega_l' \right\rangle^l\right)$ and $H\left(\left\langle \omega_l' \right\rangle^l\right)$ are larger than 0.05. Therefore, this map can be used to estimate regions for which the additional terms may play a role. All the curves arrive at a plateau when Pe is relatively large, and the values of $U_l^{*'}\left(\left\langle \omega_l' \right\rangle^l\right)$ and $H\left(\left\langle \omega_l' \right\rangle^l\right)$ are mainly determined by Da and n under such circumstances. The curves for $U_l^{*'}\left(\left\langle \omega_l' \right\rangle^l\right)$ with $n = 5$ are not present because $U_l^{*'}\left(\left\langle \omega_l' \right\rangle^l\right)$ is always smaller than 0.05 in the studied range. Typically, the additional coefficients may be important for relatively large Pe and small Da, and have a strong impact on the *apparent* nonlinear reaction rate coefficient. This impact is much stronger for the 3D geometry than for the 2D geometry in the case of small Da, as observed in Figs. 4.21a and 4.21b.

To test these ideas the pore-scale equations (later referred to as DNS) were solved for case I illustrated by Fig. 4.20a, composed of 65 periodic elements arranged along the x-direction with all the solid phase soluble, and in case II corresponding to the geometry depicted in Fig. 4.20b, containing insoluble materials. The pore-scale problem introduced in Chap. 2 was transformed into dimensionless form, with the diameter of the circles as the characteristic

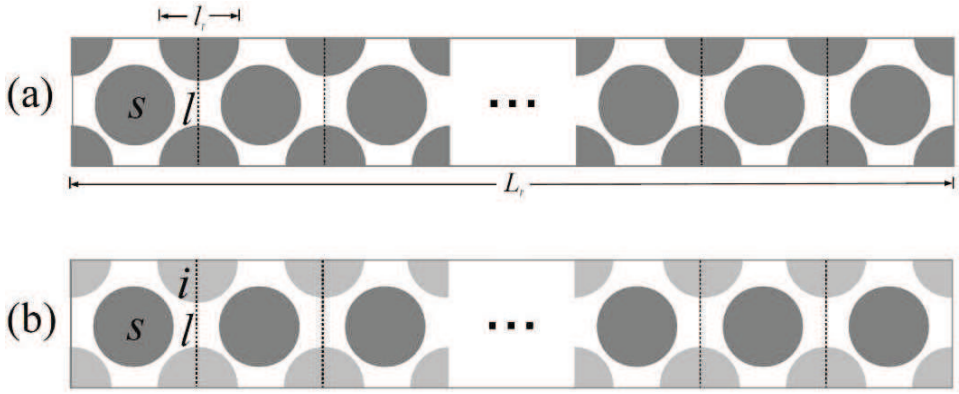

Figure 4.20: 2D geometries for the DNS: (a) without insoluble material; (b) with insoluble material.

length. The corresponding boundary conditions at the entrance and the exit were $\omega_l^{'} = 0$ and convective conditions, respectively. The Navier-Stokes equations were solved with low Reynolds number to get a periodic velocity field of constant average velocity. The corresponding macro-scale problem is 1D, i.e., a line along the x-direction with the same length as the 2D geometry, L_r. For case I, a significant impact of the additional terms with $n = 3$ was observed successfully. In the nonlinear reactive case, since Da is a function of the mass fraction, its value decreased quickly along the x-direction due to the mass fraction distribution. For case II it was difficult to keep a relatively large Da to see the impact of the additional non-classical terms and hence the linear reactive case was chosen as an example. Since the mass fraction disappears in the definition of Da for a linear reactive case, $H\left(\left\langle\omega_l^{'}\right\rangle^l\right)$ and $U_l^{*'}\left(\left\langle\omega_l^{'}\right\rangle^l\right)$ become constant independent of $\left\langle\omega_l^{'}\right\rangle^l$ denoted H and $U_l^{*'}$. A large Pe and a proper Da were used to study the impact of the non-classical terms, avoiding too large Da, because in such circumstances the pore-scale boundary condition would be close to the one of thermodynamic equilibrium. Numerical simulations for both the DNS and the macro-scale model were performed with COMSOL®.

Let us estimate a reactive coefficient for the DNS results using the following definition

$$\alpha_{DNS} = \frac{\frac{1}{V^{'}}\int_{ls}\mathbf{n}_{ls}\cdot\rho_l^{'}D_l^{'}\nabla^{'}\omega_l^{'}dA^{'}}{\left(1-\frac{\left\langle\omega_l^{'}\right\rangle^l}{\omega_{eq}^{'}}\right)}, \tag{4.99}$$

and computed at the centroid of each unit cell. The fact of not using very large Da ensured that $1-\frac{\left\langle\omega_l^{'}\right\rangle^l}{\omega_{eq}^{'}} \neq 0$ to avoid any numerical problem in estimating

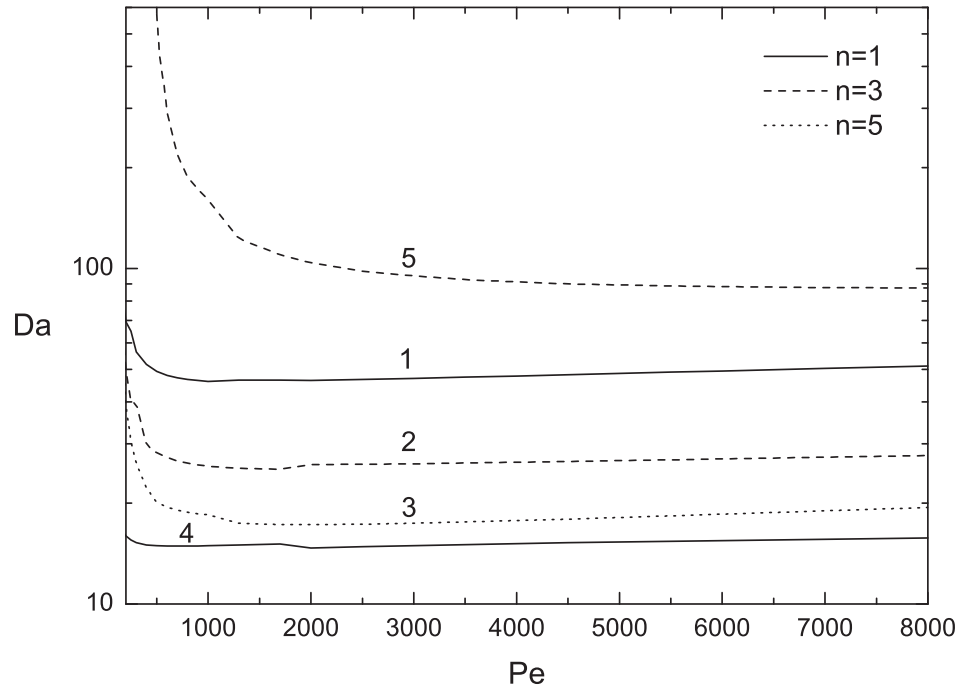

(a)

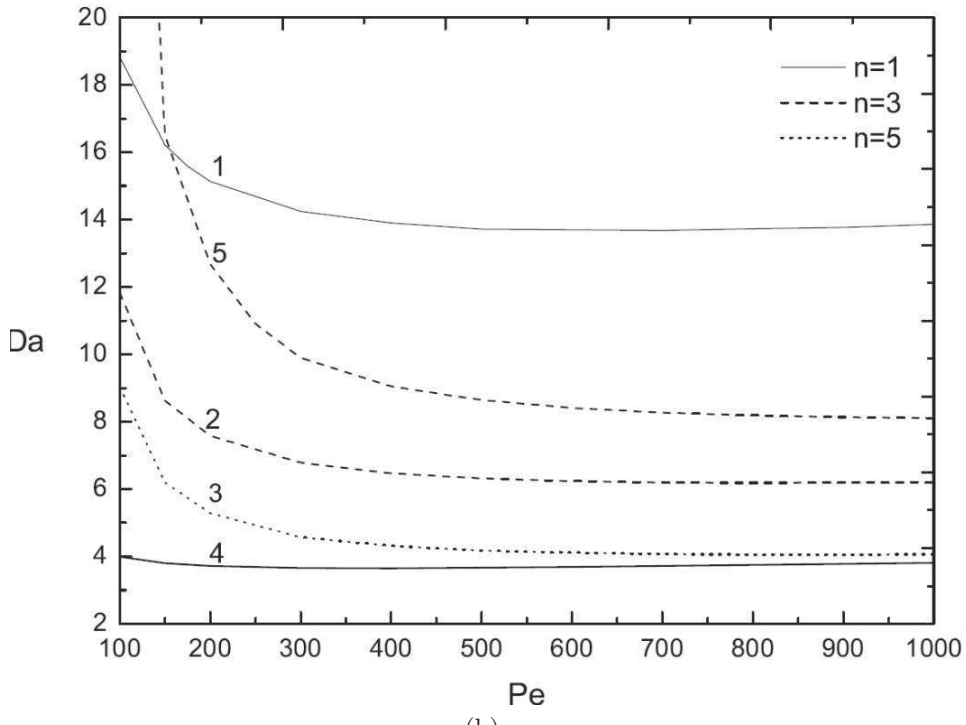

(b)

Figure 4.21: Pe-Da diagram for $U_l^{*'}\left(\left\langle\omega_l'\right\rangle^l\right) = 0.05$ (curves 4 and 5) and $H\left(\left\langle\omega_l'\right\rangle^l\right) = 0.05$ (curves 1, 2 and 3): (a) for the 2D unit cell without insoluble case; (b) for the 3D unit cell with insoluble material.

α_{DNS}. The results of α_{DNS} were compared with the apparent reactive term estimated in Eq. 4.98 for the macro-scale model. Four cases were tested with different non-traditional effective parameters taken into account: the apparent reactive term α_{L1} was obtained by solving the macro-scale equation with both $H\left(\left\langle\omega_l^{'}\right\rangle^l\right)$ and $U_l^{*'}\left(\left\langle\omega_l^{'}\right\rangle^l\right)$, α_{L2} without $H\left(\left\langle\omega_l^{'}\right\rangle^l\right)$, α_{L3} without $U_l^{*'}\left(\left\langle\omega_l^{'}\right\rangle^l\right)$ and α_{L4} without $H\left(\left\langle\omega_l^{'}\right\rangle^l\right)$ and $U_l^{*'}\left(\left\langle\omega_l^{'}\right\rangle^l\right)$. For case I, the results are only presented for regions far from the entrance region, as illustrated in Fig. 4.22a. The reactive coefficients decrease along the x-axis because they are dependent on the mass fraction field. Considering the non-traditional effective properties improved the results and the best results were obtained by considering all the effective properties, including $H\left(\left\langle\omega_l^{'}\right\rangle^l\right)$ and $U_l^{*'}\left(\left\langle\omega_l^{'}\right\rangle^l\right)$. It must be pointed out that, in this nonlinear case, two errors are accumulated. First, dispersion terms are not entirely controlled by the assigned value of the Pe number because of nonlinearities in the effective dispersion tensor. In our case they induce a minor but visible effect of about a few percent over the estimated DNS reaction rate. Furthermore, because of the entrance region effect, the macro-scale concentration field lags a little bit behind the DNS value, which in turn impacts the estimation of the effective exchange rate. Improving the solution would require the introduction of a non-local theory taking care of the entrance region effect. From the results presented in Fig. 4.22b for case II, one observes a relatively large discrepancy in the entrance region, which may be attributed to the fact that the periodic assumption for the upscaling breaks down in this area. This would call for a specific non-local treatment, which is beyond the scope of this study. But in the regions with an *established regime*, materialized by a constant α_{DNS}, the relative errors become very small and, among the four choices, α_{L4} gives the worst results, while the results are improved by taking into consideration the non-traditional parameters. Nevertheless, our results emphasize the importance of the additional terms in order to recover the correct mass exchange in the established regime, as was emphasized in [166] for a simpler flow problem and the case of thermodynamic equilibrium.

4.5 Conclusion

The upscaling of a mass transport problem involving a nonlinear heterogeneous reaction typical of dissolution problems has been carried out using a first order Taylor expansion for the reaction rate when developing the equations for

the concentration deviation. A full model including all couplings and the interface velocity has been obtained. Several limiting cases have been developed emphasizing the coherence of the proposed theory with results available in the literature for these limiting cases, the only difference being due to some additional coupling terms, which, however, may correct the estimated effective reaction rate by tenths of percent.

The closure problems providing the effective properties have been solved analytically for a stratified unit cell and numerically for the stratified, 2D and 3D unit cells with a quasi-steady approximation. Effects of the pore-scale Damköhler and Péclet number were investigated, as well as the impact of the coefficient n appearing in the nonlinear reaction rate. The influence of the proportion of insoluble material was studied by comparing the 3D cases with the solid phase completely soluble or partially insoluble. Results for the classical effective properties such as dispersion coefficient and effective reaction rates are compatible with previous findings on active dispersion. In particular, tortuosity and dispersion effects becomes smaller when the Damköhler number increases, due to the homogenization of concentration at the interface. The nonlinear reaction rate coefficient tends to increase the impact of Da. The behavior of the non-traditional terms that appear in the development has been investigated based on comparisons between DNS of the pore-scale equations and macro-scale results. It was shown that they may play a role for large Pe and small Da, at least for the simple unit cells considered in this study. This latter aspect deserves more investigation in terms of parameter range, complexity of the representative unit cell, form of the nonlinear reaction rate, etc.

The framework developed in this study is applicable to simulate dissolution process in various research areas, for instance in the evolution of karstic structures, CO_2 storage and in the application of acid injection in petroleum wells to improve oil recovery. The development was based on a bundle of assumptions, such as constant fluid parameters, negligible interface velocity, pseudo component for the dissolved material, etc. Also, the calculations of effective parameters in the applications provided were not based on an actual dissolved pore-scale geometry. Real conditions are much more complicated so great attention should be paid where such assumptions may break down. For example, the dissolution of the porous matrix may lead to significant variation of porosity and consequently permeability and other effective parameters. In addition, the dissolving front may become unstable and may lead to the development of

wormhole structures. Under some circumstances, hydrodynamic instabilities may also be induced by density change, such as in the case of salt dissolution in water. It is beyond the scope of this conclusion to review all the perspectives associated with these questions. Concerning the coupling with the pore-scale geometry evolution, if one is not satisfied with the geochemistry assumption, i.e., dependence of the effective parameters on the porosity, our developments offer a framework for a coupled solution between the macro-scale equation, on one hand, and the pore-scale closure problems under the full version including the transient aspects, on the other hand.

More coupling and nonlinear effects can be introduced in the development, such as variation of fluid properties and reaction rate with concentration, more complicated geochemistry, etc. We believe that the idea of first-order corrections at the closure level can be extended to such cases, of course at the expense of some additional complexity.

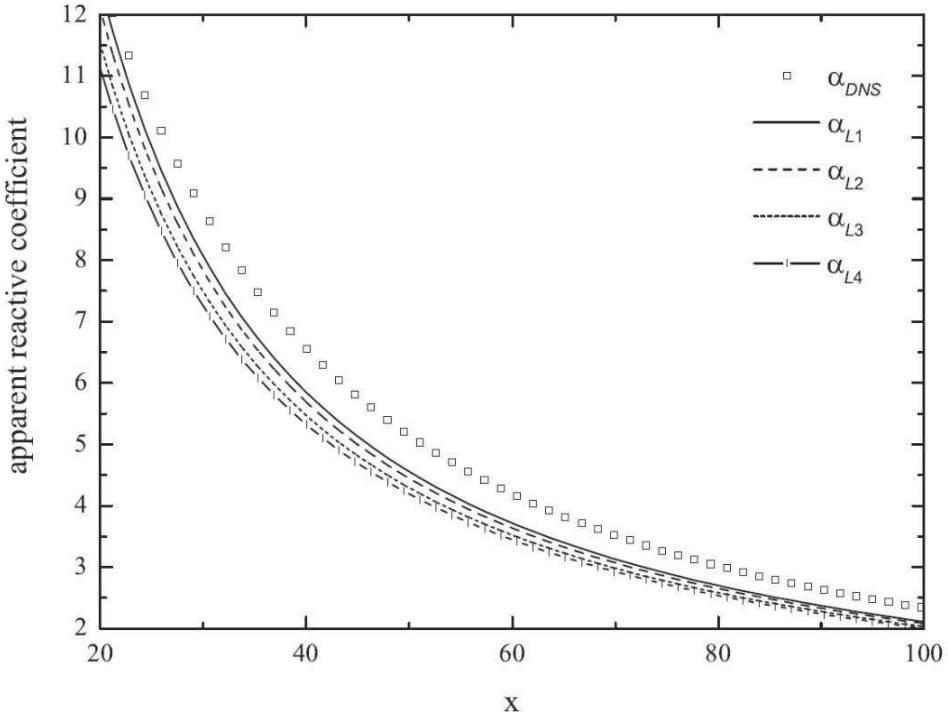

(a)

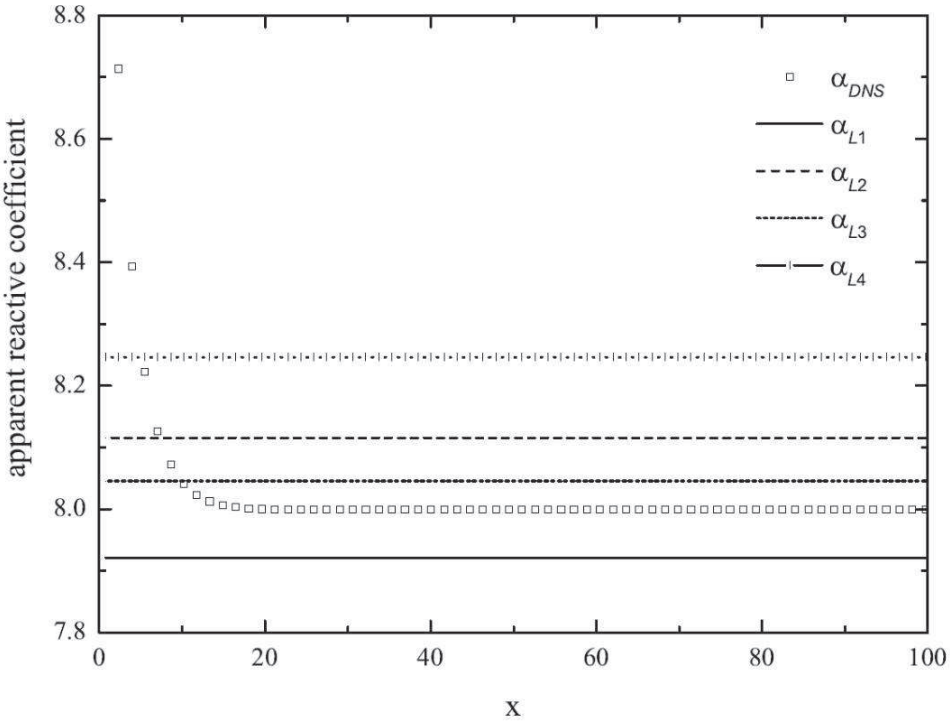

(b)

Figure 4.22: Comparison of apparent reactive term between DNS and the macro-scale model: (a) for case I (nonlinear reactive order $n = 3$ without insoluble material) with Pe =1000 and $\mathrm{Da}\big|_{\left\langle \omega_l' \right\rangle^l = 0} = 80$; (b) for case II (linear reactive case with insoluble material) with $\mathrm{Pe} = 1000$ and $\mathrm{Da} = 10$.

Chapter 5

A framework for the modeling of gypsum cavity dissolution within geomechanical studies

5.1 Introduction

Given the research background about dissolution models, the objective set in this chapter is a discussion about the modeling workflow for large-scale (decametric scales) dissolution problems representative of situations which may be encountered in the geotechnical or geomechanical fields. Sinkholes are examples among others. While the quantitative conclusions presented in this study are specific to the gypsum case, the methodology may be reproduced for salt or carbonate dissolution problems.

According to the discussion in Chap. 2, the approximation of an equilibrium boundary condition at the solid-liquid interface seems suitable. Based on this assumption, a macro-scale non-equilibrium model can be built, for instance using the method of volume averaging [10, 120, 163] as presented in Chap. 4.

Before introducing the 3D large-scale model for gypsum dissolution, the dissolution model was applied to two large-scale different cases in Sec. 5.2, the first corresponding to a porous gypsum formation, the second to an impermeable solid. This allowed to discuss several important modeling questions: the choice of appropriate DIM parameters, alternative choices of momentum equations, etc. In section 5.3, results for two 3D problems are presented in order to show the potentialities of the method. Two dissolution configurations were studied, one corresponding to an isolated pillar in a flooded gypsum quarry

and the other one to a gypsum lens contained within a porous rocks layer. These configurations are typical of problems often encountered in reality [7]. Geomechanical consequences (in terms of mechanical stability) of the dissolution process as evaluated using a simplified geomechanical model are presented. The simple approach considers only the effects induced by the shape change due to the leaching process, thus avoiding the need for a complete chemico-hydro-mechanical coupling as proposed by [183, 184], taking into account the changes in the constitutive models of the porous matrix. The proposed approach is complementary to current couplings [185, 186] which considers only fixed domains, while with constitutive models often depending on complex chemical processes [187]. Finally, a comparison on the same boundary value problem of the dissolution rate and the form of the cavity obtained considering gypsum or salt is presented.

5.2 Cavity formation computation

5.2.1 Description of the problem

The geometry of the studied porous medium is schematically illustrated in Fig. 5.1. The 2D domain contains a subdomain d made of three phases at the pore-scale level: two solid phases, one being soluble gypsum (s-phase), the other being insoluble material (i-phase), and a liquid phase (l-phase) which contains water and the dissolved gypsum. Subdomains a and e are only composed of the liquid phase and the insoluble solid phase, with different permeabilities and porosities. With the injection of a fluid (fresh water in this study) from the left boundary of subdomain a at a filtration velocity V_0 in the x-direction, the solid gypsum contained in subdomain d will be dissolved gradually and finally create a cavity. This geometry is typical of a case where dissolution may induce mechanisms such as subsidence or collapse which may lead to sinkhole formation, depending on the size and shape of the cavity.

The notation Ω_l is used to represent the Darcy-scale mass fraction of Ca^{2+}, $\mathbf{D}_l$ the dispersion tensor, $\mathbf{V}_l$ the Darcy velocity, S_l the fluid saturation with $S_l = \varepsilon_l/\varepsilon$, S_s the solid gypsum saturation with $S_s = \varepsilon_s/\varepsilon$, with ε_l and ε_s representing the volume fraction of the fluid and the solid gypsum, respectively. We also have $\varepsilon_l + \varepsilon_s = \varepsilon$ and $\varepsilon + \varepsilon_i = 1$, with ε_i denoting the volume fraction of the insoluble material. The DIM mass transport equations in the studied domain are summarized here:

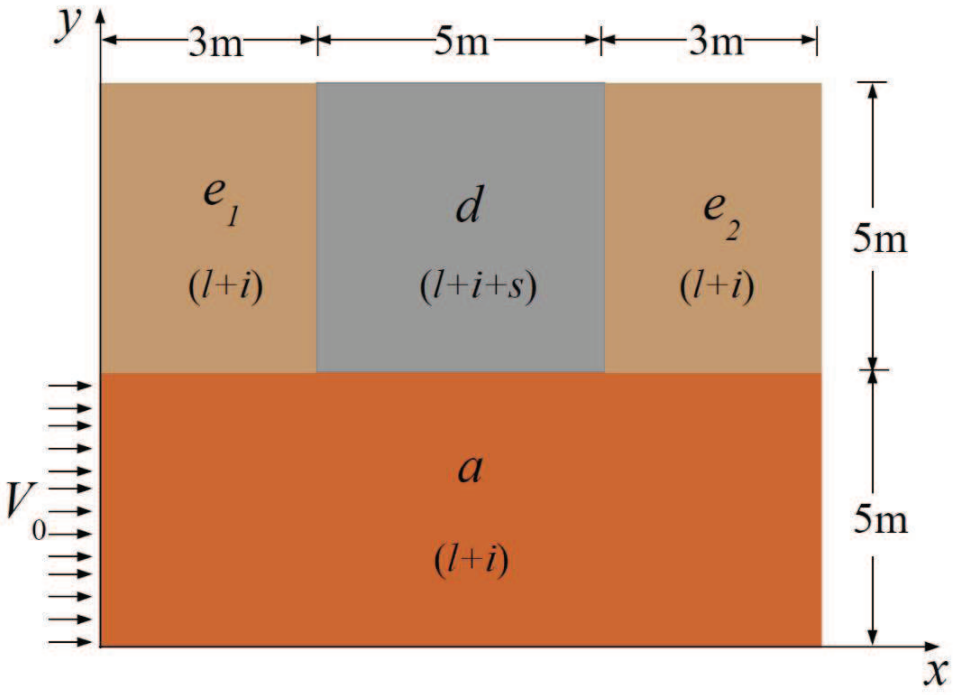

Figure 5.1: Schematic description of large-scale cavity dissolution problem at Darcy-scale.

$$\frac{\partial \varepsilon \rho_s S_s}{\partial t} = K_g, \tag{5.1}$$

$$\frac{\partial \rho_l \varepsilon S_l}{\partial t} + \nabla \cdot (\rho_l \mathbf{V}_l) = -K_g, \tag{5.2}$$

$$\frac{\partial \rho_l \Omega_l \varepsilon S_l}{\partial t} + \nabla \cdot (\rho_l \Omega_l \mathbf{V}_l) = \nabla \cdot (\varepsilon S_l \rho_l \mathbf{D}_l \cdot \nabla \Omega_l) - K_{Ca}. \tag{5.3}$$

In the local non-equilibrium macro-scale model, the mass exchange of calcium is estimated as a first-order expression in terms of the concentration difference $(\Omega_l - \omega_{eq})$, i.e.,

$$K_{Ca} = \frac{M_{Ca}}{M_g} K_g = \rho_l \alpha \left(\Omega_l - \omega_{eq}\right), \tag{5.4}$$

with K_g denoting the mass exchange of gypsum, K_{Ca} the mass exchange of Ca and α the corresponding mass exchange coefficient. The components of the dispersion tensor could be obtained from the closure problems for a given shape of the representative unit cell of the porous medium, as done in Chap. 4. However, this is not done here while the classical linear dispersion model is used. Hence, the dispersion tensor is written as [188]

$$\mathbf{D}_l = \frac{D_0}{\tau_l}\boldsymbol{I} + \alpha_T \frac{\|\mathbf{V}_l\|}{\varepsilon S_l}\boldsymbol{I} + (\alpha_L - \alpha_T)\frac{\mathbf{V}_l\mathbf{V}_l}{\|\mathbf{V}_l\|\varepsilon S_l}, \tag{5.5}$$

where the tortuosity, τ_l, the longitudinal, α_L, and transversal, α_T, dispersivities depend on the pore-scale geometry.

Regarding the momentum equations, three approaches may be used as discussed in [119, 120]: (i) Stokes equations and Darcy's law in the fluid and the porous domain, respectively; (ii) a continuous formulation such as Darcy-Brinkman equation in the entire domain; and (iii) Darcy's law in both the fluid and the porous domains. In this present study, since dissolution may lead to a true cavity without any solid phase, a modified version of the Navier-Stokes equation may be used in this dissolved region reminiscent of the Darcy-Brinkman equation

$$\frac{\partial \rho_l \mathbf{V}_l}{\partial t} + \rho_l \mathbf{V}_l \cdot \nabla \mathbf{V}_l = -(\nabla P_l - \rho_l \mathbf{g}) + \mu_l^* \nabla^2 \mathbf{V}_l - \mu_l \mathbf{K}_l^{-1} \cdot \mathbf{V}_l, \tag{5.6}$$

where μ_l^* is the so-called effective viscosity of the fluid, depending on the porous medium property. In general, μ_l^* is heterogeneous due to the large spatial variations of material properties within the domain, however, in practice it is often assumed that the effective viscosity is homogeneous and equals to μ_l for simplification [189]. If local Reynolds number is small, which is the case in this present study, the inertia effects are negligible, and Eq. 5.6 turns out to be the Darcy-Brinkman equation

$$-(\nabla P_l - \rho_l \mathbf{g}) + \mu_l^* \nabla^2 \mathbf{V}_l - \mu_l \mathbf{K}_l^{-1} \cdot \mathbf{V}_l = 0, \tag{5.7}$$

which was also successfully used in [10]. When the permeability tends to infinity the equation simplifies to Stokes equation, i.e.,

$$-(\nabla P_l - \rho_l \mathbf{g}) + \mu_l^* \nabla^2 \mathbf{V}_l = 0, \tag{5.8}$$

and when the permeability is small enough Darcy's equation is recovered

$$\mathbf{V}_l = -\frac{\mathbf{K}_l}{\mu_l} \cdot (\nabla P_l - \rho_l \mathbf{g}). \tag{5.9}$$

Combining Eqs. 5.1 and 5.2 gives

$$\nabla \cdot \mathbf{V}_l = -K_g \left(\frac{1}{\rho_l} - \frac{1}{\rho_s}\right) \tag{5.10}$$

The transport problems are in the same form for all the subdomains except that for subdomains a and e one has

$$K_{Ca} = K_g = 0, \quad \rho_s = 0 \quad \text{and} \quad \varepsilon_s = S_s = 0. \tag{5.11}$$

5.2.2 Case I - subdomain d as a porous medium

Numerical simulations were carried out employing the porous medium model described above. The parameters used are given in Table 5.1. In addition, the dispersivities are negligible compared to the effective diffusion coefficient when the pore-scale Péclet number is small, which is the case when $V_0 = 10^{-6}\,\mathrm{m\,s^{-1}}$. Therefore, the effective diffusion tensor for each subdomain is written without dispersivity, with different tortuosity in the subdomains as given in Table 5.1. The mass exchange coefficient is estimated as $\alpha = \alpha_0 S_s$, which is a function of the solid gypsum saturation. Different values for α_0 are tested in order to investigate the impact on the dissolution process and try to recover thermodynamic equilibrium at the dissolving surface. As illustrated in Table 5.1, the permeability in subdomain d, as a function of S_s, is higher than the surrounding porous media and the initial solid gypsum saturation is not very large, the fluid is therefore able to penetrate into the porous region of subdomain d. Since the permeabilities are small enough so the Darcy term overcomes the viscous and inertia terms, Darcy's law was used everywhere as the momentum balance equation.

In the cavity evolution simulations with the porous medium model, the dissolving interface between the fluid and the virgin porous medium has a finite thickness, which is dependent on α. A sharp interface is obtained when α tends to infinity, which is most of the time difficult to achieve due to the high computational costs. In the next section, the interface position is arbitrarily defined at $\frac{S_s}{S_{initial}} = 0.9$.

The simulation results regarding the mass fraction and fluid velocity fields are presented in Fig. 5.2. It can be observed from these figures that, with the continuous inlet of fresh (pure) water, the cavity grows very fast at the entrance region of subdomain d. With increasing mass fraction of the dissolved species from the entrance region to the exit region, the mass fraction gradient near the liquid-porous medium interface becomes smaller accordingly. The dissolution velocity is therefore becoming slower in the exit region, which explains the obtained cavity geometry. Considering the impact of α and V_0, when V_0 is set a constant, the variation of α_0 will affect both the thickness of the dissolution

Table 5.1: Geometric features and physical properties of the phases.

Parameters	Value	Description
D_0 ($m^2 s^{-1}$)	10^{-9}	diffusion coefficient
K_l (m^2)	10^{-12}	permeability for subdomains a
	10^{-15}	permeability for subdomains e
	$K_0 \varepsilon S_l$ with $K_0 = 10^{-11}$	permeability for subdomain d
$S_{initial}$	0	initial solid gypsum saturation in subdomains a and e
	0.75	in subdomain d
V_0($m s^{-1}$)	10^{-6}	inlet velocity
ε	0.35	porosity for subdomains a
	0.2	porosity for subdomains e
	0.9	porosity for subdomain d
τ_l	2	tortuosity of subdomains a
	1.8	tortuosity of subdomains e
	3	tortuosity of subdomains d

front (interface) and the dissolution rate (Fig. 5.2a to Fig. 5.2c). In the cases with $\alpha_0 = 10^{-7} s^{-1}$ and $\alpha_0 = 10^{-6} s^{-1}$, the fronts are highly diffusive and a cavity hardly develops. When α_0 is kept unchanged, on one hand, an increase of V_0 will accelerate the enlargement of the cavity (Fig. 5.2c to Fig. 5.2e). On the other hand, a smaller inlet velocity, which is equivalent to a longer residual time, enables more water to flow into subdomain d. These results are further illustrated in Fig. 5.3 representing the ratio $\frac{S_s}{S_{initial}}$ along the diagonal of subdomain d from the lower left corner to the upper right corner. It is more clear in this figure that with $\alpha_0 = 10^{-5}$ s^{-1}, a true cavity may develop corresponding to $\frac{S_s}{S_{initial}} \to 0$. With smaller α_0, the region where dissolution takes place remains porous. The smallest ratio of $\frac{S_s}{S_{initial}}$ is about 0.32 and 0.88 for $\alpha_0 = 10^{-6}$ s^{-1} and $\alpha_0 = 10^{-7}$ s^{-1} respectively.

5.2.3 Case II- subdomain d as a quasi-solid

The dissolution of a solid domain (as materialized in the model by a very low permeability) is studied in this subsection. This configuration is closer to a leaching process and the dynamics of the phenomenon is very different from the dissolution of a porous medium. In this case, the saturation of the solid gypsum in subdomain d is increased to a high value, typically $S_{initial} = 0.9$. As

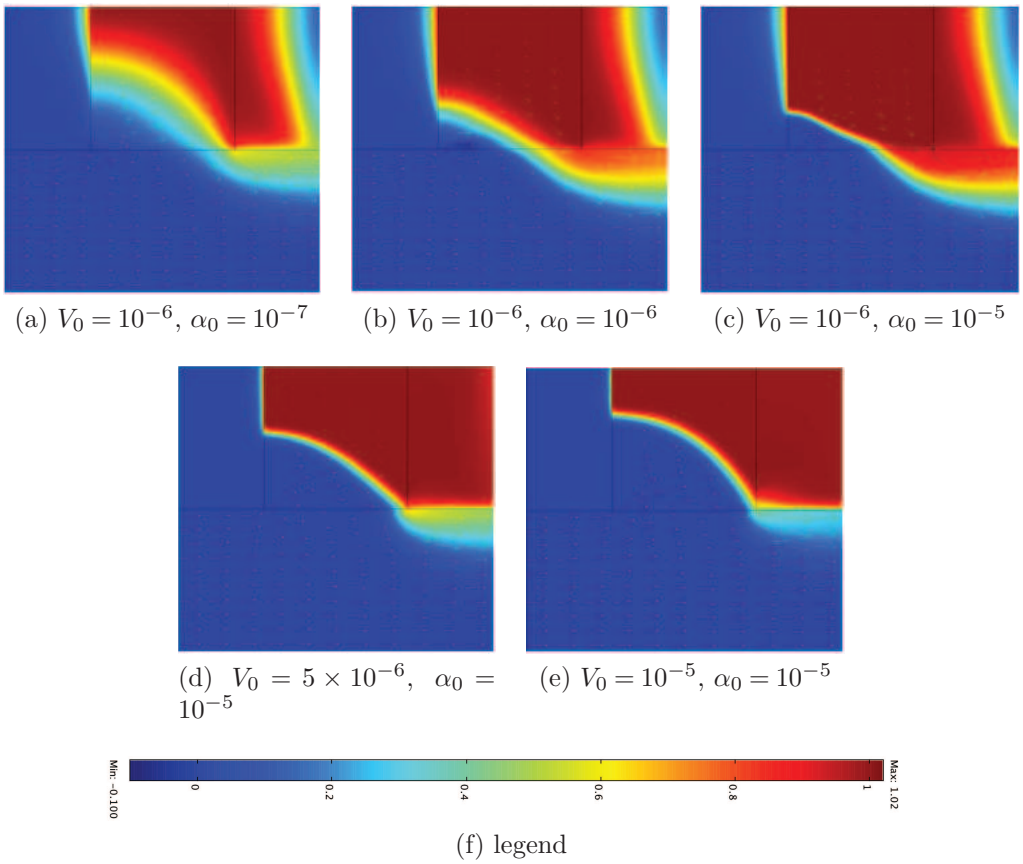

(a) $V_0 = 10^{-6}$, $\alpha_0 = 10^{-7}$ (b) $V_0 = 10^{-6}$, $\alpha_0 = 10^{-6}$ (c) $V_0 = 10^{-6}$, $\alpha_0 = 10^{-5}$

(d) $V_0 = 5 \times 10^{-6}$, $\alpha_0 = 10^{-5}$ (e) $V_0 = 10^{-5}$, $\alpha_0 = 10^{-5}$

(f) legend

Figure 5.2: Surface plot of the normalized mass fraction $\frac{\Omega_l}{\omega_{eq}}$ and fluid velocity vector $(\frac{u}{V0}, \frac{v}{V0})$ at $t = 10^9$ s, with different α_0 (s^{-1}) and different inlet velocity V_0 (m s^{-1}).

already seen from the porous medium dissolution problem, a cavity develops when α is large enough. Therefore, the DIM model is used to reproduce a quasi-solid dissolution by taking the same permeability-saturation relationship, $K_l = K_0 \varepsilon S_l$, but now with K_0 equal to 10^{-15} m^2, i.e., a very low value to make the solid quite impermeable. The permeability for the dissolved region, which is denoted K_f, has been determined after some investigations of its impact on the dissolution process since its value changes the mathematical nature of the momentum equations.

Another important issue is the choice of α, which greatly affects the results of the DIM model. Thermodynamic equilibrium is achieved when α is infinitely large, which is also the condition to recover a sharp solid-liquid interface. However, because sharpening the interface leads to expensive computational costs, α cannot be taken as large as required to recover a perfect thermodynamic equilibrium condition with a very thin dissolving interface. The result is that

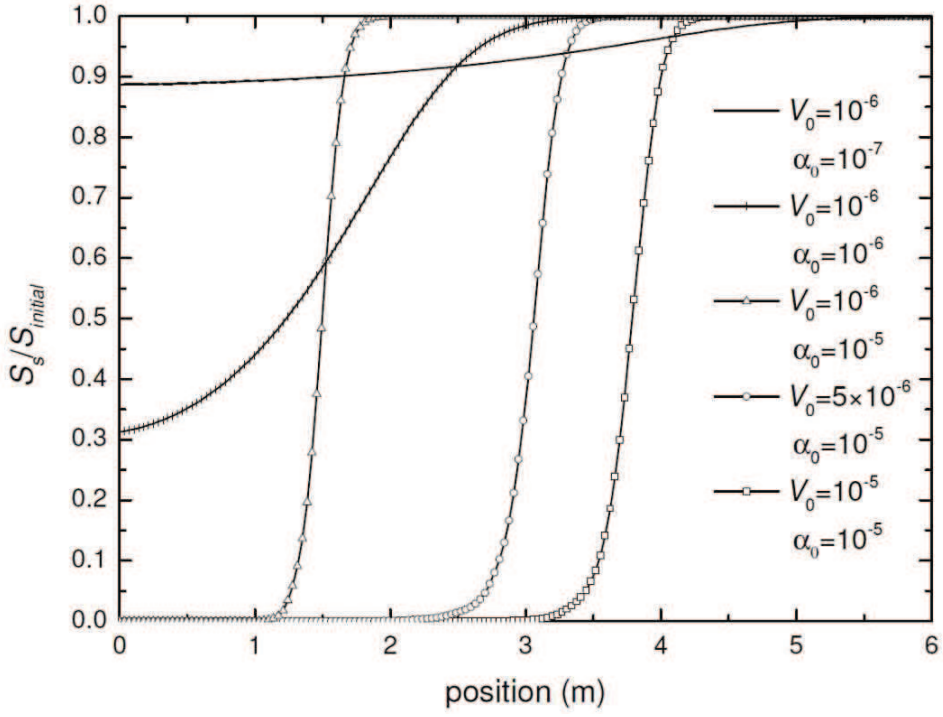

Figure 5.3: Normalized solid gypsum saturation $\frac{S_s}{S_{initial}}$ along the diagonal of subdomain d from the lower left corner to the upper right corner at $t = 10^9$ s, with different α_0 (s^{-1}) and different inlet velocity V_0 (m s^{-1}).

a diffuse interface is created in the dissolution region along with the mass and velocity boundary layers as depicted in Fig. 5.4. The local mass boundary layer thickness is denoted δ_{lc}, the velocity boundary layer thickness, δ_{lv}, and they are the only ones in the front tracking model (Fig. 5.4a) while a diffusive interface thickness, δ_D, appears in the case of the DIM model (Fig. 5.4b). In order for the DIM approach to recover approximately the correct dissolution fluxes, the diffuse interface must not perturb significantly the other boundary layers, i.e., a condition such as $\delta_D \ll \delta_{lc}, \delta_{lv}$ must be fulfilled.

5.2.3.1 The impact of three momentum equations

The first investigation is the impact of the choice of the momentum equations in subdomain d, i.e., the modified Navier-Stokes equation, the Darcy-Brinkman equation and Darcy's law, on the total mass flux over the lower boundary of subdomain d under different K_f. Darcy's law was used as the momentum equation in subdomains a and e here and after. The total mass flux was scaled by the largest value obtained and the simulation results are presented in Fig. 5.5. Due to the artificial transition of K_f in the dissolved and K_l in the undissolved region, as well as the required very fine mesh, the

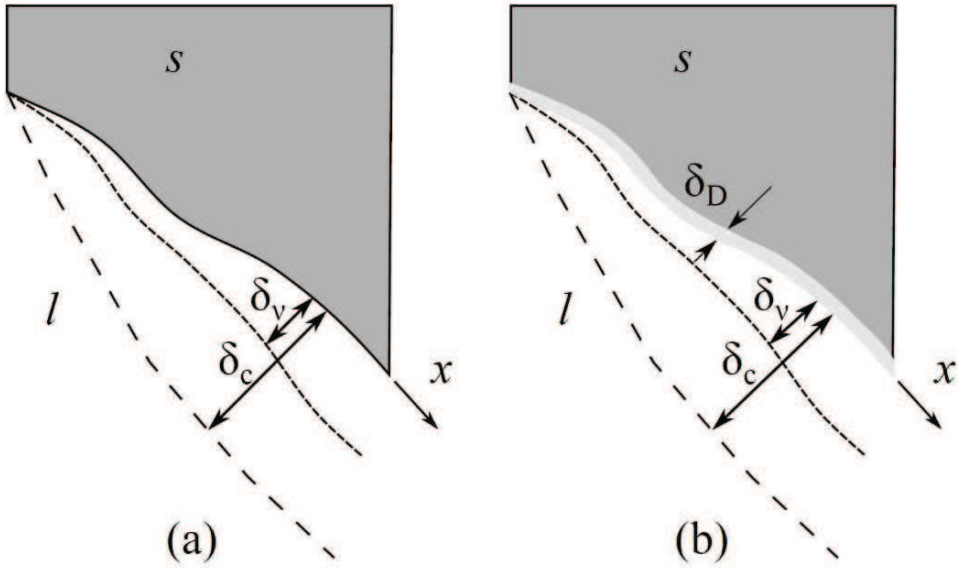

Figure 5.4: Schematic depiction of the dissolving interface in the front tracking model (a) and in the DIM model (b), as well as the corresponding length scales.

results were not converged when K_f was greater than $10^{-8}\,\mathrm{m}^2$. Therefore, the results were only obtained for $K_f \leq 10^{-8}\,\mathrm{m}^2$. One observes from Fig. 5.5 that the results obtained with the three momentum equations are similar for the whole range of K_f. The mass flux over the dissolving surface remains a constant when $K_f < 10^{-15}\,\mathrm{m}^2$ and then increases dramatically with $10^{-15}\,\mathrm{m}^2 < K_f < 10^{-11}\,\mathrm{m}^2$. After K_f reaches $10^{-10}\ \mathrm{m}^2$, further increase of the permeability leads to negligible increase of the mass flux. It may be concluded that: (i) the inertia term is not important in this study, (ii) a K_f permeability too low ($< 10^{-10}\ \mathrm{m}^2$) makes the flow in the cavity unrealistic, despite of the momentum equation used, (iii) the modified Navier-Stokes and the Darcy-Brinkman equation give the same results, which is a priori close to the physical one (i.e., the flow of a viscous fluid in a cavity), (iv) surprisingly, a pure Darcy model, with a relatively large permeability in the cavity gives almost the same dissolving flux.

This last remark is encouraging since Darcy equations are easier to solve for numerically. However, a generalization of this result has to be taken with caution. Indeed, if there is a developing boundary layer over a flat surface, classical boundary layer theory gives a Darcy Sherwood number along the boundary at a position x equal to

$$\mathrm{Sh}_x = \frac{\alpha_\mathrm{x} x}{D_0} = 0.564\mathrm{Pe}_\mathrm{x}^{1/2}. \tag{5.12}$$

where x is the position along the surface and α_x the local mass exchange coefficient at position x.

If the Schmidt number Sc ($\mathrm{Sc} = \frac{\mu_l}{\rho_l D_l}$) is small, this correlation is also the same in the case of a laminar Navier-Stokes flow. However, the Schmidt number for water is about $\mathrm{Sc} \approx 10^3$, which suggests that there should be a difference between Darcy and Navier-Stokes results. In addition, in the case of significant water density variations, there might be a departure from the classical boundary layer solution because of buoyancy effects. This may also change because of different flow conditions (heterogeneity, roughness, confinement, etc...).

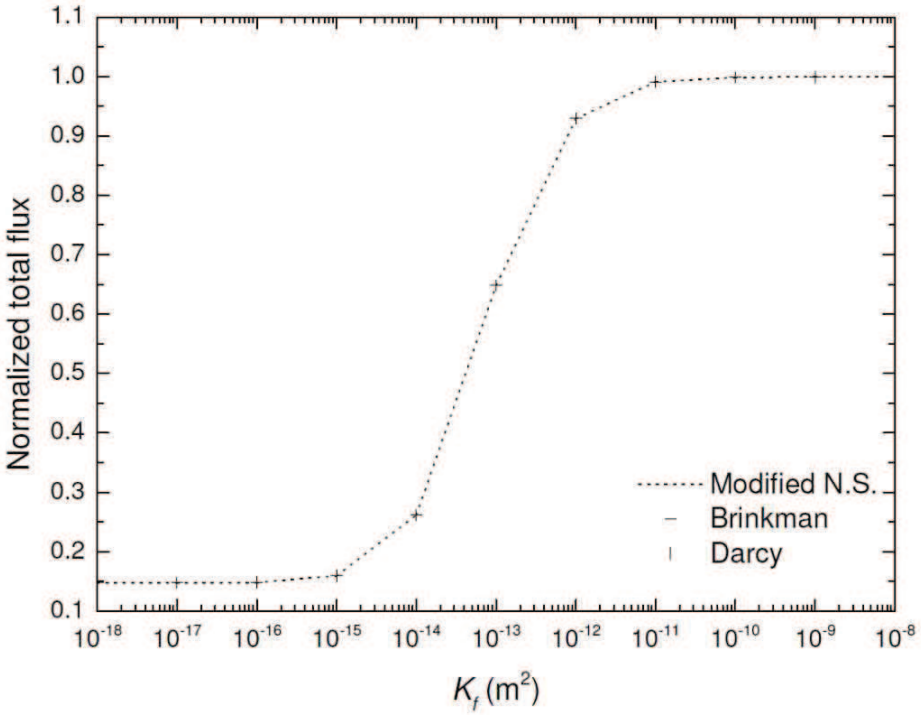

Figure 5.5: Normalized total flux over the dissolving surface as a function of cavity permeability.

In order to investigate the impact of the choice of K_f and of the momentum balance equations on the mass transfer problem, a much simpler geometry is studied corresponding to a channel with parallel walls. Since the question is to get the correct flux and given the difference between the time-scales for dissolution and the relaxation of the concentration field, the pore-scale model is implemented without the interface recession. The distance between the two walls (d_c) and the length of the channel are 0.5m and 20m, respectively. The boundary conditions were constant velocity $V_0 = 10^{-6}\,\mathrm{m\,s^{-1}}$ and constant mass fraction $\omega_l = 0$ at the entrance boundary, no-slip and thermodynamic equilibrium mass fraction at the two parallel walls and convective flux at the

exit boundary. The channel permeability and the mass flux were transformed into Darcy number and Sherwood number by

$$N_{\mathrm{Da}} = \frac{K_f}{l_r^2} \quad \text{and} \quad \mathrm{Sh} = \frac{\alpha_{\mathrm{Sh}} l_r}{D_0}, \tag{5.13}$$

respectively, where the reference length is $l_r = 2d_c$ and the mass transfer coefficient is given by

$$\alpha_{\mathrm{Sh}} = \frac{\int_{A_{ls}} \mathbf{n}_{ls} \cdot (-D_0 \nabla \omega_l)\, dA}{A_{ls}\,(\omega_b - \omega_{eq})}, \tag{5.14}$$

with the bulk mass fraction in the channel defined as

$$\omega_b = \frac{\langle u\omega_l \rangle^l}{\langle u \rangle^l}, \tag{5.15}$$

in which $\langle \star \rangle^l$ represents the area averaged variable and u represents the x-component of the channel velocity. The Darcy number is used as an indicator of the relative importance of the viscous traditional term and Darcy term in the equation, a very small Darcy number meaning that the momentum equations behaves like the classical Darcy's law.

For the channel flow, after an entry zone with a developing boundary layer for the mass fraction, the mass transfer coefficient and the corresponding Sherwood number approach an established regime with constant value. For the laminar flow in a channel with parallel plates and a Dirichlet condition (i.e., a constant mass fraction) at the walls, this established regime value of the Sherwood number is 7.541 for a velocity profile given by the Hagen-Poiseuille parabola [190]. Let us denote this Sherwood number as Sh_r. Its value will be used as a reference when analyzing Sherwood numbers obtained with different momentum equations and various permeabilities. The Sherwood numbers obtained with Navier-Stokes equation, the modified Navier-Stokes equation, Darcy-Brinkman equation and Darcy's law as the momentum equations are denoted as Sh_{ns}, Sh_{mns}, Sh_{db} and Sh_d, respectively. Their values are plotted in Fig. 5.6 together with Sh_r, as a function of the Darcy number. This figure shows the existence of two limits for the various Sherwood numbers. For large Darcy numbers, the Sherwood number for the modified Navier-Stokes equations tends as expected to the value Sh_r. On the contrary, for low Darcy number, the velocity field is a pure piston-like Darcy flow and the resulting established regime leads to a different Sherwood number, higher than Sh_r. Since inertia terms do not play a role in this tube configuration, in the absence of

turbulence, Sh_{mns} and Sh_{db} have the same value. When using Darcy's law, the increase of permeability only changes the pressure field in the channel and given that the inlet velocity remains unchanged this leads to constant value of Sh_d independent of the channel permeability. The Sherwood numbers Sh_{mns} and Sh_{db} vary between the two limits with Da due to competition between the Brinkman term and the Darcy term, which in turn modifies the concentration field. In the condition with K_f smaller than $10^{-5}\,\mathrm{m}^2$ ($N_{\mathrm{Da}} < 10^{-5}$), the Darcy term is dominant and the Darcy-Brinkman equation can be simplified into Darcy's law. Therefore, Sh_{mns} and Sh_{db} have similar values as Sh_d. The values of Sh_{mns} and Sh_{db} start to decrease dramatically with $K_f > 10^{-5}\,\mathrm{m}^2$ ($N_{\mathrm{Da}} > 10^{-5}$) until they reach another constant of about 7.565 when $K_f > 10\,\mathrm{m}^2$ ($N_{\mathrm{Da}} > 10$), which is very close to Sh_{ns} and Sh_r. In this case, the impact of the Brinkman term overcomes the Darcy term, and the Darcy-Brinkman equation plays a similarly role as the Stokes equation. These behaviors of the momentum equations agree well with the analysis of the cavity scale calculations. Differences induced by the different choice of the momentum equations were not observed, i.e., Fig. 5.5. This might be attributed to the fact that the used permeability was not probably large enough and also to the fact that the diffuse interface may have played a role since the condition $\delta_D \ll \delta_{lc}, \delta_{lv}$ is very difficult to fulfill.

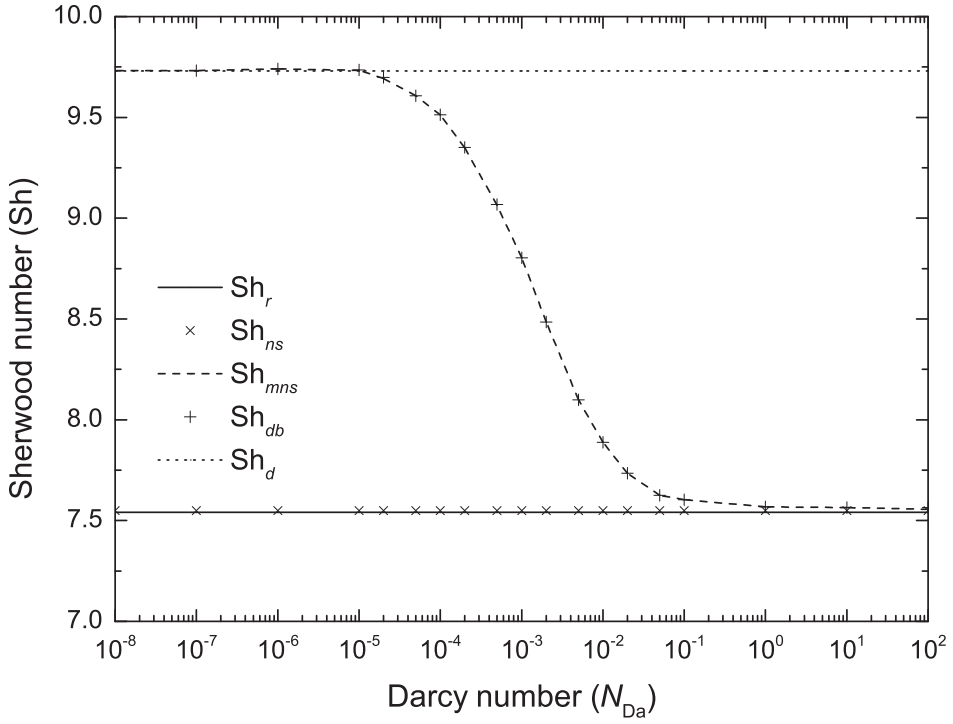

Figure 5.6: Sherwood number as a function of the channel permeability.

This observed behavior of the Sherwood numbers may be better understood by looking at the concentration fields. Examples of the velocity and mass fraction distribution (scaled as $\frac{u}{V_0}$ and $\frac{\omega_l}{\omega_{eq}}$, respectively) along a cross-section of the channel in the established region obtained with three different permeabilities are presented in Fig. 5.7. The momentum equation used was the modified Navier-Stokes equation (equivalent here to the Darcy-Brinkman equation), which incorporates both the Brinkman and the Darcy term. The three chosen permeabilities are representative of the two limit conditions and an intermediate case for the Sh_{mns} curve in Fig. 5.6. The figure shows clearly that, when the channel permeability is rather small, the velocity gradient is very close to the immobile boundaries and therefore does not impact much the concentration field which evolves like in a diffusive mass boundary layer. The thickness of the velocity boundary layer increases with the increasing permeability thus affecting correspondingly the concentration field, which is affected by a thinner mass boundary layer. These remarks must be kept in mind when evaluating the representativity of a DIM solution.

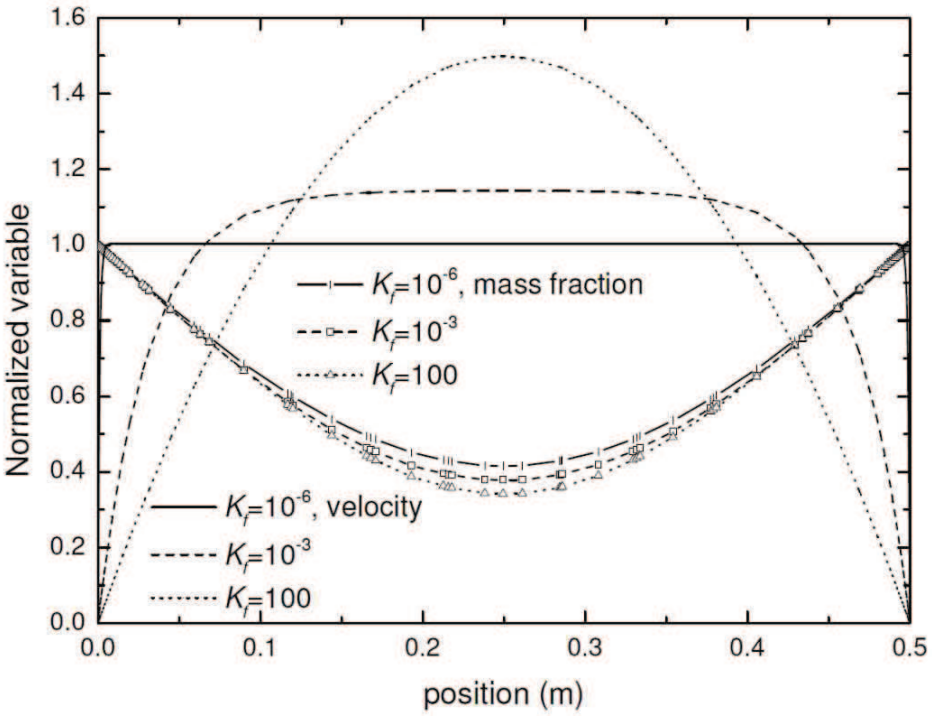

Figure 5.7: Normalized mass fraction ($\frac{\omega_l}{\omega_{eq}}$) and velocity ($\frac{u}{V_0}$) along a cross-section of the channel with various permeabilities (m^2), calculated with the modified Navier-Stokes equation.

5.2.3.2 The choice of the mass exchange coefficient

To study the impact of α on the dissolution process in this solid dissolution case, similar simulations with DIM were carried out as for case I, the dissolution of a porous medium. As the permeability in the undissolved region of subdomain d is rather low, which makes it difficult for the fluid to flow through, the flow streamlines in this case are nearly parallel to the dissolving surface. To investigate the characteristic time in such a case, the residual time is estimated approximately as

$$t = \frac{w_g}{V_l} \sim 5 \times 10^6 \,\mathrm{s}, \tag{5.16}$$

where $w_g = 5\mathrm{m}$ is the width of subdomain d. This value must be compared to the dissolution characteristic time in the DIM which is about the inverse of α. As commented before, a relatively large α is necessary to reach rapidly the thermodynamic equilibrium mass fraction along the dissolving surface in order to have an actual boundary layer similar to the one with a sharp interface. However, α cannot be infinite for computational reasons (see discussion in [120]). As discussed above, the correct exchange flux between the solid and the liquid, hence the dissolution velocity, is somehow difficult to capture with a DIM model, due to the required very fine mesh in the diffuse interface, a need for a relatively large α and the artificial tweak of K_f. Therefore, one has to verify that the flux exchanged between the solid and the fluid reaches acceptable values. Contrary to small-scale simulations, it is very difficult to carry on proper ALE simulation with moving interfaces on a large cavity problem, so a so-called fixed boundary model was used in the reference simulations, using once again the fact that the dissolution time is much longer than the relaxation time for the mass transport problem. In this fixed boundary model, the position of the *immobile* solid-liquid interface is obtained from the DIM simulations at a given time, at which one wants to check the validity of the DIM solution, by tracking the contour of $\frac{S_s}{S_{initial}} = 0.9$. The dissolution velocity obtained by the DIM model is expected to be correct if it gives mass fraction fields very similar to the fixed boundary model.

The chosen K_f was $10^{-9}\,\mathrm{m}^2$ to have a sufficiently large permeability, according to the analysis of Fig. 5.5. Even though similar results have been obtained by using different momentum equations, this point is further verified. In the two sets of simulations with DIM, the modified Navier-Stokes equations and Darcy's law were used alternatively in subdomain d. When using

small α_0, the simulations fail to produce a thin solid-liquid interface to satisfy $\delta_D \ll \delta_{lc}$ and the assumptions to use DIM break down. When increasing α_0 to $10^{-5}\,\mathrm{s}^{-1}$, similar mass fraction distribution is obtained with DIM and with the fixed boundary model, as illustrated by the results presented in Fig. 5.8. Firstly, one observes that the use of the modified Navier-Stokes equation or Darcy's law as the momentum equation give very similar results, which is not surprising given the above study for the channel flow case, Fig. 5.6, which shows that the impact of different momentum equations can only be observed when $K_f > 10^{-5}\,\mathrm{m}^2$. When K_f is relatively small the modified Navier-Stokes equation behaves like Darcy's law, as discussed previously. Secondly, the development of the mass boundary layer along the dissolving surface induces a decrease of mass flux from the entrance to the exit, which further causes the slower dissolution velocity in the exit region (cf. Figs. 5.8a and 5.8b), similar to case I (the porous medium dissolution case). Thirdly, one sees that the main differences between the DIM and the fixed boundary model are in subdomains e_1 and e_2. To further investigate the mass fraction fields in subdomain d obtained with different models, the results are plotted in Fig. 5.9 under the form of contour plots. Using Darcy's law or the modified Navier-Stokes equations produced very small differences for the mass fraction contours. Using DIM or the fixed boundary model also led to small differences, except for $\frac{\Omega_l}{\omega_{eq}} = 0.1$ in the region far from the cavity entrance.

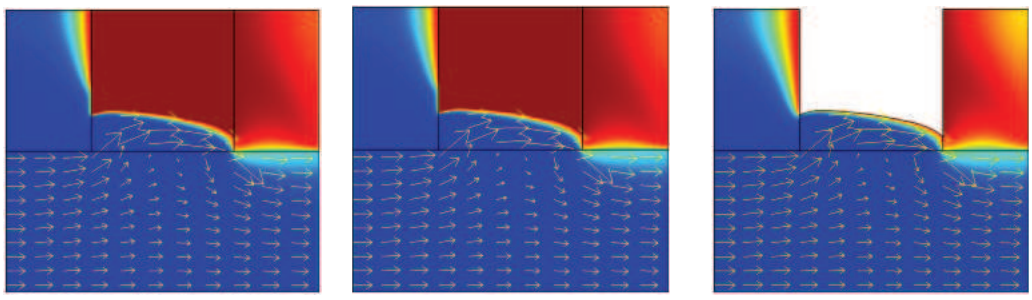

(a) DIM with modified N.S. equation

(b) DIM with Darcy' law

(c) Fixed boundary method with modified N.S.

Figure 5.8: Surface plot of the normalized mass fraction $\frac{\Omega_l}{\omega_{eq}}$ and the normalized fluid velocity vector $(\frac{u}{V0}, \frac{v}{V0})$ at $t = 8 \times 10^9$s with $\alpha_0 = 10^{-5}\mathrm{s}^{-1}$. The legend is the same as in Fig. 5.2f.

To check the length scale of the the mass fraction boundary layers and the diffusive solid-liquid interface, the profiles of $\frac{\Omega_l}{\omega_{eq}}$ and $\frac{S_s}{S_{initial}}$ along the vertical middle cross-section of subdomain d were plotted in Fig. 5.10. The abscissa represents the distance of the studied point on the cross-section from

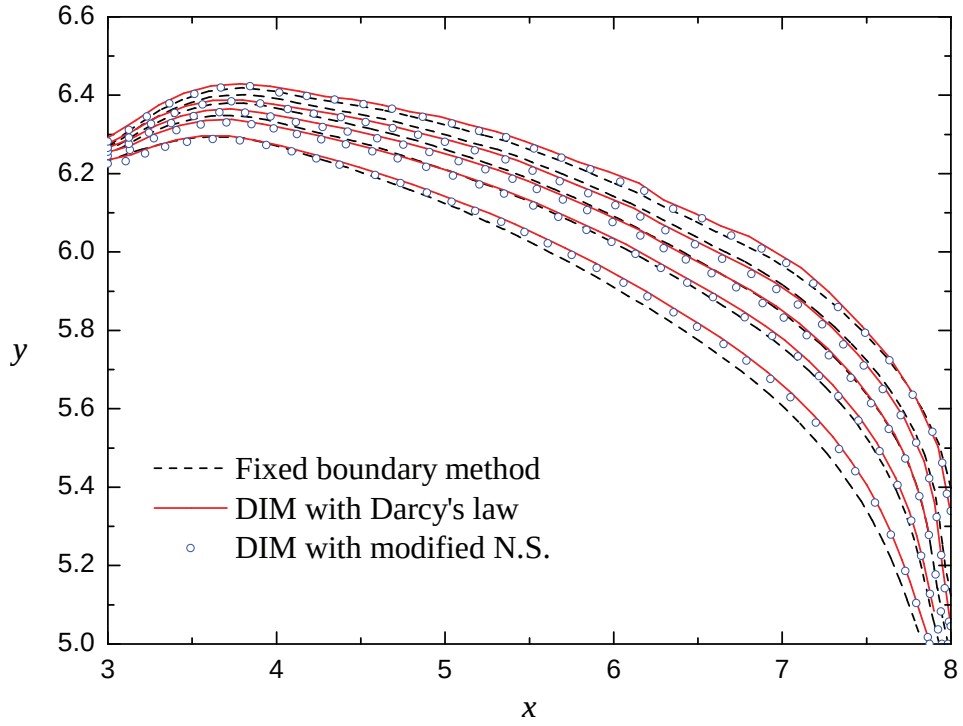

Figure 5.9: Mass fraction ($\frac{\Omega_l}{\omega_{eq}}$) contours for the range [0.1, 0.3, 0.5, 0.7, 0.9] from lower to upper part of subdomain d for the three simulations at $t = 8 \times 10^9$s with $\alpha_0 = 10^{-5}\text{s}^{-1}$.

the lower boundary of subdomain d. One sees from the figure that the diffusive interface thickness in terms of the variation of solid gypsum saturation S_s in the DIM model is indeed smaller than those of the mass fraction boundary layers obtained by different models, provided the parameters are chosen carefully.

5.2.3.3 The impact of liquid density variation

In the above studies, the fluid had a constant density. However small it is, the dissolved gypsum indeed changes the density of the fluid, which may initiate natural convection since the residence time of water along the surface is measured in months, which is enough time for the development of buoyancy plumes. This potential effect was investigated and the results are presented below. The geometry and parameters were the same as those used to obtain Fig. 5.8a, except that density variations were taken into account using Boussinesq approximation and a fluid density increase estimated as $(\rho_{max} - \rho_l)\frac{\Omega_l}{w_{eq}}$ with $\rho_{max} = 1002.63\,\text{Kg}\,\text{m}^{-3}$. Simulation results in terms of normalized mass fraction and velocity fields are displayed in Fig. 5.11. One observes the presence of small convective plumes in the entrance region of the cavity from Fig.

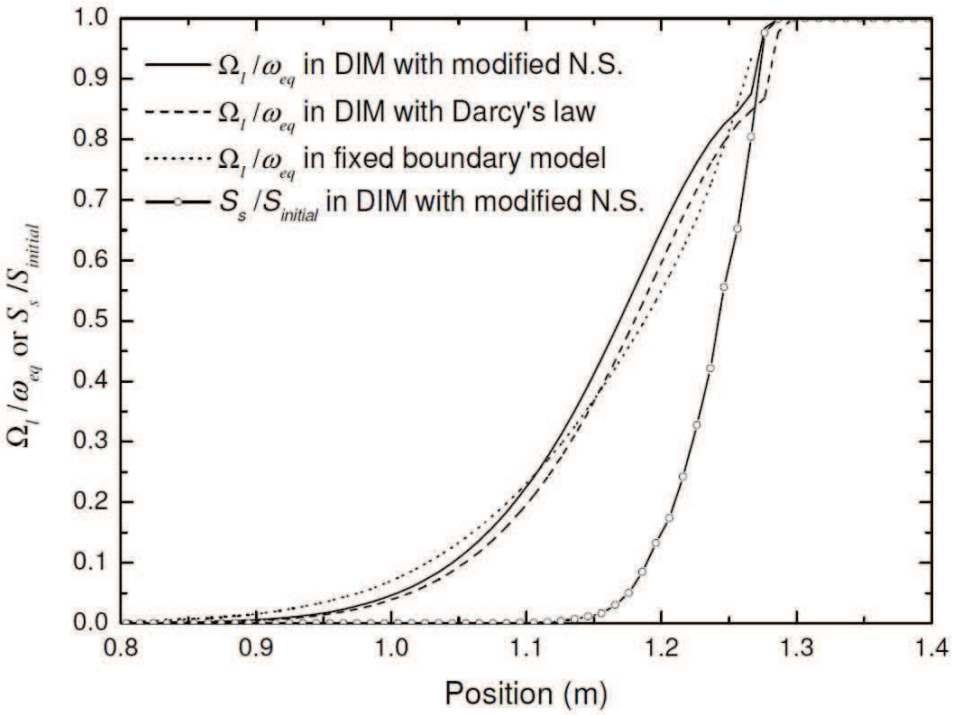

Figure 5.10: Comparison of the distribution of $\frac{\Omega_l}{\omega_{eq}}$ and $\frac{S_s}{S_{initial}}$ along the vertical middle cross-section of subdomain d. The abscissa indicates the position of the cross-section, in terms of distance from the lower boundary of subdomain d.

5.11a, while the mass boundary layer is smooth when neglecting the density variations, as illustrated in Fig. 5.11b. The differences of the mass fraction fields near the dissolving surface as shown in these two figures indicate that the fluid density variation has a potential to affect the geometry and recession rate of the dissolving surface. However, the quantitative difference remains small, even after the relatively long period of time considered in this numerical example. This would be certainly a different matter for the case of salt dissolution, as illustrated in the calculations by [120, 127] .

5.3 Three-dimensional dissolution modeling and geomechanical issues

The aim of this section is not so much to apply the methods developed previously to real cases but to show their potential applications. In order to illustrate that, the numerical modeling of dissolution for two configurations

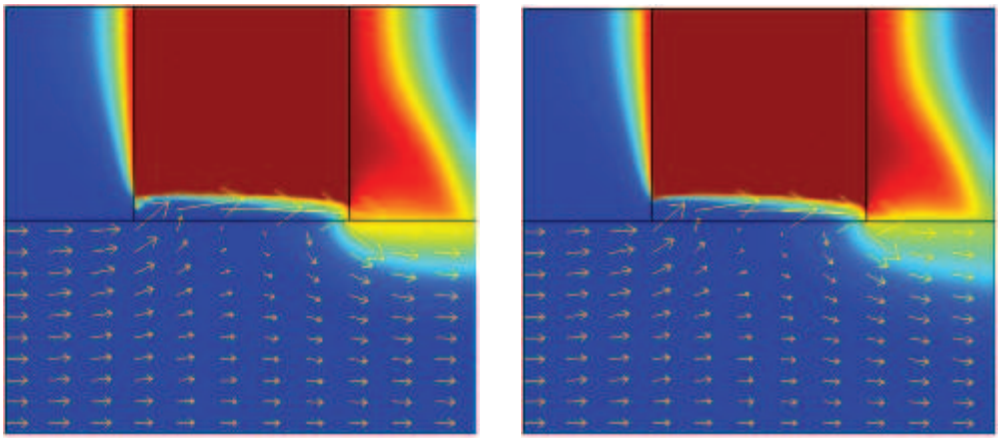

(a) Results with natural convection (b) Results without natural convection

Figure 5.11: Surface plot of normalized mass fraction of dissolved gypsum and normalized fluid velocity vector at $t = 2.1 \times 10^9$ s, with (a) and without (b) natural convection. The legend is the same as in Fig. 5.2f.

that can be met in real issues is discussed. The first relates to the dissolution of gypsum pillars subjected to a continuous flow of water. This configuration can be encountered in the case of flooded rooms in gypsum quarries as illustrated in Fig. 5.12. The conceived scenario corresponds to a time continuous forced convection of fresh water through the system. This process is of direct relevance to gypsum mining. Indeed, because gypsum dissolves easily in flowing water, a continuous flow of fresh water around pillars in a fully or partially flooded mine could decrease significantly their cross sections (near the floor level in case of partially flooded) and lead to the pillar failure. As a consequence, any gypsum mine which becomes flooded on abandonment should be subject to a hydrological study as advised by Cooper [29]. The second case corresponds to the flow of water created by a natural hydraulic gradient through a rock (porous) formation that contains a gypsum lens. This lens could be located in a porous medium between two layers of marl for instance (Fig. 5.13). The subsequent dissolution process can create hazardous mechanical collapse and sinkhole or cavity formation.

Whatever the hydro-geological configuration, the dissolution of gypsum in the ground raises the question of consequences in terms of geomechanical behavior: surface subsidence, sinkholes, caverns or pillar stability, etc. The purpose of this section is to present some examples indeed simplified, to illustrate the numerical robustness and the potentialities of the numerical dissolution approach outlined in the previous sections. Here we are interested in 3D dissolution problems with large spatial scales. Roof collapse in interstratal gypsum

Figure 5.12: Views of a pillar in the Rocquevaire abandoned quarry (Bouches-du-Rhône, France) with two different water flooding level (left in 1996 and right in 2010, by courtesy of Watelet JM, INERIS).

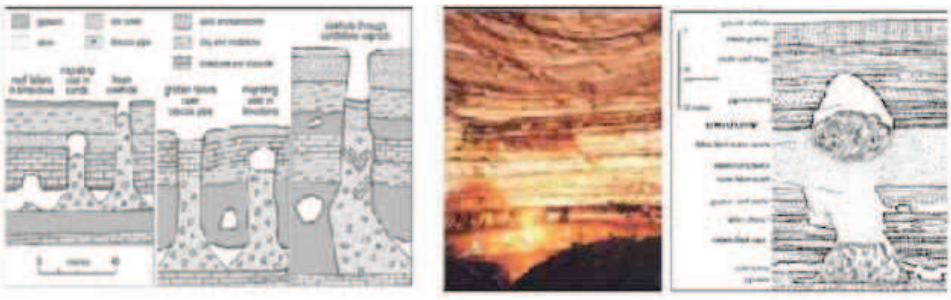

Figure 5.13: Left: illustration of the evolution of caprock sinkholes over a gypsum karst in Ukraine and England (after [7]). Middle and right: photo and schematic section through a void discovered within cover rocks of gypsum in an underground railway station in Paris (France) (After [8]).

caves creates columns of largely insoluble breakdown debris (Fig. 5.13) that are small compared to the breccia pipes (breccia pipe, also referred to as a chimney, is a mass of breccia, often in an irregular and cylindrical shape) formed over sites of deep-seated dissolution of either gypsum or salt [7]. These features constitute a significant geohazard due to their potential failure at the surface as caprock sinkholes, unless the volumetric expansion of breakdown material fills the void and stops the failure process. For instance, many surface failures occur over gypsum beneath Paris (France) [8], and the investigation of a cavity found in 1975 beneath railway engineering works revealed a failure migrating up through the cover rocks from dissolution cavities in a number of gypsum horizons (Fig. 5.13). Numerous caprock sinkholes at Ripon, U.K. lie on top of breccia pipes and are reactivated by ongoing dissolution of gypsum [191]. Over time, most caprock sinkholes with weak cover rocks degrade to a gentle depressions that may be confused with solution sinkholes unless the subsurface

is investigated or exposed. Those in stronger rocks survive as deep circular pits, as seen in Fig. 5.14 where dolomite overlies gypsum.

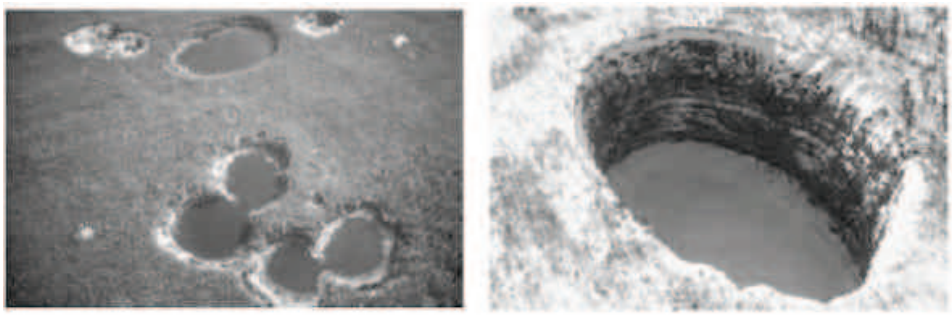

Figure 5.14: Examples of dissolution consequences: (Left) several sinkholes in wood Buffalo National Park (Canada). The interstratal dissolution of gypsum induced a collapse that propagated through dolomite cover beds and (right) Vermilion Creek doline, near Norman Wells (Canada), a sinkhole of 180 × 100 m wide and 40 m deep to the waterline. It corresponds to a collapse through calcareous shales overlying gypsum [7, 9].

The problem to be solved now is not only a complex multi-scale problem but also a strongly coupled multi-physic problem. Dissolution leads to a time evolution of the domain and boundaries, changes of rock matrix porosity and related properties. These lead in turn to rock deformations which retroactively affect the fluid flow and consequently the dissolution process. Roughly, the transient domain evolution induced by dissolution is a variable of the geomechanical boundary value problem, but the matrix dissolution and its consequences in terms of modification of the constitutive law (at the material point level) of the rock must also be considered. Such a strong coupling is currently under development. In this study, the mechanical consequences of dissolution are approached in the geomechanical calculation through a simplified analysis (weak coupling). For the mechanical response of the rock mass, only the effect of domain geometry change induced by dissolution is considered. In the examples under consideration, the dissolution process will generate growing cavities (case of lenses) or decreasing cross-section of pillars (case of rooms and pillars quarries). Thus the situation corresponds to a pure leaching process as encountered in solution mining, with no chemical impact on the mechanical constitutive model.

Dissolution may be due to a natural or anthropic hydraulic regime. The latter includes, for example, mining or civil engineering works that modify the hydraulic regime (a leaking pipe, the damage of the matrix, cracking, drying, etc.). From a geochemical point of view, the dissolution rate can also be

modified by external agents such as the increase of salinity or the change of water pH due to the dissolution of CO_2 after acid rain. The specific mechanisms of internal erosion (mechanical) or suffusion, which can be combined and added to chemical dissolution to increase the pore volume growth rate, are not considered in this study. Indeed, erosion, as characterized by the mechanical extraction of particles, is a special case of coupling with mechanics which may intervene at various scales. First, erosion increases the intensity of dissolution at the reactive surface and therefore the dissolution rate, by pulling away often passive particles. Second, erosion contributes to the change of porosity and therefore permeability. Similarly, although it may also play a role, the precipitation process is not considered in this study. All these assumptions are consistent with the fact that this part addresses essentially the impact of leaching rather than dissolution inside the porous matrix.

5.3.1 Three-dimensional modeling dissolution of a gypsum pillar and a gypsum lens

The cubic gypsum pillar (size 5 × 5 × 5 m) located in a room of pillar quarries and a gypsum lens (size 10 × 2.5 × 1.5 m) located strictly within a porous layer are depicted in Figs. 5.15 and 5.16, respectively. The model used is the same as presented in the last section. The injection velocity is V=10^{-6}m s^{-1} in the direction as presented in Figs. 5.15b and 5.16a. The dissolution process is analyzed for a period of 30 years. No flow conditions were imposed at the floor (bottom), the roof (top) levels and at the left and the right boundaries of the domain. The parameters used are illustrated in Tables 5.2 and 5.3.

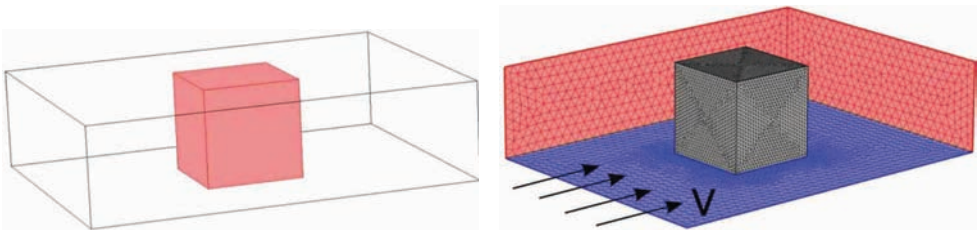

(a) (b)

Figure 5.15: (a) 3D model of a gypsum pillar (size 5 × 5 × 5 m) located in a flooded gypsum quarry; and (b) mesh of the gypsum pillar and the quarry which is subject to a fresh water flow (velocity V=10^{-6} m s^{-1}).

The pillar states at two different times (15 and 30 years) are illustrated in

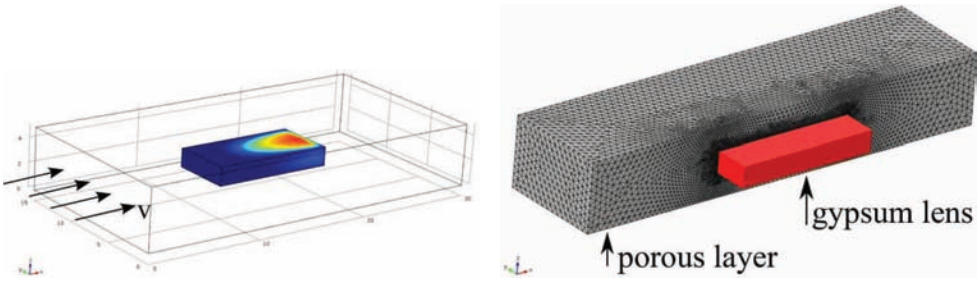

(a) (b)

Figure 5.16: (a) Lens located in a porous layer. For reasons of symmetry about the vertical mid-plane, only half model (meshed domain) was considered; and (b) the mesh corresponds to the investigated domain (field of study). The location of the gypsum lens and the porous layer may also be observed.

Table 5.2: Mechanical parameters for the pillar and gypsum lens problems.

		Young Modulus (MPa)	Poisson coefficient [-]	Friction angle (°)	Cohesion (MPa)
Lens	Overburden	4	0.3	35	0.1
	Porous layer	100	0.3	44	1
	Gypsum	35000	0.34	44	8
	Bottom Layer	2500	0.3	-	-
Pillar	Gypsum	35000	0.34	44	8
	Room	-	-	-	-

Table 5.3: Geometrical features for the pillar and gypsum lens problems.

Dimensions		Height (m)	Width (m)	Length (m)
Lens	Overburden	10	26	34
	Porous layer	5	26	34
	Gypsum	1.5	10	15
	Bottom Layer	5	26	34
Pillar	Gypsum	5	5	5
	Room	5	8	10

Figs. 5.17 and 5.18, respectively. The left figures give the normalized saturation $\frac{S_s}{S_{initial}}$ while the right figures give the meshed shape (initial and final). Because of low gradient density effects, symmetry is maintained during dissolution. However, dissolution is naturally more pronounced at the upstream and lateral sides of the pillar. The streamline shape modification of the concentration induced by the pillar shape may be observed in Fig. 5.19. The time evolution of the normalized volume of the pillar is illustrated in Fig. 5.20, with a volume reduction of about 40 % observed after 30 years.

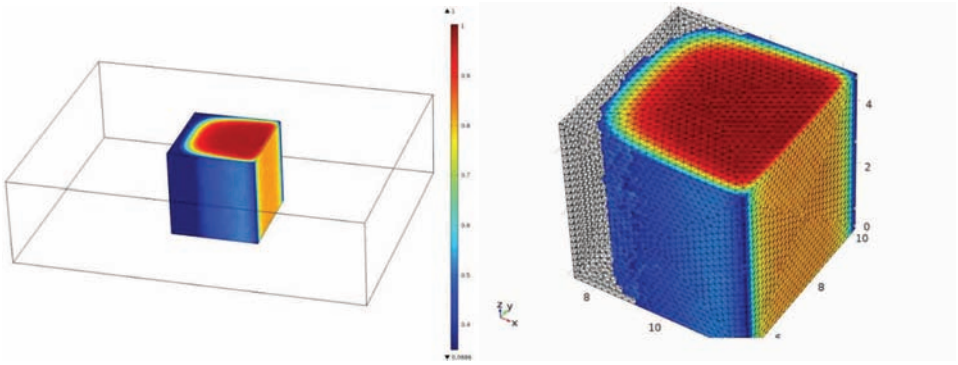

(a) (b)

Figure 5.17: (a) Example of isovalue of the normalized saturation degree; and (b) focus on the pillar shape after 15 years.

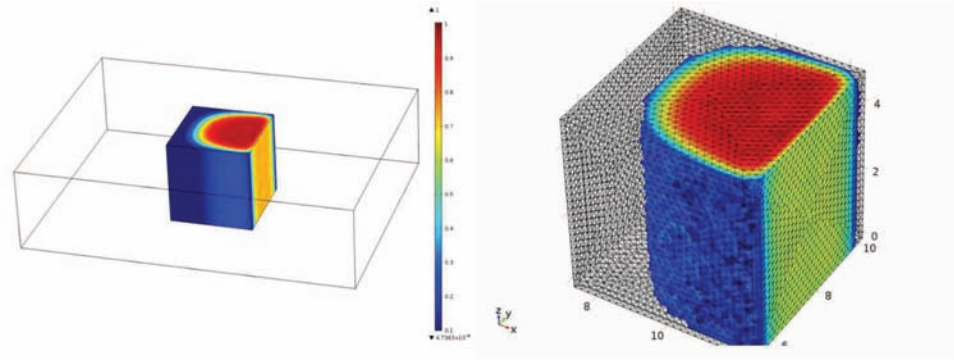

(a) (b)

Figure 5.18: (a) Example of isovalue of the normalized saturation degree; and (b) focus on the pillar shape after 30 years.

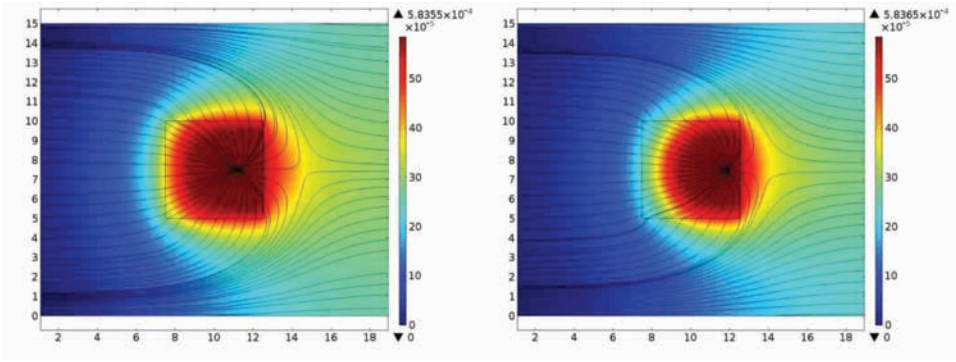

(a) (b)

Figure 5.19: Example of isovalues of the Ca concentration and flowing streamlines after 15 years (a) and 30 years (b) in a horizontal plane passing through the middle of the pillar.

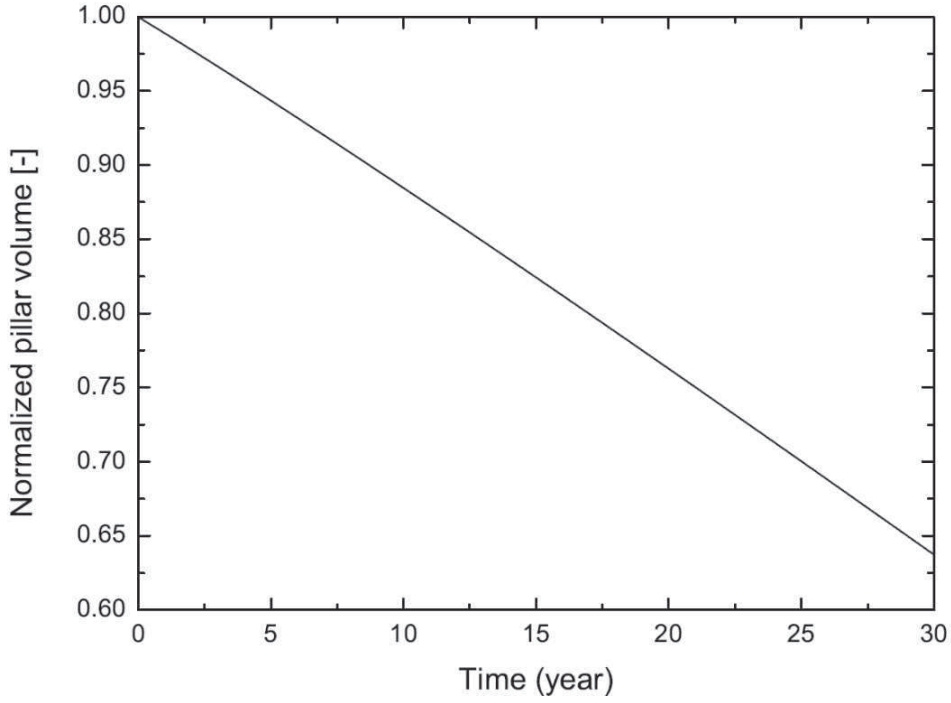

Figure 5.20: Example of time evolution of the normalized pillar volume.

The lens states at three different times (3, 15 and 30 years) are illustrated in Fig. 5.21. The shape evolution of the gypsum lens (in red) is observed. The 3D shape of the lens is reconstructed using symmetry. The blue box corresponds to the initial (half) gypsum lens. The dissolution rate of the lens is greater than the pillar dissolution rate. Indeed, this is explained, firstly, by the fact that the wetted surface is larger for the gypsum lens, and, secondly, that the ratio of gypsum volume versus reactive surface is smaller for the pillar. An example of the space distribution of the concentration at two different times (15 and 30 years) is given in Fig. 5.22. One may also observe the streamline shape modification induced by the lens shape. A representation of the lens dissolution inside the porous layer is shown in Fig. 5.23a and the flowing streamlines in a horizontal plane passing through the middle of the layer (porous layer and gypsum lens) after 30 years is presented in Fig. 5.23b. The volume reduction for the gypsum lens is 60 % after 30 years, much faster than the 40% reduction for the pillar case.

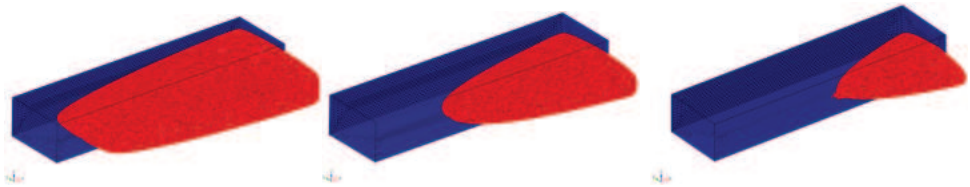

(a) (b) (c)

Figure 5.21: 3D shapes (red) of the lens after 3, 15 and 30 years for a, b and c, respectively. The initial volume is represented by the mesh domain.

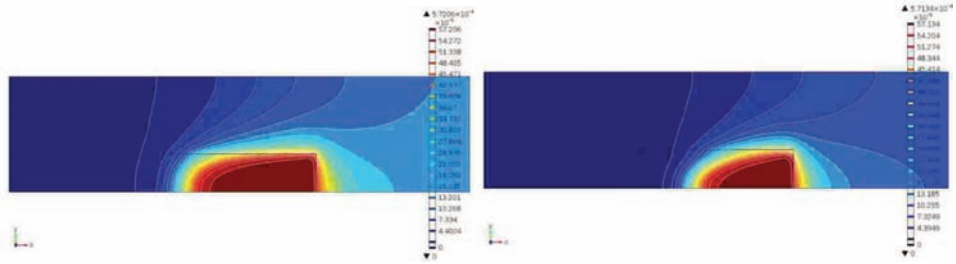

(a) (b)

Figure 5.22: Example of isovalues of the Ca concentration after 15 years (a) and 30 years (b) in a horizontal plane passing through the middle of the layer (porous layer and gypsum lens).

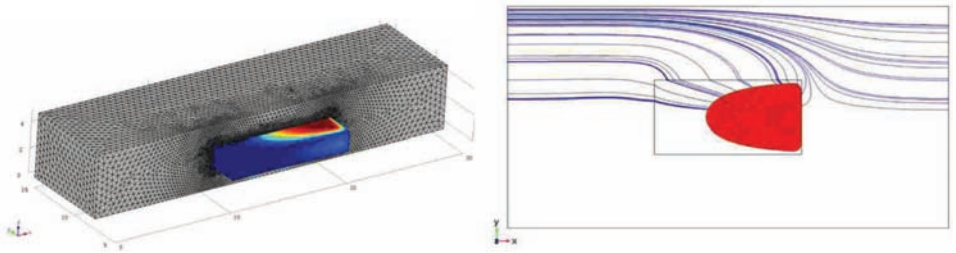

(a) (b)

Figure 5.23: (a) Representation after 30 years of the lens dissolution inside the porous layer; and (b) flowing streamlines in a horizontal plane passing through the middle of the layer (porous layer and gypsum lens) after 30 years.

5.3.2 Three-dimensional geomechanical modeling of dissolution consequences

The mechanical behavior of bonded soils or rocks can be described by constitutive models based on the classical theory of hardening plasticity or its extensions [183, 184]. Geomaterial model subject to mechanical and chemical effects are usually presented as a chemico-mechanical model or more generally a coupled thermal–hydraulic–mechanical–chemical (THMC) model. In this

framework, the chemical components are usually taken into account in the yield surface and flow rule parameters [185–187]. In some constitutive models, the chemical degradation is considered as affecting only the internal variables while not other material properties, e.g., elastic module or friction angle. This clearly limits the type of materials to which the proposed constitutive theory can be applied.

One of the shortcomings of the current approaches is that they are based on a given or estimated geometry or domain. The current numerical models fail to take into account the heterogeneous development of the porosity and the changes in the shape of the domain. Of course, it is well known that it is difficult to take into account explicitly the loss and mass transfer in a constitutive macro-scale mechanical model. A pure mechanical model (elastic-plastic Mohr-Coulomb model) is used in this study. One should note that, although the rheological model is simple and that chemical effects on the constitutive law are not taken into account, the model is consistent with our initial hypothesis of considering only the leaching process. The aim of this subsection is to emphasize some mechanical phenomena linked to dissolution.

The full or strong dissolution-mechanical coupling is not yet implemented and in order to solve for (only for illustration purpose) a time continuous dissolution-mechanical problem, a simplified approach has been adopted to couple in a weak sense the DIM and a geomechanical code. This weak coupling is developed under the finite element code Marc (Msc Software) [192] by solving a thermo-mechanical problems (with a nil expansion coefficient). An arbitrary initial temperature is applied on the initial surfaces of the pillar or lens (which are supposed to be in contact with the fluid in motion). Then a suitable thermal diffusivity is chosen such that the velocity of the temperature front reproduces the dissolution interface recession velocity obtained from the DIM. Then a criterion is defined for deactivation of finite elements, i.e., specific physic is deactivated while keeping others active in the same finite elements. In fact, when the criterion is met (i.e., a given value of temperature), the mechanical component no longer exists in the element, but it still possesses its heat transport properties.

In the pillar quarry example, the gypsum pillar is loaded on its top by a load $P = 1.875$ MPa (corresponding to an overburden of 75 m width). The specific weight is 2.5 for all material. A domain containing a gypsum pillar is illustrated in Fig. 5.24. The parameters of the model are also given in Tables 5.2 and 5.3.

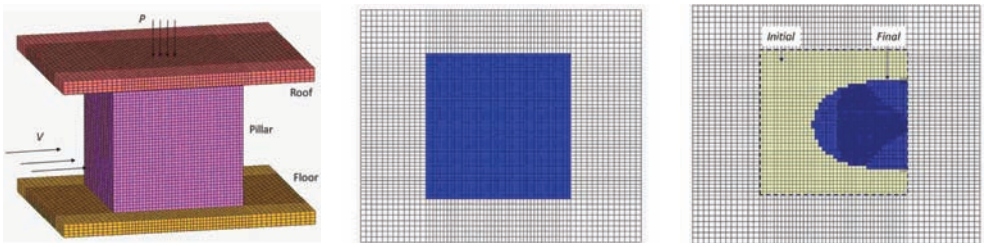

(a) (b) (c)

Figure 5.24: From left to right: pillar, roof and floor mesh and loading; initial pillar cross section and final pillar cross section.

In the pillar context, dissolution has the effect of reducing its transversal section. Consequently it increases the average vertical stress. After a given dissolution period, pillar reaches a critical size and then will no longer support the weight induced by the recovery. Then one may expect a shearing or buckling if the slenderness of the pillar is too large. A shear pillar failure induced by dissolution is illustrated in Figs. 5.25 to 5.27. The graph in Fig. 5.26 describes the vertical displacement versus increment number and shows clearly the corresponding critical (unstable) pillar state. Fig. 5.27 shows two pillar failure modes induced by the dissolution and for two overburden stiffness. The soft overburden leads to a non symmetric shear failure of the pillar. We remind that the definition of the effective plastic strain is as follows

$$\varepsilon^p_{eq} = \int_0^t \dot{\varepsilon}^p_{eq} dt \text{ with } \dot{\varepsilon}^p_{eq} = \sqrt{\frac{2}{3}\dot{\varepsilon}^p_{ij}\dot{\varepsilon}^p_{ij}}. \tag{5.17}$$

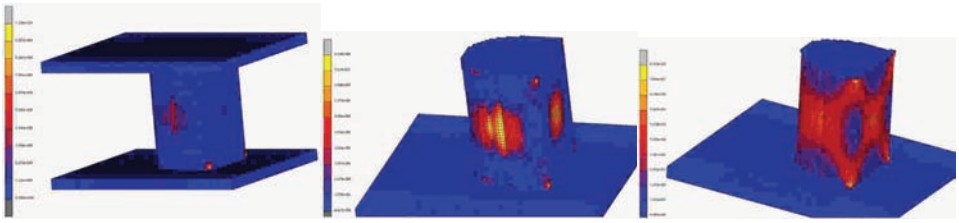

(a) (b) (c)

Figure 5.25: 3D views of the equivalent plastic strain distribution evolving with pillar decreasing (dissolution) cross section.

The case of a domain containing a gypsum lens is shown in Fig. 5.28, with the parameters given in Tables 5.2 and 5.3. The mechanical consequences of gypsum lens dissolution are illustrated in Figs. 5.29 - 5.32. The first figures give the vertical displacement evolution with time. The subsidence increases with dissolution as expected. In some cases, function of the mechanical features

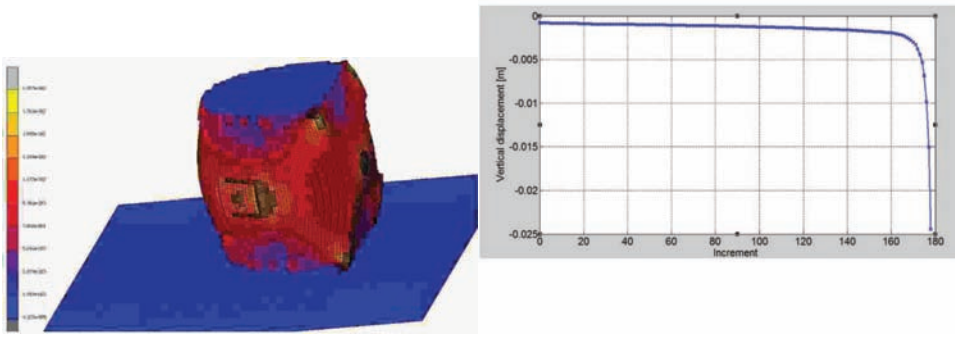

(a) (b)

Figure 5.26: 3D view of the equivalent plastic strain at collapse and "time-increment" evolution of the vertical displacement of material at a point located in the center of the roof.

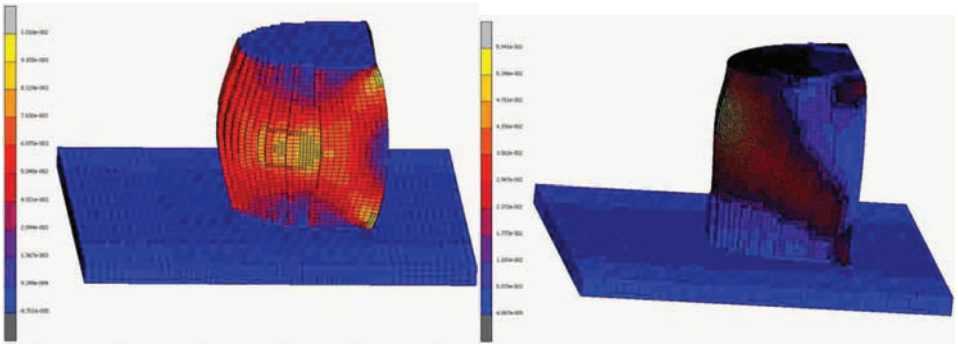

(a) (b)

Figure 5.27: Distribution of equivalent plastic strain for two top support layers: (a) stiff-rigid; and (b) soft support.

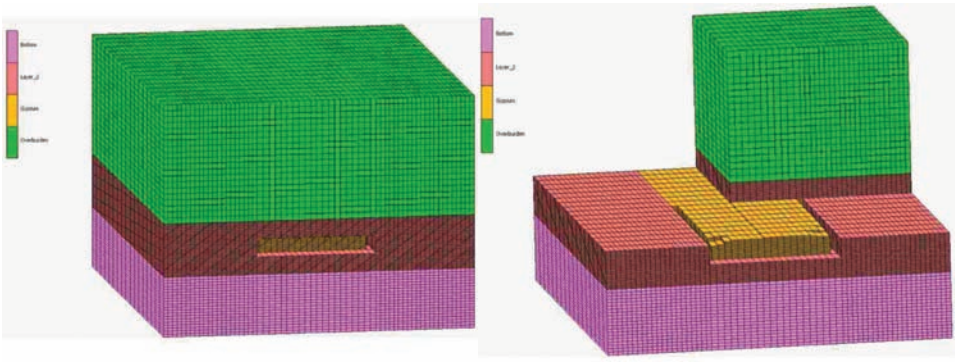

(a) (b)

Figure 5.28: (a) 3D model geomechanical model; and (b) location of the gypsum lens.

of overburden, sinkhole can develop and reach the surface. The pseudo-times

T1 to T4 stand for four states of dissolution (four cavity volumes), and the last T4 corresponds to the total dissolution. The vertical displacement along a line passing through the middle of the model for the four states of dissolution is illustrated in Fig. 5.31. It must be emphasized that even such small intensity subsidence can affect buildings. In fact, this is not so much the intensity of subsidence but the pond curvature and the position of the structure on the pond. The effective plastic strain distribution at two dissolution states (beginning and at the end) are depicted in Fig. 5.32. Although it is located in a relatively small domain, plasticity affects a part of the recovery, due to poor mechanical properties. For the lens dissolution problem, the layer containing the gypsum lens is strong enough and prevents a global collapse (sinkhole).

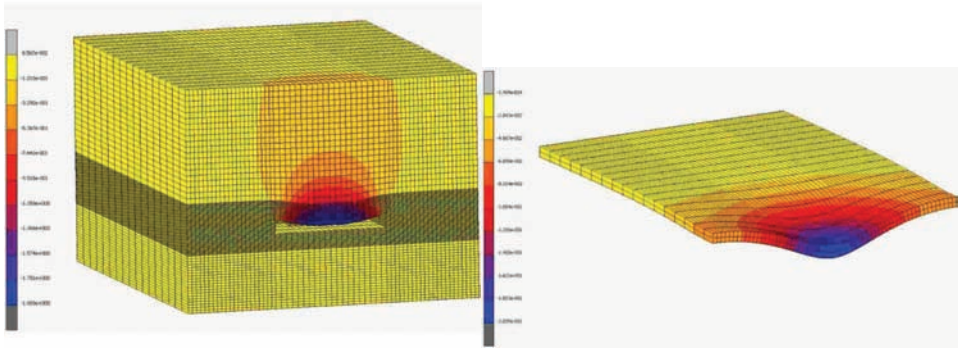

(a) (b)

Figure 5.29: Isovalue of the vertical displacement: (a) after the whole dissolution of the gypsum lens; and (b) subsidence pond.

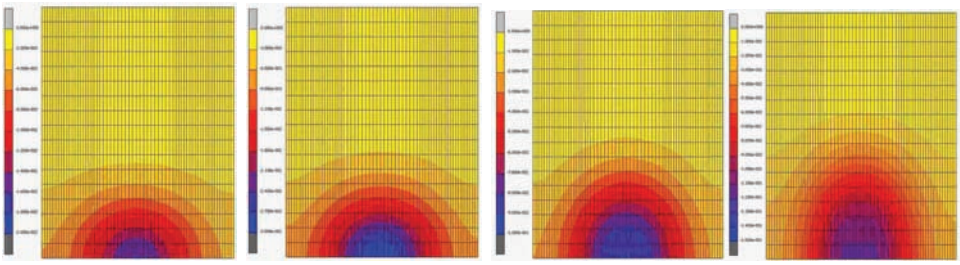

(a) (b) (c) (d)

Figure 5.30: From a to d : top views of surface vertical displacement increasing with four cavity volumes.

The objective of this subsection was to show the mechanical consequences of the dissolution. Assuming a situation closer to leaching, i.e., a sharp dissolution front, it is only necessary to solve for the geomechanical problem at different stages of dissolution, regardless of the evolution kinetics. Indeed, the

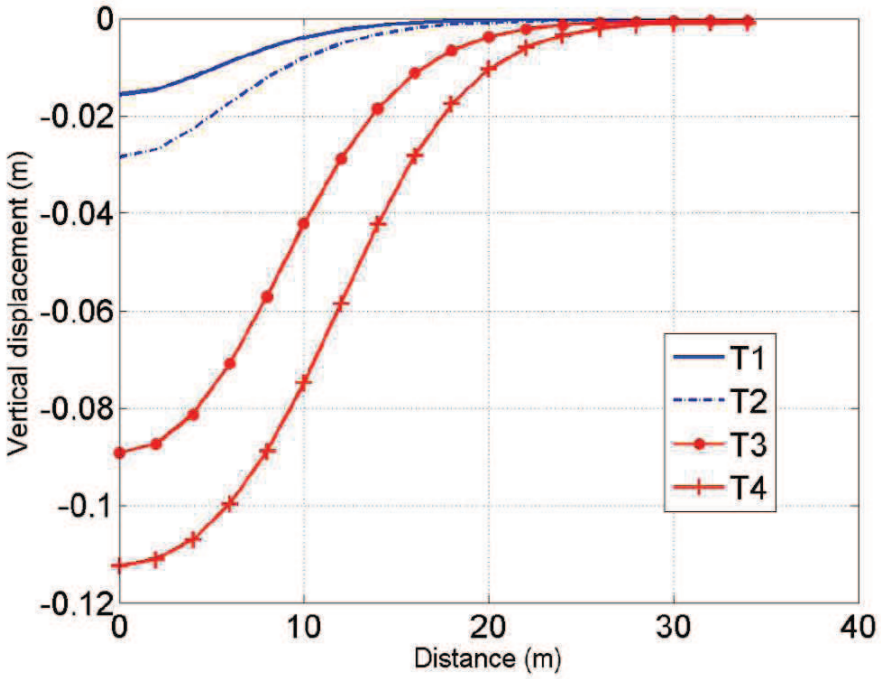

Figure 5.31: Vertical displacement (subsidence) along a line passing through the middle of the model for four (T1,.., T4) states of dissolution.

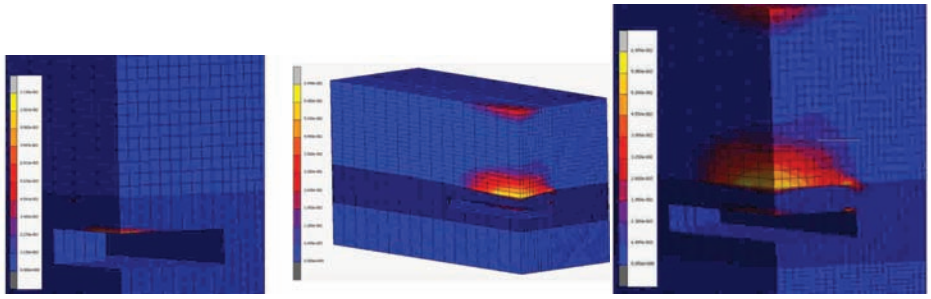

(a) (b) (c)

Figure 5.32: Effective plastic strain distribution induced by the cavity growing.

resulting coupling is weak and should be replaced by a complete numerical formulation in the case of a porous domain dissolution. One point that seems important to emphasize is that, if the geometric features of a given cavity and the hydrodynamic conditions are known properties, the dissolution model may allow us, using an inverse analysis, to deduce the history of the dissolution (time evolution of the cavity).

5.4 Range of application of the method on other evaporites

The general method developed in this study was illustrated in the case of gypsum rock dissolution. However, it has a wide range of applications as demonstrated in this section. The example presented briefly concerns the dissolution of salt. The kinetic evolution of a cavity located in salt (NaCl) or gypsum domain is also compared. The results show that the method is robust whatever the kinetics of dissolution.

Gypsum dissolves in flowing water about one hundred times more rapidly than limestone, but at only about one thousandth the rate of halite. Another major difference lies in the fact that density variations with concentration are much more pronounced in the case of halite dissolution than in the case of gypsum. It is therefore interesting to test the proposed workflow on the case of a large scale salt cavity. The test case corresponds to the solution mining situation schematically represented Fig. 5.33. A salt layer located at a depth of about 280 meters and with a thickness equal to 6.50 m is drilled with a leaching well constituted by two concentric tubes. Then a leaching process was initiated by injecting fresh water through the central annulus during 12 days [3]. The inlet flow was 3 m^3/h (0.08 ms^{-1}) during 4 days and then 1.5 m^3/h (0.04 ms^{-1}) during 8 days (Fig. 5.33) [3]. Calculations were also performed with salt material replaced by gypsum. Some numerical results are presented below to emphasize the differences in the dissolved shapes between the salt and gypsum cases.

The shapes of the cavity created in the gypsum and salt medium are illustrated in Figs. 5.34 and 5.35, respectively. As expected, one observes a very low dissolution rate and a different cavity geometry for gypsum compared to those of salt. This shape difference is attributed to the presence of natural convection effects which are very strong for salt compared to gypsum, which has a much lower solubility.

This solution mining example corresponds to an INERIS pilot site [3] for which measurements of total dissolved volume were available. The computed dissolved volume is about 12 m^3 after 4 days for an in situ measurement about 11 m^3 and about 38 m^3 after 12 days for an in situ measurement about 40 m^3, which shows a very good agreement between the large-scale simulations and the actual pilot data. Overall, this example shows that the proposed workflow works also very well for a more soluble material for which there is a strong

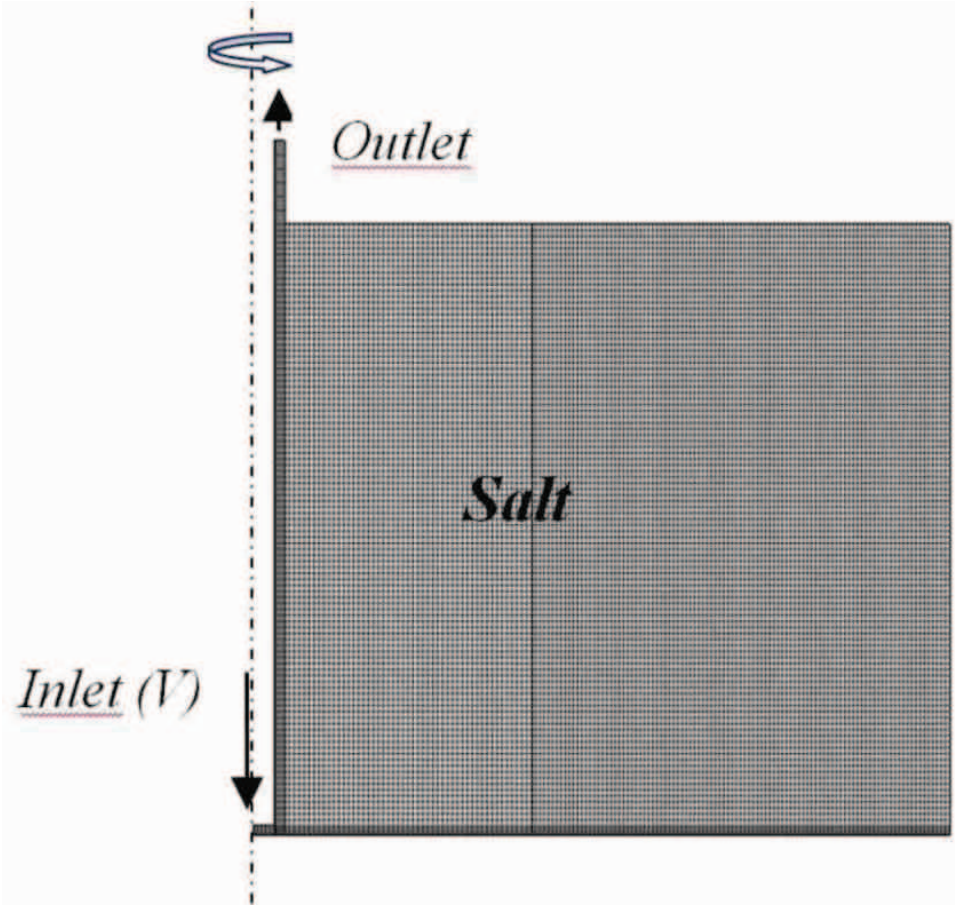

Figure 5.33: Schematic illustration of the solution mining process.

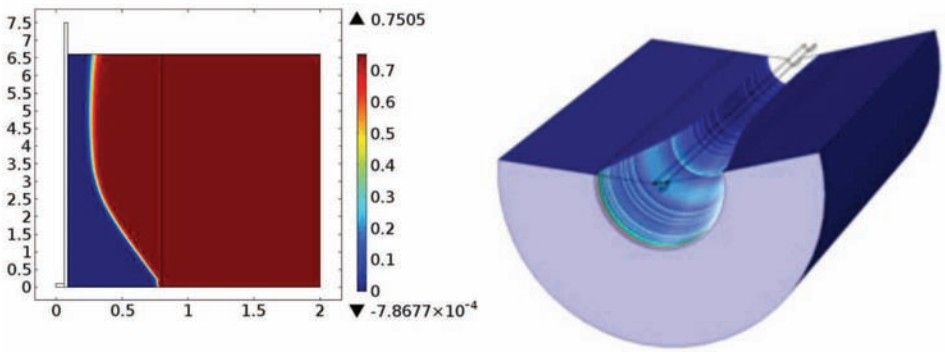

(a) (b)

Figure 5.34: 2D (blue part) and 3D illustrations of the gypsum cavity (symmetry of revolution) after 3 years of injection of fresh water at the velocity of 0.08 $\mathrm{m\,s^{-1}}$ (thickness of the layer is 6.6 m).

potential for natural convection effects, especially for large cavities.

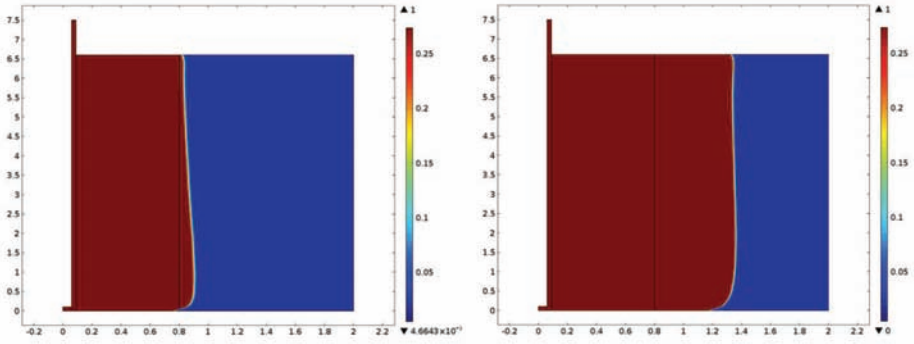

(a) (b)

Figure 5.35: Isovalue of the porosity after 4 days (a) and 12 days (b) for salt. (void is equal to unity).

5.5 Conclusion

Using the assumptions of a pseudo-component dissolving with a thermodynamic equilibrium boundary condition, a general numerical approach has been designed and tested to solve for large-scale cavity dissolution problems, typically for an aquifer situation leading to potential subsidence, sinkhole formation, etc. From a numerical view point direct interface tracking, such as ALE, was found to be very difficult to carry on and an alternate route was proposed using a DIM (Diffuse Interface Method) based on a non-equilibrium porous medium theory. A workflow was proposed to choose properly the parameters in the DIM model that would reproduce as accurately as possible the mass fraction field and fluxes and, consequently, the interface recession, for problems with various temporal and space scales, e.g. 1D tube to 3D decametric problems.

Additional tests were performed to check which type of momentum balance equation should be used. It was found that Darcy, Darcy-Brinkman or Navier-Stokes formulations gave almost the same cavity formation because the permeability used was small. This is explained by the absence of convective plumes, verified by a comparison with a model taking into account density variations through a Boussinesq approximation.

The proposed model allows to model dissolution of large scale problems over very large time periods. The potential of the approach is shown on the 3D modeling of gypsum lens and pillar in gypsum quarry which may lead to formation collapse. The strong coupling between mechanics and dissolution is not fully taken into account, but geomechanical effects induced by disso-

lution (leaching) were illustrated using a simplified approach. Results show that while gypsum is a slightly soluble material, its dissolution rate is unfortunately not zero and may impact on the long term structures and buildings mechanical stability, if dissolution is triggered by natural or anthropic factors. The developed approach, while it may be the subject of many enhancements in terms of geochemistry and mechanics, has an undeniable predictive quality.

Chapter 6

General conclusions and perspectives

In this thesis, the multi-scale features of dissolution problems were studied in the context of karstic cavity evolution. At first, a pore-scale model was developed, which describes the dissolution physics for "simple" geochemistry (typically salt and gypsum). The assumptions introduced when developing such a model were clarified. In particular, the hypothesis of working with a pseudo-component dissolution in water was justified in the case of gypsum as the soluble mineral, provided a few percent incertitude is acceptable for the mass fraction field calculation. The different choices of boundary conditions that may be prescribed at the dissolving surface, thermodynamic equilibrium, one-rate reactive or two-rate nonlinear reactive, only produced differences of a few percent in terms of mass flux at the outlet boundary, for a classical boundary value problem. The fact that reactive boundary conditions can be replaced by thermodynamic equilibrium in some circumstances provided the possibility of using a diffuse interface model in large-scale cavity evolution simulations, with proper choice of the effective parameters, which was discussed in detail in Chap. 5.

Macro-scale descriptions of the dissolution problem were obtained for two multi-scale situations, with one being developed with the concept of effective surface and the other with the method of volume averaging (an upscaling method). Thermodynamic equilibrium and reactive solid-liquid boundary conditions were both considered in the two model developments, in order to obtain complete forms of the models. While the developments of the two macro-scale models shared some common assumptions, for instance the periodicity of some properties at pore-scale, the separation of scales involved and the decomposi-

tion of the micro-scale variables, etc, there are many differences between these two approaches, such as the way of defining macro-scale variables and the stage of employing periodicity assumption, etc. With further discussions available in [78] for the porous medium homogenization process, the working procedures of these two approaches performed in this study can be summarized as follows.

For the model developed with the effective surface concept (ESCM), the study concerns mass (and momentum) transfer for a laminar flow over a heterogeneous rough surface characterized by *mixed* boundary conditions. Assuming local periodicity of the flow near the surface, then multi-domain decomposition was used to partition the domain under investigation into a macro-scale subdomain and a range of micro-scale unit cells. The global problem was then rewritten for the macro- and micro-scale domains, respectively. The micro-scale variables were decomposed into a macro-scale term and a deviation term. Considering $\epsilon \ll 1$ ($\epsilon = l_{cell}/L$) allowed to simplify the IBVPs, followed by the definition of the structure of the deviation solution via the first order Taylor expansion estimation of the macro-scale term. Solutions of the deviations by solving the closure problems and consequently the description of the problem with macro-scale variables were obtained. Hence, the effective boundary conditions for an arbitrary choice of the effective surface can be prescribed, Navier condition for the momentum boundary condition and "reactive condition" for the Robin type mass condition. The effective boundary conditions which recover no-slip or thermodynamic equilibrium condition are of special interests. According to the recovery of such particular boundary conditions, the position of the effective surface can be determined by solving the corresponding closure problems.

For the macro-scale porous medium model (PMM) obtained with the method of volume averaging, upscaling was carried out for a mass transport problem involving a nonlinear heterogeneous reaction typical of dissolution problems, starting from the pore-scale problem described in Chap. 2. Volume averages were first defined and applied to average the pore-scale model. "Average-plus-deviation" decompositions were introduced to the pore-scale variables, thus the pore-scale problem was rewritten with coupled parameters at different scales. First order Taylor expansion was also used for estimating the reaction rate when developing the equations for the concentration deviation, and the solution structure was determined accordingly for the perturbation terms. Based on the resolution of the closure problems, two classical effective parameters, the dispersion tensor, the effective reaction rate coefficient and two non-classical

effective parameters, the effective velocity and the gradient term coefficient were obtained. Compared to the previous published works as mentioned in the main body, a full couplings of the two closure variables as well as the interface velocity were kept in the closure problems, in addition to the consideration of the non-classical effective parameters.

After the homogenization of either ESCM or PMM, the impact of some properties were investigated, as summarized in Table. 6.1. It is observed that both the two models were affected by the geometry under consideration, the flow properties and the chemical features of the media. The representativity of the macro-scale models were validated by comparing the results with DNS, both showing good agreements except for the discrepancy created in the entrance region, where the periodicity assumption breaks down.

The above developed macro-scale porous medium model is also capable to behave as a diffuse interface model (DIM), which is an alternative way of simulating cavity evolutions at large-scale, while it is numerically difficult to use explicit interface tracking methods such as ALE. A workflow was proposed to choose properly the effective parameters in the DIM model in order to reproduce the mass fraction field, mass fluxes and consequently the interface recession with good accuracy, for problems with various temporal and space scales. In addition, numerical tests illustrated that to use Darcy, Darcy-Brinkman or Navier-Stokes formulations as the momentum equations gave almost the same cavity formation because of the small permeability being used. The absence of convective plumes in the case of gypsum was verified by a comparison with a model taking into account density variations through a Boussinesq approximation.

The potential of the approach to model dissolution of large scale problems over very large time periods was shown in the 3D modeling of gypsum lens and pillar in gypsum quarry which may lead to formation collapse. Geomechanical effects induced by dissolution (leaching) were illustrated using a simplified approach, without considering a strong coupling between mechanics and dissolution. Results showed the impact of gypsum dissolution on the long term structures and buildings mechanical stability, which may be triggered by natural or anthropic factors.

The framework developed in this thesis is applicable to simulate dissolution process in various research areas, for instance in the evolution of karstic structures, drying, CO_2 storage and in the application of acid injection in petroleum wells in enhanced oil recovery. As indicated in the introduction,

Table 6.1: Summary of the impact of various parameters on the macro-scale models.

parameters	ESCM	PMM
unit cell geometries	steep roughness shape and high roughness density inducing the effective surface position farther from the lower part of the original surface and weaker impact of flow properties	less tortuosity impact in the 1D case; important role of the insoluble materials
flow properties	negligible impact of convection: when $\mathrm{Sc} < 0.1$ and $\mathrm{Pe} < 1000$ with thermodynamic equilibrium BC; when $\mathrm{Sc} < 1$ and $\mathrm{Pe} < 1000$ with reactive BC at small $\widehat{\mathrm{Da}}$	stronger impact of dispersive term and non-classical effective parameters at large Pe
chemical properties	(1) reaction limited case under small $\widehat{\mathrm{Da}}$: acceptable to approximate the effective reaction rate coefficient by the surface average; (2) mass transport limited case under large $\widehat{\mathrm{Da}}$: effective reaction rate coefficient should be calculated by the closure problems; strong impact of flow properties; important convection	(1) under small Da: representation of the effective reaction rate coefficient by the pore-scale one; (2) under large Da: smaller impact of tortuosity and dispersion; stronger impact of reaction nonlinearity; recovery of thermodynamic equilibrium and different estimation of the mass exchange term from the reactive case
model validation compared with DNS	(1) considering: concentration and velocity contours, mass flux at the interface (2) results: good representativity and efficiency of ESCM; best choice of effective surface being the one that recovers no-slip condition	(1) considering: apparent reactive term; (2) results: good representativity of the PMM except in the entrance region; important to incorporate the non-classical effective terms

one of the motivation for this study was to model phenomena taking place at "dissolving" interfaces. Therefore, the surface geometry is not given a priori

but is a result of the process. Even though the development of PMM kept interface velocity in all the steps, the resolution of the closure problems, like in the development of ESCM, were conducted assuming quasi-steady state. Also, the calculations of effective parameters in the applications provided were not based on an actual dissolved pore-scale geometry. In addition, the development of the macro-scale models, either the ESCM or PMM, was based on a bundle of assumptions, such as constant fluid parameters, negligible interface velocity, pseudo component for the dissolved material, etc. However, real conditions are much more complicated and great attention should be paid where such assumptions may break down. For example, (i) the periodicity assumption may be not valid in the entrance region of the considered domains; (ii) the dissolution of the porous matrix may lead to significant variation of porosity and consequently permeability and other effective parameters; (iii) the dissolving front may become unstable and may lead to the development of wormhole structures; and (iv) under some circumstances, hydrodynamic instabilities may also be induced by density change, such as in the case of salt dissolution in water. It is beyond the scope of this conclusion to review all the perspectives associated with these questions.

Concerning the coupling with the pore-scale geometry evolution, if one is not satisfied with the geochemistry assumption, i.e., dependence of the effective parameters on the porosity, our developments offer a framework for a coupled solution between the macro-scale equation, on one hand, and the pore-scale closure problems under the full version including the transient aspects, on the other hand.

Conclusions générales et perspectives en français

Dans cette thèse, on a étudié certains aspects multi-échelles rencontrés dans l'étude de l'évolution de cavités souterraines. Dans un premier temps, on a étudié un modèle de dissolution à l'échelle du pore pour une géochimie simple, pouvant être appliquée à la dissolution de cavités salines ou de gypse. Les hypothèses pour pouvoir développer un tel modèle sont clarifiées. En particulier, on discute de la possibilité d'utiliser le concept de pseudo-constituant pour le cas de la dissolution de gypse dans l'eau, à condition qu'une erreur de quelques pour cents soit acceptable. Par ailleurs, les différents choix possibles de conditions aux limites sur l'interface soluble, à savoir équilibre thermodynamique, conditions réactive non-linéaire, produisent également une différence de quelques pour cents sur les bilans de masse ou flux de sortie, pour un problème aux limites classique. Si on peut remplacer des conditions réactives par des conditions d'équilibre, on peut alors utiliser un modèles de dissolution à interface diffuse basé sur cette condition, pour simuler des cavités à grande échelle sans suivi explicite du front de dissolution, à condition de choisir convenablement les paramètres du modèle, comme cela est expliqué dans le Chap. 5.

Deux problèmes multi-échelles ont été étudiés et les modèles macroscopiques correspondant construits: le premier correspondant au concept de surface effective, le second étant un problème classique de milieu poreux. Des conditions aux limites d'équilibre ou réactives ont été considérées dans les deux cas. Bien que de nombreuses hypothèses soient similaires entre les deux problèmes multi-échelles, par exemple certaines conditions de périodicité, les hypothèses de séparation d'échelles ou la décomposition en déviations et grandeurs macroscopiques, la mise en oeuvre reste spécifique. Par exemple, la définition des grandeurs macroscopiques est très différente. La mise en oeuvre de ces deux méthodes est succinctement décrite ci-dessous, et on se référera à [78] pour des

discussions supplémentaires sur le changement d'échelle.

Pour le modèle de surface effective (ESCM), l'étude à concerné le transfert de masse et de quantité de mouvement pour un écoulement laminaire au-dessus d'une surface rugueuse et hétérogène, avec une condition aux limites mixte pour le transfert multiconstituant. En faisant l'hypothèse de périodicité de l'écoulement près des motifs périodiques de la surface, une méthode de décomposition multi-domaine est utilisée pour partitionner le domaine en un domaine macroscopique et des sous-domaine microscopiques pour les cellules unitaires de la surface. Le problème initial est ré-écrit dans ce contexte. Les variables microscopiques sont décomposées en un terme macroscopique et un terme de déviation. En faisant l'hypothèse $\epsilon \ll 1 (\epsilon = l_{cell}/L)$ et utilisant des développements de Taylor, des simplifications permettent de proposer une solution pour les déviations en termes de la solution macroscopique (problèmes de fermeture). La résolution des problèmes de fermeture permet d'obtenir un problème fermé pour les variables macroscopiques avec des conditions aux limites effectives sur la surface séparant les deux domaines: une condition de Navier pour le bilan de quantité de mouvement et une condition de Robin *réactive* pour le transfert de masse. La méthode permet également, via des développements de Taylor, de repositionner la surface effective, ce qui donne de nouvelles conditions aux limites effectives. Certains choix permettent de retrouver la condition de non-glissement, ou une condition d'équilibre.

Le modèle macroscopique pour le cas du milieu poreux (PMM) est obtenu par une méthode de prise de moyenne volumique en partant du modèle à l'échelle du pore introduit dans le Chap. 2 et impliquant une condition réactive non-linéaire sur l'interface matériau soluble-eau. Les équations à l'échelle du pore sont d'abord moyennées. Une décomposition valeurs moyennes-déviations est ensuite introduite ce qui permet de réécrire les équations moyennes et les équations à l'échelle du pore. Une solution approchée de ce problème couplée est obtenue sous la forme d'une représentation des déviations en termes des grandeurs moyennes (problèmes de fermeture). La contribution du terme non-linéaire est traitée en utilisant une décomposition de Taylor au premier ordre. La résolution des problèmes de fermeture permets de calculer deux paramètres effectifs plus classiques (dispersion et réaction effective) ainsi que des termes non-traditionnels introduisant une vitesse effective et des termes en gradient supplémentaires. La contribution originale de la thèse correspond au traitement de la non-linéarité, la prise en compte de la vitesse de l'interface dans la fermeture et une discussion sur les termes complémentaires.

Dans le cadre de ces deux processus de macroscopisation, l'impact quantitatif de divers paramètres (géométrie, paramètres de l'écoulement et propriétés réactives et du fluide) a été étudié, comme résumé Table 6.1. La capacité prédictive des modèles macroscopiques a été testée par comparaison avec des simulations numériques directes. L'accord est excellent, avec un écart observable seulement dans la zone d'entrée pour laquelle l'hypothèse de périodicité ne tient pas.

Le modèle de milieu poreux développé est aussi utilisable comme un modèle de dissolution à interface diffuse (DIM), dans le cas d'une condition d'équilibre sur la surface liquide-soluble. Une telle méthode est une alternative aux méthodes de suivi explicite de l'interface, comme la méthode ALE qui rencontre souvent des difficultés à cause de la déformation particulière de l'interface en dissolution. De nombreuses difficultés numériques doivent être résolues dues à la physique à petite échelle conduisant à la récession de l'interface. Une méthodologie particulière est proposée pour estimer correctement les paramètres dans le DIM permettant de simuler correctement les flux et donc la vitesse de récession. En outre, des tests ont été effectués pour vérifier l'impact du choix du modèle macroscopique de bilan de quantité de mouvement Darcy, Darcy-Brinkamn, Darcy-Navier-Stokes. Aucune différence significative n'a été observée pour un problème de dissolution de cavité typique, à cause de la faible perméabilité utilisée. L'absence d'impact significatif de la convection naturelle dans le cas du gypse a été vérifié par des simulations dans le cadre de l'hypothèse de Boussinesq.

Le potentiel de la méthodologie proposée pour simuler l'évolution de cavités sur du long terme (plusieurs années) a été illustré sur un problème à grande échelle 3D: dissolution d'un pilier dans une carrière souterraine de gypse inondée. Les effets géomécaniques induits par la dissolution du pilier ont été évalués de manière simplifiée sans considérer un couplage fort géomécanique-géochimie. Les résultats montrent un impact fort de la dissolution, provoquée par des causes naturelles ou anthropiques, sur la stabilité mécanique des structures.

La méthodologie proposée dans la thèse est applicable à la simulation de la dissolution dans divers domaines, karsts, stockage de CO_2, injection d'acide en génie pétrolier, etc... Comme indiqué dans l'introduction, une des motivations de l'étude était la prise en compte des transferts sur une interface en évolution lors de la dissolution, qui n'est donc pas donnée à priori mais un résultat du processus lui-même. Même si le développement du modèle de milieu poreux

garde l'évolution de l'interface dans les problèmes de fermeture, ceux-ci n'ont été résolus que pour des interfaces données à priori. De nombreuses hypothèses complémentaires ont été également introduite dans le développement: pseudo-constituant, propriétés du fluide constantes, quasi-stationnarité des problèmes de fermeture, etc... Ces hypothèses ont été présentées avec attention et il est souhaitable que, dans un cas d'application réel, celles-ci soient vérifiées précisément. Par exemple, (i) la condition de périodicité n'est pas vérifiée dans la zone d'entrée, (ii) la dissolution peut amener à des variations significatives de la géométrie et des propriétés effectives, (iii) le front de dissolution peut devenir instable (wormholing), (iv) des instabilités hydrodynamiques peuvent prendre naissance dans les couches limites près de la surface de dissolution à cause des variations de densité du fluide induisant une structure particulière de l'interface. Ces points doivent faire l'objet de travaux complémentaires.

En ce qui concerne le problème fondamental du couplage avec l'évolution de la géométrie de l'espace poral, le modèle proposé offre la possibilité de traiter de manière couplée les équations macroscopiques et les problèmes de fermeture de façon à actualiser en permanence la géométrie porale et les propriétés effectives en liaison avec le processus macroscopique étudié.

Bibliography

[1] F. Gutiérrez, M. Parise, J. De Waele, and H. Jourde. A review on natural and human-induced geohazards and impacts in karst. *Earth-Science Reviews*, 138(0):61 – 88, 2014.

[2] G. Kaufmann. Geophysical mapping of solution and collapse sinkholes. *Journal of Applied Geophysics*, 111:271–288, 2014.

[3] A. Charmoille, X. Daupley, and F. Laouafa. *Analyse et Modélisation de l'évolution Spatio-temporelle des Cavités de Dissolution*. Report DRS-12-127199-10107A. INERIS, 2012.

[4] S. Békri and O. Vizika. Pore-network modeling of rock transport properties: application to a carbonate. In *International Symposium of the Society of Core Analysts, Trondheim, Norway, Sept*, pages 12–16, 2006.

[5] S. Youssef, E. Rosenberg, N. Gland, S. Békri, and O. Vizika. Quantitative 3D characterisation of the pore space of real rocks: improved μ-CT resolution and pore extraction methodology. *Int. Sym. Soc. Core Analysts, Calgary*, 2007.

[6] S. Békri, S. Renard, and F. Delprat-Jannaud. Pore to core scale simulation of the mass transfer with mineral reaction in porous media. *Oil & Gas Science and Technology–Revue d'IFP Energies nouvelles*, 2015.

[7] T. Waltham, F. G. Bell, and M. Culshaw. *Sinkholes and subsidence: karst and cavernous rocks in engineering and construction*. Springer Science & Business Media, 2005.

[8] M. Toulemont. Les risques d'instabilité liés au karst gypseux lutétien de la région parisienne. *Prevision en cartographie. Bull. Liaison Laboratiore Physique et Chimie*, 150:151, 1987.

[9] R. O. Van Everdingen. Morphology, hydrology and hydrochemistry of karst in permafrost terrain near Great Bear Lake, Northwest Territories. *National Hydrology Research Institute Paper*, (11), 1981.

[10] F. Golfier, C. Zarcone, B. Bazin, R. Lenormand, D. Lasseux, and M. Quintard. On the ability of a Darcy-scale model to capture wormhole formation during the dissolution of a porous medium. *Journal of Fluid Mechanics*, 457:213–254, 2002.

[11] J. M. Nordbotten and M. A. Celia. *Geological Storage of* CO_2*: Modeling Approaches for Large-scale Simulation*. John Wiley & Sons, 2011.

[12] J. D. Waele, L. Plan, and P. Audra. Recent developments in surface and subsurface karst geomorphology: An introduction. *Geomorphology*, 106(1–2):1–8, 2009.

[13] A. Cooper. Halite karst geohazards (natural and man-made) in the United Kingdom. *Environmental Geology*, 42(5):505–512, February 2002.

[14] F. Gutiérrez, J. Guerrero, and P. Lucha. A genetic classification of sinkholes illustrated from evaporite paleokarst exposures in Spain. *Environmental Geology*, 53(5):993–1006, 2008.

[15] A. C. Waltham and P. G. Fookes. Engineering classification of karst ground conditions. *Quarterly Journal of Engineering Geology and Hydrogeology*, 36(2):101–118, 2003.

[16] H. Karimi. *Hydrogeology - A Global Perspective*, chapter 1, pages 1–42. InTech, 2012.

[17] D. Gechter, P. Huggenberger, P. Ackerer, and H. N. Waber. Genesis and shape of natural solution cavities within salt deposits. *Water Resources Research*, 44(11), 2008.

[18] A. N. Palmer. Origin and morphology of limestone caves. *Geological Society of American Bulletin*, 103:1–21, 1991.

[19] A. B. Klimchouk. Speleogenesis in gypsum. *Int. J. Speleol.*, 25(3 – 4):61–82, 1996.

[20] A. B. Klimchouk. Large gypsum caves in the western Ukraine and their genesis. *Cave Sci.*, 19(1):3 – 11, 1992.

[21] M. D. Rose, A. Federico, and M. Parise. Sinkhole genesis and evolution in Apulia, and their interrelations with the anthropogenic environment. *Natural Hazards and Earth System Sciences*, 4:747–755, 2004.

[22] M. Parise and P. Lollino. A preliminary analysis of failure mechanisms in karst and man-made underground caves in Southern Italy. *Geomorphology*, 134(1–2):132 – 143, 2011.

[23] G. Li and W. Zhou. Sinkholes in karst mining areas in China and some methods of prevention. *Engineering Geology*, 52(1–2):45 – 50, 1999.

[24] M. Heidari, G. R. Khanlari, A. R. T. Beydokhti, and A. A. Momeni. The formation of cover collapse sinkholes in North of Hamedan, Iran. *Geomorphology*, 132:76–86, 2011.

[25] J. D. Martinez, K. S. Johnson, and J. T. Neal. Sinkholes in evaporite rocks: Surface subsidence can develop within a matter of days when highly soluble rocks dissolve because of either natural or human causes. *American Scientist*, 86(1):38–51, 1998.

[26] B. F. Beck and W. C. Sinclair. *Sinkholes in Florida: An introduction.* Florida Sinkhole Research Institute, 1986.

[27] K. S. Johnson. Gypsum-karst problems in constructing dams in the USA. *Environmental Geology*, 53(5):945–950, 2008.

[28] R. Brinkmann, M. Parise, and D. Dye. Sinkhole distribution in a rapidly developing urban environment: Hillsborough County, Tampa Bay area, Florida . *Engineering Geology*, 99(3–4):169 – 184, 2008.

[29] A. H. Cooper. Subsidence hazards caused by the dissolution of Permian gypsum in England: geology, investigation and remediation. *Geological Society, London, Engineering Geology Special Publications*, 15(1):265–275, 1998.

[30] M. Van Den Eeckhaut, J. Poesen, M. Dusar, V. Martens, and Ph. Duchateau. Sinkhole formation above underground limestone quarries: A case study in South Limburg (Belgium). *Geomorphology*, 91(1–2):19 – 37, 2007.

[31] Y. Lu and Anthony H Cooper. Gypsum karst geohazards in China. *The Engineering*, pages 117–126, 1997.

[32] M. Parise L. Plan J. De Waele, F. Gutiérrez. Geomorphology and natural hazards in karst areas: A review. *Geomorphology*, 134:1–8, 2011.

[33] D. C. Ford and P. W. Williams. *Karst Geomorphology and Hydrology*. Unwin Hyman, 1989.

[34] W. B. White. *Geomorphology and Hydrology of Karst Terrains*. Oxford University Press, 1988.

[35] W. H. Langer. *Potential Environmental Impacts of Quarrying Stone in Karst — A Literature Review*. U.S. Geological Survey Open-File Report 0 F-01-0484, 2001.

[36] P. Lollino, V. Martimucci, and M. Parise. Geological survey and numerical modeling of the potential failure mechanisms of underground caves. *Geosystem Engineering*, 16(1):100–112, 2013.

[37] F. Mancini, F. Stecchi, M. Zanni, and G. Gabbianelli. Monitoring ground subsidence induced by salt mining in the city of Tuzla (Bosnia and Herzegovina). *Environmental Geology*, 58(2):381–389, 2009.

[38] R. Salvati and I. D. Sasowsky. Development of collapse sinkholes in areas of groundwater discharge. *Journal of Hydrology*, 264(1–4):1 – 11, 2002.

[39] T. Hiller, D. Romanov, F. Gabrovsek, and G. Kaufmann. The creation of collapse dolines: A 3D modeling approach. *ACTA CARSOLOGICA*, 43:241–255, 2014.

[40] A. M. Tartakovsky, D. M. Tartakovsky, T. D. Scheibe, and P. Meakin. Hybrid simulations of reaction-diffusion systems in porous media. *SIAM J. Sci. Comput.*, 30(6):2799–2816, 2008.

[41] C. Varloteaux, M. T. Vu, S. Békri, and P. M. Adler. Reactive transport in porous media: Pore-network model approach compared to pore-scale model. *Physical Review E*, 87(2):023010, 2013.

[42] C. Introïni, M. Quintard, and F. Duval. Effective surface modeling for momentum and heat transfer over rough surfaces: Application to a natural convection problem. *International Journal of Heat and Mass Transfer*, 54(15–16):3622–3641, 2011.

[43] S. Veran, Y. Aspa, and M. Quintard. Effective boundary conditions for rough reactive walls in laminar boundary layers. *International Journal of Heat and Mass Transfer*, 52(15–16):3712 – 3725, 2009.

[44] W. Dreybrodt, J. Lauckner, Liu Zaihua, U. Svensson, and D. Buhmann. The kinetics of the reaction $CO_2 + H_2O \rightarrow H^+ + HCO_3^-$ as one of the rate limiting steps for the dissolution of calcite in the system $H_2O - CO_2 - CaCO_3$. *Geochimica et Cosmochimica Acta*, 60(18):3375 – 3381, 1996.

[45] J. Colombani. Measurement of the pure dissolution rate constant of a mineral in water. *Geochimica et Cosmochimica Acta*, 72(23):5634 – 5640, 2008.

[46] W. Dreybrodt. Kinetics of the dissolution of calcite and its applications to karstification. *Chemical Geology*, 31(0):245–269, 1980–1981.

[47] L. Eisenlohr, K. Meteva, F. Gabrovšek, and W. Dreybrodt. The inhibiting action of intrinsic impurities in natural calcium carbonate minerals to their dissolution kinetics in aqueous H_2O– CO_2 solutions. *Geochimica et Cosmochimica Acta*, 63(7–8):989–1001, 1999.

[48] U. Svensson and W. Dreybrodt. Dissolution kinetics of natural calcite minerals in CO_2-water systems approaching calcite equilibrium. *Chemical Geology*, 100(1–2):129–145, 1992.

[49] A. A. Jeschke, K. Vosbeck, and W. Dreybrodt. Surface controlled dissolution rates of gypsum in aqueous solutions exhibit nonlinear dissolution kinetics. *Geochimica et Cosmochimica Acta*, 65(1):27–34, 2001.

[50] M. Alkattan, E. H. Oelkers, J. L. Dandurand, and J. Schott. Experimental studies of halite dissolution kinetics, 1 The effect of saturation state and the presence of trace metals. *Chemical Geology*, 137(3–4):201 – 219, 1997.

[51] A. C. Lasaga and A. Luttge. Variation of crystal dissolution rate based on a dissolution stepwave model. *Science*, 23:2400–2404, 2001.

[52] W. Dreybrodt. The role of dissolution kinetics in the development of karstification in limestone: A model simulation of karst evaluation. *The Journal of Geology*, 98:639–655, 1990.

[53] W. Dreybrodt. Principles of early development of karst conduits under natural and man-made conditions revealed by mathematical analysis of numerical models. *Water Resources Research*, 32(9):2923–2935, 1996.

[54] L. N. Plummer and T. M. L. Wigley. The dissolution of calcite in CO_2-saturated solutions at 25 °C and 1 atmosphere total pressure. *Geochimica et Cosmochimica Acta*, 40:191–202, 1976.

[55] C. Rehrl, S. Birk, and A. B. Klimchouk. Conduit evolution in deep-seated settings: Conceptual and numerical models based on field observations. *Water Resources Research*, 44(11), 2008.

[56] P. E. Dijk and B. Berkowitz. Precipitation and dissolution of reactive solutes in fractures. *Water Resources Research*, 34(3):457–470, 1998.

[57] S. Birk, R. Liedl, M. Sauter, and G. Teutsch. Hydraulic boundary conditions as a controlling factor in karst genesis: A numerical modeling study on artesian conduit development in gypsum. *Water Resources Research*, 39(1), 2003.

[58] F. J. Valdés-Parada, C. G. Aguilar-Madera, and J. Álvarez Ramírez. On diffusion, dispersion and reaction in porous media. *Chemical Engineering Science*, 66(10):2177 – 2190, 2011.

[59] P. Szymczak and A. J. C. Ladd. The initial stages of cave formation: Beyond the one-dimensional paradigm. *Earth and Planetary Science Letters*, 301(3–4):424 – 432, 2011.

[60] L. N. Plummer, T. M. L. Wigley, and D. L. Parkhurst. The kinetics of calcite dissolution in CO_2 -water systems at 5° to 60°C and 0.0 to 1.0 atm CO_2. *American Jounal of Science*, 278:179–216, 1978.

[61] K. Al-Barrak and D. L. Rowell. The solubility of gypsum in calcareous soils. *Geoderma*, 136(3–4):830 – 837, 2006.

[62] O. Al-Rawi, S. Ghannam, and H. R. Al-Ani. Dissolution of gypseous rocks under different circumstances. *Jordan Journal of Civil Engineering*, 5(3):357–379, 2011.

[63] W. Dreybrodt, L. Eisenlohr, B. Madry, and S. Ringer. Precipitation kinetics of calcite in the system $CaCO_3 - H_2O - CO_2$: The conversion to CO_2 by the slow process $H^+ + HCO_3^- \rightarrow CO_2 + H_2O$ as a rate limiting step. *Geochimica et Cosmochimica Acta*, 61(18):3897 – 3904, 1997.

[64] J. Colombani. Dissolution measurement free from mass transport. *Pure Appl. Chem.*, 85, 2012.

[65] R. S. Schechter and J. L. Gidley. The change in pore size distribution from surface reactions in porous media. *AIChE Journal*, 15(3):339–350, 1969.

[66] S. Békri, J. F. Thovert, and P. M. Adler. Dissolution of porous media. *Chemical Engineering Science*, 50(17):2765 – 2791, 1995.

[67] S. Békri, J. F. Thovert, and P. M. Adler. Dissolution and deposition in fractures. *Engineering Geology*, 48(3–4):283 – 308, 1997.

[68] L. Chen, Q. Kang, B. Carey, and W. Tao. Pore-scale study of diffusion–reaction processes involving dissolution and precipitation using the lattice Boltzmann method. *International Journal of Heat and Mass Transfer*, 75(0):483 – 496, 2014.

[69] Q. Kang, D. Zhang, S. Chen, and X. He. Lattice Boltzmann simulation of chemical dissolution in porous media. *Physical Review E*, 65(3):036318, 2002.

[70] J .J. Monaghan. Smoothed particle hydrodynamics. *Reports on Progress in Physics*, 68 (8):1703 – 1759, 2005.

[71] A. M. Tartakovsky, P. Meakin, T. D. Scheibe, and B. D. Wood. A smoothed particle hydrodynamics model for reactive transport and mineral precipitation in porous and fractured porous media. *Water resources research*, 43(5), 2007.

[72] E. M. Ryan and A. M. Tartakovsky. A hybrid micro-scale model for transport in connected macro-pores in porous media. *Journal of contaminant hydrology*, 126(1):61–71, 2011.

[73] C. Pan, M. Hilpert, and C. T. Miller. Lattice-boltzmann simulation of two-phase flow in porous media. *Water Resources Research*, 40(1), 2004.

[74] P. Szymczak and A. J. C. Ladd. Microscopic simulations of fracture dissolution. *Geophysical Research Letters*, 31(23), 2004.

[75] P. Szymczak and A. J. C. Ladd. A network model of channel competition in fracture dissolution. *Geophysical Research Letters*, 33(5), 2006.

[76] D. W. Holmes, J. R. Williams, and P. Tilke. Smooth particle hydrodynamics simulations of low Reynolds number flows through porous media. *International Journal for Numerical and Analytical Methods in Geomechanics*, 35(4):419–437, 2011.

[77] I. Babuška. Homogenization approach in engineering. In R. Glowinski and J.L. Lions, editors, *Computing Methods in Applied Sciences and Engineering*, volume 134 of *Lecture Notes in Economics and Mathematical Systems*, pages 137–153. Springer Berlin Heidelberg, 1976.

[78] Y. Davit, C. G. Bell, H. M. Byrne, L. S. Chapman, L. A. C.and Kimpton, G. E. Lang, J. M. Leonard, K. H. L.and Oliver, N. C. Pearson, R. J. Shipley, et al. Homogenization via formal multiscale asymptotics and volume averaging: How do the two techniques compare? *Advances in Water Resources*, 62:178–206, 2013.

[79] M. David, J. J. Marigo, and C. Pideri. Homogenized interface model describing inhomogeneities located on a surface. *Journal of Elasticity*, 109(2):153–187, 2012.

[80] P. C. Vinh and D. X. Tung. Homogenization of very rough interfaces separating two piezoelectric solids. *Acta Mechanica*, 224(5):1077–1088, 2013.

[81] P. C. Vinh and D. X. Tung. Homogenization of rough two-dimensional interfaces separating two anisotropic solids. *Journal of Applied Mechanics*, 78(4):041014, 2011.

[82] C. Mocenni, E. Sparacino, and J. P. Zubelli. Effective rough boundary parametrization for reaction-diffusion systems. *Applicable Analysis and Discrete Mathematics*, 8(1):33–59, 2014.

[83] S. Haouala and I. Doghri. Modeling and algorithms for two-scale time homogenization of viscoelastic-viscoplastic solids under large numbers of cycles. *International Journal of Plasticity*, 70:98–125, 2015.

[84] J. Zhao. Homogenization of the boundary value for the Neumann problem. *Journal of Mathematical Physics*, 56(2):–, 2015.

[85] G. L. Vignoles, Y. Aspa, and M. Quintard. Modelling of carbon–carbon composite ablation in rocket nozzles. *Composites Science and Technology*, 70(9):1303–1311, 2010.

[86] K. Kumar, T. van Noorden, and I. S. Pop. Upscaling of reactive flows in domains with moving oscillating boundaries. *Discrete and Continuous Dynamical Systems - Series S*, 7(1):95–111, 2014.

[87] Y. Achdou, O. Pironneau, and F. Valentin. Effective boundary conditions for laminar flows over periodic rough boundaries. *Journal of Computational Physics*, 147(1):187 – 218, 1998.

[88] Y. Achdou, P. Le Tallec, F. Valentin, and O. Pironneau. Constructing wall laws with domain decomposition or asymptotic expansion techniques. *Computer Methods in Applied Mechanics and Engineering*, 151(1–2):215 – 232, 1998.

[89] Y. Amirat, O. Bodart, U. De Maio, and A. Gaudiello. Effective boundary condition for Stokes flow over a very rough surface. *Journal of Differential Equations*, 254(8):3395 – 3430, 2013.

[90] G. S. Beavers and D. D. Joseph. Boundary conditions at a naturally permeable wall. *J. Fluid Mech*, 30:197–207, 1967.

[91] P. G. Saffman. On the boundary condition at the interface of a porous medium. *Stud. Appl. Math*, 1:93–101, 1971.

[92] G. Dagan. The generalization of Darcy's law for nonuniform flows. *Water Resources Research*, 15(1):1–7, 1979.

[93] W. Jäger and A. Mikelić. On the boundary conditions at the contact interface between a porous medium and a free fluid. *Annali della Scuola Normale Superiore di Pisa - Classe di Scienze*, 23:403–465, 1996.

[94] W. Jäger, A. Mikelić, and N. Neuss. Asymptotic analysis of the laminar viscous flow over a porous bed. *SIAM Journal on Scientific Computing*, 22(6):2006–2028, 2001.

[95] W. Jäger and A. Mikelić. Modeling effective interface laws for transport phenomena between an unconfined fluid and a porous medium using homogenization. *Transport in Porous Media*, 78:489–508, 2009.

[96] J. A. Ochoa-Tapia and S. Whitaker. Momentum transfer at the boundary between a porous medium and a homogeneous fluid—I. Theoretical development. *International Journal of Heat and Mass Transfer*, 38(14):2635–2646, 1995.

[97] J. A. Ochoa-Tapia and S. Whitaker. Momentum transfer at the boundary between a porous medium and a homogeneous fluid—II. Comparison with experiment. *International Journal of Heat and Mass Transfer*, 38(14):2647 – 2655, 1995.

[98] B. Goyeau, D. Lhuillier, D. Gobin, and M.G. Velarde. Momentum transport at a fluid–porous interface. *International Journal of Heat and Mass Transfer*, 46(21):4071 – 4081, 2003.

[99] M. Chandesris and D. Jamet. Boundary conditions at a planar fluid–porous interface for a Poiseuille flow. *International Journal of Heat and Mass Transfer*, 49(13–14):2137–2150, 2006.

[100] F. J. Valdés-Parada, J. A. Ochoa-Tapia, and J. Alvarez-Ramirez. Diffusive mass transport in the fluid–porous medium inter-region: Closure problem solution for the one-domain approach. *Chemical Engineering Science*, 62(21):6054 – 6068, 2007.

[101] M. Chandesris and D. Jamet. Jump conditions and surface-excess quantities at a fluid/porous interface: A multi-scale approach. *Transport in Porous Media*, 78(3):419–438, 2009.

[102] S. Whitaker. *The Method of Volume Averaging*. Kluwer Academic Publishers, Dordrecht, The Netherlands, 1999.

[103] G. Taylor. Dispersion of soluble matter in solvent flowing slowly through a tube. *Proceedings of the Royal Society of London. Series A. Mathematical and Physical Sciences*, 219(1137):186–203, 1953.

[104] G. Taylor. The dispersion of matter in turbulent flow through a pipe. *Proceedings of the Royal Society of London. Series A. Mathematical and Physical Sciences*, 223(1155):446–468, 1954.

[105] R. Aris. On the dispersion of a solute in a fluid flowing through a tube. *Proceedings of the Royal Society of London. Series A. Mathematical and Physical Sciences*, 235(1200):67–77, 1956.

[106] H. Brenner. *Dispersion Resulting from Flow Through Spatially Periodic Porous Media*. Philosophical transactions of the Royal Society of London. Royal Society, 1980.

[107] A. Eidsath, R. G. Carbonell, S. Whitaker, and L. R. Herrmann. Dispersion in pulsed systems—III: comparison between theory and experiments for packed beds. *Chemical Engineering Science*, 38(11):1803–1816, 1983.

[108] R. Mauri. Dispersion, convection, and reaction in porous media. *Physics of Fluids A: Fluid Dynamics (1989-1993)*, 3(5):743–756, 1991.

[109] M. Quintard and S. Whitaker. Convection, dispersion, and interfacial transport of contaminants: Homogeneous porous media. *Advances in Water resources*, 17:221–239, 1994.

[110] A. Ahmadi, A. Aigueperse, and M. Quintard. Calculation of the effective properties describing active dispersion in porous media: from simple to complex unit cells. *Advances in Water Resources*, 24(3–4):423 – 438, 2001.

[111] C. E. Cohen, D. Ding, M. Quintard, and B. Bazin. From pore scale to wellbore scale: Impact of geometry on wormhole growth in carbonate acidization. *Chemical Engineering Science*, 63(12):3088–3099, 2008.

[112] F. Golfier, R. Lenormand B. Bazin, and M. Quintard. Core-scale description of porous media dissolution during acid injection - part I: Theoretical development. *Computational and Applied Mathematics*, 23:173–194, 2004.

[113] F. Golfier, M. Quintard, B. Bazin, and R. Lenormand. Core-scale description of porous media dissolution during acid injection - part II: calculation of the effective properties. *Computational & Applied Mathematics*, 25:55 – 78, 2006.

[114] F. Golfier, M. Quintard, F. Cherblanc, B. A. Zinn, and B. D. Wood. Comparison of theory and experiment for solute transport in highly heterogeneous porous medium. *Advances in Water Resources*, 30(11):2235 – 2261, 2007.

[115] F. Javadpour. CO_2 injection in geological formations: Determining macroscale coefficients from pore scale processes. *Transport in Porous Media*, 79(1):87–105, 2009.

[116] H. Brenner. *Macrotransport Processes*. Butterworth-Heinemann, 1993.

[117] A. Jourak, J. G. I. Hellström, T. S. Lundström, and V. Frishfelds. Numerical derivation of dispersion coefficients for flow through three-dimensional randomly packed beds of monodisperse spheres. *AIChE Journal*, 60(2):749–761, 2014.

[118] C. Zhao, B. E. Hobbs, and A. Ord. *Fundamentals of Computational Geoscience: Numerical Methods and Algorithms*. Lecture Notes in Earth Sciences. Springer, 2009.

[119] C. Zhao, T. Poulet, K. Regenauer-Lieb, and B. E. Hobbs. Computational modeling of moving interfaces between fluid and porous medium domains. *Computational Geosciences*, 17(1):151–166, 2013.

[120] H. Luo, M. Quintard, G. Debenest, and F. Laouafa. Properties of a diffuse interface model based on a porous medium theory for solid–liquid dissolution problems. *Computational Geosciences*, 16(4):913–932, 2012.

[121] H. Luo, F. Laouafa, J. Guo, and M. Quintard. Numerical modeling of three-phase dissolution of underground cavities using a diffuse interface model. *Int. J. Numer. Anal. Meth. Geomech*, 38:1600–1616, 2014.

[122] P. Szymczak and A. J. C. Ladd. Instabilities in the dissolution of a porous matrix. *Geophysical Research Letters*, 38:L07403, 2011.

[123] C. Zhao, B. E. Hobbs, and A. Ord. Theoretical analyses of nonaqueous phase liquid dissolution-induced instability in two-dimensional fluid-saturated porous media. *International Journal for Numerical and Analytical Methods in Geomechanics*, 34(17):1767–1796, 2010.

[124] C. Zhao, B. E. Hobbs, and A. Ord. Effects of domain shapes on the morphological evolution of nonaqueous-phase-liquid dissolution fronts in fluid-saturated porous media. *Journal of contaminant hydrology*, 138:123–140, 2012.

[125] J. S. Turner. *Buoyancy effects in fluids*. Cambridge Univ. Press, New York, 1973.

[126] P. E. Dijk and B. Berkowitz. Buoyancy-driven dissolution enhancement in rock fractures. *Geology*, 28(11):1051 – 1054, 2000.

[127] C. Oltéan, F. Golfier, and M. A. Buès. Numerical and experimental investigation of buoyancy-driven dissolution in vertical fracture. *Journal Of Geophysical Research: Solid Earth*, 118:1–11, 2013.

[128] B. Gebhart, B. Hassard, S. P. Hastings, and N. Kazarinoff. Multiple steady-state solutions for buoyancy-induced transport in porous media saturated with cold pure or saline water. *Numerical Heat Transfer*, 6(3):337–352, 1983.

[129] E. De Boever, C. Varloteaux, F. H. Nader, A. Foubert, S. Békri, S. Youssef, and E. Rosenberg. Quantification and prediction of the 3D pore network evolution in carbonate reservoir rocks. *Oil Gas Sci. Technol. – Rev. IFP Energies nouvelles*, 67(1):161–178, 2012.

[130] T. Sun. *Upscaling and multiscale simulation by bridging pore scale and continuum scale models.* PhD thesis, The University of Texas at Austin, 2012.

[131] L. Algive, S. Békri, F. H. Nader, O. Lerat, and O. Vizika. Impact of diagenetic alterations on the petrophysical and multiphase flow properties of carbonate rocks using a reactive pore network modeling approach. *Oil & Gas Science and Technology–Revue d'IFP Energies nouvelles*, 67(1):147–160, 2012.

[132] C. Varloteaux, S. Békri, and P. M. Adler. Pore network modelling to determine the transport properties in presence of a reactive fluid: From pore to reservoir scale. *Advances in Water Resources*, 53(0):87 – 100, 2013.

[133] J. P. Nogues, J. P. Fitts, M. A. Celia, and C. A. Peters. Permeability evolution due to dissolution and precipitation of carbonates using reactive transport modeling in pore networks. *Water Resour Res*, 49(9):6006–6021, 2013.

[134] T. D. Scheibe, A. M. Tartakovsky, D. M. Tartakovsky, G. D. Redden, and P. Meakin. Hybrid numerical methods for multiscale simulations of subsurface biogeochemical processes. In *Journal of Physics: Conference Series*, volume 78, page 012063. IOP Publishing, 2007.

[135] I. Battiato, D. M. Tartakovsky, A. M. Tartakovsky, and T Scheibe. On breakdown of macroscopic models of mixing-controlled heterogeneous reactions in porous media. *Advances in water resources*, 32(11):1664–1673, 2009.

[136] M. T. Balhoff, K. E. Thompson, and M. Hjortsø. Coupling pore-scale networks to continuum-scale models of porous media. *Computers &Geosciences*, 33(3):393 – 410, 2007.

[137] I. Battiato, D .M. Tartakovsky, A. M. Tartakovsky, and T. D. Scheibe. Hybrid models of reactive transport in porous and fractured media. *Advances in Water Resources*, 34(9):1140–1150, 2011.

[138] P. Tomin and I. Lunati. Hybrid multiscale finite volume method for two-phase flow in porous media. *Journal of Computational Physics*, 250:293–307, 2013.

[139] J. Chu, B. Engquist, M. Prodanović, and R. Tsai. A multiscale method coupling network and continuum models in porous media II—Single- and two-phase flows. In Roderick Melnik and Ilias S. Kotsireas, editors, *Advances in Applied Mathematics, Modeling, and Computational Science*, volume 66 of *Fields Institute Communications*, pages 161–185. Springer US, 2013.

[140] F. Gabrovšek and W. Dreybrodt. A model of the early evolution of karst aquifers in limestone in the dimensions of length and depth. *Journal of Hydrology*, 240(3–4):206–224, 2001.

[141] C. G. Groves and A. D. Howard. Minimum hydrochemical conditions allowing limestone cave development. *Water Resour. Res.*, 30:607–615, 1994.

[142] C. G. Groves and A. D. Howard. Early development of karst systems: 1. Preferential flow path enlargement under laminar flow. *Water Resour. Res.*, 30:2837–2846, 1994.

[143] A. D. Howard and C. G. Groves. Early development of karst systems: 2. turbulent flow. *Water Resour. Res.*, 31:19–26, 1995.

[144] G. Kaufmann and J. Braun. Karst aquifer evolution in fractured rocks. *Water Resources Research*, 35(11):3223–3238, 1999.

[145] G. Kaufmann and J. Braun. Karst aquifer evolution in fractured, porous rocks. *Water Resources Research*, 36(6):1381–1391, 2000.

[146] T. Clemens, D. Hückinghaus, M. Sauter, R. Liedl, and G. Teutsch. A combined continuum and discrete network reactive transport model for

the simulation of karst development. *IAHS PUBLICATION*, pages 309–320, 1996.

[147] F. Gabrovšek, D. Romanov, and W. Dreybrodt. Early karstification in a dual-fracture aquifer: the role of exchange flow between prominent fractures and a dense net of fissures. *Journal of Hydrology*, 299(1):45–66, 2004.

[148] S. Birk, R. Liedl, M. Sauter, and G. Teutsch. Simulation of the development of gypsum maze caves. *Environmental Geology*, 48(3):296–306, 2005.

[149] F. Gabrovšek and W. Dreybrodt. Karstification in unconfined limestone aquifers by mixing of phreatic water with surface water from a local input: A model. *Journal of Hydrology*, 386(1–4):130–141, 2010.

[150] J. O. Schwarz and F. Enzmann. Simulation of fluid flow on fractures and implications for reactive transport simulations. *Transport in Porous Media*, 96:501–525, 2013.

[151] R. Kuechler, K. Noack, and T. Zorn. Investigation of gypsum dissolution under saturated and unsaturated water conditions. *Ecological Modelling*, 176(1–2):1 – 14, 2004.

[152] D. L. Parkhurst and C. A. J. Appelo. *User's Guide to Phreeqc (version 2)— A Computer Program for Speciation, Batch-reaction, One-dimensional Transport, and Inverse Geochemical Calculations*. U.S. GEOLOGICAL SURVEY, 1999.

[153] F. Bouchelaghem. A numerical and analytical study on calcite dissolution and gypsum precipitation. *Applied Mathematical Modelling*, 34(2):467 – 480, 2010.

[154] M. Quintard, L. Bletzacker, D. Chenu, and S. Whitaker. Nonlinear, multicomponent, mass transport in porous media. *Chemical Engineering Science*, 61(8):2643 – 2669, 2006.

[155] Y. Li and S. Gregory. Diffusion of ions in sea water and in deep-sea sediments. *Geochimica et Cosmochimica Acta*, 38(5):703–714, 1974.

[156] M. Suzuki and S. Maeda. On the mechanism of drying of granular bed—mass transfer from discontinuous source. *Journal of Chemical Engineering of Japan*, 1(1):26–31, 1968.

[157] R. Avissar and R. A. Pielke. A parameterization of heterogeneous land surfaces for atmospheric numerical models and its impact on regional meteorology. *Monthly Weather Review*, 117:2113–2136, October 1989.

[158] A. Carrau. Modélisation numérique d'un écoulement sur paroi rugueuse. *PhD Thesis*, 1992.

[159] Y. Achdou and N. Tchou. Boundary value problems with nonhomogeneous Neumann conditions on a fractal boundary. *Comptes Rendus Mathematique*, 342(8):611–616, 2006.

[160] Y. Achdou, C. Sabot, and N. Tchou. Transparent boundary conditions for the Helmholtz equation in some ramified domains with a fractal boundary. *Journal of Computational Physics*, 220(2):712 – 739, 2007.

[161] W. Jäger and A. Mikelić. On the roughness-induced effective boundary conditions for an incompressible viscous flow. *Journal of Differential Equations*, 170(1):96–122, 2001.

[162] J. Guo, M. Quintard, and F. Laouafa. Dispersion in porous media with heterogeneous nonlinear reactions. *Transport in Porous Media*, 109(3):541–570, 2015.

[163] M. Quintard and S. Whitaker. Dissolution of an immobile phase during flow in porous media. *Industrial & engineering chemistry research*, 38(3):833–844, 1999.

[164] F. A. Coutelieris, M. E. Kainourgiakis, A. K. Stubos, E. S. Kikkinides, and Y. C. Yortsos. Multiphase mass transport with partitioning and inter-phase transport in porous media. *Chemical Engineering Science*, 61(14):4650 – 4661, 2006.

[165] C. Soulaine, G. Debenest, and M. Quintard. Upscaling multi-component two-phase flow in porous media with partitioning coefficient. *Chem Eng Sci*, 66:6180–6192, 2011.

[166] F. Golfier, M. Quintard, and S. Whitaker. Heat and mass transfer in tubes: An analysis using the method of volume averaging. *J. Porous Media*, 5:169–185, 2002.

[167] S. Whitaker. Transport processes with heterogeneous reaction. In S. Whitaker and A. E. Cassano, editors, *Concepts and Design of Chemical Reactors*, pages 1–94. Gordon and Breach Publishers, New York, 1986.

[168] D. A. Edwards, M. Shapiro, and H. Brenner. Dispersion and reaction in two-dimensional model porous media. *Physics of Fluids A: Fluid Dynamics (1989-1993)*, 5(4):837–848, 1993.

[169] M. Shapiro and H. Brenner. Dispersion of a chemically reactive solute in a spatially periodic model of a porous medium. *Chemical Engineering Science*, 43:551–571, 1988.

[170] S. Whitaker. The method of volume averaging: An application to diffusion and reaction in porous catalysts. *Proc. Natl. Sci. Counc. ROC(A)*, 15(6):465–474, 1991.

[171] B. D. Wood, K. Radakovich, and F. Golfier. Effective reaction at a fluid–solid interface: Applications to biotransformation in porous media. *Advances in Water Resources*, 30(6–7):1630 – 1647, 2007. Biological processes in porous media: From the pore scale to the field.

[172] F. Heße, F. A. Radu, M. Thullner, and S. Attinger. Upscaling of the advection–diffusion–reaction equation with Monod reaction. *Advances in water resources*, 32(8):1336–1351, 2009.

[173] L. Orgogozo, F. Golfier, M. Buès, and Quintard M. Upscaling of transport processes in porous media with biofilms in non-equilibrium conditions. *Adv Water Resour*, 33:585–600, 2010.

[174] J. H. Cushman, L. S. Bennethum, and B. X. Hu. A primer on upscaling tools for porous media. *Advances in Water Resources*, 25(8–12):1043 – 1067, 2002.

[175] G. Dagan. *Flow and Transport in Porous Formations*. Springer, 1989.

[176] J. Cushman and T. R. Ginn. Nonlocal dispersion in media with continuously evolving scales of heterogeneity. *Transport in Porous Media*, 13:123–138, 1993.

[177] A. Bensoussan, J. L. Lions, and G. Papanicolau. *Asymptotic Analysis for Periodic Structures*. North-Holland Publishing Company, 1978.

[178] M. Quintard and S. Whitaker. Transport in ordered and disordered porous media V: Geometrical results for two-dimensional systems. *Transport in Porous Media*, 15:183–196, 1994.

[179] M. Quintard and S. Whitaker. Transport in ordered and disordered porous media I: The cellular average and the use of weighting functions. *Transport in Porous Media*, 14:163–177, 1994.

[180] M. Quintard and S. Whitaker. Transport in ordered and disordered porous media II: Generalized volume averaging. *Transport in Porous Media*, 14:179–206, 1994.

[181] M. Quintard and S. Whitaker. Transport in ordered and disordered porous media III: Closure and comparison between theory and experiment. *Transport in Porous Media*, 15:31–49, 1994.

[182] M. Quintard and S. Whitaker. Transport in ordered and disordered porous media IV: Computer generated porous media for three-dimensional systems. *Transport in Porous Media*, 15:51–70, 1994.

[183] M. E. Gurtin, E. Fried, and L. Anand. *The Mechanics and Thermodynamics of Continua*. Cambridge, 2013.

[184] O. Stephansson, J. Hudson, and L. Jing. *Coupled Thermo-Hydro-Mechanical-Chemical Processes in Geo-systems*. Elsevier, 2004.

[185] L. Laloui L. Vulliet, B. Schrefler. *Environmental Geomechanics*. EPFL Press, 2002.

[186] O. Coussy. *Poromechanics*. John Wiley & Sons, 2004.

[187] T. Hueckel. Special issue on chemo-mechanical interaction in geomaterials. *Computers and Geotechnics*, 34(4), 2007.

[188] J. Bear. On the tensor form of dispersion in porous media. *J. Geophys. Res.*, 66:1185–1197, 1961.

[189] I. Ligaarden, M. Krotkiewski, K. A. Lie, M. Pal, and D. Schmid. On the Stokes-Brinkman equations for modeling flow in carbonate reservoirs. In *12th European Conference on the Mathematics of Oil Recovery*, 2010.

[190] H. D. Baehr and K. Stephan. *Heat and Mass Transfer*. Springer, 2006.

[191] A. H. Cooper. Subsidence resulting from the dissolution of Permian gypsum in the Ripon area; its relevance to mining and water abstraction. *Geological Society, London, Engineering Geology Special Publications*, 5(1):387–390, 1988.

[192] MARC. *User Manuel*. Msc Software, 2011.

Appendix A

Simplified closure problems

In this appendix it is assumed that the interface velocity is small. The closure problems in 4.2.2 may be written as

Problem I: for $\langle \omega_l \rangle^l$

$$\frac{\partial s_l}{\partial t} + \mathbf{v}_l \cdot \nabla s_l = \nabla . (D_l \nabla s_l) + \varepsilon_l^{-1} X_l, \tag{A.1}$$

$$\text{BC 1} \qquad \mathbf{n}_{ls} \cdot \nabla s_l = -\frac{M_{Ca} k_s}{\rho_l \omega_{eq} D_l} \left(1 - \frac{\langle \omega_l \rangle^l}{\omega_{eq}} \right)^{n-1} (1 + n\, s_l) \qquad \text{at } A_{ls}(t), \tag{A.2}$$

$$\text{BC 2} \qquad \mathbf{n}_{li} \cdot \nabla s_l = 0 \quad \text{at } A_{li}, \tag{A.3}$$

$$\langle s_l \rangle = 0, \tag{A.4}$$

$$s_l (\mathbf{x} + \mathbf{l}_i) = s_l (\mathbf{x}), \tag{A.5}$$

$$X_l = -\frac{1}{V} \int_{A_{ls}} \mathbf{n}_{ls} \cdot D_l \nabla s_l dA. \tag{A.6}$$

Problem II: for $\nabla \langle \omega_l \rangle^l$

$$\frac{\partial \mathbf{b}_l}{\partial t} + \mathbf{v}_l \cdot (\nabla \mathbf{b}_l + s_l \mathbf{I}) + \tilde{\mathbf{v}}_l - \varepsilon_l^{-1} \langle \tilde{\mathbf{v}}_l s_l \rangle = \nabla \cdot (D_l (\nabla \mathbf{b}_l + s_l \mathbf{I})) + \varepsilon_l^{-1} \mathbf{u}_l, \tag{A.7}$$

$$\text{BC 1} \qquad \mathbf{n}_{ls}\cdot\left(\left(\nabla\mathbf{b}_l+s_l\mathbf{I}\right)\right)+\mathbf{n}_{ls}=-n\frac{M_{Ca}k_s}{\rho_l\omega_{eq}D_l}\left(1-\frac{\langle\omega_l\rangle^l}{\omega_{eq}}\right)^{n-1}\mathbf{b}_l \quad \text{at } A_{ls}(t), \tag{A.8}$$

$$\text{BC 2} \qquad \mathbf{n}_{li}\cdot\left(-\left(\nabla\mathbf{b}_l+s_l\mathbf{I}\right)\right)=\mathbf{n}_{li} \quad \text{at } A_{li}, \tag{A.9}$$

$$\langle\mathbf{b}_l\rangle=0, \tag{A.10}$$

$$\mathbf{b}_l\left(\mathbf{x}+\mathbf{l}_i\right)=\mathbf{b}_l\left(\mathbf{x}\right), \tag{A.11}$$

$$\mathbf{u}_l=-\frac{1}{V}\int_{A_{ls}}\mathbf{n}_{ls}.D_l\left(\nabla\mathbf{b}_l+s_l\mathbf{I}\right)dA-\frac{1}{V}\int_{A_{li}}\mathbf{n}_{li}\cdot D_l\left(\nabla\mathbf{b}_l+s_l\mathbf{I}\right)dA. \tag{A.12}$$

While the interface velocity does not appear anymore in the equations, it must be reminded that the evolving geometry is still there and this is emphasized by the introduction of the notation $A_{ls}(t)$. As discussed in the text body, the classical geochemistry problem are faced here, either to solve coupled pore-scale (here the closure problems) and macro-scale equations at each time step in order to compute the interface evolution, or assume a given interface evolution and solve the closure problem for each realization, which in turn yields effective properties dependent on, for instance, the medium porosity. This difficulty is not further discussed which is well known when solving dissolution or crystallization problems. It is interesting to put the closure problem under a dimensionless form using the following scaling

$$x' = x/l_r, \tag{A.13}$$
$$\mathbf{b}_l^{'} = \mathbf{b}_l/l_r, \tag{A.14}$$
$$\mathbf{v}_l^{'} = \mathbf{v}_l/U_r, \tag{A.15}$$
$$t' = \frac{D_l}{l_r^2}\ t. \tag{A.16}$$

which leads to

Problem I: for $\langle\omega_l\rangle^l$

$$\frac{\partial s_l}{\partial t'} + \mathrm{Pe}\,\mathbf{v}_l^{'} \cdot \nabla' s_l = \nabla' \cdot \left(\nabla' s_l\right) + \varepsilon_l^{-1} X_l^{'}, \tag{A.17}$$

$$\begin{aligned} &\mathrm{BC}\,1 \qquad \mathbf{n}_{ls} \cdot \nabla' s_l = \\ &-\mathrm{Da}\,(1 + n\, s_l) \qquad \text{at } A_{ls}(t'), \end{aligned} \tag{A.18}$$

$$\mathrm{BC}\,2 \qquad \mathbf{n}_{li} \cdot \nabla' s_l = 0 \quad \text{at } A_{li}, \tag{A.19}$$

$$\langle s_l \rangle^{'} = 0, \tag{A.20}$$

$$s_l\left(\mathbf{x}' + \mathbf{l}_i^{'}\right) = s_l\left(\mathbf{x}'\right), \tag{A.21}$$

$$X_l^{'} = -\frac{1}{V'} \int_{A_{ls}^{'}} \mathbf{n}_{ls} \cdot \nabla' s_l dA' = \frac{l_r^2}{D_l} X_l. \tag{A.22}$$

where the Péclet and Damköhler[1] numbers are defined as

$$\mathrm{Pe} = \frac{U_r l_r}{D_l}, \tag{A.23}$$

$$\mathrm{Da} = \frac{M_{Ca}}{\rho_l \omega_{eq}} \frac{l_r k_s}{D_l} \left(1 - \frac{\langle \omega_l \rangle^l}{\omega_{eq}}\right)^{.n-1} \tag{A.24}$$

Problem II: for $\nabla \langle \omega_l \rangle^l$

$$\frac{\partial \mathbf{b}_l^{'}}{\partial t'} + \mathrm{Pe}\,\mathbf{v}_l^{'} \cdot \left(\nabla' \mathbf{b}_l^{'} + s_l \mathbf{I}\right) + \mathrm{Pe}\,\tilde{\mathbf{v}}_l^{'} - \varepsilon_l^{-1} \mathrm{Pe} \left\langle \tilde{\mathbf{v}}_l^{'} s_l \right\rangle^{'} = \nabla' \cdot \left(\nabla' \mathbf{b}_l^{'} + s_l \mathbf{I}\right) + \varepsilon_l^{-1} \mathbf{u}_l^{'}, \tag{A.25}$$

$$\mathrm{BC}\,1 \qquad \mathbf{n}_{ls} \cdot \left(\nabla' \mathbf{b}_l^{'} + s_l \mathbf{I}\right) + \mathbf{n}_{ls} = -n\,\mathrm{Da}\,\mathbf{b}_l^{'} \quad \text{at } A_{ls}(t'), \tag{A.26}$$

$$\mathrm{BC}\,2 \qquad \mathbf{n}_{li} \cdot \left(-\left(\nabla' \mathbf{b}_l^{'} + s_l \mathbf{I}\right)\right) = \mathbf{n}_{li} \quad \text{at } A_{li}, \tag{A.27}$$

[1] For convenience, $\frac{M_{Ca}}{\rho_l \omega_{eq}}$ has been included in the definition.

$$\left\langle \mathbf{b}_l^{'} \right\rangle^{'} = 0, \tag{A.28}$$

$$\mathbf{b}_l^{'}\left(\mathbf{x}' + \mathbf{l}_i^{'}\right) = \mathbf{b}_l^{'}\left(\mathbf{x}'\right), \tag{A.29}$$

$$\mathbf{u}_l^{'} = -\frac{1}{V'}\int_{A_{ls}'} \mathbf{n}_{ls} \cdot \left(\nabla' \mathbf{b}_l^{'} + s_l \mathbf{I}\right) dA' - \frac{1}{V'}\int_{A_{li}'} \mathbf{n}_{li} \cdot \left(\nabla' \mathbf{b}_l^{'} + s_l \mathbf{I}\right) dA' = \frac{l_r^2}{D_l}\mathbf{u}_l. \tag{A.30}$$

Now the two limiting cases: small and large Damköhler numbers may be examined.

Appendix B

Small Da numbers

In the limit $\mathrm{Da} \to 0$, the closure problems become

Problem I: for $\langle \omega_l \rangle^l$

$$\frac{\partial s_l}{\partial t'} + \mathrm{Pe}\, \mathbf{v}_l^{'} \cdot \nabla' s_l = \nabla' \cdot \left(\nabla' s_l \right) + \varepsilon_l^{-1} X_l^{'}, \tag{B.1}$$

$$\mathrm{BC}\,1 \qquad \mathbf{n}_{ls} \cdot \nabla' s_l = 0 \qquad \text{at } A_{ls}(t'), \tag{B.2}$$

$$\mathrm{BC}\,2 \qquad \mathbf{n}_{li} \cdot \nabla' s_l = 0 \quad \text{at } A_{li}, \tag{B.3}$$

$$\langle s_l \rangle^{'} = 0, \tag{B.4}$$

$$s_l \left(\mathbf{x}' + \mathbf{l}_i^{'} \right) = s_l \left(\mathbf{x}' \right), \tag{B.5}$$

$$X_l^{'} = 0, \tag{B.6}$$

and the resulting s_l is zero since there is no source terms in the equations.

Problem II: for $\nabla \langle \omega_l \rangle^l$

$$\frac{\partial \mathbf{b}_l^{'}}{\partial t'} + \mathrm{Pe}\, \mathbf{v}_l^{'} \cdot \left(\nabla' \mathbf{b}_l^{'} \right) + \mathrm{Pe}\, \tilde{\mathbf{v}}_l^{'} = \nabla' \cdot \nabla' \mathbf{b}_l^{'} + \varepsilon_l^{-1} \mathbf{u}_l^{'}, \tag{B.7}$$

$$\mathrm{BC}\,1 \qquad \mathbf{n}_{ls} \cdot \nabla' \mathbf{b}_l^{'} + \mathbf{n}_{ls} = 0 \quad \text{at } A_{ls}(t'), \tag{B.8}$$

$$\mathrm{BC}\,2 \qquad \mathbf{n}_{li} \cdot \nabla' \mathbf{b}_l^{'} = -\mathbf{n}_{li} \quad \text{at } A_{li}, \tag{B.9}$$

$$\left\langle \mathbf{b}_l^{'} \right\rangle^{'} = 0, \tag{B.10}$$

$$\mathbf{b}_l^{'}\left(\mathbf{x}' + \mathbf{l}_i^{'}\right) = \mathbf{b}_l^{'}\left(\mathbf{x}'\right), \tag{B.11}$$

$$\mathbf{u}_l^{'} = -\frac{1}{V'}\int_{A_{ls}^{'}} \mathbf{n}_{ls} \cdot \nabla' \mathbf{b}_l^{'} dA' - \frac{1}{V'}\int_{A_{li}^{'}} \mathbf{n}_{li} \cdot \nabla' \mathbf{b}_l^{'} dA' = \nabla \varepsilon_l = 0. \tag{B.12}$$

One recovers the closure problem for *passive dispersion*.

Appendix C

Large Da numbers

In order to obtain a limit $\mathrm{Da} \to \infty$, two conditions, as emphasized in Sec. 4.2.4, must be fulfilled:

1. the physical parameters must be such that $\frac{M_{Ca}}{\rho_l \omega_{eq}} \frac{l_r k_s}{D_l} \gg 1$,
2. and $n = 1$ (since $\langle \omega_l \rangle^l$ as a tendency to grow up to ω_{eq}).

In that case, the closure problems become

Problem I: for $\langle \omega_l \rangle^l$

$$\frac{\partial s_l}{\partial t'} + \mathrm{Pe}\, \mathbf{v}_l^{'} \cdot \nabla' s_l = \nabla' \cdot \left(\nabla' s_l \right) + \varepsilon_l^{-1} X_l^{'}, \tag{C.1}$$

$$\mathrm{BC}\,1 \qquad s_l = -1 \qquad \text{at } A_{ls}(t'), \tag{C.2}$$

$$\mathrm{BC}\,2 \qquad \mathbf{n}_{li} \cdot \nabla' s_l = 0 \quad \text{at } A_{li}, \tag{C.3}$$

$$\langle s_l \rangle^{'} = 0, \tag{C.4}$$

$$s_l \left(\mathbf{x}' + \mathbf{l}_i^{'} \right) = s_l \left(\mathbf{x}' \right), \tag{C.5}$$

in which

$$X_l^{'} = -\frac{1}{V'} \int_{A_{ls}^{'}} \mathbf{n}_{ls} \cdot \nabla' s_l dA' = \frac{l_r^2}{D_l} X_l. \tag{C.6}$$

Problem II: for $\nabla \langle \omega_l \rangle^l$

$$\frac{\partial \mathbf{b}_l^{'}}{\partial t'} + \mathrm{Pe}\,\mathbf{v}_l^{'} \cdot \left(\nabla' \mathbf{b}_l^{'} + s_l \mathbf{I}\right) + \mathrm{Pe}\,\tilde{\mathbf{v}}_l^{'} - \varepsilon_l^{-1}\mathrm{Pe}\left\langle \tilde{\mathbf{v}}_l^{'} s_l \right\rangle^{'} = \nabla' \cdot \left(\nabla' \mathbf{b}_l^{'} + s_l \mathbf{I}\right) + \varepsilon_l^{-1} \mathbf{u}_l^{'}, \tag{C.7}$$

$$\text{BC 1} \qquad \mathbf{b}_l^{'} = 0 \quad \text{at } A_{ls}(t'), \tag{C.8}$$

$$\text{BC 2} \qquad \mathbf{n}_{li} \cdot \left(-\left(\nabla' \mathbf{b}_l^{'} + s_l \mathbf{I}\right)\right) = \mathbf{n}_{li} \quad \text{at } A_{li}, \tag{C.9}$$

$$\left\langle \mathbf{b}_l^{'} \right\rangle^{'} = 0, \tag{C.10}$$

$$\mathbf{b}_l^{'}\left(\mathbf{x}' + \mathbf{l}_i^{'}\right) = \mathbf{b}_l^{'}\left(\mathbf{x}'\right), \tag{C.11}$$

in which

$$\mathbf{u}_l^{'} = -\frac{1}{V'}\int_{A_{ls}^{'}} \mathbf{n}_{ls} \cdot \left(\nabla' \mathbf{b}_l^{'} + s_l \mathbf{I}\right) dA' - \frac{1}{V'}\int_{A_{li}^{'}} \mathbf{n}_{li} \cdot \left(\nabla' \mathbf{b}_l^{'} + s_l \mathbf{I}\right) dA' = \frac{l_r^2}{D_l}\mathbf{u}_l. \tag{C.12}$$

It must also be emphasized that the resulting effective parameters do not depend anymore on Da and are purely defined by the transport problem towards the surface (diffusion controlled case).

It is worth noting the following relationship

$$\rho_l X_l = \frac{1}{V}\int_{A_{ls}} \mathbf{n}_{ls} \cdot \rho_l s_l \left(\mathbf{v}_l - \mathbf{w}_{sl}\right) dA - \frac{1}{V}\int_{A_{ls}} \mathbf{n}_{ls} \cdot \rho_l D_l \nabla s_l dA. \tag{C.13}$$

Appendix D

Case of a linear reaction rate

This case is obtained when $n = 1$. Eq. 2.21 can be written as

$$\text{B.C.1} \qquad \mathbf{n}_{ls} \cdot \left(\rho_l \omega_l \left(\mathbf{v}_l - \mathbf{w}_{sl}\right) - \rho_l D_l \nabla \omega_l\right) = -M_{Ca} k_s \left(1 - \frac{\omega_l}{\omega_{eq}}\right) \qquad \text{at } A_{ls}, \tag{D.1}$$

The Damköhler number becomes

$$\mathrm{Da} = \frac{M_{Ca}}{\rho_l \omega_{eq}} \frac{l_r k_s}{D_l}, \tag{D.2}$$

The simplified closure problems become

Problem I: for $\langle \omega_l \rangle^l$

$$\frac{\partial s_l}{\partial t'} + \mathrm{Pe}\, \mathbf{v}_l^{'} \cdot \nabla' s_l = \nabla' \cdot \left(\nabla' s_l\right) + \varepsilon_l^{-1} X_l^{'}, \tag{D.3}$$

$$\begin{aligned} &\text{BC 1} \qquad \mathbf{n}_{ls} \cdot \nabla' s_l = \\ &-\mathrm{Da}\,(1 + s_l) \qquad \text{at } A_{ls}(t'), \end{aligned} \tag{D.4}$$

$$\text{BC 2} \qquad \mathbf{n}_{li} \cdot \nabla' s_l = 0 \quad \text{at } A_{li}, \tag{D.5}$$

$$\langle s_l \rangle^{'} = 0, \tag{D.6}$$

$$s_l\left(\mathbf{x}' + \mathbf{l}_i^{'}\right) = s_l\left(\mathbf{x}'\right), \tag{D.7}$$

$$X_l^{'} = -\frac{1}{V'}\int_{A_{ls}^{'}} \mathbf{n}_{ls}\cdot\nabla' s_l dA' = \frac{l_r^2}{D_l}X_l. \tag{D.8}$$

Problem II: for $\nabla\langle\omega_l\rangle^l$

$$\frac{\partial \mathbf{b}_l^{'}}{\partial t'} + \mathrm{Pe}\,\mathbf{v}_l^{'}\cdot\left(\nabla'\mathbf{b}_l^{'} + s_l\mathbf{I}\right) + \mathrm{Pe}\,\tilde{\mathbf{v}}_l^{'} - \varepsilon_l^{-1}\mathrm{Pe}\left\langle\tilde{\mathbf{v}}_l^{'}s_l\right\rangle^{'} = \nabla'\cdot\left(\nabla'\mathbf{b}_l^{'} + s_l\mathbf{I}\right) + \varepsilon_l^{-1}\mathbf{u}_l^{'}, \tag{D.9}$$

$$\text{BC 1} \qquad \mathbf{n}_{ls}\cdot\left(\nabla'\mathbf{b}_l^{'} + s_l\mathbf{I}\right) + \mathbf{n}_{ls} = -\mathrm{Da}\,\mathbf{b}_l^{'} \quad \text{at } A_{ls}(t'), \tag{D.10}$$

$$\text{BC 2} \qquad \mathbf{n}_{li}\cdot\left(-\left(\nabla'\mathbf{b}_l^{'} + s_l\mathbf{I}\right)\right) = \mathbf{n}_{li} \quad \text{at } A_{li}, \tag{D.11}$$

$$\left\langle\mathbf{b}_l^{'}\right\rangle^{'} = 0, \tag{D.12}$$

$$\mathbf{b}_l^{'}\left(\mathbf{x}' + \mathbf{l}_i^{'}\right) = \mathbf{b}_l^{'}\left(\mathbf{x}'\right), \tag{D.13}$$

$$\mathbf{u}_l^{'} = -\frac{1}{V'}\int_{A_{ls}^{'}} \mathbf{n}_{ls}\cdot\left(\nabla'\mathbf{b}_l^{'} + s_l\mathbf{I}\right)dA' - \frac{1}{V'}\int_{A_{li}^{'}} \mathbf{n}_{li}\cdot\left(\nabla'\mathbf{b}_l^{'} + s_l\mathbf{I}\right)dA' = \frac{l_r^2}{D_l}\mathbf{u}_l. \tag{D.14}$$

The mass exchange rate, from Eq. 4.55, becomes

$$\frac{\omega_{eq}}{M_{Ca}}K_{Ca} = -a_{vl}k_{s,eff}\left(\omega_{eq} - \langle\omega_l\rangle^l\right) + a_{vl}k_s\langle\mathbf{b}_l\rangle_{ls}\cdot\nabla\langle\omega_l\rangle^l, \tag{D.15}$$

where an *effective reaction rate*, $k_{s,eff}$ has been introduced such as

$$\frac{k_{s,eff}}{k_s} = (1 + \langle s_l\rangle_{ls}). \tag{D.16}$$

Two limit cases with respect to the Da number lead to

1. $\mathrm{Da}\to 0$: we have $s_l = 0$ and hence $\frac{k_{s,eff}}{k_s} = 1$
2. $\mathrm{Da}\to\infty$: the effective reaction rate becomes independent of Da and is only controlled by the transport problem.

Now a stratified unit cell is considered as represented Fig. D.1, in which there is no insoluble material.

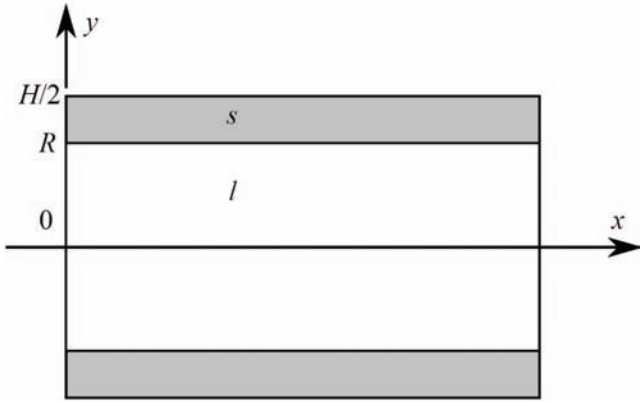

Figure D.1: Stratified Unit Cell.

The medium volume fraction is

$$\varepsilon_l = \frac{2R}{H}, \tag{D.17}$$

and the specific area

$$a_{vl} = 2/H. \tag{D.18}$$

Problem I may be solved analytically in the steady-state case to obtain

$$s_l = \frac{R'^2 - 3y'^2}{2R'^2 + 6R'/\mathrm{Da}}, \tag{D.19}$$

where $l_r = H$ has been adopted.

In terms of effective reaction rate, one has

$$k_{s,eff}/k_s = (1 + \langle s_l \rangle_{ls}) = 1 - \frac{2R'^2}{2R'^2 + 6R'/\mathrm{Da}} = \frac{1}{1 + \frac{1}{3}R'\mathrm{Da}}, \tag{D.20}$$

which can be written

$$k_{s,eff}/k_s = \frac{1}{1 + \frac{1}{6}\varepsilon_l \mathrm{Da}}. \tag{D.21}$$

It is classically obtained that the effective coefficient does not depend upon the velocity field for such a Unit Cell. It must be understood that this result, because of the periodicity condition, corresponds to a fully developed concentration field, i.e., at some distance of the entrance region (see [166]). If one wants to take into account precisely the entrance region effect (i.e., dissolution at the beginning of the front), one has to develop a non-local closure in which

the distance from the front beginning will play a role.

The limit $\mathrm{Da} \to 0$ leads to

$$k_{s,eff}/k_s = 1, \tag{D.22}$$

and the limit $\mathrm{Da} \to \infty$ leads to

$$k_{s,eff}/k_s = 0. \tag{D.23}$$

However, this latter result cannot be used to calculate the mass exchange term and the expression Eq. 4.66 has to be reverted

$$K_{Ca} = \omega_{eq} K_g + \rho_l \alpha_l \left(\langle \omega_l \rangle^l - \omega_{eq} \right) + \rho_l \mathbf{h}_l \cdot \nabla \langle \omega_l \rangle^l, \tag{D.24}$$

where

$$\alpha_l = \frac{1}{V} \int_{A_{ls}} \mathbf{n}_{ls} \cdot (-D_l \nabla s_l)\, dA, \tag{D.25}$$

and

$$\mathbf{h}_l = \left(\frac{1}{V} \int_{A_{ls}} \mathbf{n}_{ls} \cdot (-D_l \nabla \mathbf{b}_l)\, dA \right). \tag{D.26}$$

The mass exchange coefficient can be calculated as

$$\frac{\alpha_l H^2}{D_l} = -\frac{1}{V'} \int_{A'_{ls}} \mathbf{n}_{ls} \cdot \nabla' s_l dA' = \frac{12}{\varepsilon_l}. \tag{D.27}$$

Plots of the effectiveness factor $k_{s,eff}/k_s$ are shown in Fig. D.2.

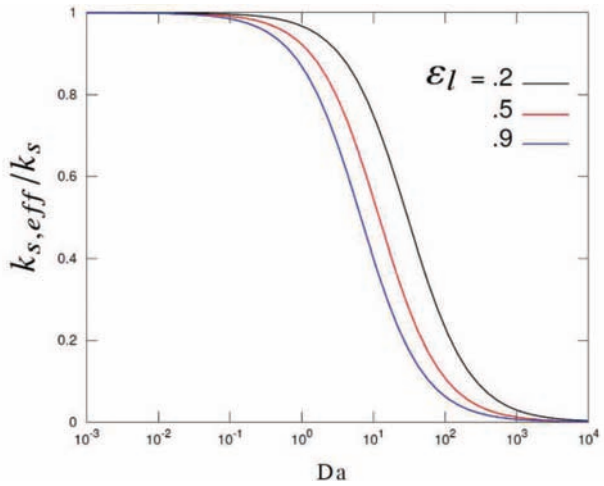

Figure D.2: Effectiveness factor as a function of the Damköhler number.

Appendix E

Decomposition of the closure variables

Owing to the definition of $\mathbf{u}_l^{'}$ and $X_l^{'}$, the closure problems related to s_l and $\mathbf{b}_l^{'}$ involves integro-differencial equations. However, it is possible to find a more convenient way, decomposing the mapping variables, to solve such problems, as done in [109, 165]. The decompositions for s_l and $\mathbf{b}_l^{'}$ write

$$s_l = -\frac{1}{n} + X_l' \psi_s, \tag{E.1}$$

$$\mathbf{b}_l^{'} = \mathbf{b}_0^{'} + \psi_b \mathbf{u}_l^{'}. \tag{E.2}$$

Closure problems for ψ_s, $\mathbf{b}_0'$ and ψ_b are presented below.

Problem Ia: for ψ_s

$$\frac{\partial \psi_s}{\partial t'} + \mathrm{Pe}\, \mathbf{v}_l^{'}.\nabla' \psi_s = \nabla'.\left(\nabla' \psi_s\right) + \varepsilon_l^{-1}, \tag{E.3}$$

$$\begin{aligned} &\mathrm{BC}\,1 \qquad \mathbf{n}_{ls}.\nabla^{'} \psi_s = \\ &-n\,\mathrm{Da}\,\psi_s \qquad \text{at } A_{ls}(t'), \end{aligned} \tag{E.4}$$

$$\mathrm{BC}\,2 \qquad \mathbf{n}_{li}.\nabla' \psi_s = 0 \quad \text{at } A_{li}, \tag{E.5}$$

$$\psi_s\left(\mathbf{x}^{'} + \mathbf{l}_i^{'}\right) = \psi_s\left(\mathbf{x}^{'}\right). \tag{E.6}$$

Problem IIa: for $\mathbf{b}_0^{'}$

$$\frac{\partial \mathbf{b}_0^{'}}{\partial t'} + \mathrm{Pe}\,\mathbf{v}_l^{'}.\left(\nabla^{'}\mathbf{b}_0^{'} + s_l\mathbf{I}\right) + \mathrm{Pe}\,\tilde{\mathbf{v}}_l^{'} - \varepsilon_l^{-1}\mathrm{Pe}\left\langle \tilde{\mathbf{v}}_l^{'} s_l \right\rangle^{'} = \nabla'.\left(\nabla^{'}\mathbf{b}_0^{'} + s_l\mathbf{I}\right), \quad \text{(E.7)}$$

$$\text{BC 1} \qquad \mathbf{n}_{ls}.\left(\nabla^{'}\mathbf{b}_0^{'} + s_l\mathbf{I}\right) + \mathbf{n}_{ls} = -\,n\,\mathrm{Da}\,\mathbf{b}_0^{'} \quad \text{at } A_{ls}(t'), \quad \text{(E.8)}$$

$$\text{BC 2} \qquad \mathbf{n}_{li}.\left(-\left(\nabla^{'}\mathbf{b}_0^{'} + s_l\mathbf{I}\right)\right) = \mathbf{n}_{li} \quad \text{at } A_{li}, \quad \text{(E.9)}$$

$$\mathbf{b}_0^{'}\left(\mathbf{x}^{'} + \mathbf{l}_i^{'}\right) = \mathbf{b}_0^{'}\left(\mathbf{x}^{'}\right). \quad \text{(E.10)}$$

Problem IIb: for ψ_b

$$\frac{\partial \psi_b}{\partial t'} + \mathrm{Pe}\,\mathbf{v}_l^{'}.\nabla^{'}\psi_b = \nabla^{'}.\left(\nabla^{'}\psi_b\right) + \varepsilon_l^{-1}, \quad \text{(E.11)}$$

$$\text{BC 1} \qquad \mathbf{n}_{ls}.\left(\nabla^{'}\psi_b\right) = -\,n\,\mathrm{Da}\,\psi_b \quad \text{at } A_{ls}(t'), \quad \text{(E.12)}$$

$$\text{BC 2} \qquad \mathbf{n}_{li}.\left(-\nabla^{'}\psi_b\right) = 0 \quad \text{at } A_{li}, \quad \text{(E.13)}$$

$$\psi_b\left(\mathbf{x}^{'} + \mathbf{l}_i^{'}\right) = \psi_b\left(\mathbf{x}^{'}\right). \quad \text{(E.14)}$$

The constrains of Eqs. C.4 and C.10, i.e., the averages of s_l and of $\mathbf{b}_l^{'}$ are 0, allow us to write

$$X_l^{'} = \frac{\varepsilon_l}{n\left\langle \psi_s \right\rangle}, \quad \text{(E.15)}$$

and

$$\mathbf{u}_l^{'} = -\frac{\left\langle \mathbf{b}_0^{'} \right\rangle}{\left\langle \psi_b \right\rangle}. \quad \text{(E.16)}$$